SCIENCE ▪ PASSION ▪ TECHNOLOGY

TU Graz

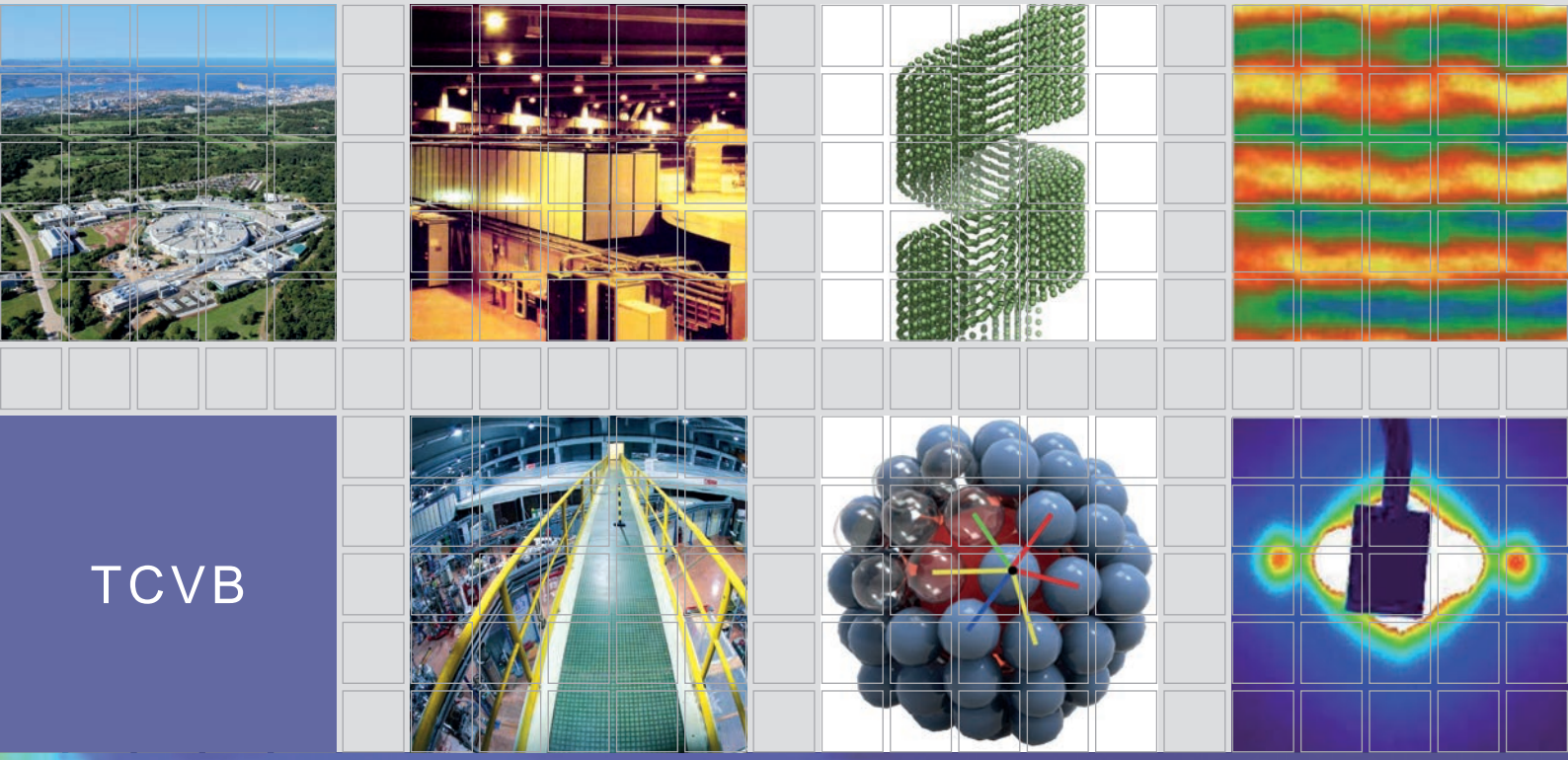

TCVB

ANNUAL REPORT 2011

Austrian SAXS Beamline at elettra

Austrian Small Angle X-ray Scattering (SAXS) Beamline at ELETTRA

Annual Report 2011

Compiled by Sigrid Bernstorff & Heinz Amenitsch

Cover pictures taken from the user contributions:

S. Haviar et al. pages 53-55 (front cover picture & backside right down)
A. Turković et al. pages 67-68 (front middle right up)
E. M. F. Vieira et al. pages 69-71 (front right up)
R. Asor et al. pages 73-74 (front middle right down)
G.R Mitchell et al. pages 61-62 (front right down)

A. Yaghmur et al. pages 97-98 (backside cover right up)
A. Yaghmur et al. pages 99-101 (backside cover middle right up)
K. Kornmüller et al. pages 78-79 (backside cover middle right down)

Table of Contents

Preface

Peter Laggner
Past Director of
Institute of Biophysics and Nanosystems Research
Austrian Academy of Sciences

This is the 15th Annual Report since we began this series with the issue of 1996/97, and it is the last one for which I have the pleasure and honor of writing a preface. I have retired at the end of 2011 at the age of 67 – one year ahead of time - from my position as a Director of IBN, when I realized that I could not be of any great help any more in this capacity. It is reassuring that this has meanwhile led to a new organization of the scientific capacities of the former IBN.

It is well worth browsing through all the previous issues, which are compiled in the web under: http://www.elettra.trieste.it/lightsources/elettra/elettra-beamlines/saxs/annual-report.html. It makes me feel happy to see the ambitious and growing efforts, year by year by a great user community in a common pursuit - to use SAXS as a central method with many clever variations. In the beginning we had the clear vision that the high brilliance and flux of the X-ray beam would mainly benefit the time-resolved, cinematographic application of SAXS, e.g. on phase transitions of liquid–crystalline mesophases. This was true over the years - it was as early as 1997, when 10-µs time resolved SAXS was first demonstrated in a pilot experiment – but it was at least equally impressive to see the field of thin-film analytics by GISAXS growing. The analysis of nanodots, or other nanopatterns on surfaces with high technological promise, or the cinematographic realization of the growth mechanism of mesoporous films had great effects on the respective fields. Other innovations in the sector of materials research were e.g. the microfluidic and gas-phase approaches by SAXS. The expertise we gained paved the way for a number of very fruitful collaborative projects within the different EU-Frameworks.

Bio-medical and pharmaceutical orientation was the other half of the program. The entire spectrum of biologically relevant sizes, from whole organisms – plants, bones, tissue - down to the complex supramolecular structures of membranes and proteins was in the scope of studies that made the pages of Nature, PNAS, Cell and other formidable journals. A particular case was the hair - breast cancer affair in 1999, which even made it to the New York Times, among others. It is amazing to see that this story still flares up here or there.

I think it is a particular speciality of our SAXS-beamline that we constantly engaged in innovative combinations of SAXS with other methods and techniques. This comes from the realization that SAXS by itself gives generally ambiguous results, but together with other tools, such as temperature/pressure scanning, shear, or mechanical deformation, gains enormously in information content. The emerging term is ‘hybrid analytics’ whereby the combination of different thermodynamic, spectroscopic and structural techniques is used to

overcome the natural limitations of each single technique and to gain a broader picture. I am convinced that this approach will be the future of complex system analytics.

In looking back I feel happiness and gratitude. Happiness, because I caught the right time for this project. A few years earlier there was no synchrotron, and a few years later the spirit of freshness and enterprise would have faded. It was the only Austrian project of that kind in the past two decades. Gratitude, I owe to the many people who have devoted energy and idealism, and without whom it would not have happened.

In Austria I want to mention two friends, among many others: the late Karl Schlögl, General Secretary of the Academy in Vienna, who had the spirit to put his weight to the project, and Wolfgang Reiter, the Ministerialrat in Vienna, who not only believed but also channeled public money into the project until it finally stood.
In Italy, in Trieste, initially Luciano Fonda and Renzo Rosei, then it was first Giorgio Margaritondo who was a perfect partner in the many delicate negotiations here and there (as often in reality: contracts come after the official opening), the late Paolo Fasella, Massimo Altarelli, and finally Carlo Rizzuto with Alfonso Franciosi.
And of course, Sigrid Bernstorff and Heinz Amenitsch as masters of the beam-line, and their team – to praise their credits is beyond the limits of space here.

The Austrian SAXS-beamline will continue to exist, not under the roof of the Austrian Academy of Sciences, but as a unit belonging to the Technical University of Graz. I see this as a very natural and positive transition, as the days of pioneering are over and a stronger emphasis on student training and community formation could start in this new framework. Also, the opportunities offered by the Free Electron Laser source FERMI might perhaps find positive resonance there.

Ad Multos Annos to the Austrian SAXS beamline at ELETTRA!
With some nostalgia to a great period I say Good Bye and Fare Thee Well to all my friends and colleagues!

Alfonso Franciosi
Chief Executive Officer
Sincrotrone Trieste S.C.p.A.

We are very pleased to have the opportunity to write this preface to the Annual Report of the SAXS Beamline of the Austrian Academy of Sciences. The remarkable scientific production of the SAXS Beamline shows how the Beamline is attracting a wider user community and seeing a continued high demand. All of these make the SAXS Beamline an example of what a successful international scientific partnership can achieve.

In the last year the SAXS Beamline has been able to exploit the enhanced capabilities of Elettra, with its increased stability, reproducibility and average brightness as a result of top-up. The Elettra third-generation light source is one the few synchrotron radiation sources in the world that operate routinely in top-up mode, both at 2.0 and 2.4 GeV. As a result of this, in 2011-2012 uptime was 95-96%, with record-breaking uninterrupted top-up stints for users of 18 and 33 days. Also, beam-based alignment has been successfully implemented to ensure achievement of an ideal orbit, i.e., an orbit that passes through the magnetic center of the steering quadrupole magnets with maximum accuracy.

The new performances of Elettra are attracting new institutional partners. An agreement was reached with the International Atomic Energy Agency (IAEA) that will fund the construction of a state-of-the-art endstation for the new X-ray fluorescence beamline currently under construction. Construction continues of the new beamlines XRD2, for x-ray diffraction and spectroscopy, and XPRESS, for high-pressure diffraction, which will use the light emitted by the upgraded superconductive wiggler. Construction of XRD2 and XPRESS is being partially supported by the Indian Department of Science and Technology through the Indian Institute of Sciences (Bangalore).

In the future, we hope to involve our Austrian Partners in the exploitation of our new free-electron laser (FEL) source FERMI@Elettra. FERMI@Elettra is presently the only FEL facility exploiting from the very beginning a *seeding* scheme, i.e., a laser optical signal to obtain the initial stimulated emission from the electron bunches. Synchronization in the femtosecond range between the seed laser and the electron beam is provided by an all-optical timing distribution system. All this allows for a far better control on the intensity and lineshape of the output FEL pulses as compared to other FEL projects in the United States (LCLS), Germany (FLASH and XFEL) and JAPAN (SCSS) that use the alternate self-amplified spontaneous emission (SASE) method, where the random nature of the spontaneous emission process yields large variations in pulse intensity and lineshape.

The FERMI FEL-1 line, that uses a 1.2 GeV normal conducting linac to send electrons through a planar undulator (the modulator) and six APPLE-II undulators (the radiators) was

design to provide wavelength between 100 and 20 nanometers. The wavelength of the FEL radiation can be varied thanks to the variable undulator gap, down to 10 mm.
Commissiong of FEL-1 has been completed and the source now exceeds all design specifications. The measured photon flux exceeds 10^{13} photons per pulse with pulse bandwidth close to the Fourier limit. The central wavelength jitter is below 10^{-4}, the spectral bandwidth stability is below the 3% level and the intensity jitter is about 10%. Unlike the complex, multi-mode emission produced by SASE FELs, emission from FERMI is a single-mode TM_{00}, and full control of polarization, from linear to circular, is afforded by the APPLE II undulators produced by our spin-off company Kyma S.r.l. This, together with the dramatically increased stability in wavelength, spectral bandwidth and intensity, are important advantages that seeded FELs such as FERMI offer relative to SASE FELs.

The new FERMI FEL-1 source has been officially opened to external users through a call for beamtime proposals published at the end of 2011. An international peer-review panel has assigned beamtime to about half of the proposal received, with first experiments from external users scheduled at the end of 2012. Three beamlines and endstations for diffraction and projection imaging (DIPROI), elastic scattering from materials under extreme conditions (EIS-TIMEX) and atomic, molecular and cluster spectroscopy (LDM) are currently available. Additional beamlines and experimental stations for inelastic scattering (EIS-TIMER), magnetic dynamics (MAGNEDYN) and terahertz spectroscopy (TeraFERMI) will be completed next year.

The FEL-2 line runs parallel to the FEL-1 line at a distance of 1 meter. A 1.5 GeV linac energy and a High Gain Harmonic Generation (HGHG) double cascade scheme are adopted for FEL-2. The first stage involves one modulator and two radiators and is followed by a second stage with one modulator and six radiators. The first harmonic wavelength for FEL-2 will range from 20 nm to 4 nm, with substantial on-axis intensity expected in the third harmonic (1.3 nm or 960 eV).
On October 11, 2012 the new FERMI FEL-2 source has generated its first coherent photons. This was the first experimental demonstration worldwide of a seeded FEL configured as a two-stage cascade operating in the fresh bunch injection mode, where the second stage is seeded by the light produced by the first stage. In this configuration the photons in the second stage are generated from a fresh portion of the electron bunch, which has not been heated by the seed of the first stage, overcoming the problem of the induced energy spread, which limits the order of the harmonic conversion in a high-gain harmonic-generation seeded FEL.

The European role of our institution will be further expanded with the start of the new EU Framework Program thanks to the participation in European Research Infrastructure Consortia (ERIC) as per Council Regulation (EC) No. 723/2009 of 25 June 2009. Elettra will represent the Italian government and act as coordinating institution and statutory seat of the Central European Research Infrastructure Consortium (C-ERIC). Initial participants in this ERIC will include the Italy, the Czech Republic, Hungary, Poland and Slovenia, while Austria, Croatia, Romania, and Serbia are scheduled to join at al later stage. The next few months will be devoted to develop the C-ERIC operations and scientific offer to international users. Our long-standing relation with our Austrian partners will play a major role.

We take this opportunity to thank our Austrian partners for their professionalism and steady dedication over the years. We at Elettra look forward to expanding the scope and depth of our collaboration and exploring together the frontiers that the new upgraded Elettra and FERMI will open for all of us.

The SAXS Group

HEAD OF PROJECT: Peter Laggner [1)]

e-mail: peter.laggner@oeaw.ac.at

SCIENTISTS: Heinz Amenitsch [1), 3)]

e-mail: amenitsch@elettra.trieste.it

Sigrid Bernstorff [2)]

e-mail: bernstorff@elettra.trieste.it

Benedetta Marmiroli [1, 3)] (since 1.6.2011)

e-mail: benedetta.marmiroli@elettra.trieste.it

Michael Rappolt [1), 3)]

e-mail: michael.rappolt@elettra.trieste.it

POST DOCS: Fernando Cacho [1), 3)]

e-mail: fernando.cacho@elettra.trieste.it

Dražan Jozić [2)] (until 30.9.2011)

e-mail: drazan.jozic@elettra.trieste.it

Benedetta Marmiroli [1, 3)] (until 31.5.2011)

e-mail: benedetta.marmiroli@elettra.trieste.it

SCIENTIFIC ASSISTANT: Barbara Sartori [1, 3)]

e-mail: barbara.sartori@elettra.trieste.it

TECHNICIAN: Christian Morello [2)]

e-mail: christian.morello@elettra.trieste.it

1) Institute for Biophysics and Nanosystems Research, Austrian Academy of Sciences, Schmiedlstraße 6, 8042 Graz, Austria.
Tel 0043-316-4120 302
Fax 0043-316-4120 390

2) Sincrotrone Trieste, Strada Statale 14, km 163.5, 34012 Basovizza (TS), Italy.
Tel 0039-040-375 81
Fax 0039-040-938 0902

3) Institute for Biophysics and Nanosystems Research, Austrian Academy of Sciences
c/o Sincrotrone Trieste

The SAXS-Beamline in General

Small Angle X-ray Scattering has become a well known standard method to study the structure of various objects in the spatial range from 1 to 1000 Å, and therefore instruments capable to perform such experiments are installed at most of the synchrotron research centers. The high-flux SAXS beamline at ELETTRA is mainly intended for time-resolved studies on fast structural transitions in the sub-millisecond time region in solutions and partly ordered systems with a SAXS-resolution of 10 to 1400 Å in real-space.
The photon source is the 57-pole wiggler whose beam is shared and used simultaneously with a Macromolecular Crystallography beamline. The wiggler delivers a very intense radiation between 4 and 25 keV of which the SAXS-Beamline accepts 3 discrete energies, namely 5.4, 8 and 16 keV. The beamline optics consists of a flat double crystal monochromator and a double focusing toroidal mirror.
A versatile SAXS experimental station has been set-up, and an additional wide-angle X-ray scattering (WAXS) detector monitors simultaneously diffraction patterns in the range from 1 to 9 Å. The sample station is mounted move-able onto an optical table for optimising the sample detector distance with respect to SAXS resolution and sample size.
Besides the foreseen sample surrounding the users have the possibility to install their own specialised sample equipment. In the design phase, besides technical boundary conditions, user friendliness and reliability have been considered as important criteria.
The optimisation of the beamline with respect to high-flux and consequently high flux density, allows to perform the following experiments:

- Low Contrast Solution Scattering
- Grazing Incidence Scattering and Surface Diffraction
- Micro-Spot Scanning
- X-ray Fluorescence Analysis
- Time-Resolved Studies ≥ 11 μs
- Simultaneously Performed Small- and Wide-Angle Measurements (SWAXS) on:
    - Gels
    - Liquid Crystals
    - (Bio) Polymers
    - Amorphous Materials
    - Muscles

Furthermore, using 5.4 and 16 keV energies, the beamline is widely applicable also to very thin, e.g. single muscle fibers, and optically thick (high Z) specimen, as often used in e.g., material science and solid state physics.

THE INSERTION DEVICE

The wiggler for the SAXS beamline consists of three 1.5 m long segments, each having 19 poles. The device can work with a minimum gap of 20 mm, which corresponds to K=20 at 2 GeV. The main parameters of the wiggler are:

- Critical Energy 4.1 keV
- Radiation Power 8.6 kW
- Flux 3.5×10^{14} ph/s/mrad/0.1%BW (at 400 mA)

The wiggler radiation cone has a horizontal width of 9 mrad. From this the SAXS-beamline accepts vertically 0.3 mrad, and horizontally +/-0.5 mrad at a 1.25 mrad off-axis position. The resulting source size for 8 keV photons is 3.9 x 0.26 mm^2 (horiz. x vert.).

THE OPTICS

The optics common with the diffraction beamline consists of:

- C-Filter and Beryllium window assembly to reduce the power load on the first optical elements by a factor of 2 and to separate the beamline vacuum from the storage ring.
- Beam defining slit chamber which allows to define the SAXS beam on three sides before the monochromator in order to reduce the straylight in the downstream beamline sections.

The SAXS beamline optics consists of:

- A double-crystal monochromator consisting of four individual chambers, in which three interchangeable asymmetric Si(111) crystal pairs are used to select one of three fixed energies. Each of the crystal pairs is optimised for the corresponding energy to accomplish a grazing angle of 2°. The energy resolution $\Delta E/E$ of the monochromator is in the range of 0.7 - 2.5 10^{-3}.
- A baffle chamber after the monochromator is used as an adjustable straylight fenditure.
- A segmented toroidal mirror focuses the light in horizontal and vertical direction with a 1/2.5 magnification onto the SAXS-detector.
- An aperture slit reduces the straylight after the monochromator and the toroidal mirror.
- A guard slit defines the illuminated region around the focal spot. The spot size on the detector is 1.6 mm horizontally and 0.6 mm vertically. The calculated flux at the sample is in the order of 10^{13} ph/s at 400 mA. For a maximum sample size of 5.4 x 1.8 mm^2 correspondingly a flux density of 10^{12} ph/s/mm^2 has been calculated.

SAMPLE STAGE

The multipurpose sample stage allows to perform fast time-resolved relaxation studies based on temperature- or pressure-jumps as well as stopped flow experiments. Shear jump relaxation experiments are planned. Specifically, T-jumps can be induced by an infra-red light pulse (2 ms) from an Erbium-Glass laser, raising the temperature about 20 °C in an aqueous sample volume of 10 µl. A hydrostatic pressure cell with a maximal accessible angular range of 30° for simultaneous SAXS and WAXS measurements is available. P-jumps are realised by switching fast valves between a low and a high pressure reservoir, increasing or decreasing the hydrostatic pressure in the range from 1 bar to 2.5 kbar within a few ms. A Differential Scanning Calorimeter (DSC) allows for DSC-scans simultaneously to SWAXS measurements. In an overview, the following sample manipulations are possible (further details, see pages 25 and 29-36):

- Temperature Manipulations: Ramps, Jumps and Gradient Scans
- Pressure Manipulation: Scan and Jumps
- Stopped Flow Experiments
- SWAXS Measurements Applying Mechanical Stress
- Calorimetric measurements

Scientific Applications	Low Contrast Solution Scattering, Grazing Incidence Surface Diffraction, Micro-Spot Scanning, X-ray Fluorescence Analysis, Time-Resolved Studies ≥ 11 μs and Simultaneously Performed Small- and Wide-Angle Measurements (SWAXS) on: Gels Liquid Crystals (Bio) Polymers Amorphous Materials Muscles
Source characteristics	Wiggler (NdFeB Hybrid): Period: 140 mm No. full poles: 57 Gap: 20 mm B_{max}: 1.607 T Critical Energy ε_c: 4.27 keV Power (9 mrad): 8.6 kW Effective source size FWHM: 3.9 x 0.26 mm^2(h x v)
Optics	Optical elements: *Double crystal monochromator*: Si (111) asym. cut, water cooled. *Mirror*: two–segment,toroidal, Pt coated. Distance from source: 18.4 m / 26.5 m Acceptance: 1 mrad/0.3 mrad (h x v) Energy (3 selectable): 5.4, 8, 16 keV (0.77, 1.54, 2.3 Å) Energy resolution ΔE/E: 0.7-2.5 x 10^{-3} Focal spot size FWHM: 1.2 x 0.6 mm^2 (h x v) Spot at Sample FWHM: 5.4 x 1.8 mm^2(h x v) Flux at sample: 7.5 x 10^{12} ph s^{-1}(2 GeV, 300 mA, 8 keV)
Experimental apparatus	Resolution in real space: 10-1400 Å (small-angle), 1- 9 Å (wide-angle) Sample stage: temperature manipulations: ramps, jumps and gradient scans, pressure manipulation: scan and jumps, stop flow experiments, SWAXS measurements applying mechanical stress, SWAXS measurements applying magnetic fields. In-line calorimetric measurements simultaneously with SWAXS. Detectors: 1D gas-filled detectors for simultaneous small- and wide-angle (Gabriel type), 2D CCD (Photonic Science) and Mar300 Image Plate for small-angle, Vantec-1D (Bruker AXS), Pilatus 2D detector.
Experiment control	Beamline control: Program-units written in LabView for Windows 1 D detector control: PC-card and software from Hecus X-ray Systems GmbH, Graz. 2 D detector control: Software from corresponding detector system.

CURRENT STATUS

The beamline has been built by the Institute for Biophysics and Nanosystems Research (IBN), Austrian Academy of Science in collaboration with staff members from Sincrotrone Trieste, and is in user operation since September 1996. The set-up of the beamline started at the beginning of January 1995 with the installation of the support structure. Until the end of 1995, the 8 keV single energy system had been realised. The upgrade to the full three energy system was finished in spring 1998. Time resolved experiments require fast X-ray detectors and data acquisition hard- and software. Depending on the desired resolution in time and in reciprocal space, on isotropic or anisotropic scattering of the sample, one-dimensional position sensitive (delay-line type) or two-dimensional CCD detectors are employed.

In August 2002 our chemistry and X-ray laboratory went into operation. The chemistry unit serves mainly for sample preparation and analysis for both, in house research and external user groups, whereas the X-ray laboratory allows on-site testing of samples before moving on to the SR beamline (see page 36).

In May 2008 we extended about 3 m also our experimental hutch. It is now possible to increase the sample to detector distance and therefore improve our minimum SAXS resolution or maximise the flux density at sample position for certain experiments.

In conclusion, due to wide versatility of the beamline and the highly flexible sample stage, there are nearly no limits for the realisation of an experiment, and you are welcome by our team to propose any interesting and highlighting investigation for the benefit of material and life sciences.

Application for Beamtime at ELETTRA

1. Beamtime Policy at SAXS beamline

According to the agreement from March 2001 regarding the co-operation between the Austrian Academy of Sciences and Sincrotrone Trieste, at the Austrian SAXS-beamline the available beamtime of about 5000 hours/year is distributed as follows:

- 35% for Austrian Users, type: "CRG" (Collaborating Research Group)
- 35% for Users of Sincrotrone Trieste (General Users (GU))
- 30% is reserved for beamline maintenance and in-house research

In both user beamtime contingents also any industrial, proprietary and confidential research can be performed according to the "General User Policy" of Sincrotrone Trieste.

To apply for CRG and GU user beamtime proposals must be submitted according to the rules of Sincrotrone Trieste. The international review committee at ELETTRA will rank the proposals according to their scientific merit assessment. Based on this decision beamtime will be allocated according to the specific quotes for the beamtimes (CRG/GU) either for the following semester ("normal application") or for the next two years ("long term application"). However, at the moment no more than a maximum of 10% of the beamtime will be assigned to "long term" projects.

2. How to apply for beamtime

There are two deadlines each year for proposals, namely August 31st and February 28th. Accepted proposals will receive beamtime either in the then following first or second half year period, respectively. The Application Form must be completed on-line according to the following instructions.

ELETTRA USERS OFFICE
Strada Statale 14 - km 163.5
34012 Basovizza (Trieste), ITALY
Tel: +39 040 375 8628 / 8538- fax: + 39 040 375 8565
e-mail: useroffice@elettra.trieste.it

INSTRUCTIONS GIVEN BY THE USERS OFFICE
(see also http://www.elettra.trieste.it/UserOffice/)

1. Read carefully the General Guidelines.

2. Connect to the Virtual Unified Office: https://vuo.elettra.trieste.it/pls/vuo/guest.startup using your favorite browser with JavaScript enabled.

3. Select the Virtual Unified Office link.

4. When prompted, insert your ID and password. If you are a new user fill in the registration form with your data and choose your institution with the search button; in case your institution does not appear in the list, please contact useroffice@elettra.trieste.it giving all the details about it. When registered, you will receive an acknowledgment with your ID and password. You can change your password, if you wish. In case you forget your password, please don't register again but contact useroffice@elettra.trieste.it. At any moment you can select the help button and view more detailed instructions. By inserting your ID and password you will be able to continue.

5. Select the proposals button in the User functions group.

6. Select add and fill in on-line the proposal form. Please, type your proposal in English. Repeat this procedure for each proposal you intend to submit.

7. In case of continuation proposal: a) attach the experimental report of previous measurements; b) give your previous proposal number.

8. When finished, submit the proposal electronically, selecting the save button.

9. Print the proposal form together with each related safety form.

10. Sign the safety form(s).

11. Mail all signed safety form(s) as printed copy to the Users Office.

NOTE:

For technical questions related to proposals submission or other practical issues, contact useroffice@elettra.trieste.it

For scientific questions related to the possibility of performing a given experiment, contact bernstorff@elettra.trieste.it or amenitsch@elettra.trieste.it

Users and institutes performing experiments in 2011

Australia

La Trobe University, Melbourne

MUBIN Muhammad Shamsul Huda

Austria

Austrian Academy of Science, Institute of Biophysics and Nanosystems Research, Graz

AMENITSCH Heinz
BOULGAROPOULOS Beate
CACHO-NERIN Fernando
KORNMUELLER Karin
LAGGNER Peter
MARMIROLI Benedetta
PABST Georg
PRASSL Ruth
RAPPOLT Michael
SARTORI Barbara
THEOCHARIS Ioannis
VONACH Caroline

Laboratory of Polymer Engineering LKT-TGM and University of Vienna, Faculty of Physics, Dep. Physics of Nanostructured Materials

WILHELM Harald

Johannes Kepler University, Institute of Semiconductor and Solid State Physics, Linz

KEPLINGER Mario
SPRINGHOLZ Gunther

Medical University of Graz, Institute of Cell Biology, Histology and Embryology

LEITINGER G.

Montanuniversity Leoben, Department of Physics

ERKO Maxim
LECHNER Rainer T.
PARIS Oskar

University of Vienna, Faculty of Physics

GHAFFAR Abdul
KREXNER Gerhard
PICHL Wolfgang

University of Vienna, Faculty of Physics, Dep. Physics of Nanostructured Materials

POLT Gerald
SCHAFLER Erhard
SCHUSTER Roman
SPIECKERMANN Florian
ZEHETBAUER Michael J.

Brazil

Universidade Federal do Rio Grande do Sul, Instituto de Física, Porto Alegre, RS

TEIXEIRA Cilâine Verônica

Croatia

Faculty of Sciences, Physics Department, Zagreb

SKOKO Željko

Institute of Physics, Zagreb

SALAMON Krešimir

"Ruđer Bošković" Institute, Zagreb

BULJAN Maya
CAPAN Ivana
DASOVIć Jasna
DUBčEK Pavo
GRACIN, Davor
JERČINOVIČ Marko
JURAIć Krunoslav
PIVAC Branko
RADIć Nikola
RISTIć Mira
SIKETIC Z.
TURKOVIC Aleksandra
ZORC Hrvoje

University of Split, Faculty of Chemistry and Technology, Dept. of Organic Technology, Split

ERCEG Matko
PERINOVIC Sanja

University of Split, Faculty of Chemistry and Technology, Department of Inorganic Technology, Split

JOZIĆ Dražan

Cyprus

University of Cyprus, Department of Chemistry, Nicosia

ANDREOU Ioanna
LEONTIDIS Epameinondas

Czech Republic

Charles University, Faculty of Mathematics and Physics, Prague

ENDRES Jan
HAVIAR S.

HOLY Vaclav
MATOLÍN V.
VALEŠ Vaclav

Denmark

University of Copenhagen, Department of Pharmacy, Faculty of Health and Medical Sciences, Copenhagen

JENSEN H.
LARSEN C.
NILSSON Christa
ØSTERGAARD J.
WENG LARSEN S.
YAGHMUR Anan

Finland

University of Helsinki, Division of Biopharmacy and Pharmaco-kinetics, and Centre for Drug Research

SCHMITT Mechthild

University of Helsinki, Faculty of Pharmacy, Centre for Drug Research

URTTI Arto

France

Université de Paris-sud, Faculté de Pharmacie, UMR CNRS, Chatênay-Malabry

BOURGAUX Claudie
ELISE Lepeltier
JEAN - JACQUES Vachon
TRUONG CONG Tri

UMR CNRS 8612 – Institut Galien Paris-Sud, Châtenay-Malabry

FAIVRE Vincent
TRUONG CONG T.
LESIEUR S.

Université Pierre et Marie Curie, Laboratoire Chimie de la Matière Condensée, Paris

GROSSO David

Centre de Recherche sur la Matiére Divisée, Orleans

SINTUREL Christophe
VAYER Marylène

Germany

University of Erlangen-Nuremberg, Institute of Crystallography and Structural Physics, Erlangen

GERTH Stefan

MAGERL Andreas
SCHIENER Andreas
UNRUH Tobias
WILL Johannes
WLOCHOWITZ Tobias

University of Freiburg, BIOSS
RITTMAN Martyn

Hungary

Hungarian Academy of Sciences, Biological Research Center, Institute of Plant Biology, Szeged
GARAB Gyozo
KOVÁCS L.
LAMBREV P.
MILOSLAVINA Y.

Hungarian Academy of Sciences, Research Institute for Solid State Physics and Optics, Budapest
UNNEP R.

Hungarian Academy of Sciences, Research Institute for Solid State Physics and Optics, Budapest, and Paul Scherrer Institute, Villigen, Switzerland
NAGY G.

India

Indian Institute of Science, Solid State and Structural Chemistry Unit, Bangalore
BHATTACHARYYA Aninda Jiban
MANDAL Soumit Sankar
MAZUMDAR Sayanta

UGC-DAE Consortium for Scientific Research, University Campus, Indore
GUPTA Ajay
KOYILOTH VAYALIL Sarathla
PANDIT Pallavi

Israel

The Hebrew University of Jerusalem, Institute of Chemistry
ASOR Roi
GINSBURG Avi
HARRIES D.
KLER Stanislav
OPPENHEIM A.
RAVIV Uri
SAPER G.
STEINER Ariel

Italy

C.N.R., Istituto di Biochimica delle Proteine, Napoli
PISANI F.M.
SANNINO V.

CNR, Institute of Chemistry and Polymer Technology, Pozzuoli
DURACCIO Donatella
PEZZUTO Marilena

CNR, IMM, Bologna
PARISINI Andrea

CNR, Institute of Materials Structure, Monterotondo (Rome)
SUBER Lorenza

CNR, Institute of Crystallography, Monterotondo (Rome)
CAMPI Gaetano

CNR, Istituto Processi Chimico-Fisici, Messina
CALANDRA Pietro
LOMBARDO Domenico

CNR, ISC, Istituto dei Sistemi Complessi, Roma
TRIOLO Alessandro

Sincrotrone Trieste S.C.p.A., Trieste
BERNSTORFF Sigrid
JOZIĆ Dražan
KRASTANOVA I.
MORELLO Christian
ONESTI Silvia Caterina Elvira

SISSA, Laboratory of Prion Biology, Department of Neuroscience, Trieste
BENETTI Federico
GIACHIN Gabriele
RASPADORI Andrea

SISSA, and Sincrotrone Trieste
LEGNAME Giuseppe Antonio

Universita di Cagliari, Dip. di Scienze Chimiche
CANNAS Carla

Università di Messina, Dipartimento di Chimica Industriale e Ingegneria dei Materiali, Messina
CALANDRA Pietro
PROVERBIO E.

Università di Padova, Dipartimento di Biologia, Padova
BELTRAMINI Mariano

MINUTE Fabrizio
TODERO Giulia

Università di Palermo, Dipartimento di Chimica Fisica, Palermo
LO CELSO Fabrizio
SCIACCA Ivan Diego

Università Politecnica delle Marche, Depart. of Biology, Ancona
ORTORE Maria Grazia

Università Politecnica delle Marche, Depart. Science of Life and Environment, Ancona
BELTRAMINI M.
MARIANI Paolo
MINUTE F.
ORTORE Maria Grazia
SPINOZZI Francesco

Sapienza Università di Roma, Dipartimento di Chimica
IMBIMBO Emilia
MASCI Giancarlo

University of Trieste, Center of Excellence for Nanostructured Materials (CENMAT), INSTM and Department of Pharmaceutical Sciences, Trieste
Da ROS Tatiana
TOMA Francesca Maria

Morocco

Faculté des Sciences et Techniques, Physics Department, Tanger
CHAHBOUN Adil

Oman

Sultan Qaboos University, College of Science, Physics Dept., Al Khodh - Muscat
CARBONI Carlo
CARBONI David Guy

Portugal

University of Lisbon, Physics Department and ICEMS, Lisbon
CONDE Olinda

Universidade do Minho, Centro de Física, Braga
GOMES Maria.J.M.
LEVICHEV Sergey
MARTÍN-SÁNCHEZ J.
ROLO Anabela G.
VIEIRA Eliana M. F.

Russia

Institute of Solid State Chemistry, Ural Branch of the Russian Academy of Sciences, Ekaterinburg

REMPEL Andrey

Spain

Universitat Autonoma de Barcelona, Faculty of Medicine, Biophysics Unit, Bellaterra, Barcelona

TEIXEIRA Cilâine Verônica

Sweden

Royal Institute of Technology, Div. Surface and Corrosion Science, Stockholm

CLAESSON Per Martin
DUNER Gunnar
KRIVOSHEEVA Olga
TILTON Robert

Ytkemiska Institutet AB, (YKI, Institute for Surface Chemistry), Lipid Structures Life Science and Chemical Industries Section YKI, Stockholm

KALNIN Daniel

United Kingdom

Keele University, Department of Physics, Keele

ARUMUGAM Mahendrasingam
CHONG Peng Siong
RASBURN John
SWANN Nichola
WYE Steve

Structural Genomics Consortium, Oxford

GILEADI O.

University of Reading, Polymer Science Centre, Whiteknights, Reading

SQUIRES Adam

University of Reading, Polymer Science Centre, Whiteknights, Reading

MITCHELL Geoffrey R.

USA

North Carolina Central University, Durham

VLAHOVIC Branislav
WU Marvin

List of Performed Experiments

2011 (first half year)

Proposal	Proposer	Institute	Country	Title	Research Field
20105023	RITTMAN Martyn	Univ. of Reading, Dept. of Chemistry	United Kingdom	GISAXS of amphiphile cubic phases	Life Sciences
20105076	LECHNER Rainer T.	Montanuniversitaet Leoben, Dep. of Physics	Austria	In-situ SAXS/WAXS studies of mesocrystal growth based on nanocrystals in solution	Materials Science
20105077	LEONTIDIS Epameinondas	Univ. of Cyprus, Department of Chemistry	Cyprus	GISAXS investigation of mesoporous silica, titania and tantala films containing nanoparticles with known photocatalytic action	Chemistry
20105131	RAPPOLT Michael	Inst. of Biophysics and Nanosystems Research (IBN), AustrianAcademy of Sciences (AAS), Graz	Austria	Online spontaneous curvature determination in model membranes by combining micro-fluidic mixing and time-resolved SAXS	Life Sciences
20105158	MARMIROLI Benedetta	IBN, AAS, Graz	Austria	Investigation of the confinement effect on fast chemical reactions using a free jet micromixer in combination with SAXS	Chemistry
20105162	MECHLER Adam	La Trobe Univ., Melbourne	Australia	Towards biomimetic membranes: structure and evolution of liposomes in a physiological buffer	Life Sciences
20105211	FAIVRE Vincent	C.N.R.S. - Univ. de Paris Sud	France	Rutin and quercetin nanoformulations	Life Sciences
20105222	STANGL Julian	Johannes Kepler Univ., Linz	Austria	In-situ GISAXS studies of PbTe quantum dot formation in bulk CdTe by thermal annealing	Materials Science
20105227	KREXNER Gerhard	Universität Wien, Fakultät für Physik	Austria	Structure of alkali metals in nanoporous confinement	Materials Science
20105322	DA ROS Tatiana	Università Trieste, Dip. di Scienze Farmaceutiche	Italy	From SAXS to cellular uptake: CNT interactions with lipids	Life Sciences
20105363	BENETTI Federico	SISSA / ISAS, Settore di Neurobiologia	Italy	A SAXS study of recombinant prion protein oligomers	Life Sciences
20105412	GOMES Maria	Univ. of Minho, Physics Dep, Braga	Portugal	GID and GISAXS investigations of flash memory structures based on semiconductor nanocrystals	Materials Science
20105415	ARUMUGAM Mahendrasingam	Keele University, Dept. of Physics,	United Kingdom	Investigation of the crystallisation kinetics and the transient phases of the triglycerides blends from the melt using time-resolved SAXS/WAXS	Life Sciences
20105452	TEIXEIRA Cilaine Veronica	Univ. Barcelona, Fac. of Medicine, Biophysics Unit	Spain	Micellar behaviour of saponin-cholesterol aqueous system	Life Sciences
20105480	DURACCIO Donatella	CNR, Inst. of Polymer Chemistry and Technology, Pozzuoli	Italy	Crystallisation behaviour of novel polymer nanocomposites for safe food packaging	Materials Science
20105496	AMENITSCH Heinz Wilfried	IBN, AAS, Graz	Austria	In situ formation of hierarchical structures in mesoporous materials by EISA in aerosol droplets	Materials Science

20105506	RAVIV Uri	Hebrew University, Inst. of Chemistry, Jerusalem	Israel	Following the time-dependent structural changes during the self-assembly process of SV40 virus	Life Sciences
Inhouse	BERNSTORFF Sigrid & JOZIC Drazan	Sincrotrone Trieste	Croatia	In-situ SWAXS study of the developing process of geopolymer structures	Chemistry
Inhouse	BERNSTORFF Sigrid & RADIC Nikola	Ruder Bošković Insitute, Zagreb	Italy & Croatia	GISAXS examination of percolation in utrathin tungsten layers	Materials Science
Inhouse	BERNSTORFF Sigrid & BULJAN Maja	Ruder Bošković Insitute, Zagreb	Italy & Croatia	Self-ordering and charge trapping properties of Ge nanocrystals deposited on flat and rippled substrates	Materials Science
Inhouse	RAPPOLT Michael & SCHMITT Mechthild	IBN, AAS, Graz & Univ. Helsinki, Viikki Drug Discovery and Development Technology Center	Austria & Finland	The dynamical behavior of injectable self-assembled ocular drug nanocarriers	Life Sciences
Inhouse	BERNSTORFF Sigrid & TURKOVIC Aleksandra	Ruder Bošković Insitute, Zagreb	Italy & Croatia	Study of Polymer Electrolyte for Zn Rechargeable Nanostructured Galvanic Cells via Combined in Situ SAXS/DSC/WAXD Measurements	Materials Science
Inhouse	BERNSTORFF Sigrid & DUBCEK Pavo	Ruder Bošković Insitute, Zagreb	Italy & Croatia	GISAXS study of Si nano structures in SiO2 matrix for solar cell applications	Materials Science
Inhouse	AMENITSCH Heinz & LINDEN Mika	IBN, AAS, Graz & ÅBO Academi University, Dept. of Physical Chemistry	Austria & Finland	Growth of metal oxide and metal nanocrystals in confined geometry	Chemistry
20105367	RAPPOLT Michael & YAGHMUR Anan	IBN, AAS, Graz & Univ. Copenhagen, Dep. of Faculty of Pharmaceutical Sciences	Denmak	The Release Properties of a Model Drug from Lipidic Nanostructured Aqueous Dispersions	Life Sciences

2011 (second half year)

Proposal	Proposer	Institute	Country	Title	Research Field
20110015	TRIOLO Alessandro	C.N.R., Inst. per i Processi Chimico-Fisici, Messina	Italy	Structural study of macromolecules dissolved in room temperature ionic liquids (RTILs)	Chemistry
20110029	PABST Georg	IBN, AAS, Graz	Austria	In Situ Study of Sphingomyelinase Activity in Plasmamembrane Mimetics	Life Sciences
20110049	HOLY Vaclav	Charles Univ., Prague	Czech Republic	Grazing-incidence small angle x-ray scattering from thin film Pt-CeO2 catalysts	Materials Science
20110067	GUPTA Ajay	Inter University Consortium for DAE Facilities, Indore	India	GISAXS study of formation of nanoripples on Si by surfactant mediated ion-beam sputtering	Materials Science
20110087	CAMPI Gaetano	C.N.R., Istituto di Cristallografia, Montelibretti / Roma	Italy	Cobalt ferrite nanoporous spheres through normal micelles routes	Chemistry
20110094	BHATTACHARY-YA Aninda Jiban	Indian Institute of Science, Solid State and Structural Chemistry	India	Study of Ligand Binding to Free and Confined Heme proteins	Life Sciences

20110121	Tobias WLOCHOWITZ	Univ. Erlangen-Nürnberg, Dep. of Crystallography + Structure Physics	Germany	Nucleation and growth of CdS quantum dots at short time scales	Materials Science
20110128	ONESTI Silvia Caterina Elvira	Sincrotrone Trieste	Italy	Structural analysis of human proteins involved in DNA replication	Life Sciences
20110188	KALNIN Daniel	C.N.R.S., Univ. de Paris Sud	France	Anionic Surfactant Binding to Polyelectrolyte Brush-Grafted Nano-particles	Life Sciences
20110202	KORNMUELLER Karin	IBN, AAS, Graz	Austria	Self-assembly of surfactant-like designer peptides	Life Sciences
20110248	SPINOZZI Francesco	Univ. Politecnica delle Marche, Scienze Fisiche, Ancona	Italy	SAXS studies of hemocyanins encapsulated in sol-gel matrices	Life Sciences
20110273	BULJAN Maja	Ruder Bošković Insitute, Zagreb	Croatia	Self-assembly of semiconductor quantum dots in amorphous alumina multilayers	Materials Science
20110307	LOMBARDO Domenico	C.N.R., Inst. per i Processi Chimico-Fisici, Messina	Italy	Pourus nanoparticle formation during zeolite synthesis	Chemistry
20110316	NILSSON Christa	Univ. Copenha-gen, Faculty of Pharmaceutical Sciences	Denmark	Avidin-activated aggregation of bio-tin-coated cubosomes and hexo-somes: in situ SAXS investigation	Life Sciences
20110328	SCHAFLER Erhard	Univ. Wien, Inst. für Material-physik	Austria	Thermal stability of dislocations in semicrystalline polymers	Materials Science
20110353	GRACIN Davor	Ruder Bošković Insitute, Zagreb	Croatia	Origins of quantum confinement effects in thin film solar cells materials - extension of previous experiments	Materials Science
20110381	SINTUREL Christophe	Univ. Orleans, Centre de Recher-che sur la Matiére Divisée, Orleans	France	GISAXS study of the self organisation of polystyrene-b-polylactide in thin films upon solvent exposure at various partial pressures	Chemistry
20110389	DUBCEK Pavo	Ruder Bošković Insitute, Zagreb	Croatia	Structural study of pulsed laser deposited GaAs	Materials Science
20110404	AMENITSCH Heinz	IBN, AAS, Graz	Austria	In situ titration experiment to resolve the early stages of CaCO3 growth in situ with SWAXS	Chemistry
20110424	AMENITSCH Heinz	IBN, AAS, Graz	Austria	In situ study of the assembly of mesoporous nanoparticles in the areosol phase	Materials Science
20105497	NAGY Gergely	Institut Laue-Langevin	France	Structural parameters and flexibility of the multilamellar thylakoid membranes	Life Sciences
20105466	BOISSIERE Cedric	Université Paris 6, Chimie de la Matiere Conden-see	France	In-situ SAXS study of the mesostructuration of submicrometric fluorescent hybrid perovskite particles during aerosol processing	Chemistry
20105001	CARBONI Carlo	Sultan Qaboos Univ., College of Science, Physics Dept., Al Khodh - Muscat	Oman	Investigation of the temperature dependence of the layer spacing in a series of low molar mass bi-mesogen organosiloxane smectic materials	Materials Science
inhouse	BERNSTORFF Sigrid & RADIC Nikola	Ruder Bošković Insitute, Zagreb	Italy & Croatia	Structural study of Ni-Nb thin films	Materials Science

inhouse	BERNSTORFF Sigrid & JOZIC Drazan	Sincrotrone Trieste & Univ. of Split, Faculty of Chem. Technology, Dep. of Inorganic Technology	Italy & Croatia	In-situ SWAXS study of the developing process of geopolymer structures	Chemistry
Inhouse	BERNSTORFF Sigrid & JOZIC Drazan	Sincrotrone Trieste & Univ. of Split, Faculty of Chem. Technology, Dep. of Inorganic Technology	Italy & Croatia	SAXS study on poly(ethylene oxide)/lithium and sodium montmorillonite composites	Chemistry
inhouse	MARMIROLI Benedetta & AMENITSCH Heinz	IBN, AAS, Graz	Austria	Investigation of the confinement effect on fast formation of Calcium Carbonate using a free jet micromixer in combination with SAXS	Chemistry
inhouse	RAPPOLT Michael & SCHMITT Mechthild	IBN, AAS, Graz & Univ. of Helsinki, Viikki Drug Discovery and Development Technology Center (DDTC)	Finland	Ocular drug delivery systems and their dynamical behavior	Life Sciences
inhouse	RAPPOLT Michael & LEONTIDIS Epameinondas	IBN, AAS, Graz & Department of Chemistry, University of Cyprus	Cyprus	Novel mesoporous oxide films for photoelectrochemical water splitting. A GISAXS investigation of the structures.	Life Sciences

User Statistics

1. Number of submitted proposals and assigned shifts from 1995 until December 2012

The Austrian SAXS-beamline at ELETTRA opened to users in September 1996. Since then many experiments have been performed related to the fields of life science, materials science, physics, biophysics, chemistry, medical science, technology and instrumentation.

The assignment of beamtime at this beamline is done separately for the group of "General Users" (GU) and the "Collaborating Research Group" (CRG), i.e., the Austrian users. Beamtime was assigned to the proposals of each group in the order of the rating received by the Scientific Committee, and up to the maximum number of shifts available to each group according to the contract between "The Austrian Academy of Sciences" and the "Sincrotrone Trieste". Until December 1997 up to 30 % of the beamtime was given to CRG, up to 55 % to GU, and 15% was reserved for maintenance purposes. From January 98 to June 2001 the quota for beamtime was up to 35 % for CRG, up to 50 % for GU, and again 15% reserved for maintenance purposes. From July 2001 on the two contingents for user proposals from CRG and GU receive up to 35% of the beamtime each. The remaining 30 % of beamtime are used for inhouse research projects as well as for maintenance purposes.

Figure 1 gives an overview of the numbers of received proposals, the numbers of requested and assigned shifts, as well as the percentage between assigned and requested shifts during the last years. As can be seen in Fig.1, the request for beamtime at the SAXS-beamline increased strongly until the first half year of 1999. Then, probably due to the high rejection rates, the number of submitted proposals decreased somewhat during 2001, which resulted in a better ratio of accepted / rejected proposals. This oscillating behaviour of beamtime request can also be seen for the period 2002 – 2012 where after higher numbers of submitted proposals slightly reduced request periods follow. The numbers for the second semester of 2007 and first of 2008 reflect also that, due to the long shut-down from 1.10.2007 to 3.03.2008 (for the new booster-electron-injector installation) less proposals were submitted, and less beamtime was available.

In 2011, in total 75 proposals (12 from CRG, and 63 from GU) were submitted. From these 3 CRG and 6 GU proposals were submitted by "new" usergroups, i.e. groups which so far had never beamtime at the SAXS beamline. From these, 3 GU and all 3 CRG proposals were accepted by the review committee.

Figure 1 (Next page). The statistical information about the beamtime periods since end of 1995 are given for the groups "CRG", and "GU" separately, as well as for both together ("Total"). Shown are, for all beamtime periods (from top to bottom):
● Number of received proposals, ● Number of requested shifts,
● Number of assigned shifts, and ● Relation between assigned and requested shifts

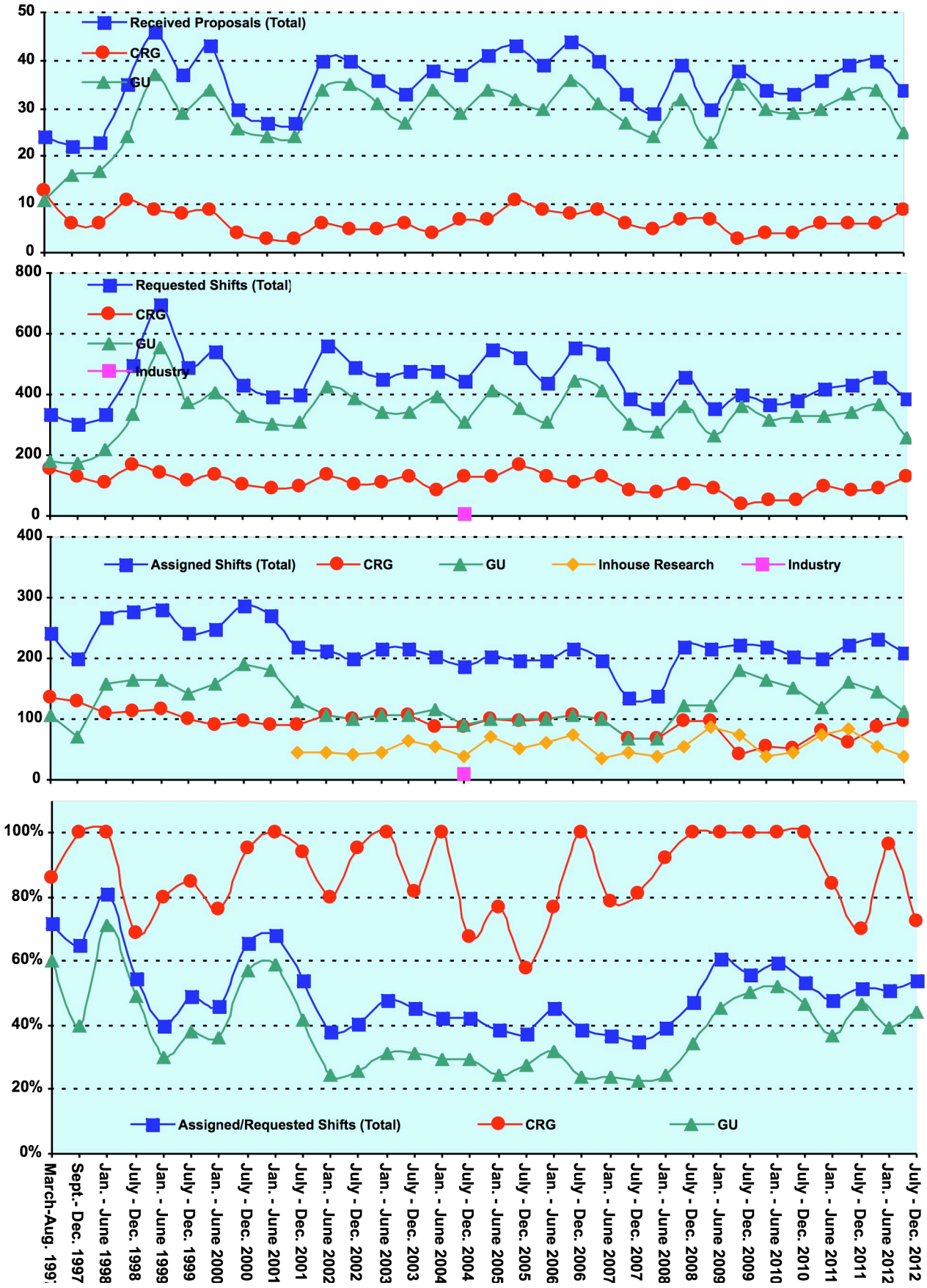
Received Proposals (Total)
CRG
GU
Requested Shifts (Total)
CRG
GU
Industry
Assigned Shifts (Total)
CRG
GU
Inhouse Research
Industry
Assigned/Requested Shifts (Total)
CRG
GU
March-Aug. 199
Sept.- Dec. 1997
Jan. - June 1998
July - Dec. 1998
Jan. - June 1999
July - Dec. 1999
Jan. - June 2000
July - Dec. 2000
Jan. - June 2001
July - Dec. 2001
Jan. - June 2002
July - Dec. 2002
Jan. - June 2003
July - Dec. 2003
Jan. - June 2004
July - Dec. 2004
Jan. - June 2005
July - Dec. 2005
Jan. - June 2006
July - Dec. 2006
Jan. - June 2007
July - Dec. 2007
Jan. - June 2008
July - Dec. 2008
Jan. - June 2009
July - Dec. 2009
Jan. - June 2010
July - Dec. 2010
Jan. - June 2011
July - Dec. 2011
Jan. - June 2012
July - Dec. 2012

2. Provenience of users

During 2011, 162 users from 62 institutes in 22 countries have performed experiments at the SAXS beamline. In Fig. 2 are shown both the provenience of these users, and of their respective institutes. Each user or institute was counted only once, even though many users performed experiments in both beamtime periods of 2011.

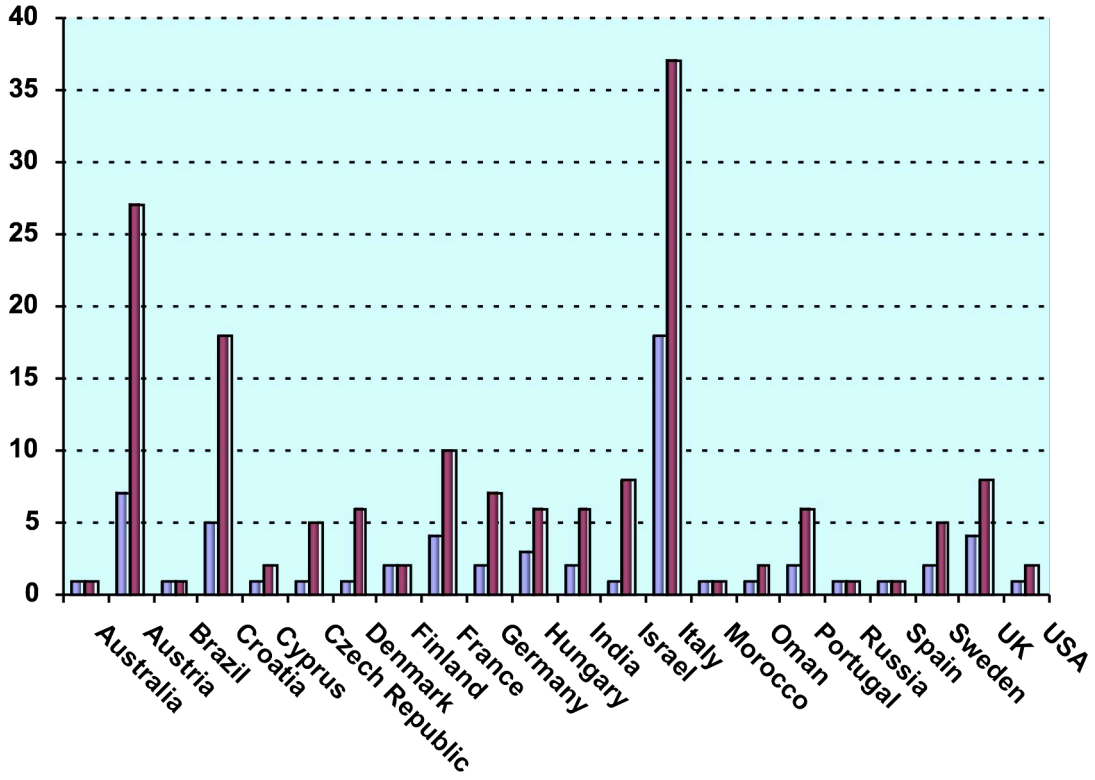

Figure 2. Nationality of the Austrian SAXS beamline users in the year 2011. The number of users (red) and the corresponding number of institutes (blue) are shown for each country.

3. Documentation of experimental results

As could be expected, with the start of user-operation at the SAXS-beamline the number of contributions to conferences started to increase strongly. With a delay of one year - the average time needed for paper publications - also the number of publications increased accordingly, as can be seen in Fig. 3.

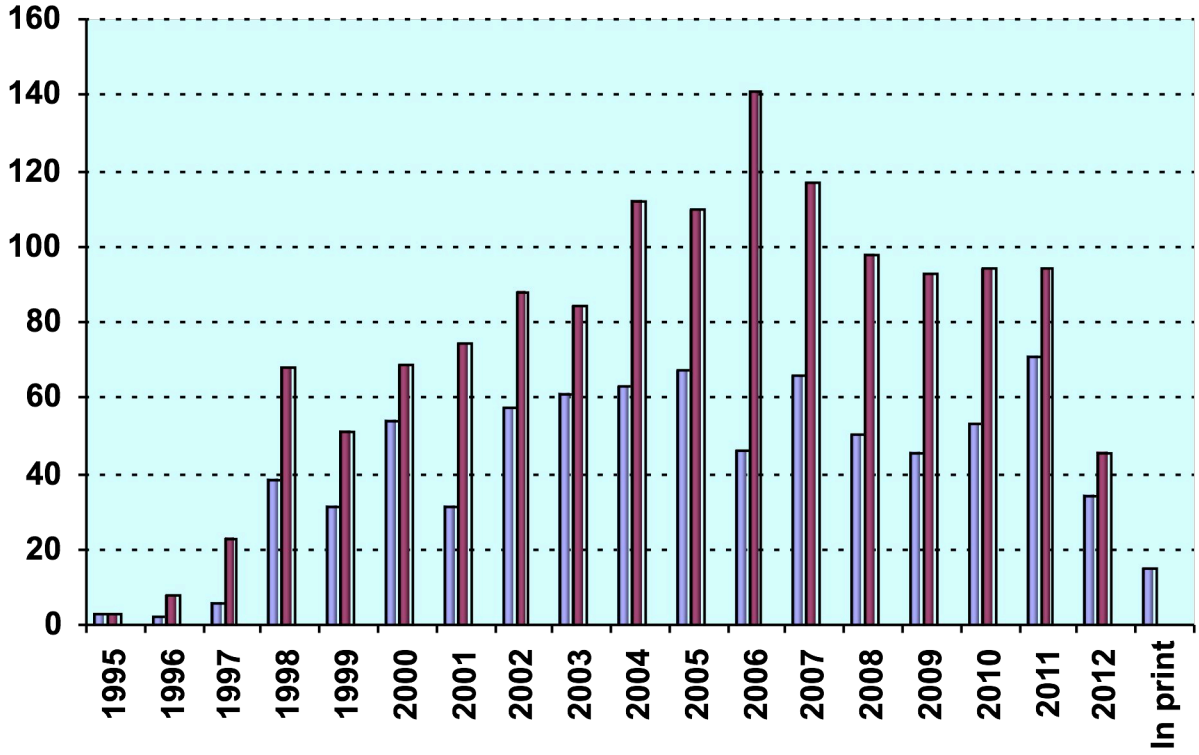

Figure 3. Number of conference contributions (blue) and of refereed paper publications (red) for the years 1995-2011. Also contributions, which have been published until Jule 2012 as well as those in print at that time are included.

In addition, from 1995 until June 2012, the following documentations based on instrumentation of the SAXS-beamline, or on data taken with it, have been produced:

Technical Reports on Instrumentation: 5
Contributions to Elettra Newsletters: 15
Contributions to Elettra Highlights: 39
Habil Thesis: 4
PhD Thesis: 91
Master Thesis: 43

Experimental Possibilities at the SAXS-beamline

1. NEW DEVELOPMENTS

Upgrading of the 2D CCD camera system

The old CCD camera system, which had been acquired in July 1998 and had been the main workhorse of the beamline, had an unrecoverable hardware failure towards the end of 2009. After a process that took the better part of 2010, the camera has been upgraded by the manufacturer (Phtotonic Science) to a GemStar/XIDIS model. This is a high resolution and sensitivity camera, providing a high dynamic range (16 bit) and advanced features such as on-camera binning and external triggering. The camera is fully software-controlled using the same Image Pro Plus software as its predecessor, and connects to the controlling computer via a Hi-Speed USB interface.

The new system, which has been available for users since the beginning of 2011, is ideal for experiments in grazing geometry (GISAXS) due to its balance between acquisition speed and sensitive area. Naturally, experiments in transmission geometry requiring medium-speed framerate and relatively large area will also benefit from this camera.

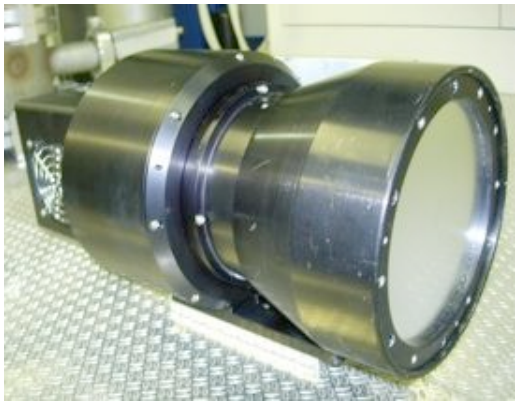

Camera specifications:

Sensitive area	82 x 74 mm (110 mm diagonal)
Image size	2048 x 2048
Pixel size	43 μm
Dynamic range	16 bit (20 bit in exposure fusion mode)
Binning	x1, x2, x4, x8 (independent X and Y, on-chip and in software)
Interface	external triggering, external gating (3.3V TTL)
Intensifier gain	12 bit (0-4095 levels, approx 200:1 max gain)
Exposure time	<1ms to 30 min
Frame rate	at x1 binning, ~800 ms readout time per frame at x8 binning (on-chip), ~145 ms readout time per frame
Image format	16bit TIFF native (Image Pro Plus allows exporting to other formats as well)

2. ACCESSIBLE SAXS AND WAXS RANGES

Simultaneous SAXS- and WAXS-measurements can be performed using a linear sensitive gas detector (Gabriel type, windows size 8 x 100 mm, active length 86.1 mm with a resolution of 0.135 mm/channel) for the WAXS-range, and either a second linear Gabriel type detector (windows size 10 x 150 mm, active length 134 mm with a resolution of 0.159 mm/channel), or the 2D CCD-system for the SAXS-range. A specially designed vacuum chamber (SWAXS-nose, see Annual Report of 1996/97, p. 32) allows to use both scattering areas below (for SAXS) and above (for WAXS) the direct beam, respectively.

Depending on the photon energy maximum SAXS resolutions of 2000 Å (5.4 keV), 1400 Å (8 keV) or 630 Å (16 keV) are available. The available possible WAXS-ranges are summarised in Table 1. The overall length of the SWAXS-nose in the horizontal direction, measured from the sample position, is 512 mm and the fixed sample to WAXS-detector distance is 324 mm. At the shortest SAXS camera-length an overlap in the d-spacings covered by the SAXS- and WAXS-detectors, respectively, is possible: then, the common regime lies around 9 Å.

Range	**2θ [deg]**	**d-spacing (Å)**		
		8 keV	5.4 keV	16 keV
1	9.4	*9.40*	14.03	4.27
	27.6	*3.23*	4.82	1.47
2	27.4	3.25	4.86	1.48
	45.6	1.99	2.97	0.90
3	45.4	2.00	2.98	0.91
	63.6	1.46	2.18	0.66
4	63.4	1.47	2.19	0.67
	81.6	1.18	1.76	0.54

Table 1. Possible d-spacing ranges in the WAXS-regime at the SAXS-beamline at ELETTRA. Since the WAXS-detector can be mounted at four different fixed positions on the SWAXS-nose (range 1-4), with the three possible energy choices (5.4, 8 and 16 keV) this results in 12 different d-spacing regimes. In italic the most common choice (8 keV, range 1) is highlighted. This range is suited for experiments, e.g., on lipid-systems and (bio)polymers.

3. CALIBRATION OF THE S-AXIS AND FLAT FIELD CORRECTION

At the SAXS beamline various standards are used for the angular (s-scale) calibration of the different detectors:

- Rat tail tendon for the SAXS detector - high resolution (rtt*.dat)
- Silver behenate for the SAXS detector – medium and low resolution (agbeh*.dat)
- Para-bromo benzoic acid for the WAXS detector – WAXS range 1 and 2 (pbromo*.dat)
- Combination of Cu, Al foils and Si powder for the WAXS detector – WAXS range 2 and higher

In Figure 1 a typical diffraction pattern of rat tail tendon is shown, depicting the diffraction orders (from the first to the 14th order) measured with a "high" resolution set-up (2.3 m) and the delay-line gas detector. The d-spacing is assumed to be 650 Å, but this value can vary depending on humidity up to 3%. Thus, the rat tail tendon is often used only to determine the position of the direct beam (zero order), while the absolute calibration is performed using the diffraction pattern of Silver behenate powder. Fig. 2 depicts a diffraction pattern of Silver behenate measured with "medium" resolution set-up (1.0 m) from the first to the 4th order (repeat spacing 58.4 Å) [1].

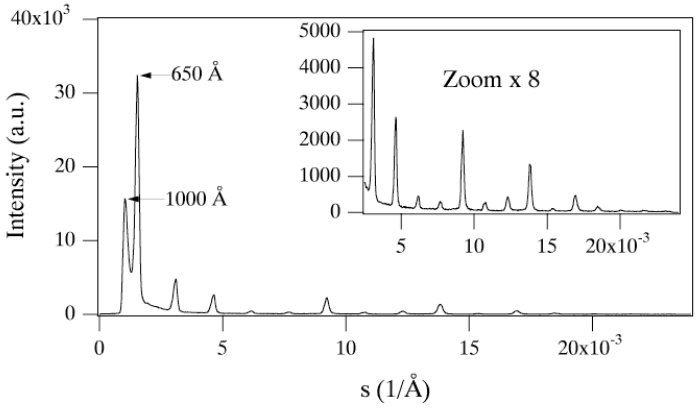

Figure 1. SAXS diffraction pattern of the collagen structure of rat tail tendon fibre at a distance of 2.3 m

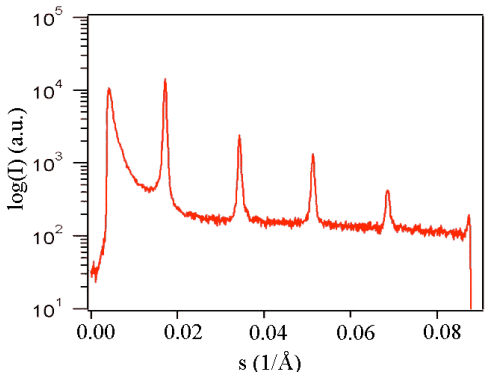

Figure 2. SAXS diffraction pattern of Ag behenate powder at a distance of 1.0 m

In Figure 3 a typical WAXS pattern of p-bromo benzoic acid is shown. The diffraction peaks are indexed according to the values given in Table 2, taken from [2].

d-spacing/Å	rel. intensity	d-spacing/Å	rel. intensity
14.72	18000	4.25	490
7.36	1200	3.96	2380
6.02	330	3.84	10300
5.67	980	3.74	26530
5.21	6550	3.68	1740
4.72	26000	3.47	760

Table 2. d-spacings and relative intensities of p-bromo benzoic acid according to [2].

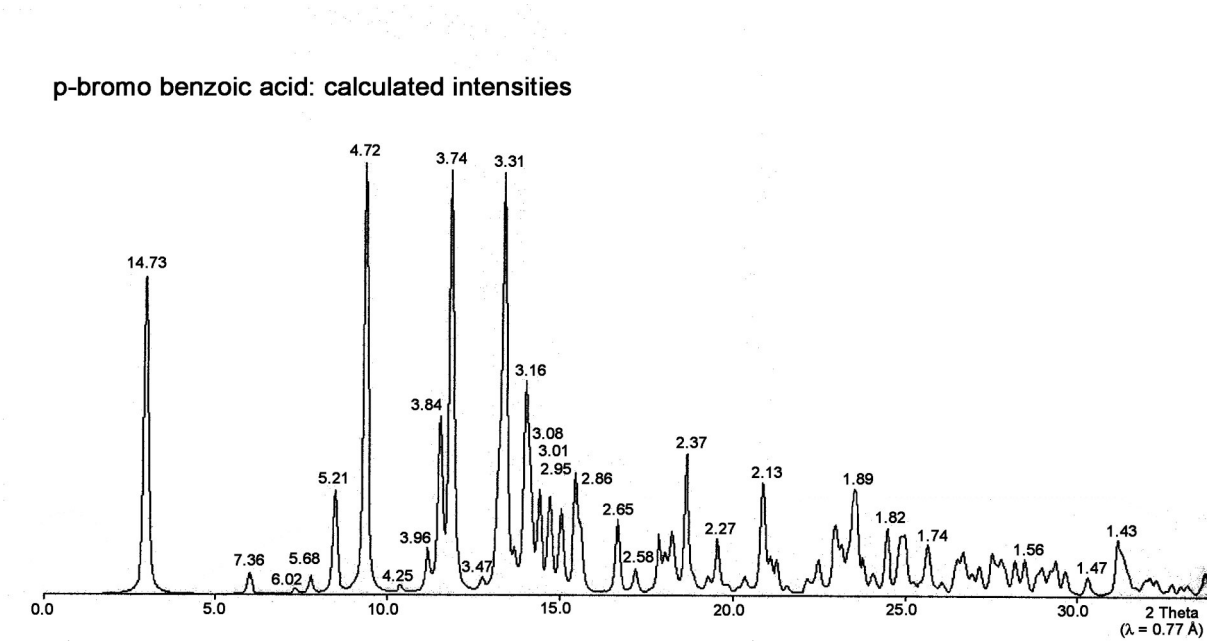

Figure 3. Calculated diffraction pattern of p-bromo benzoic acid. d-spacings are given in Å.

The s-scale for both, the SAXS and the WAXS range, can be obtained by linear regression, i.e., the linear relation between the known s-values of the calibrant versus the measured peak positions has to be found.

A further correction is regarding the flat field response (efficiency) of the detectors. For this correction, the fluorescence light of various foils are used to illuminate the detectors rather homogeneously:

At 8 keV: iron foil (100 μm thick), fluorescence energy: 6.4 keV K_α, 7.1 keV K_β (effic*.dat)
At 16 keV: copper foil (> 100 μm thick), fluorescence energy: 8.028 keV $K_{\alpha 2}$, 8.048 keV $K_{\alpha 1}$, 8.905 keV K_β (effic*.dat)

The measured scattering pattern are corrected for the detector efficiency simply by dividing them by the fluorescence pattern. Note: The average of the detector efficiency data should be set to unity and a small threshold should be applied to avoid any division by zero.

[1] T.N. Blanton et. al., Powder Diffraction 10, (1995), 91
[2] K. Ohura, S. Kashino, M. Haisa, J. Bull. Chem. Soc. Jpn. 45, (1972), 2651

4. AVAILABLE SAMPLE MANIPULATIONS STAGES

1. General

Usually the sample is mounted onto the sample alignment stage which allows the user to place the sample into the beam with a precision of 5µm (resolution: 1µm). In Fig. 5 the ranges for vertical and horizontal alignment as well as the maximum dimensions of the sample holders are given. The maximum weight on the sample stage is limited to 10 kg. In case the envelope dimensions of a sophisticated sample station provided by the users are slightly larger than those given in Fig. 5, the user can ask the beamline responsible for a check up of his space requirements. If it does not fit at all to these specifications, user equipment can also be mounted directly onto the optical table, which allows much larger spatial dimensions.

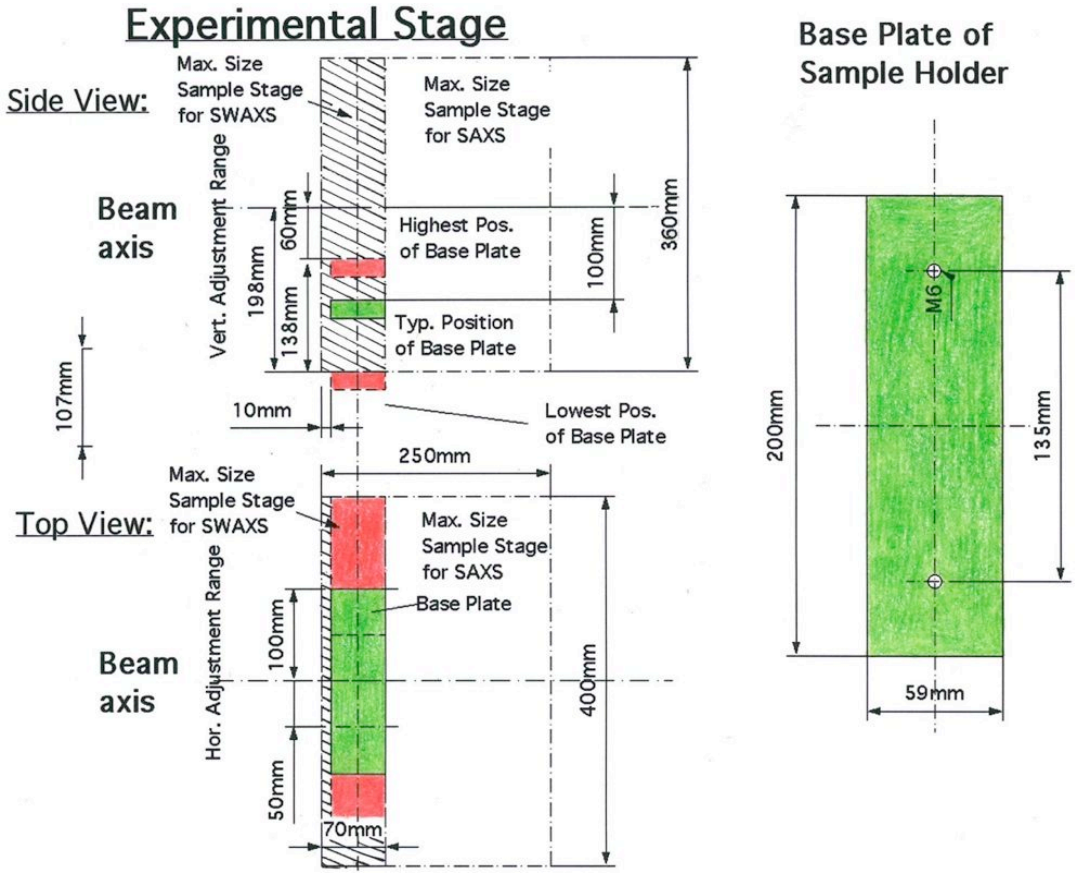

Figure 5. Maximum dimensions and alignment range of the sample holder to be mounted via a base-plate onto the standard alignment stage (left), and dimensions of the base-plate (right).

2. Sample Holders

As standard equipment for liquid samples Paar capillaries (diameter: 1 and 2 mm) are used thermostated with the KPR (Peltier heating/cooling) sample holders (Anton Paar, Graz, Austria). For use in these sample holders flow through capillaries and Gel holders are standard equipment. Temperature scans can be performed with KPR (-30-70 °C). Typically the precision and the stability of this systems is 0.1 °C. Additionally thermostats for temperature control or cooling proposes can be used at the beamline (-40 - 200 °C). Helium and Nitrogen gas bottles are available at the beamline, for other gases please contact the beamline responsible.

Multiple-sample holders can be mounted onto the standard sample manipulator. At present holders are available for measuring in automatic mode up to 30 solid samples at ambient temperature or up to 4 liquid or gel samples in the temperature range 0 – 95 °C.

3. Online Exhaust System

At the experimental station is available a custom-built fume cover and chemical exhaust system for toxic gases. Thus it is possible to e.g. study in-situ chemical reactions, during which toxic gases might develop.

4. Stopped Flow Apparatus

A commercial stopped flow apparatus (manufactured by Bio-Logic, Paris, France), especially designed for Synchrotron Radiation SAXS investigations of conformation changes of proteins, nucleic acids and macromolecules, is available. The instrument consists of a 4-syringe cell with 3 mixer modules manufactured by Bio-Logic. Each syringe is driven independently from the others by an individual stepping-motor, which allows a high versatility of the mixing sequence (flow-rate, flow duration, sequential mixing). For example, injection sequences using one or up to 4 syringes, unequal filling of syringes, variable mixing ratio, reaction intermediate ageing in three- or four-syringe mode etc.. The solution flow can be entirely software-controlled via stepping motors, and can stop in a fraction of a millisecond.

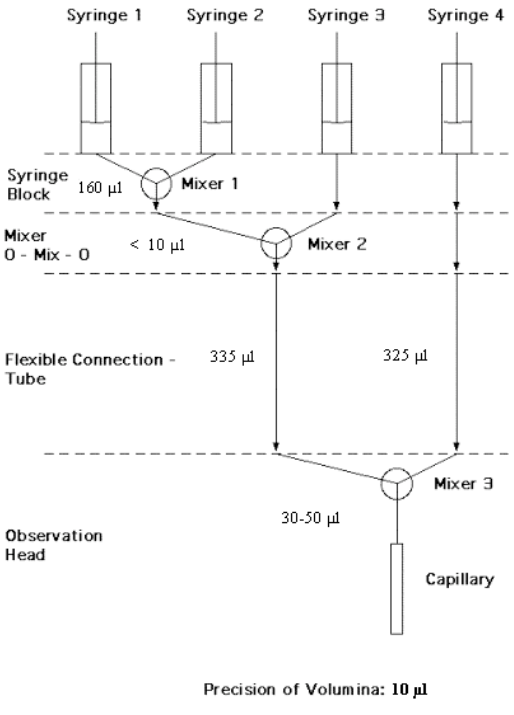

The software allows the set-up of the shot volumes of each of the 4 syringes in a certain time interval. Up to 20 mixing protocols can be programmed. Additionally macros for the repeated execution of individual frames can be defined. Furthermore, the input and output trigger accessible for user operation can be programmed. In the usual operation modus the start of rapid mixing sequence is triggered from our X-ray data-acquisition system (input trigger).

After the liquids have been rapidly mixed, they are filled within few ms into a 1 mm quartz capillary - situated in the X-ray beam- , which is thermostated with a water bath. Depending on the diffraction power of the sample time resolutions of up to 10 ms can be obtained.

Figure 6. Sketch of the stop flow system.

The main parameter of the system are:

- Thermostated quartz capillary (1 mm)
- Temperature stability 0.1 °C
- Total sample used per mixing cycle (shot volume): 100 µl
- Maximum 2θ angle of 45°
- Total Volume 8 ml
- Dead volume 550 µl
- Flow rate: 0.045 – 6 ml/s
- Duration of flow 1 ms to 9999 ms/Phase
- Dead time: 1 ms
- Reservoir volume: 10 ml each

Further information can be found at the webpage: http://www.bio-logic.fr/

5. Grazing Incidence Small Angle X-ray Scattering

Grazing incidence studies on solid samples, thin film samples or Langmuir-Blodget-films can be performed using a specially designed sample holder, which can be rotated around 2 axes transversal to the beam. Furthermore the sample can be aligned by translating it in both directions transversal to the beam. The precisions are 0.001 deg for the rotations and 5 µm for the translations. Usually the system is set to reflect the beam in the vertical direction. According to the required protocol and the actual assembly of the rotation stages ω, θ, 2θ and φ scans can be performed.

6. Temperature Gradient Cell

A temperature gradient cell for X-ray scattering investigations on the thermal behaviour of soft matter manybody-systems, such as in gels, dispersions and solutions, has been developed. Depending on the adjustment of the temperature gradient in the sample, on the focus size of the X-ray beam and on the translational scanning precision an averaged thermal resolution of a few thousands of a degree can be achieved.

7. Flow-through Cell

The flow through cell works in a simple manner: Special quartz capillaries (Glas Technik & Konstruktion, Schönwalde/Berlin) of 1.5 mm diameter and wide openings of about 3 mm at each end, can be inserted into the standard Anton Paar sample holder, which allows various temperature treatments (T-range 25-300 or –30-70 °C, respectively). Thin tubes are connected directly to the capillary ends and a constanst flow is achieved by a peristaltic pump.

8. IR-Laser T-Jump System for Time-Resolved X-ray Scattering on Aqueous Solutions and Dispersions

The Erbium-Glass Laser available at the SAXS-beamline (Dr. Rapp Optoelektronik, Hamburg, Germany) delivers a maximum of 4 J per 2ms pulse with a wavelength of 1.54 μm onto the sample. The laser-beam is guided by one prism onto the sample, which is filled in a glass capillary (1 or 2 mm in diameter) and Peltier or electronically thermostated in a metal sample holder (A. Paar, Graz, Austria). With a laser spotsize of maximal 7 mm in diameter a sample-volume of maximal 5.5 μl or 22 μl, respectively, is exposed to the laser-radiation. In a water-solutions/dispersions with an absorption coefficient of A = 6.5 cm^{-1} T-jumps up to 20°C are possible.

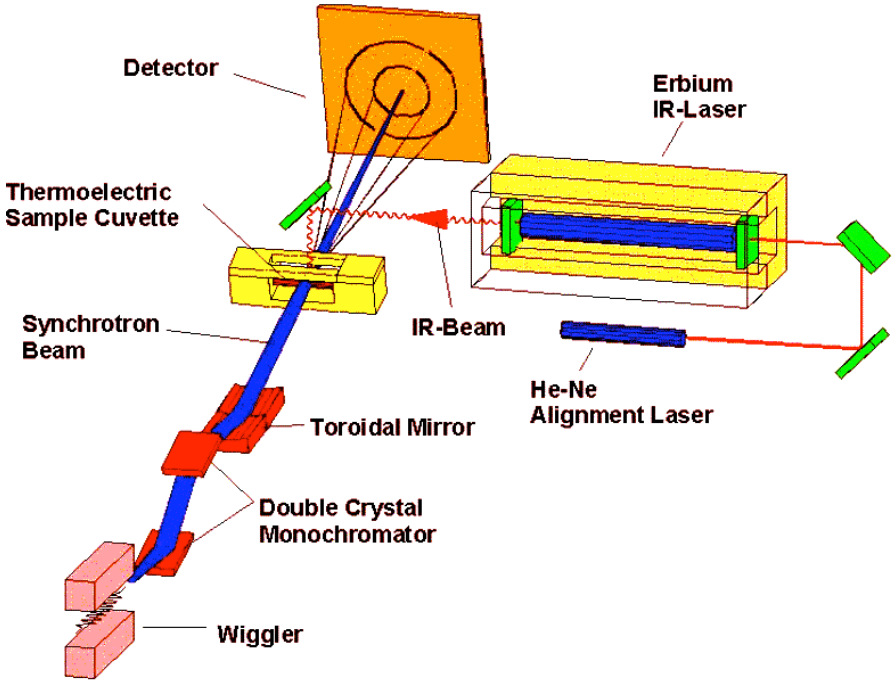

Figure 7. Sketch of the T-jump set-up.

9. High Pressure Cell System

SWAXS measurements of samples under pressure can be performed from 1 to 2500 bar, from 0 to 80 °C in the scattering angle region up to 30 degrees, both in the static or time-resolved mode, e.g. p-jump or p-scan, with a time-resolution down to the ms range. Precise pressure scans of any speed within a broad range (e.g. ca. 1.0 bar/s - 50 bar/s in the case of water as pressurising medium, and a typical sample volume) can be performed. Alternatively, dynamic processes can be studied in pressure-jump relaxation experiments with jump amplitudes up to 2.5 kbar/10ms in both directions (pressurising and depressurising jumps).
In most applications diamond windows of 0.75 mm thickness (each) are used. The transmission of one pair (entrance and exit window) is 0.1 at 8 keV, i.e. lower than 0.3, the value for the originally used 1.5 mm thick Be-windows. However the loss in intensity is more than compensated for by the considerably lower background scattering of diamond thus leading to higher q-resolution in the experiments.
The sample thickness can be 0.6-4.0 mm, with a volume of approximately 0.5-3 mm^3 completely irradiated by pin-hole collimated (< 1.0 mm diameter) X-rays.

The pressure cell system is flexible and can be built according to the needs of the particular experiment. Normally, a liquid (water, ethanol or octanol) is used as pressurising medium. But in principle, also gaseous media can be employed as well. N_2 has been successfully tested, and measurements in supercritical CO_2 became frequent.
Beside bulk measurements on samples in transmission set-up, also grazing incidence experiments using silicon wafer with highly aligned samples on its surface inserted in the high-pressure cell have been carried out successfully.

10. Oxford Cryostream Cooler

The Cryostream cooler creates a cold environment only a few millimeters from the nozzle position. The temperature and the flow of the nitrogen gas stream is controlled and regulated by a Programmable Temperatur Controller based on an 'in stream' heater and a thermo-sensor before it passes out over the sample.

The system has been especially developed for X-ray crystallography to perform diffraction experiments on e.g. shock frozen bio-crystals. However, the programmable temperature controller allows further implication for SAXS-experiments, e.g., rapid temperature drops in solvents. The design of the Cryostream Cooler facilitates:

- Nitrogen stream temperatures from -190 to 100 °C
- Stability of 0.1 °C,
- Refill without any disturbance of the temperature at the sample
- Temperature ramps can easily be carried out remotely controlled with scan rates up 6 °C/min
- Individual temperature protocols can be cycled
- T-jumps in both directions can be performed by rapid transfer of the sample in a pre-cooled or -heated capillary using an fast syringe driver reaching a minimum temperature of -80 °C. Here, typical scan rates are about 15 °C/sec with a total process time in the order of 10 sec.

Further information can be found at the webpage: http://www.oxfordcryosystems.co.uk/

11. In-line Differential Scanning Calorimeter (DSC)

The in-line micro-calorimeter built by the group of Michel Ollivon (CNRS, Paris, France) allows to take simultaneously time-resolved synchrotron X-ray Diffraction as a function of the Temperature (XRDT) and high sensitivity DSC from the same same sample.
The microcalorimetry and XRDT scans can be performed at any heating rate comprised between 0.1 and 10 °C/min with a 0.01 °C temperature resolution in the range -30/+130 °C. However, maximum cooling rates are T dependent and 10°C/min rates cannot be sustained below 30°C since cooling efficiency is a temperature dependent process. Microcalorimetry scans can be recorded independently, and also simultaniously, of X-ray patterns. The microcalorimeter head can also be used as a temperature controlled sample-holder for X-ray measurements while not recording a microcalorimetry signal. Isothermal microcalorimetry is also possible when a time dependent thermal event such as meta-stable state relaxation or self-evolving reaction, is expected. The sample capillaries have a diameter of 1.5 mm and are filled over a length of 10 mm.

12. Tension Cell

Together with the external user group Schulze-Bauer/Holzapfel the research team constructed a general-purpose tension cell. This particular cell was designed for *in-situ* tensile testing with the particular feature that the sample could be completely immersed in a solvent (e.g. physiological solution), which is of particular interest for the blood vessel or collagen fiber testing. The sample container can be attached to a thermal bath to control the temperature in the range from 5 to 95 ºC. A screw with an appropriate opening for the passage of the X-ray beam can adjust the optical thickness of the sample container continuously and optimize the set-up for different sample geometries.
The fully remote controlled system allows to control not only the fiber extension from 0 to 50 mm, but also it records simultaneously the force signal in the range from 0 to 25 N and as an option the optically determined Video extensometer signal to measure the transversal contraction of the sample.

13. Larger experimental hutch

After the prolungation of the experimental hutch by about 3m we have now the possibility to e.g. permanently install a diffractometer (roll on/roll off), or a micro focus set-up, which delivers focal spot sizes down to 10 μm and thus will allow for micro spot scanning SWAXS experiments with a new X-Y scanning stage.
On the other hand we can increase the sample to detector distance and therefore improve our minimum SAXS resolution or maximise the flux density at the sample position for certain experiments. Nevertheless this prolongation of the experimental hutch will ensure the sustainable development of the beamline also in the future by giving us the opportunity to realize new optical concepts, e.g. new mirrors, Fresnel or refractive lenses.

5. AVAILABLE DETECTORS

1. 2D Image Plate

The Mar300 Image Plate detector with a circular active area of 300mm in diameter is the largest-area detector available to users of the beamline, with a spatial resolution (pixel size) of 150μm. This detector has two modes of operation (180mm or 300mm), depending on the desired active area, which result in image sizes of 1200x1200 and 2000x2000, respectively. They are stored in the mar image format (16 bit for compactness, with higher precision extensions for values out of range), and can be processed and converted using the Fit2D program [1]. Typical applications are those that need a large Q-range with high dynamic range (typical values of 10^5), i.e. solution scattering from proteins and nanoparticles, temperature-step scans, slow processes like nanoparticle formation, mesophase formation, etc. The exposure time for the Image Plate is given in seconds, with typical values between 1 and 60. Readout time depends on the chosen active area (for 180mm mode, about 130 seconds; for 300mm mode, about 210 seconds), and therefore it is not suitable for samples where high time resolution is needed. Exposure information, number of images in the series and other information is automatically written to a summary file after each image.
So far the detector cannot be triggered by an external trigger input. Controlling an additional (external) device or experiment can only be done by hardware wiring of the TTL shutter signal.

2. 2D Pilatus 100K Detector System

The Pilatus 100K detector system (http://www.dectris.com/sites/pilatus100k.html) operates in "single photon counting" mode and is based on the CMOS hybrid pixel technology: the X-rays are directly transformed into electric charge, and processed in the CMOS readout chips. This new design has no dark current or readout noise, a high dynamic range of 1000000 (20 bits), a read-out time of less than 3 ms, a framing rate of over 200 images/s and an excellent point spread function of < 1 pixel.

3. 2D CCD-Camera System

The description of the upgraded CCD camera can be found on page 24.

4. 1D Vantec Detector

The one-dimensional high count rate capable Vantec-1 Detector from BrukerAXS Inc. has an active area of 50 x 16 mm and reaches a spatial resolution of about 50 μm, which is smaller than the resolution obtained by the presently used Gabriel Type Gas detectors. Moreover its new gas amplification principle based on the Microgap technology [1] allows much higher count rates compared to the old system. Now the main limitation is the data acquisition system with its maximum integral count rate of about 1 MHz. In the present data acquisition system HCI (Hecus X-ray Systems, Graz, Austria) the detector has the following performance:

- Minimal time resolution: 11 μs
- Maximum No. of frames: 512 (depending on the no. of channels)

- Maximum integral count rate: 1 MHz

5. 1D Gabriel-type Detector System

Two Gabriel-type detectors are available, which have an active area of 100 x 8 mm and 150 x 8 mm, respectively. Both have 1024 pixels, and thus the corresponding spatial resolution is about 135 microns and 175 microns, respectlively. They can be used simultaneously, and are run with the data acquisition system HCI (Hecus X-ray Systems, Graz, Austria). This detector system has the following performance:

- Minimal time resolution: 11 microsec
- Maximum No. of frames: 512
- Maximum integral count rate: 40 kHz

6. OFFLINE SITE LABORATORIES

In August 2002 our chemistry and X-ray laboratory went into operation. The 70 m^2 big laboratory is divided in two parts, in which the bigger share of 43 m^2 is occupied by the chemistry lab. This unit serves mainly for sample preparation and analysis for both, in house research and external SAXS user groups. In the X-ray laboratory the set-up of a SWAX camera for simultaneous small and wide angle scattering has been completed (Hecus X-ray Systems, Graz, Austria: www.hecus.at), which allows on-site testing of samples before moving on to the SR beamline. The chemistry lab is meanwhile equipped with:

- micro centrifuge (max. 13200 rpm; model 5415D from Eppendorf , Hamburg, Germany)
- Chemical fume hood, equipped with a carbon filter for general organic solvents (model GS8000 from Strola, Italy)
- vacuum drying oven (min. pressure 1 mbar; max. T: 200 °C, precision +/- 0.4°C; Binder WTB, Tuttlingen. Germany)
- balance (min.-max.: 0.001 - 220g; model 770 from Kern & Sohn, Balingen, Germany)
- Magnetic stirrer with heating plate and thermometer, temp max 260°C
- vortex for microtubes (model MR 3001 and REAX; both from Heidolph, Schwabach, Germany)
- two water baths :
  - Unistat CC, freely programmable in the range from -30 to 100°C (Huber, Offenburg, Germany);
  - Lauda M3, available for heating only (Lauda-Könighofen, Germany)
- ultrasonic bath with water heater (VWR International, Milano, Italy)
- Ultrasonic processor equipped with a 3 mm probe (Sonics VCX130, SY-LAB Geräte GmbH, Germany)
- HPLC pump, Pharmacia LKB; working range, 0,01-9,99 ml/min, 0,1-40MPa
- HPLC pump, Gilson 307; working range, 0,01- 5 ml/min, 0,1-60MPa
- three syringe pumps, low pressure; flow rate range, 1µl/hr – 2120 ml/hr
- four syringe pumps, high pressure: P max ~ 60 bar
- three high pressure infusion modules: P max ~ 690 bar

Further, four working benches (one with a water sink), two fridges (+ 4°C) and a separate freezer (- 20 °C), standard glassware, syringes and needles of different sizes, µ-pipettes (p10 - p100 - p200 - p1000), as well as some standard chemical reagents (e.g., chloroform, ethanol, methanol); deionized water (milli-RO and ultrapure milli-Q water) is available.

Figure 4. View of the Chemistry laboratory (left) and X-Ray laboratory (right).

User Contributions

Material Science

KINETICS OF INTERCALATION, CRYSTALLIZATION AND MELTING IN PEO AND PEO-b-PPO-b-PEO/MMT NANOCOMPOSITES

J. Baldrian[1], M. Steinhart[1], A. Jigounov[1], H. Amenitsch[2], S. Bernstorff[3]

1) Institute of Macromolecular Chemistry, A.S. CR, Heyrovsky Sq.2, 162 06 Prague, Czech Republic
2) Institute of Biophysics and X-ray Structure Research, A.A.S., Schmiedlstrasse 6, 8010 Graz, Austria
3) Sincrotrone Trieste, S.S.14, km 163,5 in AREA Science Park, 34012 Basovizza, Trieste, Italy

Introduction

Phase behavior, particularly intercalation of block copolymers into hosting clay layers and their crystallization kinetics, has been measured using simultaneous the SWAXS/DSC techniques during preprogrammed cooling and heating ramps. The conformation and mobility of clay intercalated PEO chains are expected to be quite different compared to bulk PEO. The polymer conformation and mobility in the PEO/clay nanocomposites are affected by the limited space and by the interaction with the charged surface of the inorganic host layers and interlayer cations.

Experimental

For this reason two types of Montmorillonite clays were selected namely Cloisite Na+ (interlayer cation) and Cloisite 10A (charged surface); (CNa+ and C10A). The studied samples were both clays combined with neat PEO and with four types of crystalline Pluronics (symmetric triblock copolymers PEO-b-PPO-b-PEO) in different compositions. All samples were treated by the same temperature treatment. At first they were melted at 70° C for 5 minutes. After that they were cooled at 1° C/min to –10° C and then heated with the same speed back to 70° C.

Results and Discussion

The left side of Fig.1 shows typical 1D WAXS diffraction patterns of Pluronic F127 with 30 wt.% of CNa+ and C10A in melted (70 °C) and solid state (-10 °C). Both samples showed well defined layer morphology with *q* ratios being 1:2. The overall layer thickness (*L*) was for 18 nm for CNa+ and 3.6 nm for C10A. Comparing with the layer thickness of pure C10A (1.86 nm) and CNa+ (1.0 nm). The thickenning of lammelar periodicities for 1.6 nm and 0.8 nm mean that clays are intercallated. The lamellar structures are well developed in molten state after crystallization is the quality of the structure preserved in the system with CNa+. The drop of intensities and broadening of reflections and partial disappearing of its 2nd order in the system with C10A mean the partial destruction of the lamellar structure during the crystallization of PEO.

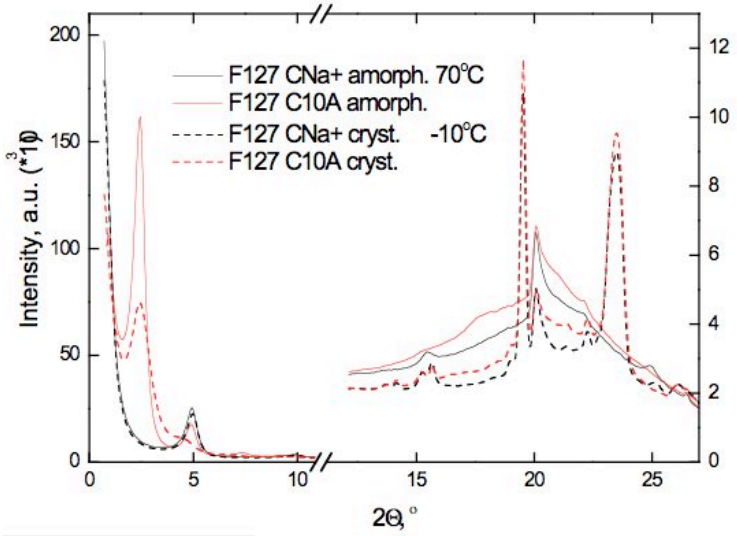

Figure 1. WAXS patterns of Pluronic/MMT systems

In the right side of Fig. 1, the WAXD profiles at 70 °C show a strong reflection at 2θ=20.0° [overlapped (110) and (020) reflections from the 2D crystals of layered silicates], superposing with an amorphous halo originating from the amorphous F127. When the temperature decreased to 39 °C, PEO outside the silicate layers started to crystallize, as shown by the (120) and mixed (032)/(132) reflections from the monoclinic PEO crystals at 19.2° and 23.5°. The changes of DSC and crystallinity on Fig.2. show, that the sample with C10A has higher crystallinity and crystallizes and melts at higher temperatures.

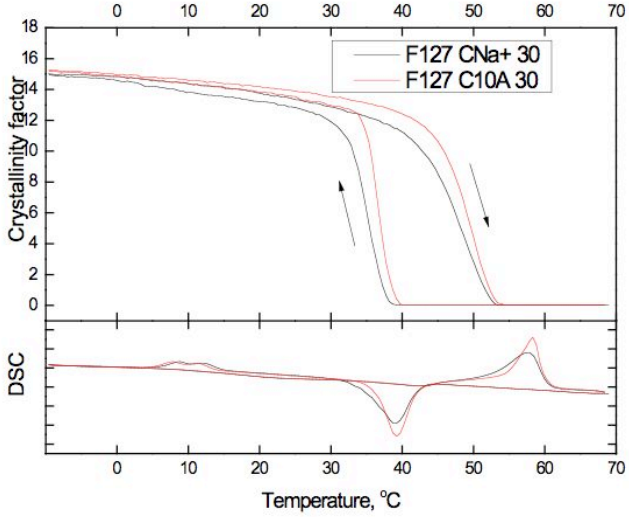

Figure 2. DSC and crystallinity changes during temperature treat-ment

The intercalation proceeds in the systems PEO/MMT and Pluronics/MMT in the same way, which indicates that the PPO blocks seem to stay outside the clay layers. In all samples with CNa+ the original periodicity increases by 0.8 nm after intercalation which corresponds to bilayers of planar PEO chains between silicate layers (Fig.3) and doesn't change during temperature treatment. The periodicity in the samples with C10A increases by 1.6 nm after intercalation. This corresponds to bilayers of PEO helices (FIG.3). The intercalated thickness of lamelae doesn't change during temperature treatment, but lamellar structure is better developed in the molten state. Stronger interaction of PEO with CNa+ causes planar conformation of chains in the contrary to the weaker interaction in the case of C10A, where the PEO chains preserve more stable helical conformation between silicate layers. This situaton is reflected also in higher crystallinity in system with C10A. Weaker interaction alows to crystallize higher amount of PEO chains outside the of intercalated stacks.

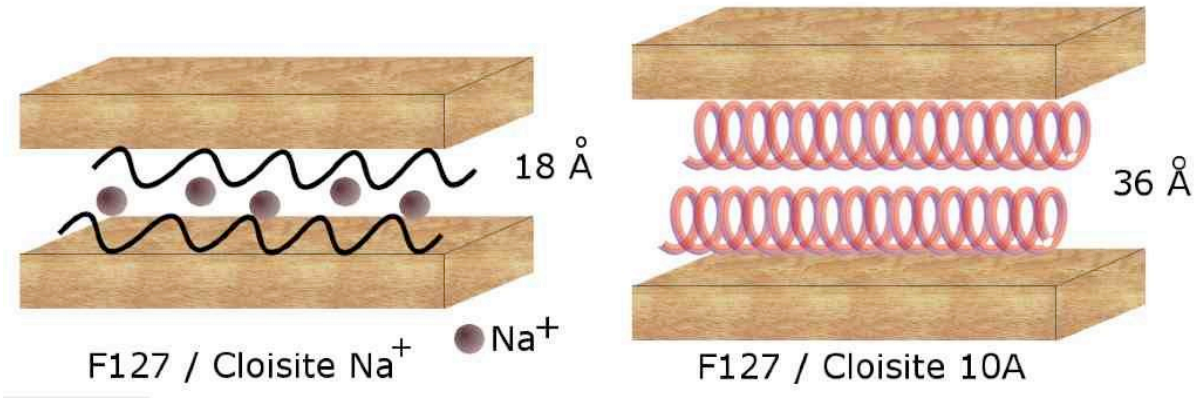

Figure 3. Structure of intercalated systems

GERMANIUM QUANTUM DOTS IN ALUMINA MATRIX: SELF-ASSEMBLY FOR ADVANCED PROPERTIES

M. Buljan[1], N. Radić[1], M. Jerčinović[1], S. Bernstorff[2] and V. Holý[3]

1.) Ruđer Bošković Institute, Bijenička cesta 54, 10000 Zagreb, Croatia
2.) Sincrotrone Trieste, SS 14 km163,5, 34012 Basovizza, Italy
3.) Charles University in Prague, Faculty of Mathematics and Physics, Czech Republic

We report on a method for the production of materials consisting of regularly ordered Ge quantum dots (QDs) in amorphous alumina matrix, with advanced properties. The regular ordering is induced by self-assembled growth during the magnetron sputtering deposition of a $(Ge+Al_2O_3)/Al_2O_3$ multilayer. The formation and regular ordering of quantum dots is achieved already at room temperature. The distances between the quantum dots and their sizes can be tuned by the deposition temperature, while the annealing temperature controls the quantum dots crystalline structure. The produced materials have a high spatial density of quantum dots with narrow size distribution, and they show a size-dependent photoluminescence in the visible light range.

Thin films consisting of 20 alternating $Ge+Al_2O_3$ and pure Al_2O_3 layers were produced by magnetron sputtering deposition on Si (111) substrate. The depositions were performed at three distinct substrate temperatures (T_d): room temperature (RT), 300 °C, and 400 °C. The structural properties of as-grown $(Ge+Al_2O_3)/Al_2O_3$ multilayer films are determined by the combination of grazing incidence small angle x-ray scattering (GISAXS), measured at the SAXS beamline of the synchrotron Elettra (Trieste), with a photon energy of 8 keV and a two dimensional image plate detector. GISAXS intensity distributions of the films grown at various substrate temperatures are shown in Figure 1(a)-(c). The regularity of the ordering of the QDs induces diffraction-like (Bragg) correlation-induced peaks in the GISAXS maps. Therefore, the distinct correlation-induced peaks are visible in all intensity maps, showing the formation of a 3D lattice of QDs for all deposition temperatures including the deposition at RT. It is worthy to note that clustering of Ge in silica-based multilayers does not result in the cluster formation at room temperature [1].

The arrangement type of the correlation-induced peaks, visible in Figure 1(a)-(c), is the same for all deposition temperatures, showing the same ordering type in all films. Another important feature is that the positions of the peaks are the same for all azimuthal orientations of the film with respect to the probing X-ray beam. This fact shows that regular ordering appears in domains that are randomly oriented with respect to the surface normal.

The GISAXS maps were numerically analyzed assuming ordering of QDs in a paracrystal-like lattice (model given in Ref. [2]) with a BCT-like structure. The simulations of the measured data obtained by the fitting process are shown in the insets of the measured GISAXS maps **(Fig. 1**(a)-(c)). The formed QD lattice in a single domain is characterized by basis vectors $\boldsymbol{a}_1$-$\boldsymbol{a}_3$ and parameters a_0 and c_0. The basis vectors $\boldsymbol{a}_1$ and $\boldsymbol{a}_2$ lay in the plane parallel to the multilayer surface (in-plane). Their length a_0, strongly depends on the deposition temperature as will be shown in the following text. The component of the basis vector $\boldsymbol{a}_3$ that is perpendicular to the multilayer surface corresponds to the multilayer period c_0. A certain degree of disorder exists in the formed QD lattices. The influence of the deposition temperature on the QD sizes and arrangement in $(Ge+Al_2O_3)/Al_2O_3$ multilayer films, found by numerical analysis of the GISAXS measurements is demonstrated in Fig. 1(d)-(f). The dependence of the main QD radius on the deposition temperature is shown in Fig. 1(d), while the deposition-temperature dependences of the basis vector parameters of the formed QD lattices are demonstrated in Fig. 1(e). From the graphs it follows that the sizes of the QDs and the in-layer distances a_0 of the QDs significantly increase with the deposition

temperature, while the inter-layer separation (i.e., the multilayer period c_0) remains nearly constant. We have analyzed the average content of Ge in the films by Rutherford backscattering and a nearly constant value of 4.0 ±0.1 atomic percents was found for the all as-grown films. So, the deposition temperature influences strongly the Ge clustering via diffusion process and enables the control of the QD sizes and their separations (i.e. the lengths of basis vectors $\boldsymbol{a}_1$-$\boldsymbol{a}_3$). Moreover, the multilayer period does not change with the deposition temperature as well as the Ge content. The deposition temperature controls the distribution of Ge atoms via the QD sizes and their in-plane separations. From the obtained parameters we have calculated the density of the formed QD arrays. A very high density of QDs of about 10^{25} QDs m^{-3} is obtained for the deposition at RT. The size distributions of the QDs obtained for various temperatures are shown in Fig. 1(f). All size distributions are quite narrow and their widths increase slightly with the deposition temperature.

We can conclude that Ge QDs in alumina based multilayer appear in BCT-like QD lattices, with a relatively small degree of disorder. The QD sizes and their distances can be adjusted by the deposition temperature. More details about structural and photoluminescence properties of the presented films are given in Ref. [3].

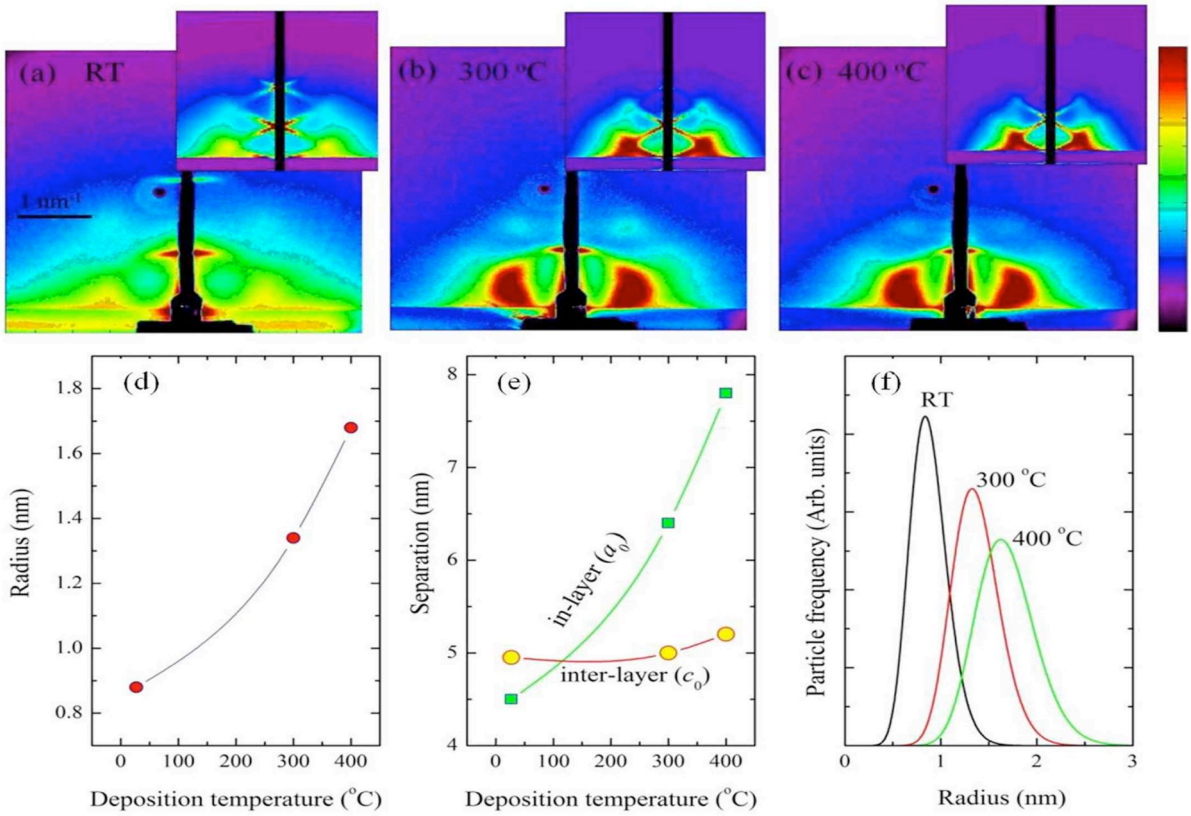

Figure 1. (a)-(c) GISAXS maps of the films deposited at various temperatures (indicated in the figure). The insets show the simulated GISAXS maps obtained by fitting of the measured spectra. The deposition-temperature dependences of the: (d) QD radius, (e) QD lattice parameters a_0 and c_0 and (f) QD size distribution.

References:

[1] M. Buljan, U. V. Desnica, G. Dražić, M. Ivanda, N. Radić, P. Dubček, K. Salamon, S. Bernstorff, V. Holý, Nanotechnology **20**, 085612 (2009)

[2] M. Buljan, N. Radić, S. Bernstorff, G. Dražić, I. Bogdanović-Radović, V. Holý, Acta Cryst. A **68**, 124 (2012)

[3] M. Buljan, N. Radić, M. Ivanda, I. Bogdanović-Radović, M. Karlušić, J. Grenzer, S. Prucnal, G.Dražić, G. Pletikapić, V. Svetličić, M. Jerčinović, S. Bernstorff and V. Holý; submitted / under consideration; (2012)

INVESTIGATION OF THE TEMPERATURE DEPENDENCE OF THE LAYER SPACING IN A SERIES OF LOW MOLAR MASS BI-MESOGEN ORGANOSILOXANE SMECTIC MATERIALS

C Carboni[1], D Carboni[1], D Jozic[2,3], S Bernstorff[3] and M Rappolt[4]

1.) Sultan Qaboos University, Physics, P O Box 36, 123 Muscat, Sultanate of Oman
2.) University of Split, Faculty of Chemistry and Technology, Department of Inorganic Technology, 21000 Split, Croatia
3.) Sincrotrone Trieste, SS 14, km 163.5, 34012 Basovizza (TS), Italy
4.) Institute of Biophysics and X-ray Structure Research, A.A.S., Schmiedlstrasse 6, 8010 Graz, Austria

In low molar mass organosiloxane liquid-crystal materials the molecule consists of mesogenic moieties attached via alkyl chains to a short siloxane chain. In the mesophases the siloxane moieties tend to micro-separate from the mesogenic moieties favouring a layered structure with alternating mesogen-rich and siloxane-rich layers. On cooling, the materials usually display a transition from the isotropic to a smectic phase [1]. It has been argued that the siloxane-rich layer can be regarded as an effective two-dimensional polymer backbone and the mesogen as side-chain pendants. The low molar mass organosiloxane liquid-crystal materials are therefore somewhere in-between the conventional low molar mass and the polymeric materials. In that respect the bi-mesogens are particularly interesting because the same material can behave either as a low molar mass material or as a polymeric material depending on the property investigated. The electro-optical response of bi-mesogenic materials in the smectic phase is determined to a large extent by the conformation of the molecule in the material confined in the specimen cell [2, 3].

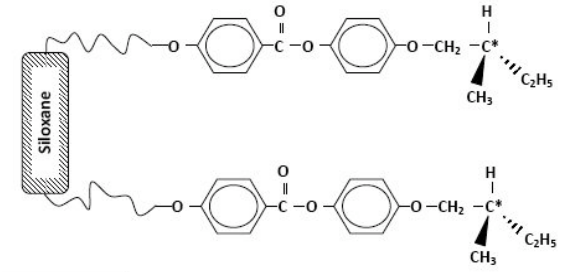

Figure 1. The schematic diagram of the molecule in the materials investigated.

The materials investigated in this project are from the series of bi-mesogens synthesised by Kaeding and Zugenmaier [4]. The schematic diagram of the molecule is shown in figure 1. The rigid core of the mesogen has two rings and the stereogenic centre is situated at the end of the short terminal chain. The siloxane moiety contains three silicon atoms. The parameter varied across the series is the number n of carbon atoms in the alkyl chain. The temperature dependence of the layer spacing of the materials with n = 11, 10 and 6 (11Dim, 10Dim and 6Dim respectively) is investigated.

In the materials 10Dim and 11Dim it is observed that, as the temperature is increased from room temperature, there is first a small but significant decrease in the layers spacing until a temperature of about 15 ^{o}C below the transition to isotropic. Above this temperature the layer spacing increases until the transition to the isotropic phase as shown in figure 2. This unusual behavior could be explained if the molecules are in V-shaped conformation [1] and, as the temperature increases, the angle of the V decreases. In the 15 degrees temperature range above the transition to isotropic there is as one might expect a gradual reduction of the interdigitation of the molecules.

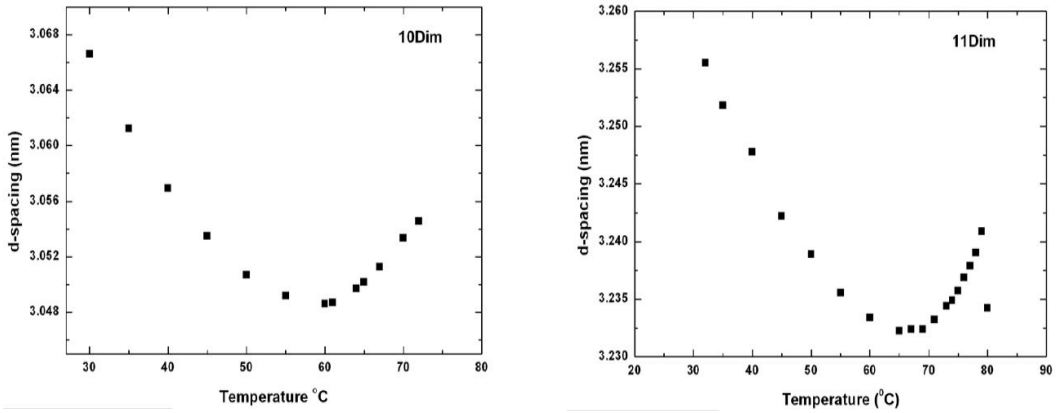

Figure 2. The temperature dependence of the layer spacing in 10Dim and 11Dim

The material 6Dim displays a transition between two yet not unequivocally identified smectic phases. The transition occurs at 35 ^{o}C. The polarized light microscopy observations show that at this temperature there is a change of texture that occurs in the form of narrow stripes [3] progressing in the direction of the smectic layers. The present X-ray data confirms that there is an abrupt change of layer spacing at the transition (figure 3) and that the two phases do coexist during the transition with one phase growing at the expense of the other (figure 4).
Work is in progress to correlate the x-ray data to the optical observations, tilt angle measurements and conformation lengths calculations to ascertain the nature of the phases and establish whether the transition is a phase transition, a change of conformation or simply that there is a jump in the amount of interdigitation of the mesogens due possibly to a steric barrier. This later possibility would not be compatible with the fact that [3] a large electric field applied to the high temperature phase can switch the specimen to a texture identical to that of the low temperature phase. More measurements in applied fields are planned to elucidate the behavior of this material. Preliminary analysis of this data was accepted for presentation at the International Liquid Crystal Conference (Mainz) [5].

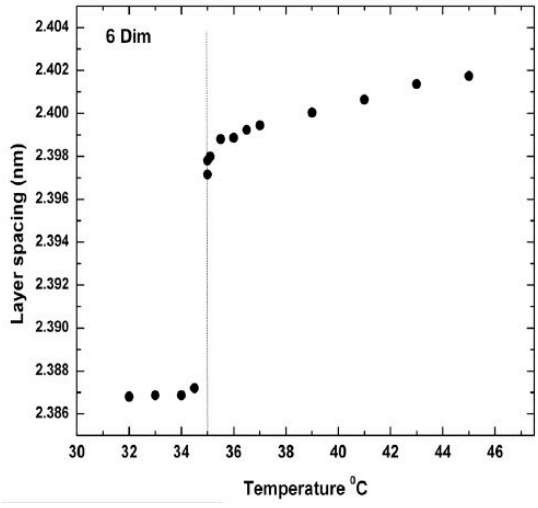

Figure 3. The temperature dependence of the layer spacing in 6Dim.

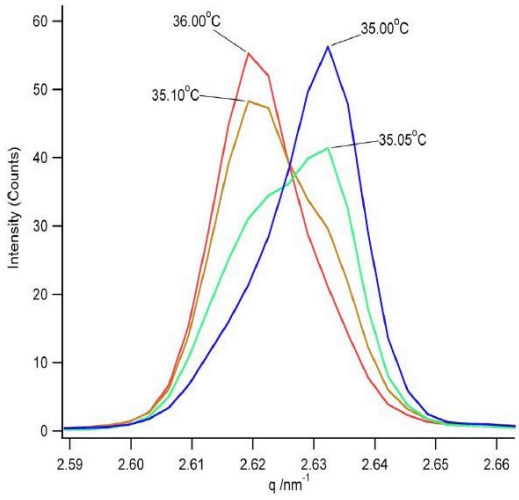

Figure 4. The scattered intensity as a function of q measured at different temperatures in the vicinity of the transition.

References

[1] W K Robinson, P Kloess, S Perkins, C Carboni, H J Coles; *Ferro electric and anti ferro electric low molar mass organosiloxane liquid crystals*; Liquid Crystals, Vol. 25, 301-307 (1998)

[2] C Carboni, A K George, W Al-Shizawi, M W Zoghaib and Jawad Naciri; *Threshold field for switching the de-Vries S_A^* phase in a low molar mass organosiloxane material*; Liquid Crystals, Vol. 37, No. 11, 1427–1431 (2010)

[3] C Carboni, A K George and W M Zoghaib; *The electro-optic response in a series of chiral bi-mesogen low molar mass organosiloxane liquid-crystal materials*, Mol. Cryst. Liq. Cryst., Vol. 546, 215–220, 2011

[4] A Kaeding and P Zugenmaier; *Investigations of a homologous series of chiral siloxane based dimesogenic compounds; Liquid Crystals*, Vol. 25, No **4**, 449-457 (1998)

[5] C Carboni, D Carboni, D Jozic, S Bernstorff and M Rappolt; *Synchrotron X-ray investigation of the layer spacing in a series of low molar mass bi-mesogen organosiloxane smectic materials*; Proceedings of the 24th International Liquid Crystal Conference, Mainz, Germany, August 19th - 24th 2012

GISAXS STUDY OF SI NANO STRUCTURES IN SIO_2 MATRIX FOR SOLAR CELL APPLICATIONS

P. Dubček[1], B. Pivac[1], I. Capan[1], H. Zorc[1], J. Dasović[1], S. Bernstorff[2], M. Wu[3] and B. Vlahovic[3]

1.) P. Bošković Institute, P.O. Box 180, Zagreb, Croatia
2.) Sincrotrone Trieste, SS 14, km 163.5, Basovizza (TS), Italy
3.) North Carolina Central University, Durham, NC, USA

Amorphous SiO_x/SiO_2 superlattices were prepared by high vacuum evaporation of alternating films of SiO_x and SiO_2 from commercially available (Balzers) solid sources. Each layer was 5 nm thick (forming a stack of 10 bilayers plus one SiO_2 capping layer) on clean Si (100) substrate held at room temperature. Rotation of the Si substrate during evaporation ensured homogeneity of the films deposition over the whole substrate surface. After deposition, the samples were annealed at different temperatures starting from 600°C to 1100 °C for 1h in vacuum better than 10^{-6} Pa to induce Si nanocrystals formation.
In Fig. 1 the GISAXS pattern for a 900°C annealed sample is shown, taken at the critical and slightly above the critical angle. At the critical angle of incidence the photon penetration is very limited (typically 10-20 nm) and thus the scattering from the interior of the film is very weak. At a wider grazing incidence angle both the surface and bulk scattering are present. Therefore, after realigning the images to the same refracted angles the difference between b and a is calculated. In that way the surface contribution is removed and the scattering signal from the bulk of the film is enhanced. The first and the second Bragg peaks, due to the repetitive structure of the multilayer film, are clearly resolved at q_z=0.7 nm^{-1} and q_z=1.3 nm^{-1}. Moreover, a large hemispherical signal in the background dominates the image, clearly indicating the presence of nanoparticles in the bulk of the film. In this approach we neglect the correlation between the surface of the film and the interfaces between the (few top) layers of the film, which can be justified by gaining of the information about the nanoparticles scattering.

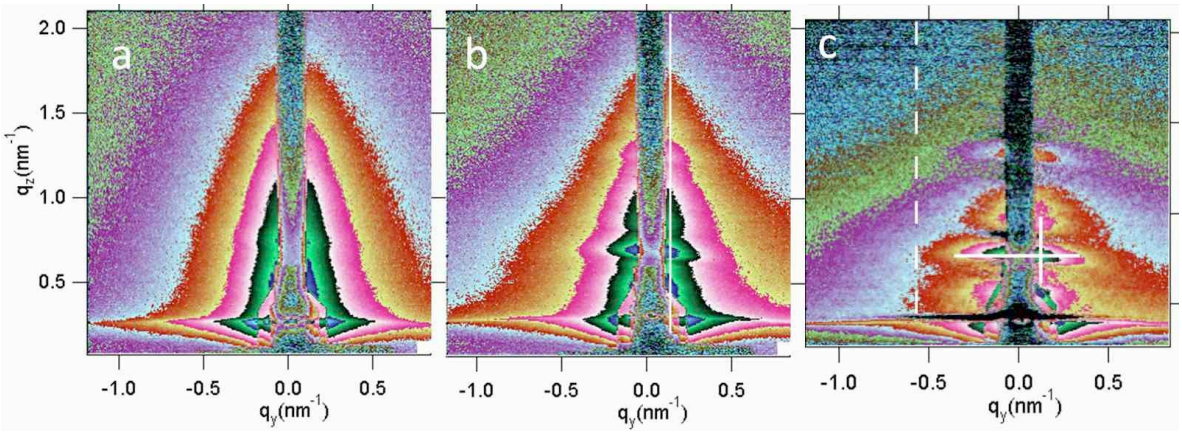

Figure 1. GISAXS pattern obtained at the critical (a) and 0.03° above the critical angle (b) from the sample annealed at 900°C, and their difference (c). The white line in the figure indicates the place where the line cut was made.

The intensities along the full white lines in Fig. 1c were used for the layer correlation evaluation based on the distorted-wave Born approximation. The results are summarized in Fig. 2, where it is shown that there is no significant variation of the lateral correlation (red open dots) of the film. The correlation is somewhat reduced upon annealing at about 900°C

and for higher temperatures it is restored again. On the other hand the vertical correlation of the interface roughness shows significant increase towards highest annealing temperatures. Upon annealing at lower temperatures, the structure of both films is being relaxed slightly. This somewhat increases the correlation, especially in the vertical direction. The effect is not so apparent in the horizontal direction, since the freedom of movement of atoms is relatively low. Still this can reduce the roughness of the SiO_x/SiO_2 interfaces of the layers, which influences more significantly the vertical correlation.

Higher temperature annealing introduces decomposition of SiO_x into SiO_2 + Si which inevitably destroys the correlation partly, and when Si particles begin to form, they somewhat enhance the scattering contrast and the correlation. Finally, at the highest temperature, both correlations are reduced slightly again.

The subtraction of the surface signal from the scattering enhances the signal from the bulk, which includes also the multilayer scattering part. In order to analyze the particle signal, we extracted part of the scattering signal away from the specular plain, where the surface contribution is minimized (the dashed line in Fig. 1c) and used the Guinier approximation. The intensities along this line can be approximated well by a Gaussian, implying that there is a dominant typical size, and the size distribution is relatively narrow.

The obtained sizes are plotted in Fig.3 for the whole temperature range, together with the multilayer d-spacing (bilayer thickness) results from the above mentioned Bragg peak analysis. We can see that the bilayer thickness is peaked at 700ºC. The slow increment at lower temperatures can be ascribed to structural annealing, while the minimum at the highest temperature is ascribed to SiO_x decomposition. The size of the detected inhomogeneities in the film is increasing slowly up to 800 – 900ºC, and there is a significant minimum at 1000ºC, which we ascribe to the onset of Si nanopaticle formation. The size of the particles is confined to 4-5 nm, justifying the role of the SiO_2 layers as diffusion barrier. The particle signal, as it is, lacks the information about the particle to particle distance, and this results from poor ordering within single the layer.

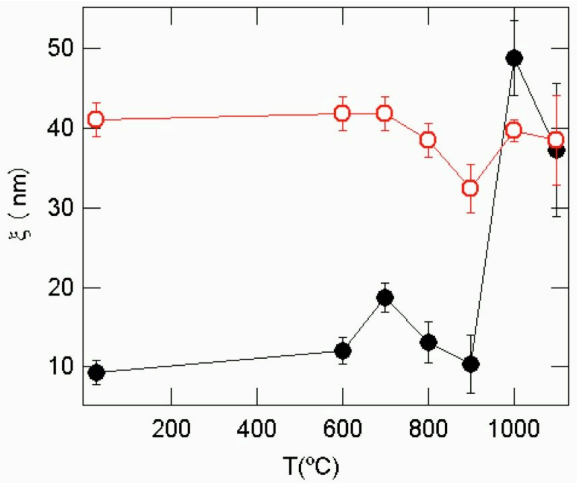

Figure 2. The horizontal (open red dots) and vertical (full black dots) correlation lengths vs. annealing temperature.

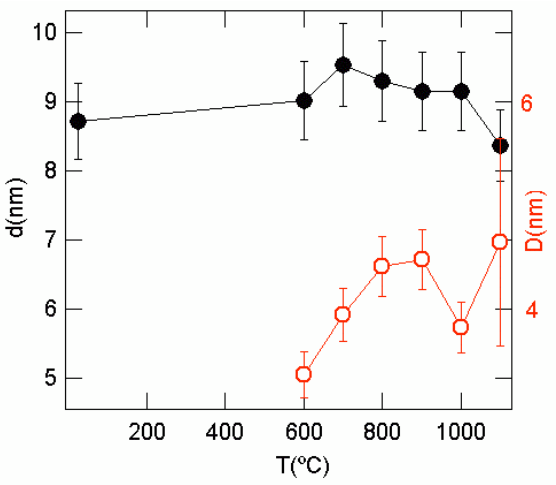

Figure 3. The thickness d of the bilayers obtained from the peak position of the Bragg peak and the diameter D of the Si nanoparticles versus annealing temperature.

STRUCTURE OF ALKALI METALS IN NANOPOROUS CONFINEMENT

A. Ghaffar[1], W. Pichl[1], G. Krexner[1], F. Spieckermann[1] and S. Bernstorff[2]

1.) University of Vienna, Faculty of Physics, Boltzmanng.5, A-1090 Vienna, Austria
2.) Sincrotrone Trieste, I-34149 Basovizza (TS), Italy

All alkali metals exhibit body-centered cubic (BCC) structure at ambient conditions. At low temperatures, structural phase transitions have been found in Li and Na which undergo martensitic transformations to HCP and 9R at 78K and 35K, respectively [1, 2]. Transitions from the ambient BCC to close-packed modifications are also found at high pressure, i.e. at 7.5 GPa for Li and at 50 GPa for Na [3]. From theoretical studies it has long been known that the relative differences of the free energies of close-packed and parent phases are very small [4] and that the transitions are associated with precursor phenomena which can be observed already far away from the transformation points. This situation raises the question whether structural changes may be induced also by geometrical constraints.

In situ synchrotron diffraction experiments during heating were performed on metallic lithium and sodium crystallized inside various nanoporous media including Vycor glass (mean pore size 9.2nm), Gelsil (2.5 nm, 5 nm, 10 nm, 20nm, 30 nm, 40 nm), alumina membranes (20 nm, 100 nm), compacted powder samples of SBA-15 (8.9 nm) and MCM-41 (2.5 nm). The thoroughly cleaned porous matrices were loaded by condensation of metal vapors produced by heating the solid metals under low pressure.

Earlier experiments on Li in Vycor with ~9.2 nm pore size had already revealed the presence of hexagonal close-packed structures (HCP and FCC) with characteristic peak broadening attributed to the nanocrystalline structure of the metal inside the pores. In addition, it had been found that no melting takes place at the bulk melting temperature of Li at 180°C but, due to its confined state, the metal remains solid up to at least 400°C.

It is expected that, with increasing pore size, the melting behavior of confined lithium gradually approaches the bulk melting temperature. However, the present experiment clearly demonstrates that, even on varying the pore size up to 40 nm, Li inside the porous network does not show the normal melting behavior at 180°C but remains solid at least up to 250°C and that bulk properties are attained only at still larger pore sizes. This result is in strong contrast to the usual melting point depression on the order of several degrees observed experimentally both in confined metals and non-metallic substances.

Confined sodium which was investigated for the first time during the present experiment and gave results similar to lithium: already at room temperature the observed structures are close-packed including HCP, FCC and 9R while there is no indication of the BCC bulk phase (see Fig.1). Likewise, also constrained Na does not melt at the bulk melting temperature of 98°C but remains solid and kept its structural state up to more than 250°C which was the maximum temperature available on the heating stage.

In summary, both confined Li and Na adopt close-packed structures already at and above room temperature thereby indicating an upward shift of the martensitic phase transition temperature by several hundred degrees due to geometrical constraints. Further, the melting point is increased by about 200 K. While the former phenomenon can be explained on the basis of model calculations comparing the free energies of BCC and various close packed structures, the latter finding is highly surprising and, at present, largely unexplained. Yet it is likely that the entropy term in the free energy plays a major role in the stabilization of nano-confined crystalline structures at higher temperatures.

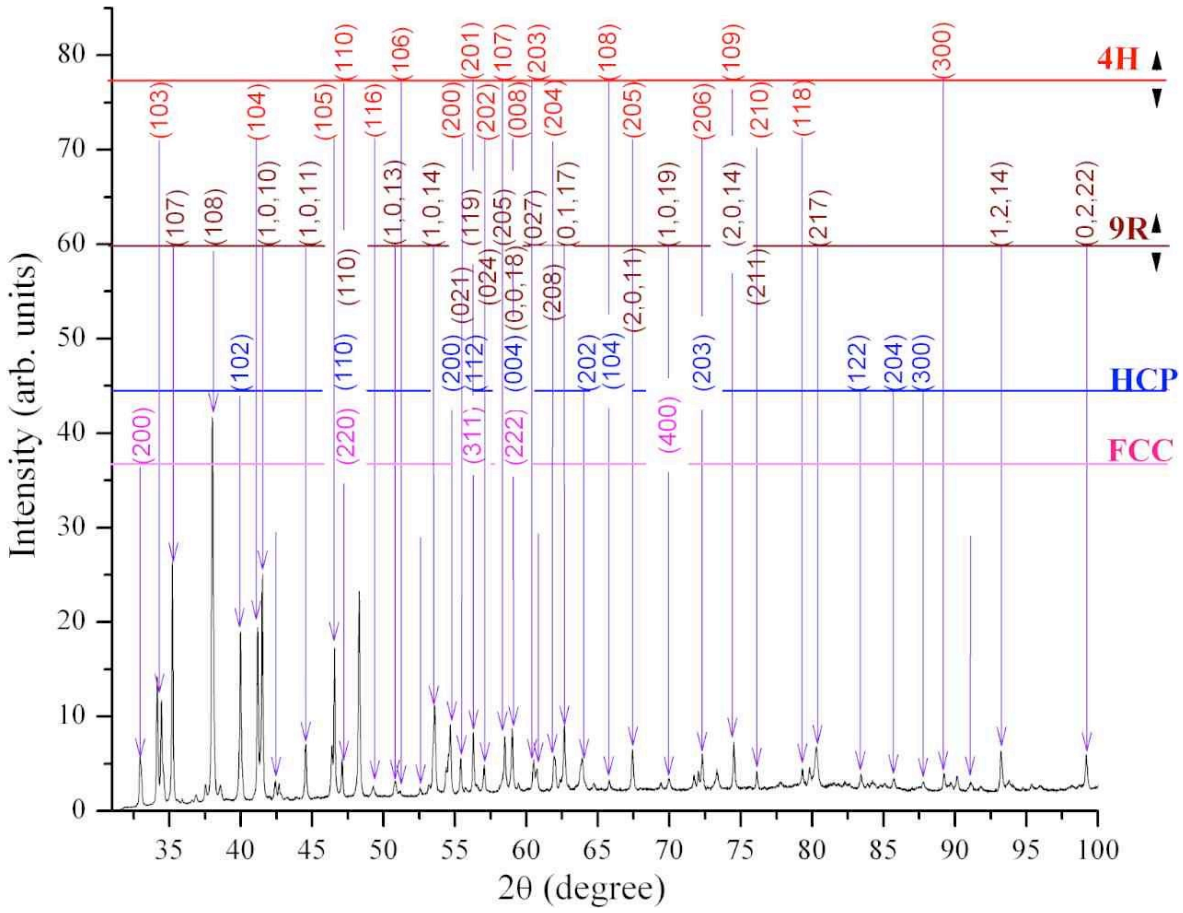

Figure 1. Synchrotron X-ray diffraction pattern of confined Na at room temperature as a function of the scattering angle 2θ. Various close-packed structures are observed while the bulk BCC phase is completely absent.

References:

[1] R. Berliner, O. Fajen, H. G. Smith, and R. L. Hitterman, "Neutron powder-diffraction studies of lithium, sodium, and potassium metal", Phys. Rev. B **40**, 12 086–12 097 (1989)

[2] O. Blaschko, V. Dmitriev, G. Krexner, and P. Tolédano, "Theory of the martensitic phase transformations in lithium and sodium", Phys. Rev. B **59**, 9095–9112 (1999)

[3] M. Prem, M. Krystian, W. Pichl, G. Krexner, and S. Klotz, "Neutron scattering investigation of pressure-induced phase transitions in Li and Ba", J. Phys.: Condens. Matt. **17**, S3165–S3171 (2005)

[4] V.G. Vaks et al., J. Phys.: Condens. Matt. **1,** 5319-5335 (1989)

THE INFLUENCE OF DEPOSITION CONDITION ON NANOSRUCTURE OF AMORPHOUS- NANOCRYSTALLINE Si FILMS

D. Gracin[1], K. Juraić[1], P. Dubček[1] and S. Bernstorff[2]

1.) Ruđer Bošković Institute, Bijenička 54, 10000 Zagreb, Croatia
2.) Sincrotrone Trieste, SS 14 km 163.5, 34149 Basovizza (TS), Italy

Amorphous-nanocrystalline Si (a-nc-Si) thin films are interesting as a possible candidate for high efficiency solar cells. These films consist of Si nanocrystals embedded in amorhous Si matrix, and their properties depend critically on the size distribution and volume contribution of the nano-crystals. The structure of a-nc-Si depends on details of the preparation which are not yet fully established.

The samples were deposited by microwave silane plasma highly diluted with hydrogen. The degree of dilution ($R= p_{SiH4} / p_{H2}+p_{SiH4}$) determinates the processes in the plasma that have a key influence on the film growth, and hence the film nano-structure. For this experiment, the dilution was varied from 40 to 100 in order to find the critical pressure for crystal formation and estimate the homogeneity of the structure in the depth of films with thickness between 400 and 600 nm.

GISAXS and GIWAXS measurements were performed simultaneously using a X-ray beam energy of 8 keV which corresponds to the wavelength $\lambda= 0.154$ nm. The grazing angle of incidence, α_i, was selected in the range $0.21° < \alpha_i < 0.25°$. The first angle corresponded to the critical angle of the sample and was slightly lower than the critical angle for silicon, indicating a less dense material. The selected range of angles corresponded to a penetration depth that was between 15 nm (surface) and equal to the thickness of the samples. GISAXS pattern were acquired by a two-dimensional position sensitive Mar-Research Image Plate detector, at a detector-to-sample distance L = 2 m. GIWAXS was measured with a 1D-Gabriel-type gas detector. The depth distribution of the 'particle' sizes was obtained by changing the grazing incident angle.

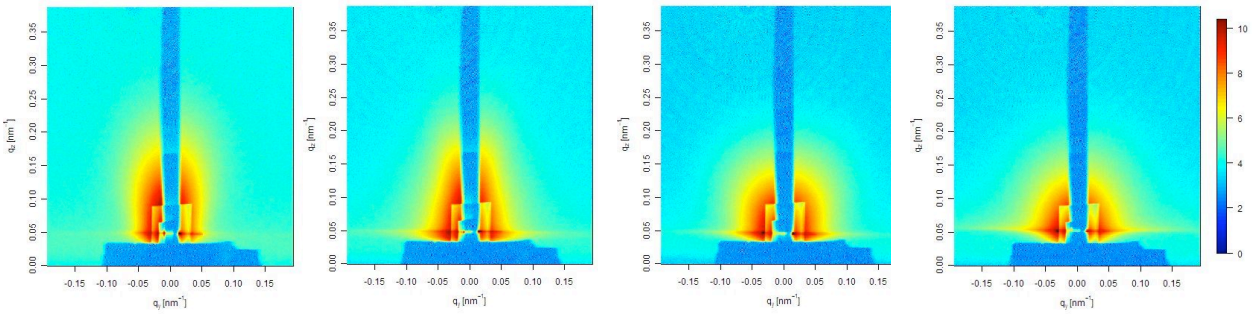

Figure 1. GISAXS patterns of samples deposited at various ratios between hydrogen (H_2) and silane (SiH_4) partial pressures $R = p_{H2}/(p_{H2}+p_{SiH4})$ in the working gas: a) R= 43, b) R=50, c) R=60 H/SiH4, and d) R= 75

In Fig.1 are plotted the GISAXS patterns recorded at the critical angle for thin Si deposited under various dilution, R, but with constant discharge power and gas flow rate. According to the GIWAXS spectra (Fig.2) the samples deposited under R = 43 were completely amorphous while those deposited with R = 50 and above were at least partially crystalline. However, the GISAXS signals are present in all samples. This fact indicates the presence of nano-sized "particles" even in the amorphous phase that can be the initial nuclei for crystals that are formed at higher R. Similar ordered domains that are not crystals were observed by GISAXS

earlier [1] and give in some cases the "boson-like" signal in the background of a typical Raman spectrum of Si-Si bonds vibrations [2]. For the first sample (Fig 1a, R = 43), the signal is elongated in the direction parallel to the surface and very similar to the patterns obtained on bare glass substrate. The samples deposited under R = 60 and above (Fig 1b-1d) have a different shape, their signals are more rounded indicating a spherical symmetry or randomly oriented small crystals.

The GIWAXS spectra, plotted in Fig.2, show a gradual change with increasing gas ratio R. The spectrum of the sample deposited with R = 43 consists of two Gaussian like, broad peaks that correspond to amorphous structure. At slightly elevated R, R = 50, the crystalline peaks that correspond to the crystalline phase become clearly visible.

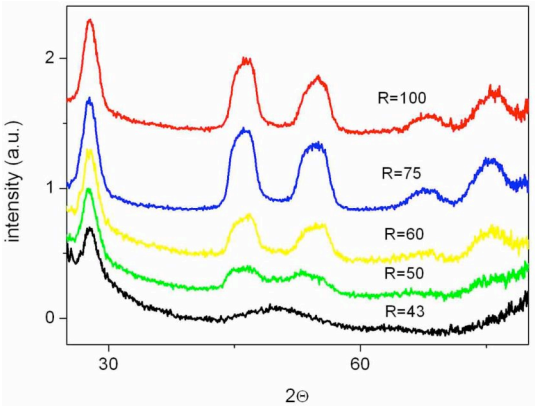

Figure 2. GIWAXS patterns of samples deposited at various ratio between hydrogen (H_2) and silane (SiH_4) partial pressures in the working gas

The radii of gyration, R_G, were estimated using the Guinier approximation [3] and are plotted in Fig.3. The R_G increase with increasing dilution ratio, R, and do not change markedly over the depth of the sample which indicates a homogeneous structure.

The size of the nano-crystals were estimated from the GIWAXS peaks [4] assuming that the line broadening of the characteristic Braggs peaks were a consequence of the size of the crystals, the instrumental profile and the strain. Since the sizes of the crystals were in the range 4-8 nm and the crystal fraction was between 0 and 40 vol %, the strain was neglected in the first approximation. The instrumental line broadening, w_{INSTR} was estimated using the NIST standard LaB_6 powder. The crystal size is then estimated using the Sherrer formula [4]:

$$D_{GIWAXS} = K\lambda \left((w_{GIWAXS} - w_{INSTR})*\cos\theta\right)^{-1} \qquad \text{(eq.1)}$$

where w is the full width at half maximum of the peak at the corresponding angle θ.

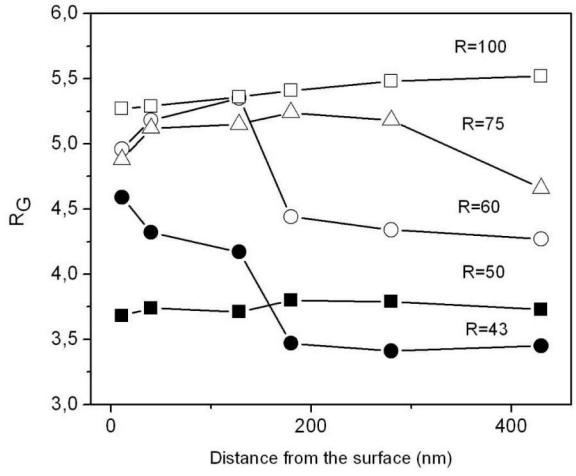

Figure 3. Gyro radii as a function of distance from the surface with dilution ratio, R, as the parameter

In Fig.4 are plotted the size of nano-crystals, D, versus the gyro radii, R_G.. There is an apparent proportionality between D and R_G with the D values being slightly larger. Since the GISAXS "particles" and GIWAXS nano-crystals had the same size, it was concluded that the particles in our case were closely related to the ordered Si domains or domains itself. Furthermore, since the crystal sizes D obtained by GIWAXS, are similar to the crystal sizes obtained by GISAXS means that the layers are indeed free of strain.

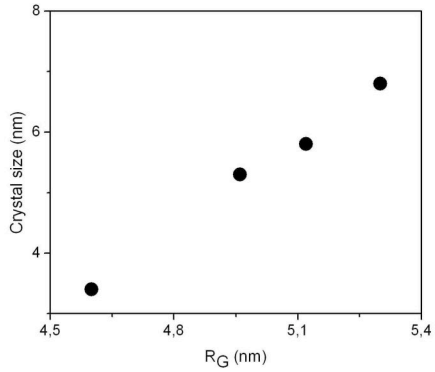

Figure 4. Size of crystals estimated from the GIWAXS spectra using eq.1 versus the corresponding gyro radii R_G for samples with a measurable crystal fraction at the first angle above critical angle.

References:

[1] D.Gracin, K.Juraić, P.Dubček, A.Gajović and S.Bernstorff, Appl.Surf.Sci. 252 (2006) 5598–5601
[2] M.Ivanda, K. Furić, O. Gamulin, M. Peršin, D. Gracin, Journal of Applied Physics. **70** (1991), 8; 4637-4639
[3] O.Glatter, O.Kratky, Small Angle x-Ray Scattering, Academic Press, London, 1982, 272
[4] K.Williamson, W.H.Hall, Acta Metall. 1 (953) 22

X-RAY SMALL-ANGLE SCATTERING FROM SPUTTERED CeO_2/C BILAYERS

S. Haviar[1], V. Matolín[1], V. Valeš[1], J. Endres[1], V. Holý[1], M. Buljan[2] and S. Bernstorff[3]

1) Charles University in Prague, Ke Karlovu 5, 121 16 Praha, Czech Republic
2) Rudjer Bošković Institute, Bijenička 54, HR-10000 Zagreb, Croatia
3) Sincrotrone Trieste, 34149 Basovizza, Trieste, Italy

CeO_2-based thin layers are intensively studied recently because of their broad application as catalysts; their catalytic activity substantially depends on the surface morphology. Usually, the surfaces of CeO_2/C and CeO_2(Pt)/C bilayers are investigated by transmission electron microscopy (TEM), and by scanning techniques (atomic-force microscopy – AFM, or scanning electron microscopy – SEM). The TEM method is destructive and rather time-consuming, the resolution of the scanning methods is not sufficient for the investigation of tiny details on surfaces of very thin layers.

The aim of our study was to develop an x-ray scattering technique for a rapid and simple characterization of the surface morphology of CeO_2/C bilayers grown by magnetron sputtering on Si substrates. We used a standard GISAXS method with a fixed incidence angle of 0.25 deg (just above the critical angle of total external reflection) and with the photon energy of 8 keV. For various thicknesses of the CeO_2 layers, two types of the experimental scattering patterns have been observed. Samples with CeO_2 layers thicker than approx. 5 nm yielded GISAXS intensity distributions that could be simulated by a standard model of fractal roughness [1] (see Fig. 1), for thinner CeO_2 layers (independently from the thickness of the carbon interlayer), we obtained GISAXS patterns with pronounced lateral satellites (Fig. 2) that do not correspond to the standard roughness model.

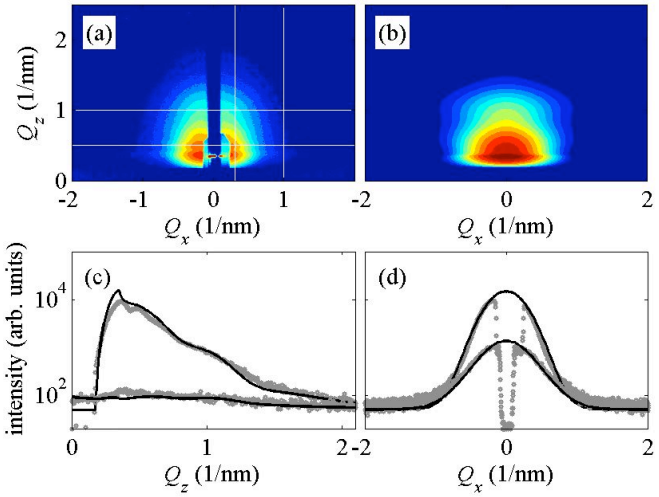

Figure 1. Measured (a) and simulated (b) reciprocal-space distribution of the scattered intensity (GISAXS method) from a continuous CeO_2/C bilayer. White lines in panel (a) denote the reciprocal-space trajectories of vertical and horizontal scans extracted from the measured data. The panels (c) and (d) depict the extracted vertical (c) and horizontal (d) scans (points) along with their fits (lines).

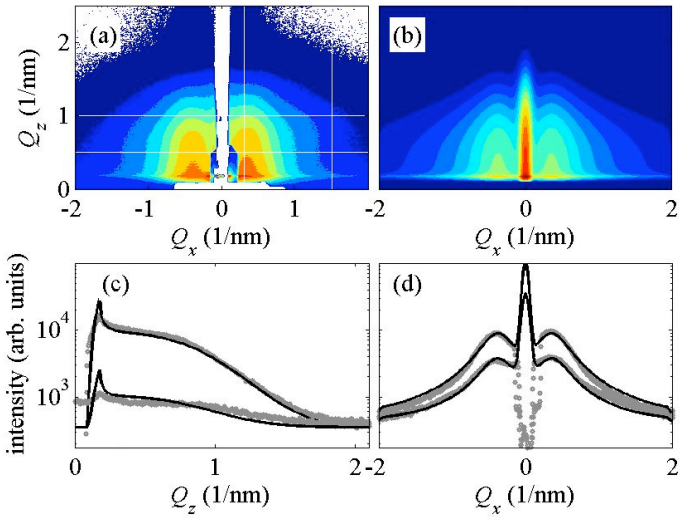

Figure 2. The same situation as in Fig. 1, a discontinuous CeO_2/C bilayer.

In the case of thinner layers, the sample structure consists of randomly distributed islands (see the SEM picture in Fig. 3). Therefore, for the description of the scattering we used a simple one-dimensional model of a non-continuous bilayer, sketched schematically in Fig. 4. The model is a modification of a two-level surface model formulated in Ref. [2]. In this model we assume that a random sequence of CeO_2/C pillars occurs on the Si surface, the widths of the pillars and of the gaps between them are random with the mean values $L_{P,G}$, and root-mean square (rms) deviations $\sigma_{P,G}$, respectively. The CeO_2/C interfaces in the pillars as well as the CeO_2 top pillar surfaces are rough with the rms roughness σ, and lateral and vertical correlation lengths $\xi_{\|,\perp}$. The formulas for the scattered intensity are quite cumbersome and they will be published soon in our paper [3]; the distance ΔQ_y of the lateral satellites is inversely proportional to the mean distance of the pillars $\Delta Q_y = 2\pi/(L_P + L_G)$.

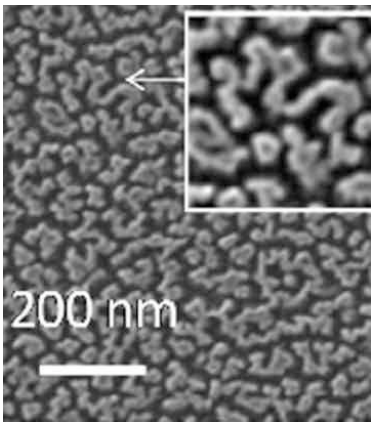

Figure 3. A SEM image of the surface of a discontinuous CeO_2/C bilayer. The inset shows a zoomed area of the surface.

We have compared the measured GISAXS data with the simulations and determined the mean widths $L_{P,G}$ of the pillars and the gaps and the rms roughness σ of the interfaces. Figures 1 and 2 show the measured and simulated GISAXS maps for samples with thicker and thinner CeO_2 layers. We have fitted the vertical and horizontal linear scans extracted from the measured GISAXS maps to the theory (panels c and d in Figs. 1 and 2, respectively) and simulated whole intensity distributions in the reciprocal Q_yQ_z plane perpendicular to the sample surface and to the primary x-ray beam (panels b).

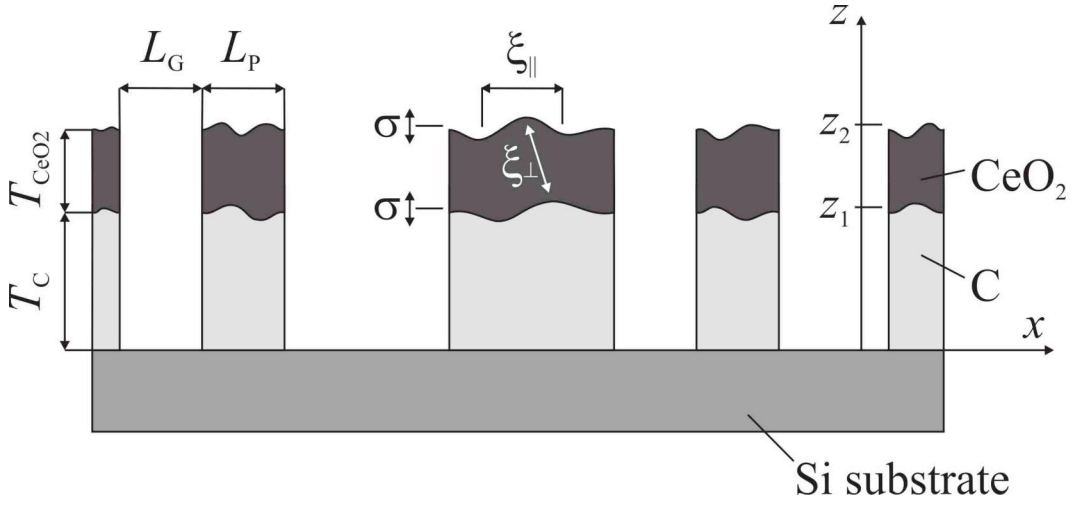

Figure 4. Sketch of the structure model of a discontinuous bilayer.

The mean size of the pillars and the gaps determined from the GISAXS data have been compared with the parameters determined from SEM measurements. The mean distances of the pillars $L_P + L_G$ determined from GISAXS and SEM coincided with the accuracy of 10%, the pillar widths L_P determined from GISAXS were approx. two-times smaller than from SEM. This difference can be explained using the fact that the actual shape of the CeO_2/C islands is rather conical. The SEM method detects the base width of the islands, while the pillar-gap model used in GISAXS determines the *mean* width of the islands that is approx. half of the base width.
In summary, we have developed a structure model for discontinuous CeO_2/C bilayers that makes it possible to determine the parameters of the bilayers from GISAXS data.

References:

[1] U. Pietsch, V. Holý and T. Baumbach; High-Resolution X-Ray Scattering From Thin Films to Lateral Nanostructures (Springer-Verlag Berlin, Heidelberg, New York 2004)
[2] P. R. Pukite, C. S. Lent and P. I. Cohen; Diffraction from stepped surfaces, II. Arbitrary terrace distributions; Surf. Science **161**, 39-68 (1985)
[3] S. Haviar, M. Dubau, I. Khalakhan, M. Vorokhta, I. Matolínová, V. Matolín, V. Valeš, J. Endres, V. Holý, M. Buljan and S. Bernstorff; X-ray small-angle scattering from sputtered CeO2/C bilayers; J. Appl. Phys., submitted (2012)

IN-SITU SAXS/WAXS STUDIES ON THE FORMATION OF COLLOIDAL NANOCRYSTAL SOLIDS

R.T. Lechner[1], M. Erko[1], M. Yarema[2], W. Heiss[2] and O. Paris[1]

1.) Institute of Physics, Montanuniversitaet Leoben, A-8700 Leoben, Austria
2.) Institute of Semiconductor and Solid State Physics, Johannes Kepler Universitaet Linz, A-4040 Linz, Austria.

Colloidal crystals using crystalline nanoparticles (NCs) as individual building blocks, recently named as nanocrystal solids, offer the opportunity for designing artificial crystalline solids with tailored electronic, magnetic, and optical properties [1].

In this work, we studied *in-situ* the template free self-assembled growth of nanocrystal solids (NC-solids) made of 17 nm sized Bi NCs with a quite spherical shape as derived from TEM measurements [2]. Recently, Bi NC-solids with typical sizes from 10 to 30 micron were grown using a slow destabilization approach by diffusion of a non-solvent into the colloidal dispersion [2]. The knowledge of the self-assembled growth mechanism of these 3D SLs is crucial for the controlled fabrication of novel tailored meso-devices.

We have first recorded SAXS spectra of NC ensembles solved in toluene with a concentration of 1-2 wt% to avoid particle-particle interactions. By analysing the recorded spectra (see Fig. 1(a)) we found a nearly monodisperse size distribution. This allowed applying a shape retrieval treatment, which is normally used for biological structures, based on the ATSAS software developed by D. Svergun. The error between the experimental (blue) and calculated curve (red) was minimized by adjusting iteratively the shape used for the calculation of the scattering curve. This resulted in a final averaged shape of a *truncated* sphere with a mean diameter of 16 nm.

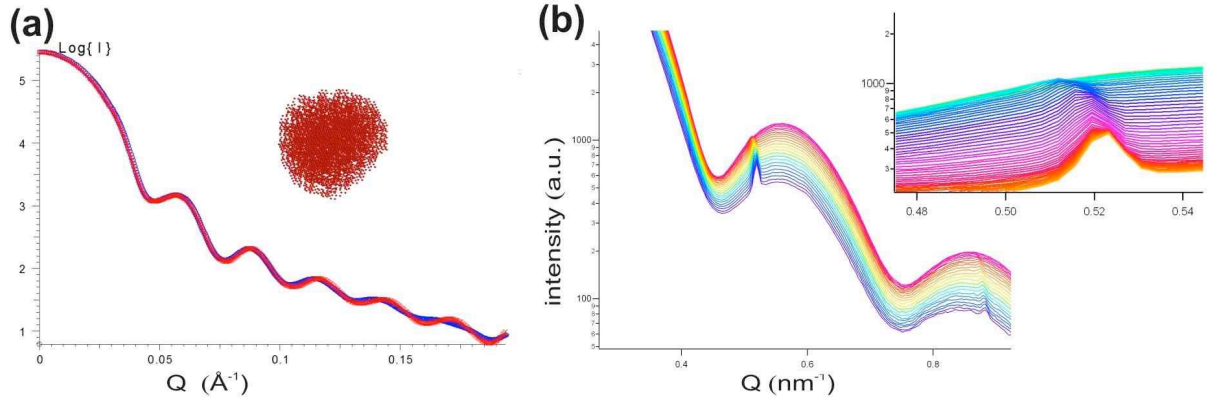

Figure 1. **(a)** SAXS intensity over scattering vector Q of Bi NCs in solution (blue) with a mean diameter of 16 nm. The nearly monodisperse size-distribution allows to retrieve the mean shape of the single Bi NCs by minimizing the error between the experimental (blue) and calculated curve (red) by adjusting iteratively the shape used for the calculation (inset); used the ATSAS-software by D. Svergun. **(b)** SAXS curves with a time resolution of 5 min (from red to blue) depicting the onset of the crystallisation of the colloidal crystals; inset: zoom on the first correlation peak.

We now realised within a 1.5 mm quartz-glass capillary a solvent/non-solvent interface by injecting carefully on top of the NC-toluene solution ethanol as a non-solvent. We recorded numerous SAXS spectra at different positions along the capillary, starting directly at the interface and moving down to the bottom of the capillary. Directly at the interface immediately, i.e. within our time resolution of ca. 5 min, correlation peaks were observed

indicating the onset of crystallisation. 2 mm below the interface, however, the SAXS-spectra still prove non-interacting nanoparticles. At this fixed position we started our time-resolved measurements with time steps of around 5 min.
Hence, we were able to record the onset of the colloidal crystallisation as a function of the diffusion time of ethanol within toluene [see Fig. 1(b)]. Following carefully the position of the first correlation peak we were able to observe peak shifts during the crystal formation indicating dynamic changes of the lattice properties [see inset of Fig. 1(b)]. After long enough diffusion time the SAXS pattern of non-interacting NCs vanished totally and only pronounced Bragg peaks remained related to the full formation of an artificial nanocrystal solid formed by the Bi NCs. The analysis of the Bragg peak positions to reveal the crystal structure is in progress. These experiments were also repeated for different concentration values of the NC-solutions to investigate their influence on the crystallization time.
Additionally, during all SAXS-scans WAXS spectra of the atomic Bragg peaks of orthorhombic Bi were recorded. From the analysis of these WAXS peaks we aim to derive the strain state of the Bi-NCs during the formation of the colloidal crystals.
The gained experimental results will improve the understanding of the nanocrystal solid formation process in solution without a surface-template. The fast appearance of the first correlation peaks, however, showed strongly the necessity of a better time resolution in the ms time regime in planned future experiments at the Austrian SAXS beamline. Furthermore, a precise control of the NC-concentration and of the amount of the non-solvent to form the interface is needed for a full understanding of the fast crystallization onset.

References:

[1] Talapin, D.V., MRS Bull. 37, 63-71 (2012)
[2] Yarema, M., Kovalenko, M.V., Hesser G., Talapin, D.V., Heiss W., JACS 132, 15158–15159 (2010)

NUCLEATION AND GROWTH OF CdS NANOPARTICLES OBSERVED BY ULTRAFAST SAXS

A. Magerl[1], T. Wlochowitz[1], S. Gerth[1], T. Unruh[1], A.A. Rempel[2], A. Schiener[1] and H. Amenitsch[3]

1.) Chair for Crystallography and Structural Physics, University of Erlangen-Nuremberg, Staudtstraße 3, D-91034 Erlangen, Germany
2.) Institute of Solid State Chemistry, Ural Branch of the Russian Academy of Sciences, 620990 Ekaterinburg, Russia
3.) Institute of Biophysics and Nanosystems Research, Austrian Academy of Sciences, A-8042 Graz, Austria

Introduction:

To date very little is known about the nucleation and growth process for rapid synthesis conditions as expected in case of II-VI quantum dots like cadmium sulfide (CdS) [1].We have performed ultrafast SAXS experiments at the small angle beamline to access early stages down to the 200 µs range using a T-mixer. The experiments were performed both in the laminar and in the turbulent flow regime, and it turns out that the flow conditions have a strong influence on the reaction rates in line with previous experiments [1, 2].

Experimental:

A stainless steel T-mixer (figure 1) was mounted on the SAXS beamline to perform in-situ measurements of the early nucleation states of CdS. The feed streams of aqueous solutions containing $CdCl_2$ and Na_2S with different concentrations (1.25 mM, 5 mM, and 12.5 mM) were driven by two gear pumps (Ismatec, MCP-Z Standard) to ensure stable flow velocities (3.1, 5.8, 10.6, and 15.4 m/s) at the outlet nozzle. To access different reaction times, five different positions from the mixing point (3.0, 4.5, 6.0, 7.5 and 9.0 mm) were used at the ejected free jet from the outlet nozzle. This setup accesses the particle formation for reaction times between 0.2 to 2.9 ms.

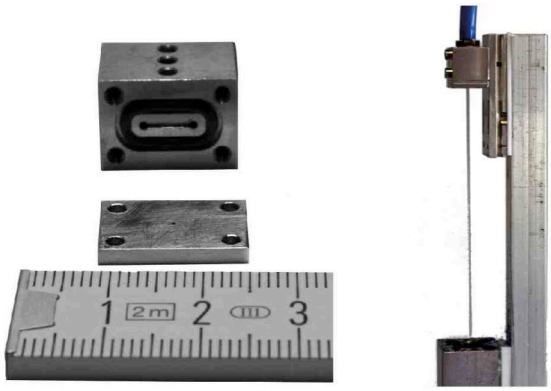

Figure 1. Dismounted T-mixer with a cm length scale. The thickness of the ground plate is 2 mm, and the nozzle diameter amounts to 0.5 mm (left). The ejected free jet of the mixed reactants (right).

Results:

The raw data was reduced into a radial intensity pattern as a function of the wave vector variable |Q| by using the software package Fit2D. The reduced small angle scattering profiles in figure 2 show that no particle formation occurs 3 mm from the mixing point for laminar flow at 3.1 m/s, whereas particle formation is well on its way under turbulent flow at 15.4 m/s (left). Figure 2 shows further reduced scattering profiles at a flow velocity of 15.4 m/s for different positions along the free jet (right). The increasing scattering signal at larger distances from the mixing point indicates particle formation and growth.

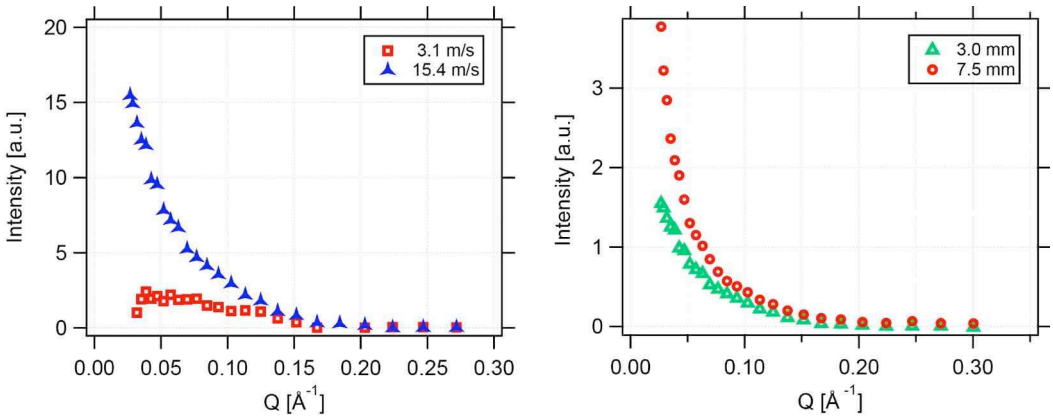

Figure 2. Reduced scattering profiles for a 5 mM CdS solution at a distance of 3 mm from the mixing point for 3.1 m/s and 15.4 m/s flow velocity (left). Reduced scattering profiles at a flow velocity of 15.4 m/s for different distances (3.0 and 7.5 mm) from the mixing point (right).

The increasing SAXS signal both with the turbulence of the flow and with reaction time provides evidence for particle formation in the sub millisecond time range under the condition of turbulent mixing. The data require fitting by a cylinder model, and the generated parameters are the specific scattering volume, the median of the cylinder radius, and the cylinder length. Figure 3 shows the time evolution of the geometrical parameters. While the length of the cylinder remains constant at a value of about 20 Å, the radius increases as a function of time. A faster radial growth rate is observed for higher flow velocities due to vortex formation as observed by Haberkorn [3] generating a large interface which favors CdS particle formation on short time scales.

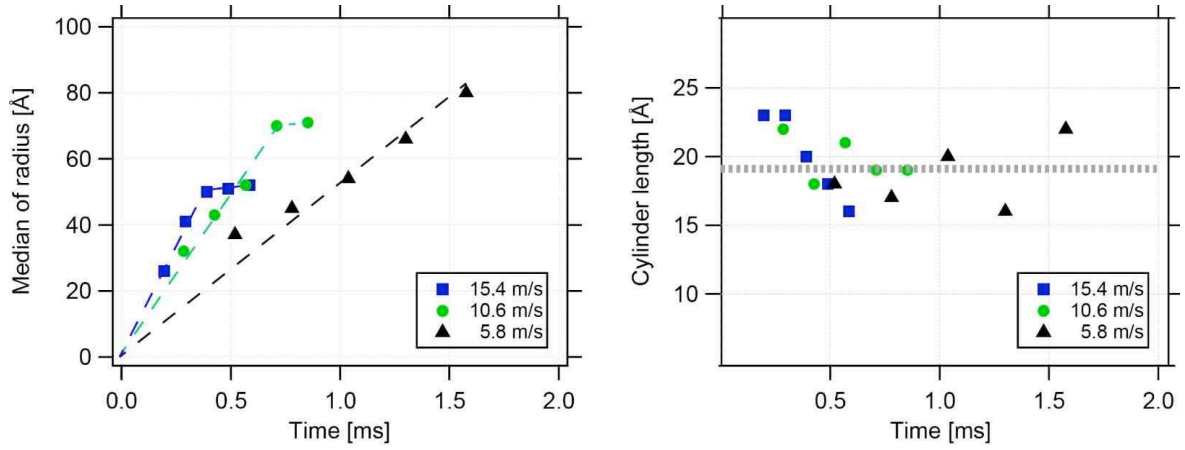

Figure 3.: Time dependence of the median of the cylinder radius (left) and of the cylinder length of a 5 mM CdS solution (right). The dashed lines are guide to the eye.

References:

[1] T. L. Sounart, P. A. Safier, J. A. Voigt, J. Hoyt, D. R. Tallant, C. M. Matzke and T. A. Michalske, Spatially-resolved analysis of nanoparticle nucleation growth in a microfluidic reactor, Lab Chip **7**, 908-915 (2007)

[2] W. Schmidt, P. Bussian, M. LindeĬn, H. Amenitsch, P. Agren, M. Tiemann and F. Schueth, Accessing Ultrashort Reaction Times in Particle Formation with SAXS Experiments: ZnS Precipitation on the Microsecond Time Scale, J. Am. Chem. Soc. **132**, 6822–6826 (2010)

[3] H. Haberkorn, D. Franke, T. Frechen, W. Goesele and J. Rieger, Early stages of particle formation in precipitation reactions – quinacridone and boehemite as generic examples, J. Colloid and Interf. Science **259**, 112–126 (2003)

DEFINING CRYSTAL MORPHOLOGY USING SELF-ASSEMBLING ADDITIVES

G.R Mitchell[1], D. Duraccio[2], M. Pezutto[2] and S. Bernstorff[3]

1.) University of Reading, Polymer Science Centre, Whiteknights, Reading RG6 6AF UK
2.) CNR di Pozzuoli - Istituto di Chimica e Tecnologia dei Polimeri (ICTP)
3.) Sincrotrone Trieste, AREA Science Park, 34149 Basovizza/Trieste, Italy

The properties of semi-crystalline polymers such as polyethylene, polyethylene oxide polypropylene or poly(ε-caprolactone) depend as much on the morphology which develops during processing as they do on the chemical configuration of the polymer. We have set out to explore in this work the impact of two types of mineral based nanoparticles, specifically montomorillonite clay platelets and halloysite nanotubes. Small quantities of these particles were dispersed in polyethylene oxide using a twin screw extruder. The different geometries of the two particulate systems are expected to exhibit different behavior in the applied sheared flow field. On cooling, polymer crystallisation is directed by these particles and by chains extended by the shear flow.

We mounted our special shear stage [1] on the SAXS beam line. This allows us to closely define the flow and temperature environment of the polymer. For both SAXS and WAXS, the incident x-ray beam was normal to the plane of the sample. As a consequence, for the SAXS measurements the scattering vector probing the structure lies more or less in the plane of the sample, while for the WAXS, the scattering vector is tilted out of this plane by an angle, (θ), corresponding to the particular scattering angle, (2θ), of interest. In this work, the maximum scattering angle was ~20° and hence the largest value of θ or the tilt was ~10°. The WAXS detector is set to measure the scattering along the equatorial axis, i.e. normal to the flow field. This is a particular benefit of the flexibility of the Elettra beam line. On most SAXS/WAXS beam-lines, the WAXS detector is fixed on the meridional axis i.e. parallel to the shear flow and is from a practical point of view immoveable. Whereas, at Elettra, the WAXS detector can be placed freely. In the current experiments, the accessible WAXS peaks are of the form (hk0) and therefore most intense on the equator for a high level of preferred orientation [2,3]. The shear cell was based on a parallel plate geometry, the shear rate varied across the radius. The radius of the rotating plate in the shear system was 9.5 mm, which coupled to the position of the incident beam meant that the recorded scattering pattern averaged over a range of shear rates ~4%. The curved nature of the flow field, essentially tangential to the rotating plate, means that the scattering is also averaged over a range of slightly different orientations between the flow direction and the scattering vector; this variation was limited to ±1º.

This arrangement allowed us to obtain quantitative time-resolved SAXS data with a time-cycle of 10s as well as 1d-WAXS data over a complete cycle of melting, shearing and crystallization. We were able to follow the crystallisation processes from the very earliest stages which enabled us to identify the orientation of the dominant structures which grew first.

We use time-resolved small-angle x-ray scattering (SAXS) to quantitatively follow the orientation of the nanoparticles and the subsequent directed crystallisation. The simultaneous WAXS capability available on the SAXS beamline at Elettra allows us, after data analysis, to follow the development of crystallinity in the polymer matrix. The 2D nature of the SAXS data collection allows us, after data analysis, to evaluate the length scales and the level of orientation present before, during and after shear flow.

Crystallisation from a sheared PEO melt can lead to a high level of preferred orientation of the crystal lamellae as shown in Figure 1. Whether this happens depends on the time between the shear flow and the point of crystallization. If the delay in terms of time is sufficient the memory of the shear is lost through chain relaxation. An isotropic SAXS pattern results. For PEO without nanoparticles the level of preferred orientation obtained from the SAXS patterns reaches a maximum for a shear temperature of 65°C. Addition of clay platelets (2%) had no effect on the variation of preferred orientation with shear temperature indicating that the addition of the platelets neither increased the extent of chain extension or any platelet nucleation. In contrast the addition of 2% of Halloysite nanotubes leads to a significant reduction in the shear temperature for maximum preferred orientation to 60°C [2,4].

We also used a small amount of beam time to complete a systematic study of the crystallization behavior of isotactic polypropylene nanocomposites containing montomorrilonite which was initiated in earlier Elettra experiments [5].

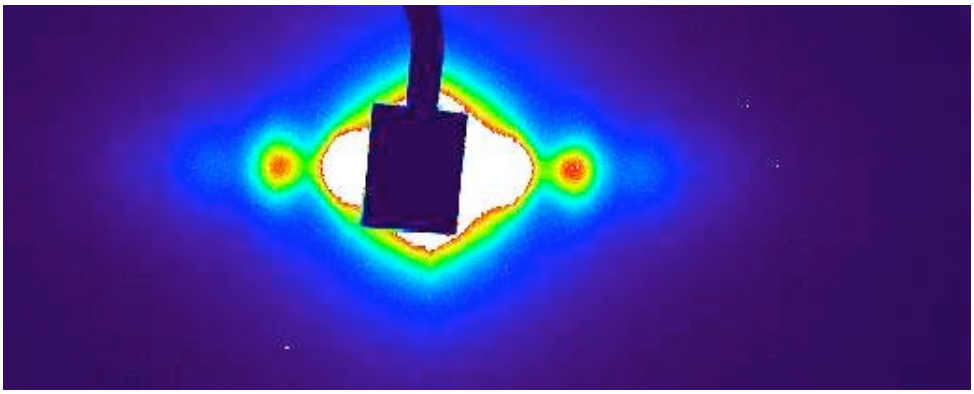

Figure 1. SAXS pattern of a sample of polyethylene oxide crystallised from a sheared melt (10s-1, 1000 shear units Ts=65°C). The flow direction was horizontal.

References:

[1] Nogales A., Thornley S.A., Mitchell G.R., J. Macrom. Sci: Phys. B43 1161-1170 (2004)

[2] G.R.Mitchell "*Nanoenhancers for Plastics*" Pan Stanford 2014 ISBN 978-981-4411-52-3

[3] G.R.Mitchell Characterisation of safe nanostructured polymers in *Ecosustainable Polymer nanomaterials for food packaging;* Edited by Clara Silvestre and Sossio Cimmino Taylor and Francis January 2013 ISBN 978-90-0420-737-0

[4] G.R.Mitchell, D.Duraccio, M.Pezutto and Sigrid . The crystallisation behaviour of polyethylene oxide containing mineral based nano particles to be submitted to Polymer

[5] M.Pezutto, D.Donatella, C.Silvestre and G.R.Mitchell Crystallisation of nanocomposites of isotactic polypropylene and montomorilonite from a sheared melt. In preparation to be submitted to J Mat Sci

Thermal stability of dislocations in semicrystalline polymers

G. Polt[1], F. Spieckermann[1], H. Wilhelm[1,2], E. Schafler[1], S. Bernstorff[3] and M. Zehetbauer[1]

1.) Research Group Physics of Nanostructured Materials, Faculty of Physics, University of Vienna, Boltzmanngasse 5, Wien, Austria
2.) Laboratory of Polymer Engineering LKT-TGM, Wexstrasse 19-23, 1200 Wien, Austria
3.) Sincrotrone Trieste, Strada Statale 14 km 163.5 in AREA Science Park, 34149 Basovizza, Trieste, Italy

Experiments on PET, gamma and alpha phase iPP and PE were performed. In order to study the thermal stability of defects, the samples have been cold rolled to different degrees of deformation up to strains of 0.80 which ensures that a high density of defects is introduced in the material [1-4]. To avoid relaxation, the pre-deformed samples were subsequently stored in liquid nitrogen. A temperature stage of the Type LEYKAM TMS 90 was applicable allowing to span the relevant temperature range between -180 °C to 400 °C during the measurement. A special procedure which has already been successfully applied in proposal 20085194 was used to mount the cold samples on the already cold temperature stage in order to provide an unchanged sample state. The measurements have been performed using an in-situ temperature WAXS setup including a newly installed DECTRIS Pilatus 100K hybrid pixel detector allowing for 2 dimensional data acquisition with extraordinary low noise.

The X-ray line profiles of the measured samples especially of Polyethylene terephthalate (PET) could not be evaluated by means of the Multiple Whole Profile Analysis (MWPA) since the corresponding program does not support triclinic lattice structures. Instead, the evaluation was carried out by the modified Williamson and Hall (WH) analysis [5,6], as well providing information about the density of comprised defects such as dislocations on the one hand and about the size of coherently scattering domains (CSD-size) on the other hand. The latter can be related to the lamellae thickness in polymers. In order to speed up the evaluation a computer program was designed which fits the diffraction patterns by mathematical functions and subsequently uses the broadening of the peaks for the modified-WH analysis.

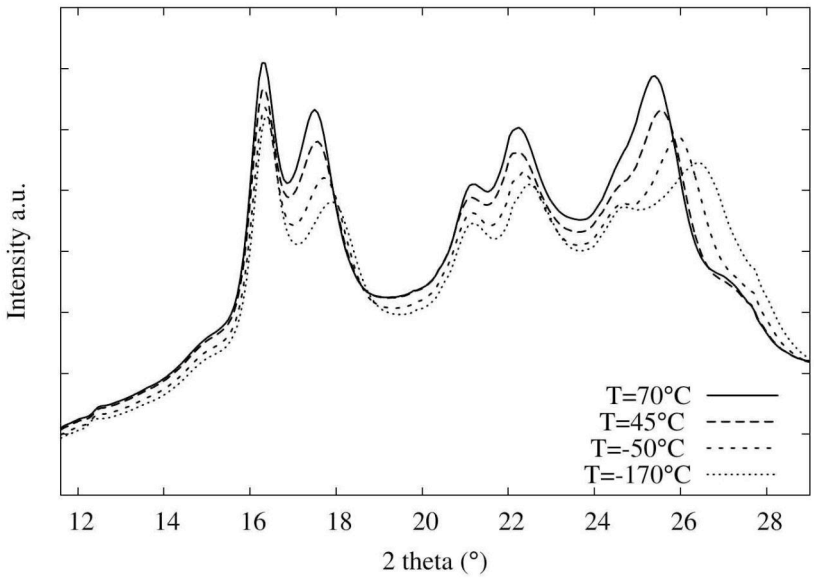

Figure 1. X-ray line profiles of PET at different annealing temperatures. The sample was pre-deformed by cold rolling to a true strain of ε =0.45 and then subsequently stored in liquid nitrogen to prohibit relaxation.

Figure 1 shows the X-ray line profiles of pre-deformed Polyethylene terephthalate (PET) at different annealing temperatures. A significant peak shift to lower two theta angles can be observed during annealing caused by changes in the lattice constants induced by stress relaxations within the crystalline phase. Moreover, a slight reduction in peak broadening can be seen. By applying the modified-WH method it was found that the initial dislocation density of about 2.5x10^16 (1/m²) decreases with increasing temperature by a magnitude of 10 while the CSD-size stays almost constant (figure 2). This behavior can be interpreted as an annealing of the dislocations within the crystalline regions or their evacuation into the adjacent amorphous phase. Above the glass transition temperature of 0 °C the dislocation density stays at a constant level. A possible explanation is that the backstresses of the amorphous phase have relaxed and are therefore no longer stabilizing the defects within the crystalline phase. For a more detailed investigation on this behavior unloading experiments at low temperatures will be necessary.

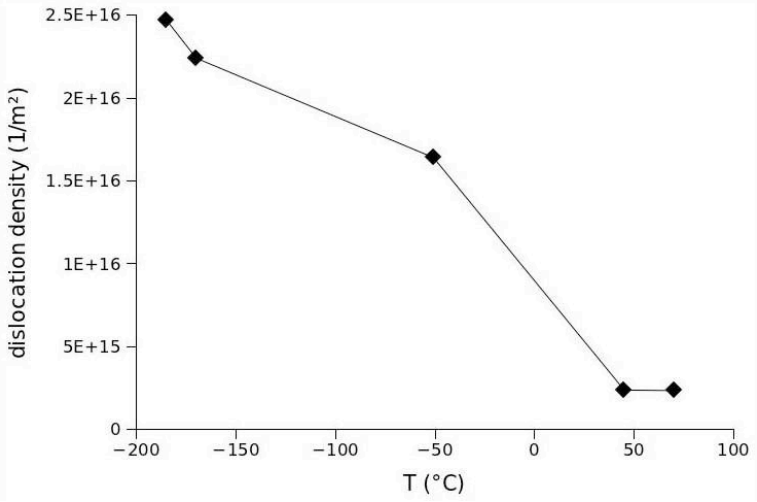

Figure 2. Evaluation of the diffraction patterns from figure 1 by the modified WH analysis. The decrease in the dislocation density at increasing annealing temperature points at an annihilation of dislocations or their evacuation into the amorphous phase.

References:

[1] Spieckermann, F.; Polt, G.; H.Wilhelm; Kerber, M.; Schafler, E. & Zehetbauer, M., 'The role of dislocations for the plastic deformation of semicrystalline polymers as investigated by multi-reflection X-ray line profile analysis', Journal of Applied Polymer Science 125 (6), pp. 4150-4154 (2012)

[2] Spieckermann, F.; Wilhelm, H.; Kerber, M.; Schafler, E.; Polt, G.; Bernstorff, S.; Addiego, F. & Zehetbauer, M., 'Determination of lamella thickness distributions in isotactic polypropylene by X-ray line profile analysis', Polymer 51(18), 4195-4199 (2010)

[3] Spieckermann, F.; Wilhelm, H.; Schafler, E.; Kerber, M.; Bernstorff, S. & Zehetbauer, M., 'Plasticity and X-ray Line Profile Analysis of the semicrystalline polymer poly(3-hydroxybutyrate)', Journal of Physics: Conference Series 240(1), 012146 (2010)

[4] Wilhelm, H.; Paris, A.; Schafler, E.; Bernstorff, S.; Bonarski, J.; Ungar, T. & Zehetbauer, M., 'Evidence of dislocations in melt-crystallised and plastically deformed polypropylene', Materials Science and Engineering A 387-389, 1018-1022 (2004)

[5] Ungar, T. & Borbely, A., 'The effect of dislocation contrast on x-ray line broadening: A new approach to line profile analysis', Appl. Phys. Lett., AIP, 69, 3173-3175 (1996)

[6] Kerber, M.; Zehetbauer, M.; Schafler, E.; Spieckermann, F.; Bernstorff, S. & Ungar, T., 'X-ray line profile analysis: An ideal tool to quantify structural parameters of nanomaterials', JOM Journal of the Minerals, Metals and Materials Society 63, 61-70 (2011)

STRUCTURAL STUDY OF Ni-Nb THIN FILMS

N. Radić[1], P. Dubček[1], S. Bernstorff[2], Ž. Skoko[3], M. Ristić[1], Z. Siketić[1]

1.) Boskovic Institute, Bijenicka 54, 10000 Zagreb, Croatia
2.) Sincrotrone Trieste, Strada Statale 14, km163.5, 34149 Basovizza, Italy
3.) Faculty of Sciences, Physics Department, Bijenicka 32, 10000 Zagreb, Croatia

Ni-Nb thin films (500 nm) have been prepared in a full range of compositions (from pure Ni to pure Nb) by magnetron co-deposition onto various substrates (mono-Si, sapphire, alumina, fused silica, and glass). The chemical compositions of the alloys have been determined by nuclear microanalysis methods (time-of-flight elastic recoil detection analysis (TOF-ERDA)), while the structure of the as-deposited films has been determined by X-Ray Diffraction. It has been found that the glass-forming range (25-85 at.% Ni) conforms very well with the glass forming ability estimated from molecular dynamics simulations and Miedema's theory. Below 10 at.% Nb content, the prepared films are bcc crystalline Ni(Nb) solid solutions. The Ni(Nb) (nano)crystallites (20-30 nm) are preferentially (111) oriented in the direction perpendicular to the film plane.

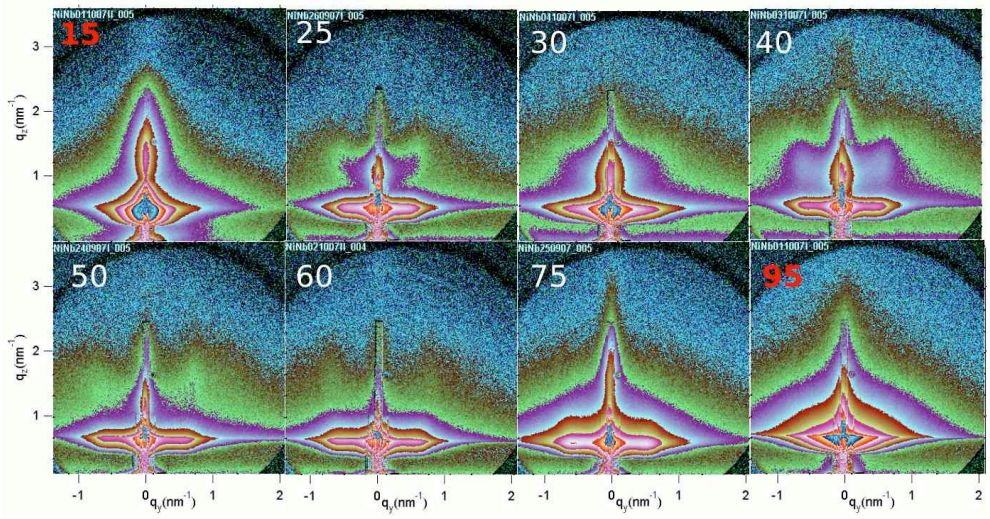

Figure 1. X-ray scattering pattern of NiNb films. The numbers denote the nickel concentration, and those in white are in the glass forming range.

Grazing incidence small angle x-ray scattering (GISAXS) results indicate that the surface contributions dominate in the GISAXS patterns from the nickel rich samples, where the scattering is relatively diffuse due to the irregular surface. Augmenting the Nb content of the samples, the sample surfaces become smoother, and the GISAXS pattern become better defined. In the glass-forming range, the surface structure becomes island-like, with a narrow size distribution both vertically and horizontally. When scattering pattern taken at wider angles are compared to those taken at the critical angle, the bulk contribution scattering can also be deduced. The sizes of the bulk features are fairly similar for most concentrations. However, the values that stand out are in the glass-forming range, as well as with 90%Ni content, where the bulk features appear to be 50% bigger. Also, in the whole glass forming range, surface scattering contains a contribution from correlated particles. These are consistently about 10nm in size, and distanced by about 20nm. The existance of vertical fringes means that their height distribution is quite narrow, and the relatively sharp lateral correlation maximum indicates that the interparticle distance distribution is also narrow. Compared to the size of the crystallites as obtained from diffraction, and keeping in mind that they are preferentially oriented perpendicularly to the surface, we could assign these surface particles to partly protruding crystallites.

GISAXS study of formation of nanoripples on Si (100) substrate by surfactant assisted ion-beam sputtering

K.V. Sarathlal[1], A. Gupta[1], S. Bernstorff [2]

1.) UGC-DAE Consortium for Scientific Research, University Campus, Khandwa Road, Indore, India 452001
2.) Sincrotrone Trieste, SS 14 km 163.5, 34149 Basovizza (TS), Italy

Pattern formation on Si surface induced by noble gas ion beam sputtering has been extensively studied. The most widely accepted theory for nanopattern formation has been the so called linear model of Bradley and Harper [1] which has been subsequently extended to incorporate nonlinear terms [2]. As per these theories nanopattern formation is a result of a competition between curvature dependent sputtering and surface diffusion. However, more recently it has been suggested that for nanopattern formation, the presence of metal impurities is essential [3]. Hofsäss et al., did a detailed study of surfactant driven nanopattern formation on Si substrate in which Si substrate was eroded with energetic Xe ions in the presence of a constant flux of Fe atoms which act as surfactant [4]. They proposed that curvature dependent sputtering does not play any role in nanopattern formation. As per their model, initially a thin metal silicide film is formed at the Si surface. As a result of further ion irradiation, phase separation takes place at the surface resulting in metal rich and metal depleted silicide. Subsequently, different sputtering rates of Fe rich and Fe depleted regions result in pattern formation at the surface. On the other hand, Bradley has further extended his theory to explain the impurity assisted nanopattern formation [5]. According to this theory nanopattern formation and phase separation should proceed simultaneously.

The objective of the present study is to see if the phase separation precedes the ripple formation or both the processes occur simultaneously, as this aspect is crucial in order to differentiate among different models. A number of samples of Si (100) were irradiated with different fluences of 1keV Ar ions in the presence of a constant flux of Fe ions, using a geometry shown schematically in figure 1(a). Samples were characterized by AFM measurements, in order to see the development of surface topography with ion fluence. Because of the scattering contrast between metal rich and metal depleted regions, GISAXS can provide information also about possible phase separation. Thus, while AFM will see only the development of surface topography, in GISAXS contrast will be due to both phase separation as well as surface topography. Thus, a comparison of the results of AFM and GISAXS as a function of ion fluence can provide valuable information about the phase separation and topographical changes.

Figures 1(b) and 1(c) give the typical AFM and 2D GISAXS pictures of irradiated Si (100) surface. Figure 2(a) gives the 1D power spectral density as obtained from AFM measurements. The peaks in the power spectral density due to the periodicity of the ripples are clearly seen. This is analogous to the SAXS profile, which also shows peaks corresponding to the periodicity of the ripples (Figure 2(b)). In both the cases, a peak occurs around q~0.13 nm which corresponds to the periodicity of the ripples. In the case of AFM the height of the peak is proportional to the amplitude of the ripples, while in case of SAXS the peak intensity is determined by the amplitude of the ripples as well as the electron density contrast due to the phase separation. In case a phase separation precedes the ripple formation, then in SAXS the intensity of the peak should increase at a faster rate for low fluences. Figure 2(c) gives the variation in the intensity of the first peak in the cases of both AFM and SAXS. Heights of the peaks are normalized at a fluence of 7.2×10^{17} ions cm^{-2}, at which the ripple pattern is fully developed. One can see that both AFM and SAXS results follow qualitatively the same curve. This shows that the phase separation does not precede the ripple formation,

rather it develops simultaneously with the ripples. This observation contradicts the model proposed by Hofsäss et al [4] and is in agreement with the theory of Bradley et al [5].

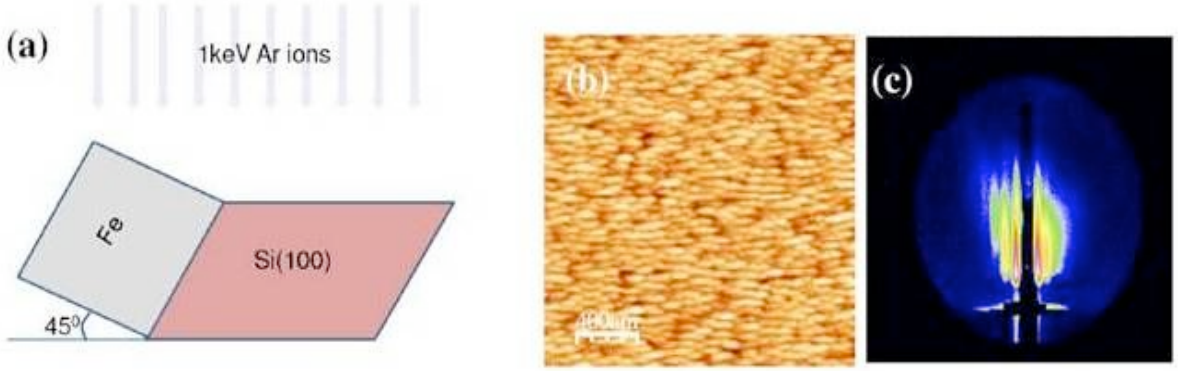

Figure 1. (a) Schematic of the geometry used for ion beam erosion, (b) and (c) show respectively the AFM and GISAXS images of Si (100) substrate irradiated at an Ar ion fluence of $7.2X10^{17}$ ions cm^{-2}

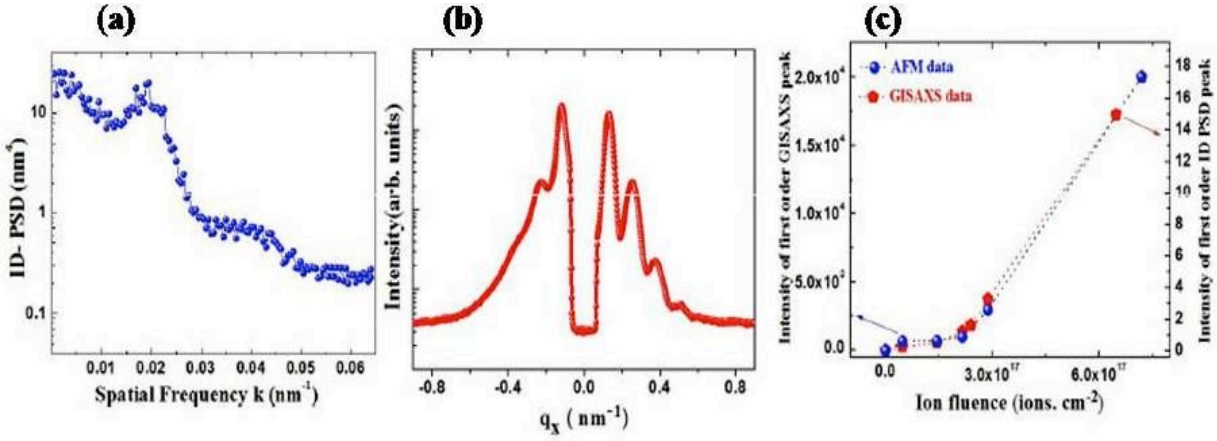

Figure 2. (a) 1D power spectral density plot as obtained from AFM image, (b) the GISAXS plot at a fixed q_z of the image shown in figure 1, and (c) the variation in the intensity of the first peak in the cases of both PSD of AFM and GISAXS. Heights of the peaks are normalized at a fluence of 7.2×10^{17} ions cm^{-2}

References:

[1] Bradley R M and Harper J M, J. Vac. Sci. Technol. A 6 (1988) 2390
[2] Park S, Kahng B, Jeong H and BarabásiA L, Phys. Rev. Lett. 83 (1999) 3486; MunosGarcía J, Gago R, Vazquez L, Angel, SánchezGarcía J and Cuerno R, Phys. Rev. Lett.104 (2010) 026101
[3] Sven Macko et al, Nanotechnology 21 (2010) 085301
[4] Kun Zhang, Marc Brötzmann and Hans Hofsäss, New J. Phys. 13 (2011) 013033
[5] P. D. Shipman, R. M. Bradley, Phys. Rev. B 84, 085420 (2011); R. M. Bradley, P. D. Shipman, Appl. Surf. Sci. 2011

IN SITU SAXS/DSC/WAXD STUDY OF POLYMER ELECTROLYTE FOR Zn RECHARGEABLE NANOSTRUCTURED GALVANIC CELLS

A. Turković[1], P. Dubček[1], K. Juraić[1] and S. Bernstorff[2]

1.) R. Bošković Institute, P.O. Box 180, Zagreb, Croatia
2.) Sincrotrone Trieste, SS 14, km 163.5, Basovizza (TS), Italy

Polymer electrolytes as nanostructured materials are very attractive components for batteries and opto-electronic devices. Environment friendly galvanic cells as well as solar cells of the second generation are to be constructed with nanocomposite polymer as electrolyte. In our study, $(PEO)_8ZnCl_2$ polymer electrolytes were prepared from PEO and $ZnCl_2$. The nanocomposites $(PEO)_8ZnCl_2$ themselves contained TiO_2, Al_2O_3, MgO, ZnO and V_2O_5 nanograins. In this work, the influence of the Al_2O_3, MgO and V_2O_5 nanograins to the morphology and ionic conductivity of the nanocomposite was systematically studied by transmission small-angle X-ray scattering (SAXS) simultaneously recorded with wide-angle X-ray diffraction (WAXD) and differential scanning calorimetry (DSC). The SAXS/DSC/WAXD measurements yielded insight into the temperature-dependent changes of the grains of the electrolyte. The heating and following cooling rate was 1 °C/min.
Figure 1 shows the SAXS, WAXS and DSC results obtained from polymer electrolyte nanocomposite with three nanofillers. The evolution of the average radii of the grain sizes obtained from the Guinier approximation is compared to the corresponding DSC and WAXD spectra behavior.
In the heating cycle the superionic phase transition can be seen as the sudden drop of the nanograin sizes at the phase transition temperature. In the cooling part a hysteresis can be seen as the phase transition occurs at lower temperature. The endothermic and exothermic peaks found in DSC during the same temperature cycle follow the sudden changes in the average nanograin sizes as obtained from the SAXS measurements and the intensity drops in the WAXD spectra. There are two trends in SAXS in the heating cycle: first an increasing of the grain size up to 64.1°C and then a sudden drop at this phase transition temperature.

Table 1. Changes of the average grain radius <R>/nm by SAXS; and phase transition temperatures t (in °C) in $(PEO)_8ZnCl_2$ polyelectrolyte with different nanofillers (x) during heating and cooling (with 1°C/min) as determined by SAXS/WAXS/DSC measurements.

$(PEO)_8ZnCl_2$ + x	heating				cooling			
	SAXS		WAXS	DSC	SAXS		WAXS	DSC
x/nm	t (°C)	<R> (nm)	t (°C)	t (°C)	t (°C)	<R>(nm)	t (°C)	t (°C)
Al_2O_3 /5.1	64.1	5.1-4.7	65.3	66.9	41.2	4.6	44.5	52.0
MgO /13.3	62.2	11.0-10.2	66.4	67.2	45.3	4.8	47.2	53.1
V_2O_5 /9.1	42.5	10.5-8.3	63.5	66.8	40.7	5.2	45.5	50.2;47.6

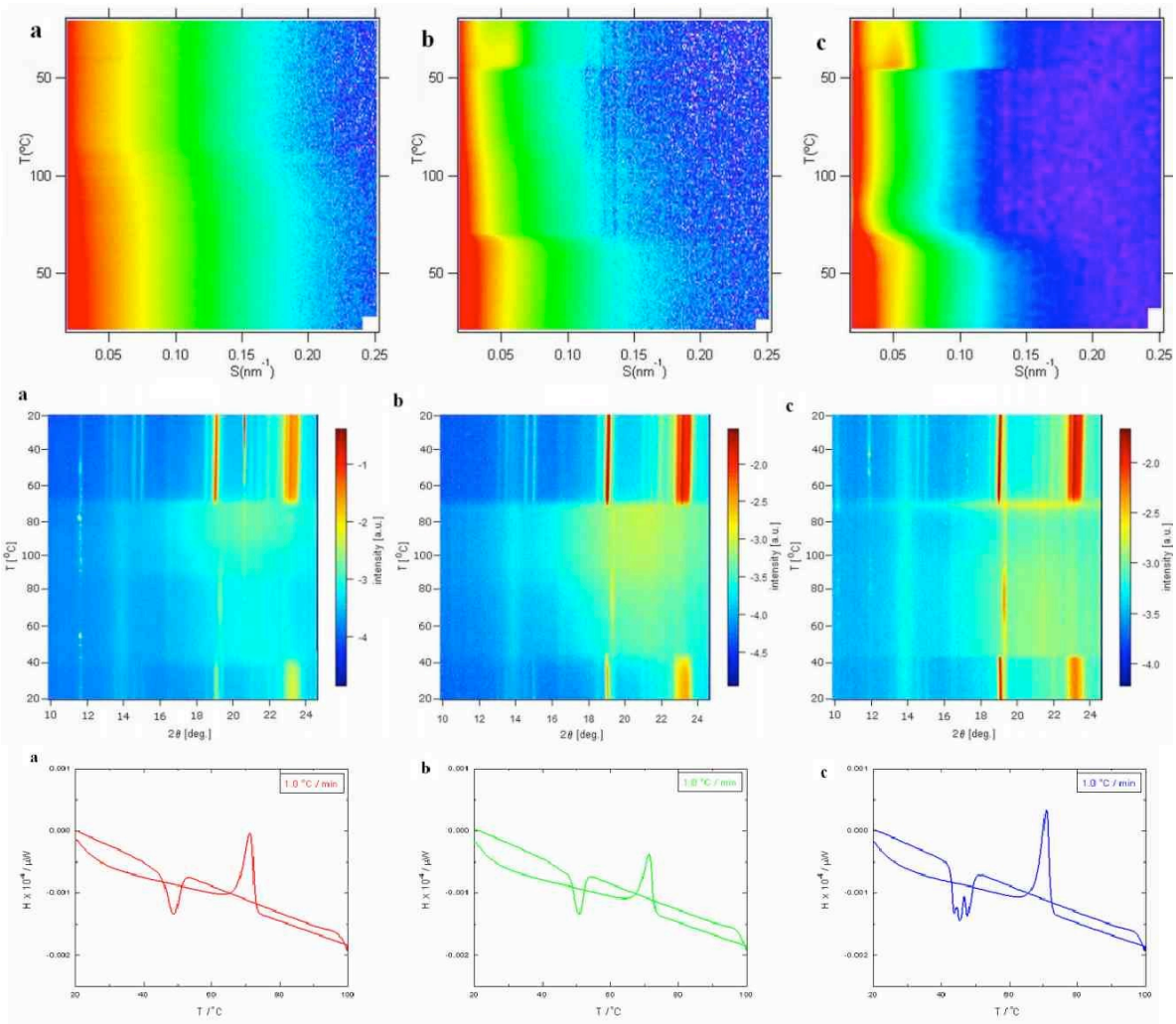

Figure 1. SAXS (top), WAXS (middle) and DSC (bottom row) results for nanocomposite polyelectrolyte (PEO)8ZnCl2 in the temperature range from 20°C to 100°C measured at the rate of 1°C/min, for a) $(PEO)_8ZnCl_2$ /Al_2O_3; b) $(PEO)_8ZnCl_2$ /MgO and c) $(PEO)_8ZnCl_2$ /V_2O_5.

The DSC spectrum shows that the phase transition temperature is 66.9°C for $(PEO)_8ZnCl_2$ / Al_2O_3, which is determined at the beginning of the peak in the heating cycle. This temperature is the melting temperature of the PEO crystallites i.e. "spherulites"[1]. Both, the SAXS and DSC data show a hysteresis, i.e. much lower phase transition temperatures than 65°C in the cooling cycle. In the case of the nanocomposite polymer electrolyte, combined forms of PEO and $ZnCl_2$, and additionally $ZnCl_2$ combined to the three different nanofillers (Al_2O_3, MgO and V_2O_5) influence the melting temperature.

Reference:

[1] I.Pucić and A.Turković, Solid State Ionics **176 (**2005) 1797

STRUCTURAL CHARACTERIZATION OF STACKED SiGe NANOCRYSTALS CONFINED IN A THIN SiGe/SiO_2 SUPERLATTICE

E. M. F. Vieira[1], S. Levichev[1], J. Martín-Sánchez[1], A. Parisini[2], M. Buljan[3], O. Conde[4], A. G. Rolo[1], A. Chahboun[1, 5], S. Bernstorff[6] and M. J. M. Gomes[1]

1.) Centro de Física, Universidade do Minho, 4710-057 Braga, Portugal
2.) CNR-IMM Sezione di Bologna, via P. Gobetti 101, 40129 Bologna, Italy
3.) Ruđjer Bošković Institute, Bijenička cesta 54, 10000 Zagreb, Croatia
4.) University of Lisbon, Physics Department and ICEMS, 1749-016 Lisboa, Portugal
5.) FST Tanger, Physics Department, BP 416, Tanger, Morocco
6.) Sincrotrone Trieste, 34149 Basovizza, Italy

Si, Ge and SiGe NCs have received great attention because of their non-toxicity, abundance in the earth resources and low cost maintaining the key advantages of state-of-the-art silicon processing which makes them suitable for applications in electronics, optoelectronics and solar cells [1-2]. For an optimal performance, it would be highly desirable to develop a fabrication process that allows one to obtain a high density of NCs with high size uniformity in a very thin and well defined two-dimensional layer embedded in a dielectric material matrix where the distance between the NCs and the substrate can be maintained constant in large areas. Usually, in order to obtain self-assembled SiGe NCs embedded in an oxide matrix, a high temperature annealing process follows the co-deposition of a SiGe-rich matrix oxide layer. However, the high temperature treatments can lead to undesired Ge diffusion or evaporation throughout the barrier matrix material with the consequent loss of abrupt and well defined interfaces [3]. Here we show an overall multilayer stability with well-organized SiGe NCs in 5nm-thick layers after performing rapid thermal annealing (RTA) at 800 ºC for 30 min. Local modifications in the multilayer (ML) composition with the formation of defective regions in the upper layers are observed. Only the first layers over the Si substrate are unaffected by this problem.

GIXRD and Raman patterns of as-grown and annealed films are in excellent agreement with the conclusion that the crystalline features start to appear at a temperature of 700 °C where well defined nanocrystalline $Si_{0.7}Ge_{0.3}$ particles (~4.6 nm size) are observed at T_{ann} = 800 ºC.

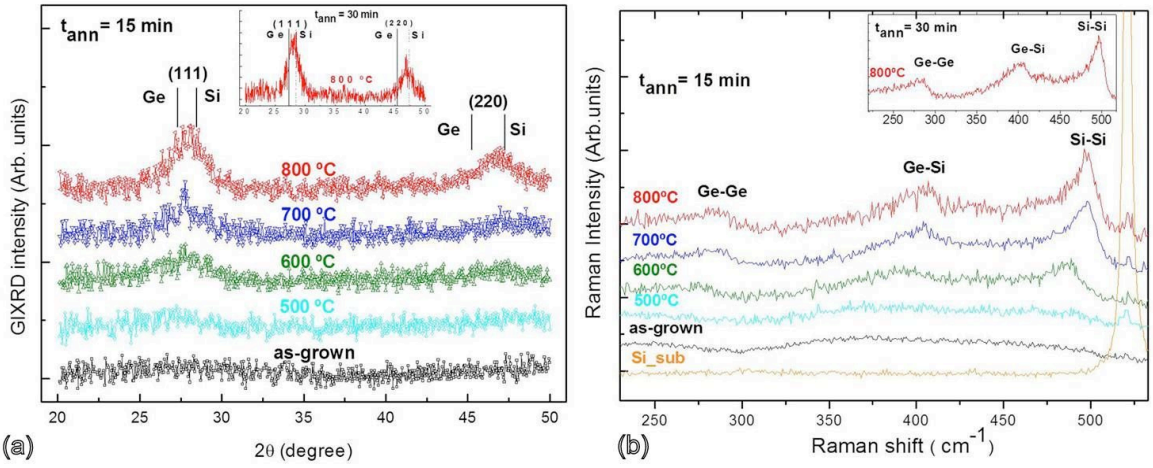

Figure 1. (a) GIXRD patterns of as-grown and annealed samples from 500 ºC to 800 ºC for 15 min. The vertical dashed lines show the position of Si and Ge diffraction peaks. (b) Corresponding Raman spectra: Ge-Ge, Ge-Si, and Si-Si optical vibration modes are shown. Insets: same for 30 min annealing time at 800 ºC [4].

GISAXS maps of the as-grown and annealed at 800ºC for 30 min films (Fig 2a,b) show very similar intensity distributions. The 1D profiles extracted along the yellow dashed lines were fitted using standard formulas for correlated roughness calculated in the distorted-wave Born approximation (DWBA) [5]. After annealing, a slight decrease of the interface roughness and a small increase in the lateral correlation length are found. The vertical correlation length and film thicknesses were approximately constant during the annealing.

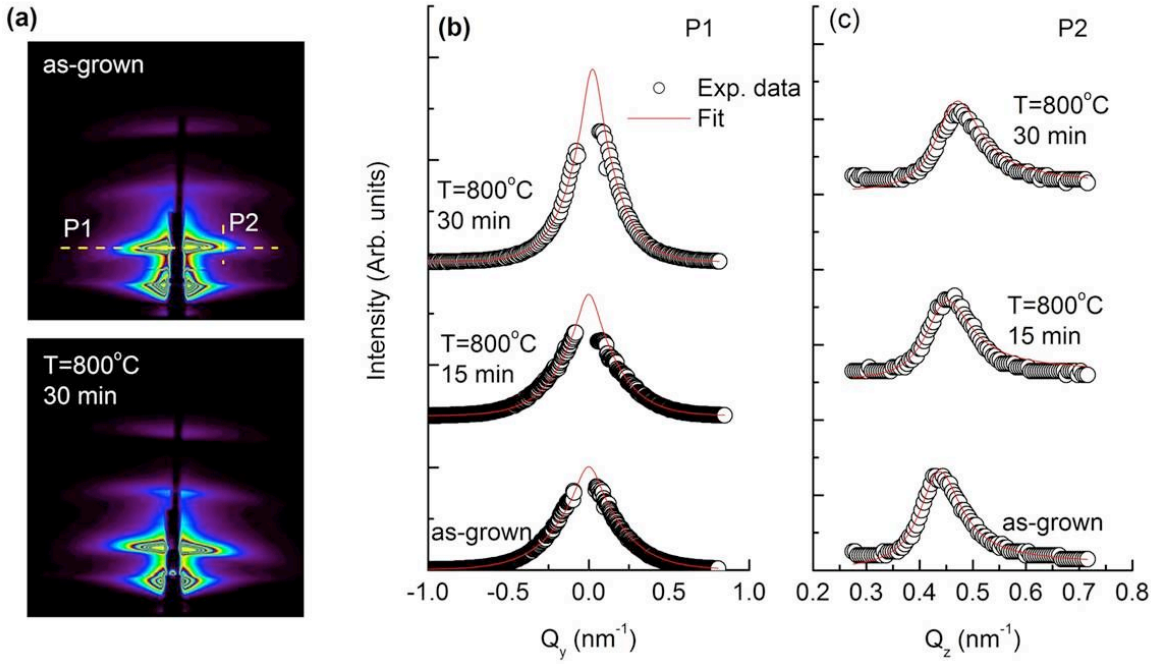

Figure 2. (a) GISAXS maps of the as-grown film and the film annealed at 800 ºC for 30 min. (b) 1D profiles were extracted along the yellow dashed lines for the fitting procedure. The extracted 1D profiles (black circles) and the corresponding fits (red lines) for the as-grown and annealed films. (c) The grazing incidence angles were 0.28º, 0.26º, and 0.24º for as-grown, 15min, and 30min annealed films, respectively [4].

Cross-sectional ADF-STEM images of the whole ML SiGe/SiO_2 structure before and after annealing (Fig. 3a,b) show the preservation of the ML structure, where no significant change in the ML periodicity is observed. Flatter interfaces were found for the first layers, whereas due to cumulative effects of interface roughness and its correlation along the ML, the top layers have rougher interfaces. This phenomenon is more evident after the annealing treatment. ADF-STEM (Fig. 3e) and EDS X-Ray (in the inset) investigation of the upper layers of the annealed ML structure show local compositional variations with the same cumulative trend followed by the layer roughness. On the high resolution transmission electron microscopy (HRTEM) image (Fig. 3f) of the region close to the Si substrate SiGe NCs with sizes from 3 to 5nm are clearly observed in thin SiO_2 layers. In the inset, a SAED diffraction pattern, obtained on a larger area, demonstrates the crystallinity of the SiGe NCs array. A good quality of the Si substrate / SiO_2 interface is observed with no clearly visible defects.

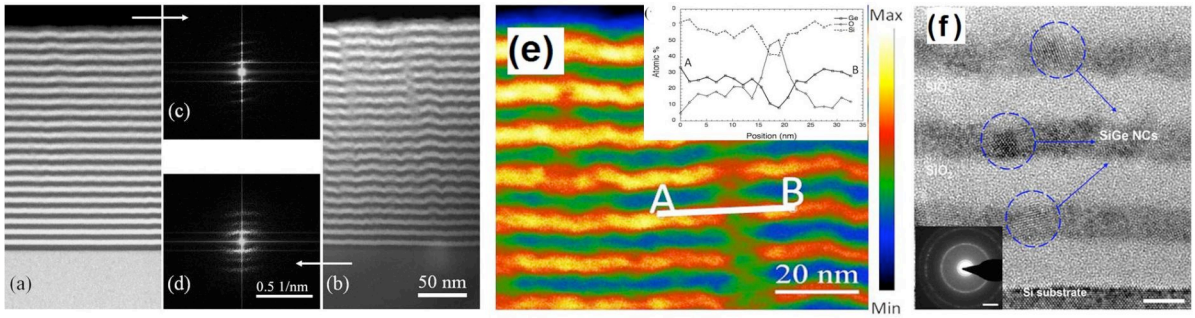

Figure 3. Cross-sectional ADF-STEM images of the whole ML SiGe/SiO2 structure before (a) and after (b) a 800 ºC thermal annealing for 30 min. In (c) and (d) the corresponding diffractograms. (e) ADF-STEM image of the top portion of the ML, EDS X-ray profiles taken along the line AB are shown in the inset; (f) Cross-sectional HRTEM micrographs of a SiGe/SiO2 ML sample annealed at 800 ºC for 30 min of the region close to the Si substrate. 5 nm-thick SiGe layers with nanocrystals (region circled with blue dotted lines) separated by SiO2 layers are shown. The inset shows a SAED diffraction pattern obtained on a larger area. The scale markers in the HRTEM and SAED micrographs correspond to 5 nm and 2nm^{-1}, respectively [4].

References:

[1] S. Gardelis, P. Manousiadis, and A. Nassiopoulou; Lateral electrical transport, optical properties and photocurrent measurements in two-dimensional arrays of silicon nanocrystals embedded in SiO_2; Nanoscale Res. Lett. 6, 227(1-6) (2011)

[2] S. K. Kim, C. H. Cho, B. H. Kim, S. J. Park, and J. W. Lee; Electrical and optical characteristics of silicon nanocrystal solar cells; Appl. Phys. Lett. 95, 143120(1-3) (2009)

[3] V. Beyer, J. Borany, and M. Klimenkov; A transient electrical model of charging for Ge nanocrystal containing gate oxides; J. Appl. Phys. 101, 094507(1-7) (2007)

[4] E. M. F. Vieira, J. Martнn-Sбnchez, A. G. Rolo, A. Parisini, M. Buljan, I. Capan, E. Alves, N. P. Barradas, O. Conde , S. Bernstorff, A. Chahboun, S. Levichev, and M. J. M. Gomes; Structural and electrical studies of ultrathin layers with Si0.7Ge0.3 nanocrystals confined in a SiGe/SiO2 superlattice; J. Appl. Phys. 111, 104323(1-9) (2012)

[5] V. Holy, C. Giannini, L. Tapfer, T. Marschner, and W. Stolz; Diffuse x-ray reflection from multilayers with stepped interfaces; Phys. Rev. B 55, 9960-9968 (1997)

Life Sciences

THE STRUCTURE OF WTSV40 IN SOLUTION

R. Asor, G. Saper, S. Kler, A. Ginsburg, A. Oppenheim, D. Harries, and U. Raviv

The Hebrew University of Jerusalem, Jerusalem, Israel

Structural analysis of the one dimensional SAXS data requires the construction of a model, which describes the geometry of the three dimensional electron density profile of the investigated structure. We used the following models to describe the electron density profile of the WTSV40 and the VLPs;

A low resolution model, that describes the virus as a multi layered spherical structure. This model describes the electron density of the virus as multiple concentric spherical shells with smoothly varying electron density profiles, represented by hyperbolic tangent functions:

$$\Delta\rho(\mathrm{r})=0.5\left\{\Delta\rho_1+\sum_{1=1}^{N-1}\left[\left(\Delta\rho_{i+1}-\Delta\rho_i\right)\right]\cdot\tanh\left[\mathrm{s_i}\left(r-R_i\right)\right]\right\} \quad (1)$$

Where, $\Delta\rho(r)$ indicates the radial electron density contrast with respect to the solvent (buffer). The index i represents the i-th layer in the sphere, with an outer radius, R_i, an electron density contrast, $\Delta\rho_i$, and linked to the subsequent layer ($i + 1$) by a slope s_i. $\Delta\rho_N = 0$ and corresponds to the solvent electron density contrast.

An improved model to the WT SV40 ($T = 7$ structure) was obtained by replacing the protein capsid layer with 72 spheres of smoothly varying electron density contrast (eq. 1 with N =2), located at the center of each VP1 pentamer in the capsid structure, represented by:

$$\begin{aligned}\Delta\rho\left(\vec{\mathrm{r}}\right)=&\sum_{i=0}^{N}0.5\left\{\Delta\rho_{Core,1}+\sum_{1=1}^{N-1}\left[\left(\Delta\rho_{Core,i+1}-\Delta\rho_{Core,i}\right)\right]\cdot\tanh\left[\mathrm{s_i}\left(\left|\vec{r}\right|-R_i\right)\right]\right\}\\&+0.5\left\{\Delta\rho_{Capsid}-\Delta\rho_{Capsid}\cdot\tanh\left[\mathrm{s}_{Capsid}\left(\left|\vec{r}\right|-a\right)\right]\right\}\otimes\sum_{n=1}^{72}\delta(\vec{r}-f\times\vec{R}_n)\end{aligned} \quad (2)$$

The first term in the expression represents the electron density profile inside the capsid as a sum of multiple concentric spherical shells, as described in eq. 1. The second term represents the arrangement of the 72 VP1 pentamers in the capsid shell. This term results from a convolution between a sphere, with an outer radius, a, and electron density $\Delta\rho_{\mathrm{Capsid}}$, and a sum of delta functions shifted by a set of vectors $f\times\vec{R}_n$. The $\vec{R}_n$ vectors represent the locations of the center of mass of the 72 VP1 pentamers derived from the crystal structure of WTSV40. The fitting parameter f enables us to change the overall radius of the VLP.

A similar model to the $T = 7$ (eq. 1) structure was used to model the electron density profile of the structure of the $T = 1$ RNA-VLPs. For this model, twelve spheres, representing the VP1 pentamers, were located at the vertices of a simple icosahedral grid.

Because, at low resolution, SV40 is nearly spherical, as seen by its crystal structure, we fit the radially integrated X-ray scattering intensities as a function of the magnitude of the momentum transfer vector, q,(fig. 1a) to a model of concentric spherical shells with a smoothly varying radial electron density (ED) profile (eq. 1). This approximation, to a low resolution model, is expected to yield a good fit at lower q values (corresponding to the larger elements of the icosahedral capsid), whereas at higher q values (~0.6nm^{-1}, corresponding to a distance of about 10 nm and less), where molecular details become important, the model is not expected to fit as well.

The best model fit for the WT SV40 virus (eq. 1) indicates high electron density at the external spherical shell and in the center (fig. 1a). This finding suggests a high ED associated

with the proteinaceous outer capsid layer (with typical ED values of 382±10 e/nm^3) and a slightly higher density of nucleosomes in the center. In the model, the SV40 capsid's outer radius is ~24.4nm, and the inner radius is ~18.1nm compared with ~24.7nm and ~17.9nm determined for the crystal structure, respectively. This allows a first, precise (sub nm) size estimate of the SV40 under physiological solution conditions. Unlike the present study, the earlier crystal structure did not provide any information about the internal organization of the minichromosomes.

As expected, the spherical shell model fit does not account for features at higher q values, reflecting the icosahedral capsid deviations from a sphere. The discrepancy is seen beginning at q >0.65nm^{-1} (fig. 1a). The deviation of the double maximum (at q≈0.7nm^{-1}) arises from the arrangement of the capsid proteins. The arrangement of the pentamers in the capsid shell defines a set of characteristic distances in the structure of the capsid that are not taken into account in the basic smooth spherical shells model. Using our more detailed model (eq. 2 and fig. 1b), we can now consider the spacing between the pentamers in the T =7 arrangement. A more accurate model enables as to reconstruct the double hump observed in the SAXS data, corresponding to a mean distance between sphere centers of 9.5nm (fig. 1d). This value is the typical distance between pentamer centers. Note that in SV40 the pentamer cores, 6-7 nm in size, are separated by gaps due to their unique binding via long carboxy-terminal arms.

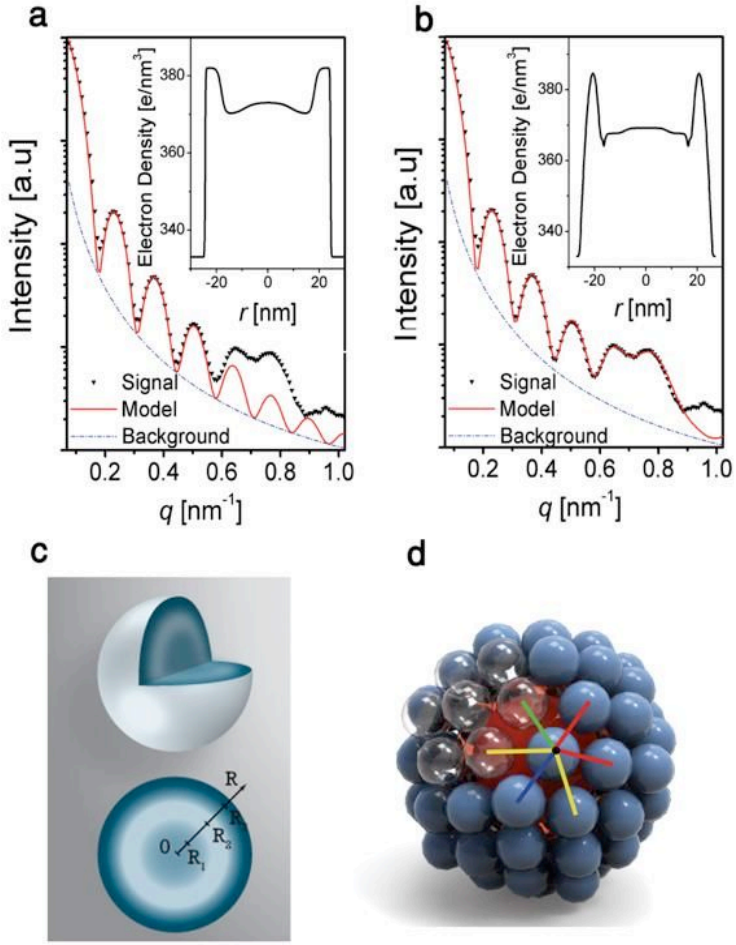

Figure 1. (a-b): Radially integrated solution SAXS intensity (open symbol) versus the magnitude of the momentum transfer vector q of WT SV40. The solid red curve is the best fitted form-factor model, (a) a smooth spherical model (eq. 1) and (b) T=7 model (eq. 2). The dashed blue curve shows the assumed background curve. The insets show the average radial electron density profile of WTSV40 as the best fitted model predicts. (c-d): Representations of the fitted geometrical models for WTSV40. (c) The smooth spherical model and (d) T =7 model. (d) The red core represents the electron density of the surrounded minichromosome and the blue spheres represent the 72 VP1 pentamers building the capsid of the virus. The blue, yellow, red and green bars correspond to inter-pentamer distances of 9.0nm, 10.3nm, 9.7nm and 8.5nm, respectively, as in the crystal structure and as the best fitted parameters establish.

As the fitting results show, both models predict a very similar radial electron density profile for the SV40. But the additional information regarding the interpentameric distances in the capsid is very important when we move forward and try to characterize the interactions between pentamers. This fit demonstrates the need in developing more accurate models that will enable us to get high resolution modeling.

MOUSE PRION PROTEIN FOLDING AND STABILITY

F. Benetti[1], G. Legname[1,2,3]

1.) Laboratory of Prion Biology, Department of Neuroscience, Scuola Internazionale Superiore di Studi Avanzati (SISSA), I-34136 Trieste, Italy
2.) Italian Institute of Technology, SISSA Unit, via Bonomea 265, I-34136 Trieste, Italy
3.) ELETTRA Laboratory, Sincrotrone Trieste S.C.p.A, AREA Science Park, Strada Statale 14 - km 163,5, I-34149 Basovizza, Trieste, Italy

Prion diseases or Trasmissible Spongiform Encephalopathies (TSEs) are neurological disorders found in humans and animals, which are due to the conversion of the native cellular prion protein (PrP^C) into a pathological PrP^{Sc} conformation. These pathologies are characterized by protein misfolding, neuronal cell loss, and deposition of amyloid fibrils in the brain. While PrP^C is mainly an α-helical protein sensible to protease digestion, PrP^{Sc} displays a high β-sheet content and resistance to protease. TSEs are unique because they can be sporadic, inherited or iatrogenic [1]. Point mutations and seeds represent a trigger to cross the energetic barriers for the genetic and infectious form and cause conformational changes bringing to the misfolded protein. Information regarding the sporadic prion diseases are still missing [2]. PrP^C is a glycoprotein linked to the external leaflet of plasma membrane through the GPI anchor. In our work we investigated the folding/unfolding mechanisms of recombinant full-length mouse PrP (MoPrP(23-231)), taking into account the physiological environments experienced by the protein. This data are crucial to understand the molecular mechanisms of conversion occurring in sporadic cases.

MoPrP(23-231) unfolding experiments were performed increasing temperature, ionic strength, and decreasing dielectric constant. These experiments were carried out at neutral and acidic pH: 7 and 5.5 respectively.

We found that thermal MoPrP(23-231) unfolding at acidic pH is fully reversible and it is characterized by a two state transition mechanism. At neutral pH, MoPrP(23-231) is more stable than at acidic pH but the unfolding process is not reversible. From these data we are calculating gyration radii and determining shape changes during unfolding. MoPrP(23-231) stability in the presence of increasing TFE concentrations (corresponding to decreasing dielectric constants) confirmed that the protein is more stable at neutral pH than at acidic pH, changing its shape at 25% and 20% TFE respectively.

These data, together with those obtained using circular dichroism, fluorescence spectroscopy and differential scanning calorimetry, demonstrated the important role of the naturally-unfolded N-terminal domain in stabilizing full-length and favoring its reversibility during unfolding processes, at acidic pH. On the contrary, at neutral pH, thermal unfolding measurements showed that N-terminal domain stabilizes the protein without favoring the unfolding process reversibility.

References:

[1] Prusiner, S. B. (1998). Prions, Proc. Natl. Acad. Sci. U.S.A. 95: 13363-13383.
[2] Benetti, F., Legname, G. (2009). De novo mammalian prion synthesis, Prion 3(4): 213–219.

LIPID SORTING BY CERAMIDE AND THE CONSEQUENCES FOR MEMBRANE PROTEINS

B. Boulgaropoulos, M. Rappolt, B. Sartori, H. Amenitsch and G. Pabst

Institute of Biophysics and Nanosystems Research, Austrian Academy of Sciences, Graz, Austria

We have performed a comprehensive structural analysis of mixtures of palmitoyl-oleoyl-phosphatidylcholine (POPC), egg-sphingomyelin (SM), cholesterol (Chol) and ceramide (Cer). In particular, we mimicked the enzymatic hydrolysis of SM by sphingomyelinase by gradually replacing SM by Cer. Results in the presence of 10 mol% Chol were compared to those in the absence of Chol. Cer in general leads to the formation of gel (L_β) domains, which coexists with fluid (L_α) domains [1-3]. In the present study we found, in particular, a decrease in the difference in lateral area/lipid in the L_β domains of Chol-free membranes (Fig. 1) that goes in hand with an increase of packing density in the L_α domains (Fig. 2) [4]. At the same time analysis of the electron density profiles determined from SAXS data showed an increase of the membrane thickness of the L_α domains from 49.5 Å to 50.2 Å.

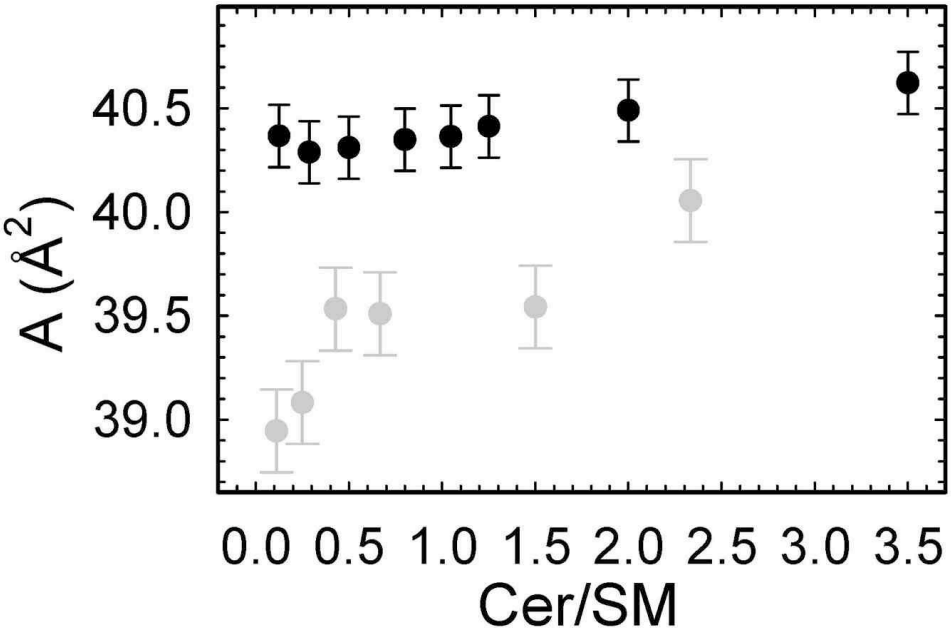

Figure 1. Comparison of lateral area/lipid of L_β domains in the presence (black circles) and absence (gray circles) of Chol as a function of the Cer/SM molar ratio. Data was determined from WAXS scattering of lipid samples.

In support of previous studies, this provides evidence that competition between Cer and Chol leads to an accumulation of Cer in L_β domains, whereas Chol enriches in L_α domains. We further estimated the spontaneous curvatures and Gaussian moduli of curvature of the coexisting phases, allowing us to address possible consequences of membrane restructuring for protein function in the case of a simple ion channel. Our calculations showed that channel opening in the L_α domains occurs with a significantly higher probability in the absence of Chol [4]. This highlights the important role of Chol in maintaining membrane stability and function. In the absence of Chol, lipid sorting by Cer induces strong shifts of the conformational equilibrium of ion channels in L_α domains toward open states, which could be detrimental to cell function and may interfere with the controlled disposal of cells during

apoptosis. In the presence of Chol, these changes are much more moderate and can possibly be more easily handled.

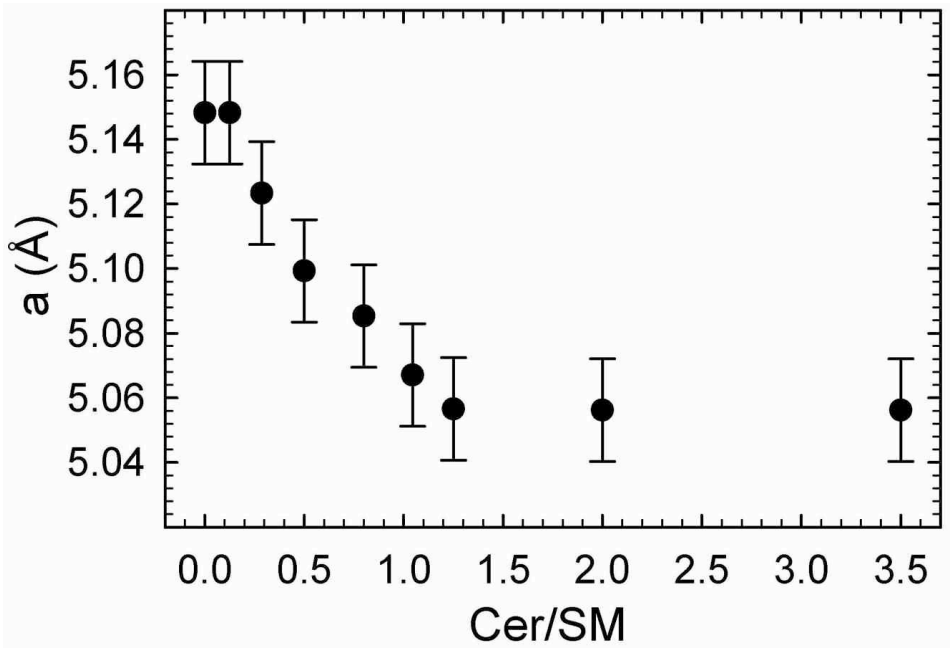

Figure 2. Average distance between acyl chains in the L_α domains as a function of Cer concentration from WAXS data analysis.

References:

[1] B. Boulgaropoulos, H. Amenitsch, P. Laggner, and G. Pabst, Implication of sphingomyelin/ceramide molar ratio on the biological activity of sphingomyelinase. Biophys. J 99: 499 – 506 (2010)

[2] G. Pabst, B. Boulgaropoulos, E. Gander, B.R. Sarangi, H. Amenitsch, V.A. Raghunathan, and P. Laggner. Effect of ceramide on nonraft proteins. J. Membrane Biol. 231: 125 – 132 (2009)

[3] B. Boulgaropoulos, Z. Arsov, P. Laggner, and G. Pabst, Stable and unstable lipid domains in ceramide-containing membranes. Biophys. J 100: 2160 – 2168 (2011)

[4] B. Boulgaropoulos, M. Rappolt, B. Sartori, H. Amenitsch, and G. Pabst, Lipid sorting by ceramide and the consequences for membrane proteins. Biophys. J 102: 2031 – 2038 (2012)

HELICAL PROPERTIES OF AN AMPHIPHILIC DESIGNER-PEPTIDE REVEALED BY SAXS

K. Kornmueller[1], C. Vonach[1], F. Cacho-Nerin[1], G. Leitinger[2], H. Amenitsch[1] and R. Prassl[1]

1.) Institute of Biophysics and Nanosystems Research, Austrian Academy of Sciences, Graz, Austria
2.) Institute of Cell Biology, Histology and Embryology, Medical University of Graz, Austria

Amphiphilic designer-peptides have recently attracted a lot of attention because of their application as building blocks for new nanomaterials. Due to their amphipathic character they are able to self-assemble into highly organized structures above a critical aggregation concentration (CAC). This self-assembly can be exploited in order to create biocompatible materials or nanoscale objects from a bottom-up approach. Applications are manifold and cover a wide range from 3D-cell culture systems, tissue engineering, gene and drug delivery systems to templates for nanowires [1].

SAXS provides an ideal tool to study structural characteristics of amphiphilic designer-peptide assemblies. Our aim was to investigate the self-assembly of the peptide GAAVILRR. The peptide monomer itself is cone-shaped with a hydrophobic part being composed of amino acids with consecutively increasing hydrophobicity whereas the hydrophilic headgroup consists of two bulky arginine residues (see figure 1). With SAXS we were able to follow the concentration-dependent structure formation process (figure 2).

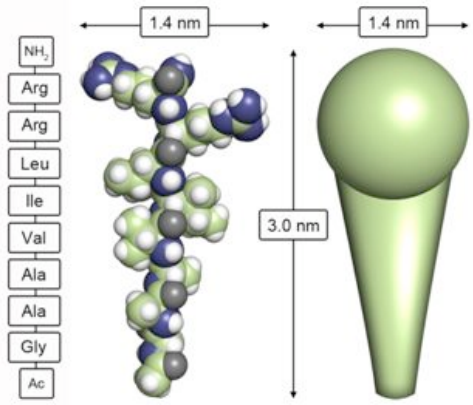

Figure 1. Atomic model of the GAAVILRR peptide monomer. Its overall structure resembles a cone.

At low concentrations the peptide monomers are coexisting with small peptide-assemblies. The data could be fitted with a sticky hard sphere model [2] combined with the theoretical form factor calculated from the pdb of the peptide monomer with CRYSOL [3]. Above the CAC we were able to observe an elongated intermediate structure followed by a stable hydrogel. Supported by transmission electron microscopy (TEM) studies, the hydrogel showed a pronounced helical propensity. In order to test the helical model and the corresponding fitting function we pursued the following approach: a theoretical helix-model was created using dummy atoms. This helix could be defined by its total length, the shape and size of its cross-section, the radius and the helical pitch. Systematic variations of every parameter led to a series of different helical models which served as template for DAMMIN, a low-resolution shape determination program [4]. The shape-reconstruction was constrained by this series of helical models which provided the search volume. According to the quality of the input-model the resulting shape reconstruction was more or less altered. Figure 3 shows a selection of three helical templates, differing only by their helical pitch (20, 16 and 12 nm) and the respective DAMMIN outputs. Among these models the 16 nm pitch gives the best solution as it maintains as only model the cross-section required for an infinite helical model, whereas the other solutions were clearly distorted.

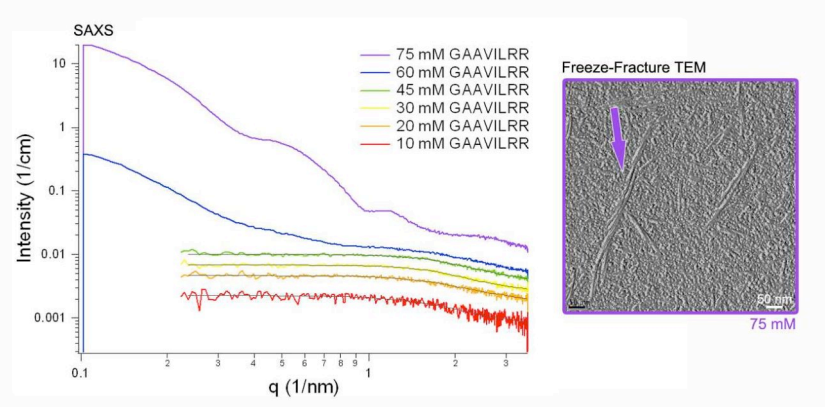

Figure 2. SAXS patterns of GAAVILRR in water. At low concentrations small stacks of monomers are formed. Intermolecular attractive forces increase as peptide concentration increases (red, orange, yellow and green curve. The gray curves represent the respective fits). At higher concentrations elongated structures occur (blue curve) and at 75 mM we obtained a hydrogel composed of cylinders with a pronounced helical supramolecular structure. The helical properties of the hydrogel could also be observed with freeze-fracture TEM.

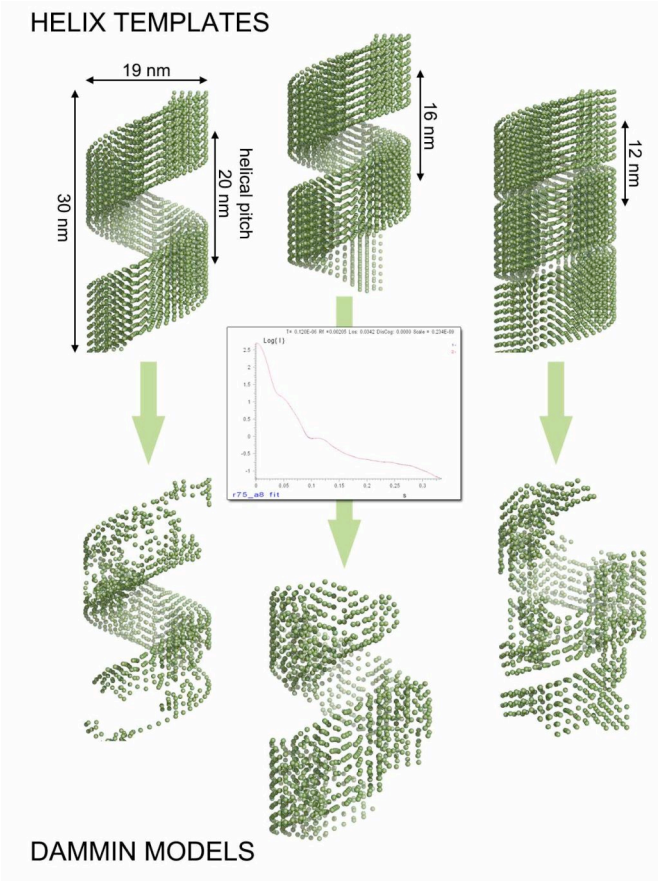

Figure 3. Helical templates that provided the search volume at DAMMIN shape reconstruction and their respective outputs. The central plot shows a perfect match of the experimental data with the DAMMIN fit.

References:

[1] X. Zhao, F. Pan, H. Xu, M. Yaseen, H. Shan, C. A. Hauser, S. Zhang, and J. R. Lu; Molecular self-assembly and applications of designer peptide amphiphiles; Chemical Society Reviews **39**, 3480-3498 (2010)

[2] D. Pontoni, S. Finet, T. Narayanan, and A. R. Rennie; Interactions and kinetic arrest in an adhesive hard-sphere colloidal system; Journal of Chemical Physics **119**, 6157-6165 (2003)

[3] D. I. Svergun, C. Barberato, M. H. J. Koch; CRYSOL – a Program to Evaluate X-ray Solution Scattering of Biological Macromolecules from Atomic Coordinates; Journal of Applied Crystallography **28**, 768-773 (1995)

[4] D. I. Svergun; Restoring Low Resolution Structure of Biological Macromolecules from Solution Scattering Using Simulated Annealing; Biophysical Journal **76**, 2879-2886 (1999)

STRUCTURAL ANF FUNCTIONAL INSIGHTS INTO THE DNA REPLICATION FACTOR CDC45

I. Krastanova[1], V. Sannino[2], H. Amenitsch[3], O. Gileadi[4], F.M. Pisani[2] and S. Onesti[1]

1.) Structural Biology Laboratory, Sincrotrone Trieste S.C.p. A. 34149 Trieste, Italy
2.) Istituto di Biochimica delle Proteine, Consiglio Nazionale delle Ricerche, 80131 Napoli, Italy
3.) Institut of Biophysics and Nanosystems Research, Austrian Academy of Sciences, Schmiedlstr. 6, 8042 Graz, Austria
4.) Structural Genomics Consortium, Oxford OX3 7DQ, United Kingdom

Cdc45 is an essential factor required for the establishment and progression of the DNA replication fork in eukaryotic cells. As many other DNA replication factors, Cdc45 is more abundant in proliferating cells, whereas it is almost absent from long-term quiescent, terminally differentiated and senescent cells. Cdc45 has been found to stably associate with Mcm2-7 and GINS to form a complex (the CMG) that is believed to act as the DNA helicase at the replication fork [1]. The critical biological function played by Cdc45 is underlined by its ubiquitous distribution and high degree of sequence conservation from yeast to man. Nevertheless, not much is known on the exact role of Cdc45 either in the pre-initiation complex or the CMG helicase, due to the lack of biochemical and structural studies on the isolated protein. Intriguingly, whereas homologues of both GINS and MCM proteins have been described in Archaea, no counterpart for Cdc45 is known.

We have carried out a bioinformatic analysis that shows a weak but significant relationship among eukaryotic Cdc45 proteins and a large family of phosphoesterases that has been described as DHH family, including RecJ ssDNA exonucleases, that catalyse the hydrolysis of phosphodiester bonds via a mechanism involving two Mn2+ ions. The similarity extends throughout the entire sequence. Only a subset of the amino acids that coordinate Mn2+ are conserved in Cdc45. We have produced recombinant human Cdc45 for biochemical studies: like the RecJ exonucleases, the human Cdc45 protein is able to bind single-stranded, but not double-stranded DNA [2]. However, it lacks the catalytic metals and has no catalytic activity.

SAXS data were collected at Elettra from highly purified samples of recombinant hCdc45 and corrected for the scattering from the buffer [2]. Ab-initio modelling was performed using the program DAMMIN, with 44 runs being averaged using the program DAMAVER. The model obtained can be described as a compact core with two lateral extensions (see Figure 1). We can fit the RecJ core (encompassing domains I and II, residues 50 to 421) from the *T. thermophilus* RecJ crystallographic structure (PDB code: 2ZXP) in the central part of the envelope. One of the two lateral extensions is larger and better defined, and can be assigned to the putative helical insertion domain that is common to both the eukaryotic Cdc45 and the archaeal RecJCdc45 proteins, as the putative insertion loop within the RecJ core is positioned in a manner compatible with this interpretation. As an example, we choose to fit to this region of the map the helical bundle from the acyl-CoA binding protein (PDB code: 2FDQ) as suggested from the results of the threading analysis. The second insertion has a more elongated shape and can be allocated to the partially unstructured insertion that is unique to the Cdc45 sequences.

This represent the first structural data on this essential eukaryotic replication factor in an isolated form. The sequence and structural similarity described has important evolutionary implications on the origin of the protein both in eukaryotic and in archaeal cells.

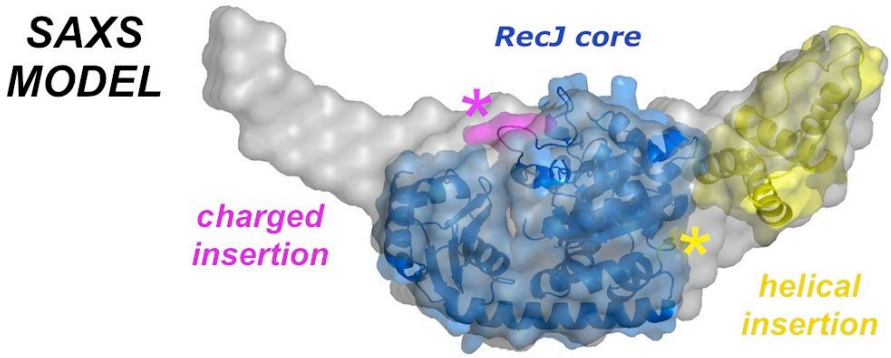

Figure 1. The *ab initio* calculated SAXS model for hCdc45 (depicted as grey light spheres) is superimposed to the crystal structure of the core of *T. thermophilus* RecJ (PDB code: 2ZXP, domains I and II), in blue. Highlighted in magenta and indicated by a magenta asterisk is the putative position of the insertion which is unique to the eukaryotic Cdc45 orthologues; highlighted in yellow and indicated by a yellow asterisk is the position of the helical bundle insertion that is common to both archaeal and eukaryotic proteins. As an example, the helical domain of the acyl-CoA binding protein (PDB code: 2FDQ) has been fitted to the map, consistently with the results of various threading algorithms.

References:

[1] A. Costa and S. Onesti; Structural biology of MCM helicases. Crit. Rev. Biochem. Mol. Biol. **44**, 326-342 (2009)

[2] I. Krastanova, V. Sannino, H. Amenitsch, O. Gileadi, F.M. Pisani and S. Onesti. Structural and functional insights into the DNA replication factor Cdc45 reveal an evolutionary relationship to the DHH family of phosphoesterases. J. Biol. Chem. **287**, 4121-4128 (2012)

STUDY OF LIGAND BINDING TO FREE AND CONFINED HEME PROTEINS

S.S. Mandal and A.J. Bhattacharyya

Indian Institute of Science, Bangalore 560012, India

Background and motivation: Several reports [1, 2] suggest beneficial influence on structure and function of proteins especially globin proteins following their confinement inside inorganic and organic substrates. Electrochemical, spectroscopic and thermal studies show no significant detrimental effects on protein structure. In fact thermal stability improved as a result of confinement compared to unconfined protein as well as immobilized on flat surfaces. The confined protein show efficient reversible binding of liquid based ligands to hemoglobin confined inside silica nanotubes. We envisage that enhancement in properties is due to the stabilization of protein in special global confirmations/structure under confinement compared to the unconfined condition. The protein conformation under confinement is strongly governed by both protein-protein as well as protein-host interactions. We have probed the protein structure under confinement via synchrotron small angle x-ray scattering (SAXS) [6] as a function of temperature in the temperature range 25-85 ^{o}C. Evaluation of the structural differences was done *vis a vis* the proteins in solution (unconfined). Apart from the fundamental interests, the work has deep implications in electrochemical biosensors.

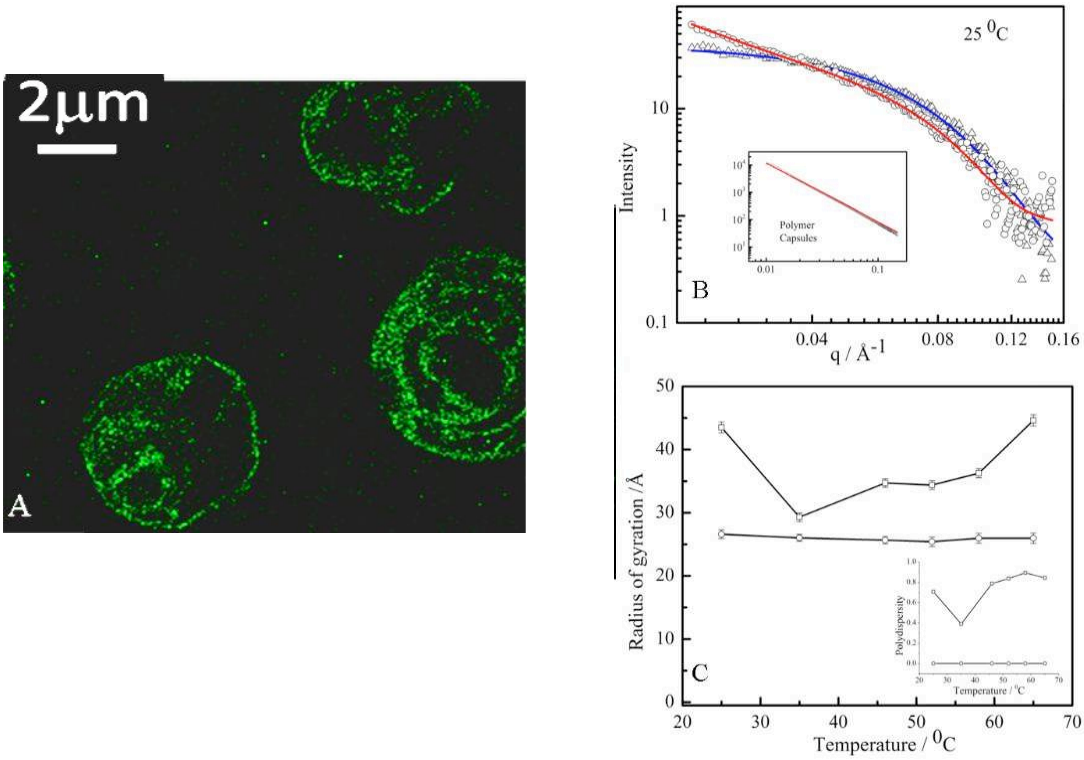

Figure 1. (A) Confocal laser scanning microscopy (CLSM) images showing FITC labeled Hb confined inside the polymer capsules. (B) Experimental small angle x-ray scattering curves obtained at 25 °C in 0.1 M PBS buffer pH 7.0 for 2.5 mg/ml Hb in buffer solution (Δ) and for Hb confined inside the polymer capsules dispersed in the buffer solution (○). The red (Hb-poly) and the blue (Hb) line represent the fitted data (see text for details). Inset: SAXS pattern of the polymer capsules fitted using Porod function (with slope B= 0.63 and m=1.2). (C) Variation in the radius of gyration, R_g of Hb in solution (□) and Hb confined within the polymer capsules (○) in the temperature range 25-65 °C. Inset: Variation in the polydispersity factor for Hb in solution (□) and Hb confined within the polymer capsules (○) in the same temperature range.

Experimental results using small angle x-ray scattering: The effect of confinement on structure of hemoglobin (Hb) within polymer capsules and submicron silica tubes was investigated here [3, 4]. Hemoglobin transformed from an aggregated state in solution to non-aggregated state when confined inside the polymer capsules and silica tubes. This was directly confirmed using synchrotron small angle x-ray scattering (SAXS) studies. The radius of gyration (R_g) and polydispersity (p) of the proteins in the confined state were smaller compared to that in solution. In fact, the R_g value is very similar to theoretical values obtained using protein structures generated from protein databank. In the temperature range (25-85 °C), the Rg values for the confined Hb remained the constant. This observation is in contrary to the increasing R_g values obtained for the bare Hb in solution. This suggested higher thermal stability of Hb when confined inside the polymer capsule/silica tubes than when in solution. Changes in protein configuration were also reflected in the protein function via enhancement of the electroactivity of Hb. While Hb in solution showed dominance of the cathodic process ($Fe^{3+} \rightarrow Fe^{2+}$) efficient reversible Fe^{3+}/Fe^{2+} redox response is observed in case of the confined Hb. This has important protein functional implications. Confinement allows the electroactive heme to take up positions favorable for various biochemical activities such as sensing of analytes of various sizes from small to macromolecules and controlled delivery of drugs.

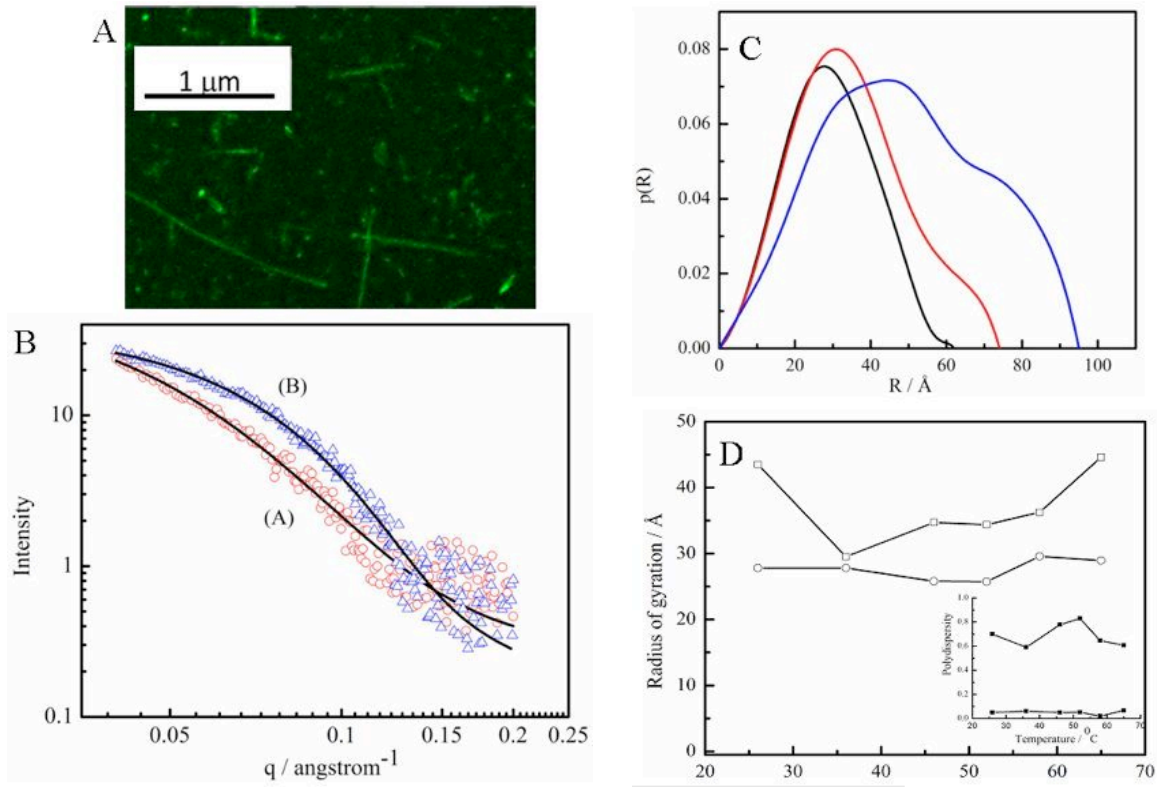

Figure 2. (A) Confocal laser scanning microscopy (CLSM) images showing FITC labeled Hb confined inside the submicron sized silica nanotubes. (B) Experimental small angle x-ray scattering curves obtained at 25 ^{0}C in 0.1 M PBS buffer pH 7.0 for 2.5 mg/ml Hb in buffer solution blue (Δ) and for Hb confined inside silica nanotubes (SNT) dispersed in the buffer solution red (◌). The black line represents the fitted data. (○) (C) Distance distribution function of Hb in solution (blue), Hb inside silica nanotubes (red) obtained from experimental solution SAXS data using the program GNOM. The black line is the p(r) function of the crystal structure of Hb (PDB code: 1HHO) (D) Variation of radius of gyration (R_g) as function of temperature (Temperature range: 25-65 ^{0}C) Inset: variation of the polydispersity factor with temperature in the same temperature range.

References:

[1] S. Kapoor, Aninda J. Bhattacharyya, "Ultrasound-triggered controlled drug delivery and biosensensing using silica nanotubes" *J. Phys. Chem. C*. 2009, *113*, 7155

[2] S. Kapoor, Soumit S. Mandal, Aninda J. Bhattacharyya, "Structure and function of hemoglobin confined inside silica nanotubes", *J. Phys. Chem. B* 2009, *113* 14189 (Cover-Art Article)

[3] Soumit S. Mandal, Satarupa Bhaduri, Heinz Amenitsch and Aninda J. Bhattacharyya, "Synchrotron small angle X-ray scattering studies of hemoglobin non-aggregation confined inside polymer capsules", J. Phys. Chem. B, 2012, ASAP Article

[4] Soumit S. Mandal, Brindha Nagarajan, H. Amenitsch and Aninda J. Bhattacharyya, "Probing hemoglobin confinement inside submicron silica tubes using synchrotron SAXS and electrochemical response", Biophys. J., 2012, to be submitted shortly

SAXS STUDIES OF HEMOCYANINS ENCAPSULATED IN SOL-GEL MATRICES

F. Minute[1], M.G. Ortore[2], M. Beltramini[1], P. Mariani[1] and F. Spinozzi[1]

1.) Dipartimento di Scienze della Vita e dell'Ambiente, via Brecce Bianche, Ancona, Italy
2.) Dipartimento di Biologia, via Ugo Bassi 58, Padova, Italy

Carcinus aestuarii hemocyanin is a protein that reversibly binds molecular oxygen and is characterized by high molecular complexity. The protein exists as oligomer of subunits whose quaternary structure has been successfully studied by SAXS [1-2]. In spite of numerous studies describing the cooperative oxygen binding of this protein, and its allosteric modulation by various solutes, a description of the structural features defining the oxygen affinity of the different conformers is still lacking. According to the two states allosteric model describing the oxygen saturation curve of hemocyanins, under anaerobic condition the protein exists as T state in the deoxygenated form (T-deoxy), while under oxygen saturation as R state in the oxygenated form (Fig. 1). However, neither T-oxy nor R-deoxy can be isolated in solution: therefore, to study their structural properties our experimental strategy is based on embedding R and T conformations within the pores of a sol-gel matrix, where the reduced mobility of water strongly decreases the rate of the conformational shift that occurs during the oxygen saturation process. Under these conditions, SAXS experiments can provide information on the structure of each conformer in both oxygenated and deoxygenated state.
The use of sol-gel to trap a particular conformational state of a protein provides advantages: the protein is not chemically modified, and the sol-gels based on silicic acid are high hydrated and have pores that allow the exchange of bulk molecules. Under these conditions, the function of the protein is maintained and its conformation is stabilized by the reduced mobility of water within the pores of the sol-gel [3-4]. In our case study, each of the two alternative conformations can bind oxygen and, once embedded in the gel, they can be equilibrated with different mixtures of oxygen and argon.
Hemocyanins inclusion in a sol-gel matrix can be useful to develop a biocompatible oxygen sensor based on spectroscopic differences between oxygenated and deoxygenated hemocyanin [5]. The study of the stability of the protein quaternary structure in the sol-gel is an important issue to demonstrate that the functional properties of the embedded protein refer to a given conformation of the oligomer (either R or T state) and to exclude dissociation.
SAXS measurements were carried out on samples of tetramethoxyl silane (TMOS) based sol-gel matrices in different polymerization conditions. A second series of SAXS measurements was performed on sol-gel matrices prepared in the previous conditions with trapped hemocyanin molecules. Before to perform SAXS experiments, in order to verify if proteins are in the R or in the T state, we measured in our laboratory curves of oxygen saturation. SAXS data should provide information on the quaternary structure of the states R and T in the four investigated conditions.
SAXS spectra were performed on all the sample conditions above described. The experimental data clearly suggest 3 main results:

1. According to the polymerization process, different features can be observed in the final sol-gels;
2. Hemocyanins in the T- and R-state, embedded in the gel matrices present different SAXS signals, hence different conformation could be extracted;
3. An ageing effect is evident. The analysis of SAS data for proteins trapped in sol-gel matrices is really complex. The scattering signal depends on the shape of the protein ("form factor", related to the conformation of the protein), the correlation of their positions within the sol-gel matrix ("structure factor") and the oxo-silanic matrix. Also, the polymerization is affected by the encapsulated proteins, as it was evidenced by a time-resolved study of the polymerization process (Fig. 3), which we performed in our beamtime, exploiting the high-brilliance of SAXS beamline.

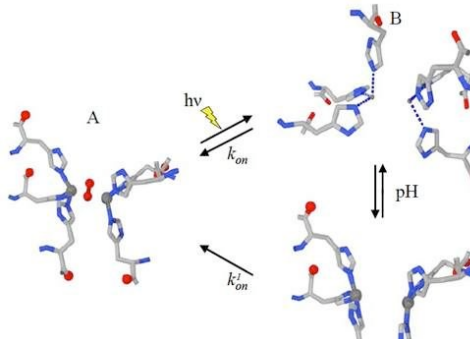

Figure 1. Reaction scheme for oxygenation of arthropod hemocyanin including a change in geometry of copper in the deoxygenated active site with pH

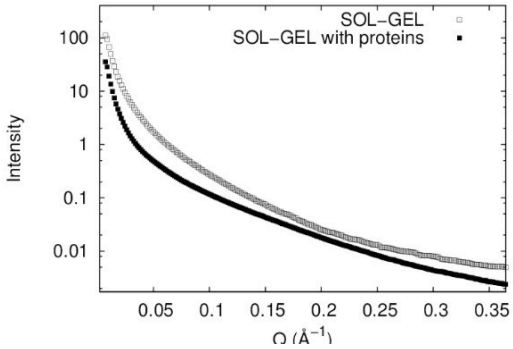

Figure 2. SAXS spectra of sol-gels with and without hemocyanins, as in the legend. Sol-gels were prepared at pH 6.5; encapsulated hemocyanins are in the T-state

Hence, as it is clear from Fig. 2, it is difficult to separate the SAXS signal from the sol-gel matrix and the one from the encapsulated proteins. Due to this crucial point, we have just performed a set of preliminary Small-Angle Neutron Scattering (SANS) experiments at ILL by contrast variation technique on a set of sol-gel matrices. Our aim is to obtain SANS spectra of the sol-gel matrices with encapsulated hemocyanins at the matching point between proteins' and buffer's signals. According to this strategy, we will obtain the sol-gel matrices' structural features in the presence of embedded proteins, without their scattering contribution. Hence a more complex analysis that simultaneously includes SAXS and SANS data may allow us to achieve a robust determination of all structural parameters of both sol-gel and immobilized proteins.

In summary, we have confirmed that hemocyanins encapsulation in this kind of sol-gels can be successfully applied to investigate proteins' structural features. Also, the time-resolved investigation of the polymerization process opens new perspectives to this kind of studies.

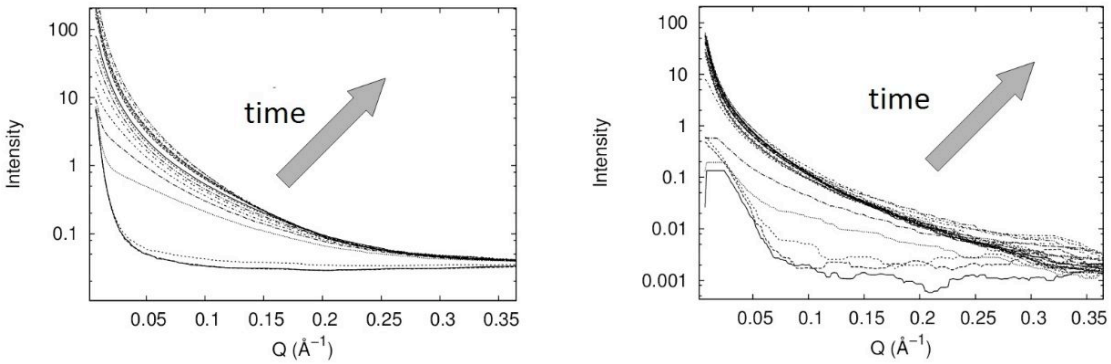

Figure 3. Left frame: polymerization without proteins. Right frame: polymerization with proteins. Sol-gels were prepared at pH 6.5 and with 25% glycerol; encapsulated hemocyanins were at 5 g l^{-1}, in the T-state

References:

[1] F. Spinozzi, E. Maccioni, C.V. Teixeira, H. Amenitsch, F. Favilla, M. Goldoni, P. Di Muro, B. Salvato, P. Mariani, M. Beltramini; Synchrotron SAXS studies on the structural stability of Carcinus aestuarii hemocyanin in solution. Biophys. J. **85**, 2661-2672 (2003)

[2] I. Mičetić, C. Losasso, P. Di Muro, G. Tognon, P. Benedetti, M. Beltramini; Solution structures of 2×6 and 4×6-meric hemocyanins from crustaceans Carcinus aestuarii, Squilla mantis and Upogebia pusilla; J. Struct. Biol. **171**, 1-10 (2010)

[3] L.L. Hench, K. K. West; The Sol-gel process; Chemical reviews **90**; 33-72 (1990)

[4] J. Livage, T. Coradine, C. Roux; Encapsulation of biomolecules in silica gels; Journal Phys: Cond Matt **13**; 673-691. Biophys. J. 98: 147-157 (2001)

[5] Zauner, G., Strianese, M., Bubacco, L., Aartsma, T., Tepper, A., Canters, G. (2008). Type-3 copper proteins as biocompatible and reusable oxygen sensors. Inorganica Chimica Acta 361: 1116–1121 (2008)

STRUCTURAL PARAMETERS AND FLEXIBILITY OF THE MULTILAMELLAR THYLAKOID MEMBRANES

G. Nagy[1,2], R. Ünnep[2], L. Kovács[3], P. Lambrev[3], Y. Miloslavina[3] and G. Garab[3]

1.) Paul Scherrer Institute, CH-5232 Villigen PSI, Switzerland
2.) Research Institute for Solid State Physics and Optics, HAS, P.O. Box 49, Budapest, 1215, Hungary
3.) Institute of Plant Biology, Biological Research Centre, HAS, PO Box 521, H-6726 Szeged, Hungary

In photosynthesis, light energy is captured by light harvesting antenna complexes (LHCs) and the excitation energy is transferred to reaction center complexes, where primary charge separations take place. These highly-specialized pigment-protein complexes can be found in the thylakoid membranes, which are embedded in an aqueous matrix of the chloroplast, the stroma [1]. Chloroplast thylakoid membranes of higher plants form a highly organised stacked multilamellar system, which is differentiated into granum and stroma lamellar (stacked and unstacked) regions and highly enriched in membrane bound protein complexes constituting the photosynthetic machinery. According to the widely accepted model, the stroma thylakoid membranes display multiple righthanded helices that are wound around the cylindrical grana stacks [2].

In nature, granal chloroplasts encounter a wide range of environmental conditions, for instance variations in the temperature and sudden and longer-term changes in the incident light intensity. Of paramount importance, the photosynthetic functions are adjusted, via multilevel regulatory mechanisms, to these variations. These regulatory processes, which are not understood in depth, involve substantial reorganizations at different levels of the hierarchically organized membrane system and the photosynthetic machinery. These reorganizations also include well discernible changes both in the lateral organization of the membranes and in their multilamellar organization [2].

The overall goal of our investigations is to identify the structural parameters of the complex multilamellar membrane system under a variety of physico-chemical environments and upon their exposure to different natural environmental conditions, such as the light intensity and temperature.

Earlier we have studied the structure of thylakoid membranes of higher plants [3,4] and in algal cells [5] with the aid of SANS measurements, which revealed small but well discernible variations in the repeat distances upon changes in the physico-chemical environments of the membranes and upon illumination. Our P-NMR and fluorescent lipid label experiments have shown that at elevated temperatures the thylakoid lipids, due to the presence of the dominant, non-bilayer lipid component of the thylakoids, i.e. due to the presence of monogalatosyl diacylglycerol (MGDG), assume non-bilayer phases that are associated with the bilayer membrane [6,7].

Experiments at the Austrian SAXS beamline of ELETTRA were performed in order to have a better understanding of these variations in the membrane systems using the facts that (i) the contrast between the different membrane and aqueous phase layers is different for neutrons and X-ray, and (ii) SAXS has a strong signature on the non-bilayer lipid phase, especially of H_{II}, the inverted hexagonal phase, the presence of which has been shown to depend on the MGDG:LHCII ratio [8].

Our SAXS experiments, performed on spinach thylakoid membranes, confirmed some of our observations with SANS – in particular, we could observed similar light induced reversible shrinkage of thylakoid membranes during the functioning of the cyclic electron transport (Figure 1); also, SANS and SAXS scattering curves showed great similarities in the entire q-range region (albeit some differences were also observed, which are to be further analyzed).

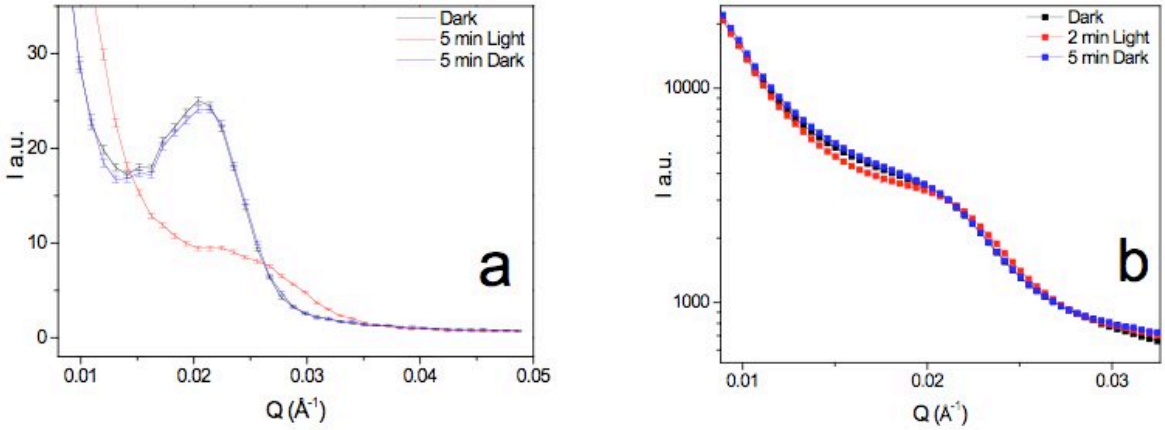

Figure 1. Effect of illumination with white light of 1700 μmol m^{-2} s^{-1} photon flux density on the SANS (a) and SAXS (b) profiles of spinach thylakoid membranes in the presence of 100 μM phenazine methosulfate.

On the other hand, we found no evidence for the presence of nonbilayer lipid phase(s) - despite the fact that we performed temperature dependent investigations of plant thylakoid membranes isolated from control and the MGDG-enriched *dgd1* lipid mutant of *Arabidopsis thaliana* leaves. In this mutant lipids are expected to be segregated from the lamellar phase, which might in principle lead to the appearance of H_{II} lipid phase. However, in our experiments we found no evidence for the presence of such a lipid phase, not even upon applying experimental conditions, such as high temperature treatments and the presence of co-solutes, which are known to lead to the appearance of electron-microscopically detectable H_{II} phase [9] or a non-bilayer phase detected by P-NMR [3]. It must thus be concluded that these lipid phases might either be present only in relatively small concentrations and/or under our experimental conditions, during which the bilayer membranes are retained, they do not assemble into well defined periodic structures detectable by SAXS.

References:

[1] Blankenship, R. E. (2002) Molecular Mechanisms of Photosynthesis, Blackwell, Oxford
[2] Mustárdy, L. and Garab, G (2003) Trends Plant Sci. 8: 117-122
[3] Posselt, D., Nagy, G., Kirkensgaard, J. J. K., Holm, J. K., Aagaard, T. H., Timmins, P., Rétfalvi, E., Rosta, L., Kovács, L. and Garab, G. (2012) Biochim. Biophys. Acta. – Bioenerg. 1817: 1220-1228
[4] Nagy, G., Posselt, D., Kovács, L., Holm, J. K., Szabó, M., Ughy, B., Rosta, L., Peters, J., Timmins, P. and Garab, G. (2011) Biochem. J. 436: 225-230
[5] Nagy, G., Szabó, M., Ünnep, R., Káli, G., Miloslavina, Y., Lambrev, P. H., Zsiros, O., Porcar, L., Rosta, L. and Garab, G. (2012) Photosynth. Res. 111: 71-79
[6] Krumova, S. B., Dijkema, C, Waard, P. de, As, H. van, Garab, G. and Amerongen, H. van (2008) Biochim. Biophys. Acta – Biomembr. 1778: 997–1003
[7] Krumova, S. B., Koehorst, R. B. M., Bóta, A., Páli, T., Hoek, A. van, Garab, G. and Amerongen, H. van (2008) Biochim. Biophys. Acta – Biomembr. 1778: 2823–2833
[8] Simidjiev, I., Stoylova, S., Amenitsch H., Jávorfi, T., Mustárdy L., Laggner P., Holzenburg A. and Garab G. (2000) Proc. Natl. Acad. Sci. U. S. A. 97: 1473–1476
[9] Williams, W.P. (1998) In: Advances in Photosynthesis. Lipids in Photosynthesis (Siegenthaler, P-A. and Murata, N., eds.) pp. 103–118, Kluwer Academic Publishers, Dordrecht

GRAZING INCIDENCE SMALL ANGLE X-RAY SCATTERING OF AMPHIPHILE CUBIC PHASES

M. Rittman[1], H. Amenitsch[2], M. Rappolt[2] and A. Squires[3]

1.) BIOSS, Univerity of Freiburg, Schänzlestr. 18, 79104 Freiburg, Germany
2.) Institute of Biophysics and Nanosystems Research, Austrian Academy of Sciences, Graz, Austria
3.) Dept of Chemistry, University of Reading, Whiteknights, RG6 6AD, UK

Cubic phases are topologically complex, non-lamellar phases of amphiphiles. They have applications in drug delivery, protein crystallization and as nanomaterials [1-3]. While various static properties of cubic phases can be easily measured, dynamic and kinetic information is more difficult to access.

Water content is a key driver in phase formation. We developed a method to measure phase properties continuously with water content using grazing incidence small angle X-ray scattering (GISAXS) of thin films. By using a sample chamber with controlled humidity, we have data where the same sample is continuously changing its water content. Measurements could be made in a slow manner, such that the phase was locally equilibrated (Fig 2a-d), or rapidly, faster than the phase change could occur, thus effectively a step change in conditions (Fig 2e-f).

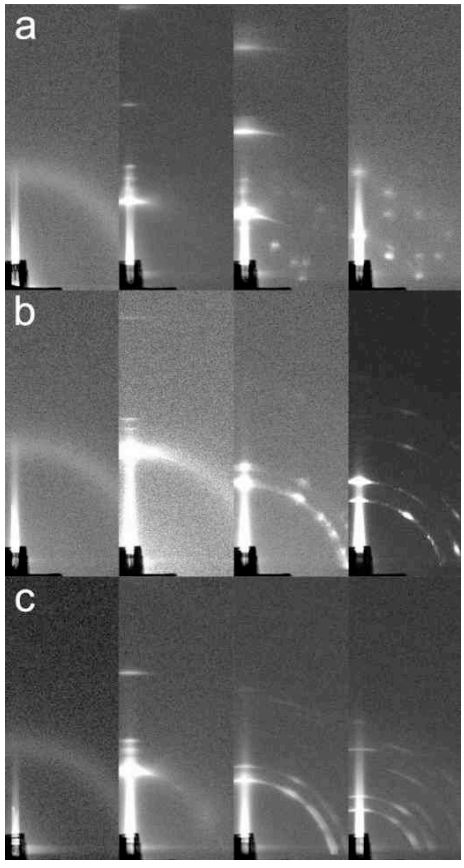

Figure 1. GISAXS patterns of a) monoolein, b) phytantriol, c) Rylo in various phases. Left to right: crystalline, fluid lamellar, gyroid cubic, diamond cubic. In the case of monoolein some lamellar remains present with the gyroid cubic phase.

We measured the phase change of three types of amphiphiles (monoolein, Rylo© and phytantriol), observing all expected phases for each (Fig 1). High amounts of orientation were observed in the thin films, evidenced by the presence of spots rather than rings in the X-ray patterns. Further analysis showed that for monoolein each cubic phase was present in a single orientation, whereas for Rylo and phytantriol two orientations of each cubic phase were present.

The method we have developed should prove useful for further kinetic and dynamic studies of amphiphiles, and the use of oriented thin films is also of interest in applications of cubic phases as nanomaterials.

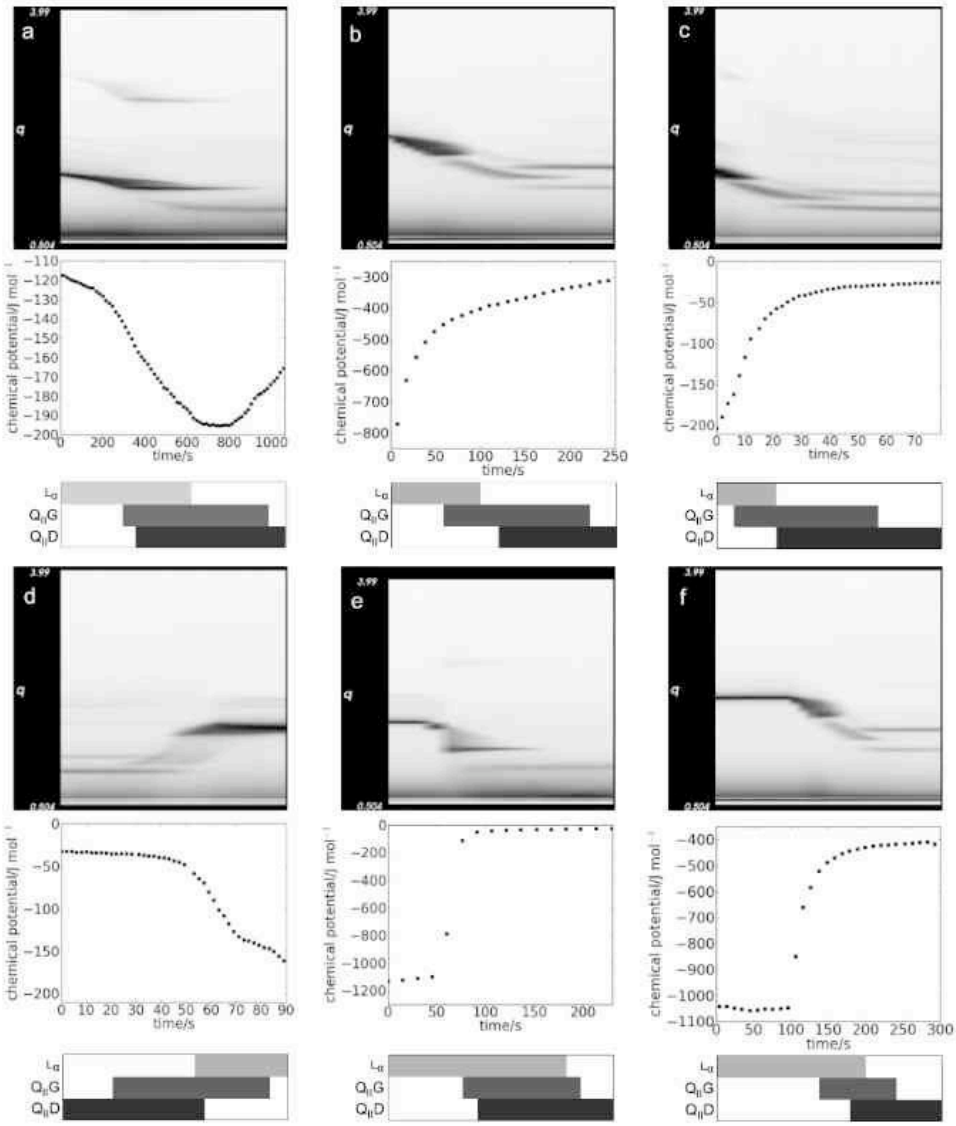

Figure 2. Each plot shows radially integrated SAXS (top), chemical potential (calculated from humidity, middle) and bar diagrams showing the phase locations (bottom) on the same horizontal time axis. a-d show slow changes, whereas e-f show rapid humidity changes. a and e are for monoolein, b and f phytantriol and c and d Rylo. c-d show humidity changes in different directions, with phase boundaries in almost identical positions in each direction.

References:

[1] C. J. Drummond and C. Fong, Surfactant self-assembly objects as novel drug delivery vehicles, Current Opinion in Colloid & Interface Science, 4, 449–456 (1999)

[2] M. Grabe, J. Neu, G. Oster, and P. Nollert, Protein interactions and membrane geometry, Biophysical journal 84, 854–68 (2003)

[3] E. M. Landau and J. P. Rosenbusch, Lipidic cubic phases: a novel concept for the crystallization of membrane proteins, Proc Natl Acad Sci, **93**, 14532–14535 (1996)

MICELLAR BEHAVIOUR OF SAPONIN-CHOLESTEROL AQUEOUS SYSTEM

C.V. Teixeira[1,2] and H. Amenitsch[3]

1.) Universitat Autonoma de Barcelona,Facultat de Medicina, Bellaterra, Barcelona, Spain
2.) Universidade Federal do Rio Grande do Sul, Instituto de Física, Av. Bento Gonçalves, 9500, Porto Alegre, 91501-970, RS, Brazil
3.) Institute of Biophysics and Nanosystems Research, Austrian Academy of Science, Schmiedlstrasse, 6, 8043, Graz, Austria

Micellar-based extraction is a topic that has gained considerable attention in Chemical, environmental and pharmaceutical fields, due to its effectiveness and low cost [1]. Particularly, the extraction of cholesterol, in the food industry and health field, has been a very important issue. It has been observed that plant extracts, like phytosterols and saponins inhibit the cholesterol uptake [2]. The increasing evidence of saponins efficiency in cholesterol lowering has brought them into focus. Besides, they exhibit several other properties, against several diseases [3]. In particular, the Quillaja Saponin (QS), originated from a South American tree, has been shown to have immunoadjuvant activity and has been tested for the preparation of vaccines against influenza, Eschirichia Coli, HIV-1, measles, malaria, leishmaniases and even for the treatment of melanoma [4], and has been shown to interact with cholesterol, being able to reduce the plasma cholesterol in several mammalians, including humans [5]. One of the most prominent applications of QS so far, due to its especial interaction with cholesterol and its immunoadjuvant properties, is the formation of ISCOMs (Immune Stimulating Complexes) [6]. They are used as a delivery for vaccine antigens, targeting the immune system, and have been tested in animals, being much more efficient than conventional vaccines. QS structure is formed by various sugar groups bound to a triterpene ring (Figure 1) and it has amphiphilic properties, forming micelles in aqueous solution. Studies showed that QS is more efficient in solubilizing cholesterol in excess than other surfactants [7]. This efficiency is closely related to the micellar properties of the surfactant, which also depends on the solvent conditions. The present work studies the behaviour of QS micelles in the presence of cholesterol, for different QS concentrations in water and different cholesterol:OS molar ratios.

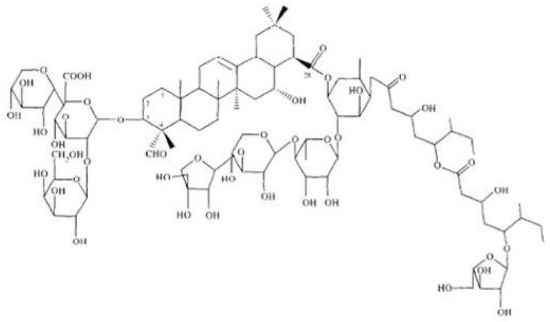

Figure 1. Structure of Quillaja Bark Saponin

The QS concentration varied from 2 to 8 wt% in water, and the cholesterol:QS ratio ranged from 1 to 50 mol%. Initially, a temperature scan was performed, from 20 to 50 °C in two hours, then from 50 to 20 °C also in two hours, without any break between both scans, for 5 wt% QS and 50 mol% cholesterol:QS. Selected curves obtained during the T-scan are shown in Figure 2. At 20 °C the curve is very similar to the one without any cholesterol added. At 50 °C there was a slight deviation of the form factor oscillation towards small q-values, and the last curve, already back at 20 °C, showed an increase in the correlation length of the micelles. After that, kinetic experiments were performed at the same QS and cholesterol concentrations, at three different temperatures: 37 °C, 50 °C and 60 °C. Figure 3a shows the variation of the

micelles correlation length with time, for the three temperatures. At 37 °C and 60 °C there is only a slight change in the correlation length, whereas at 50 °C it increases considerably and after almost 3 hours of experiment it is still increasing. As the greater changes occurred at 50 °C, further kinetics experiments were performed at this temperature, for different cholesterol concentrations and a constant QS concentration of 5 wt%. The kinetic curves were obtained for 1, 10 and 50 mol% cholesterol and the variation of the correlation length with time is shown in Figure 3b. The effect is very small for 1 mol% cholesterol, being noticeable for 10 mol% and more pronounced for 50 mol% cholesterol. Finally, static measurements were performed for samples aged in oven at 37 °C and 50 °C for 13 hours. Samples were prepared at 2, 5, 8 and 12 wt % QS and for each of them cholesterol was added at 1, 10 and 50 mol%. 1 mol% cholesterol showed no effect for all the QS concentrations studied, as already seen from the kinetics experiment; 50 mol% cholesterol had a huge effect in the micellar structure. However, the effect of 10 mol% cholesterol depends on the QS concentration: at 2 wt% QS, it presents an intermediate effect between 1 and 50 mol%; at 5 and 8 wt% QS, the curves are similar to the ones with 50 mol% cholesterol and at 12 wt% QS it is similar to the curve without any cholesterol. Comparing the curves for different QS concentrations with the same cholesterol:QS ratio (50 mol%), one sees that the differences are dominated by the QS concentrations. As an overall effect, after the samples reach the equilibrium, the cholesterol addition seems to increase the micelles size, in agreement with the previous work by Mitra [7]. However, the QS concentration plays an important role. Especially at 8 and 12 wt% cholesterol, in which intermicellar effects are already visible in the SAXS curves, two bumps are observed in the curves corresponding to 50 mol% cholesterol:QS: the first one due to the intermicellar structure factor and the second one due to the form factor oscillation. The temperature affects the adsorption of the cholesterol by QS micelles. In the pure system of QS in water, an increase in temperature also changes slightly the micelles conformation, which might be more appropriate for the cholesterol penetration. Nevertheless, the structure of the mixed cholesterol/QS micelles is more dependent on both, the QS concentration and cholesterol:Qs molar ratio, than on temperature.

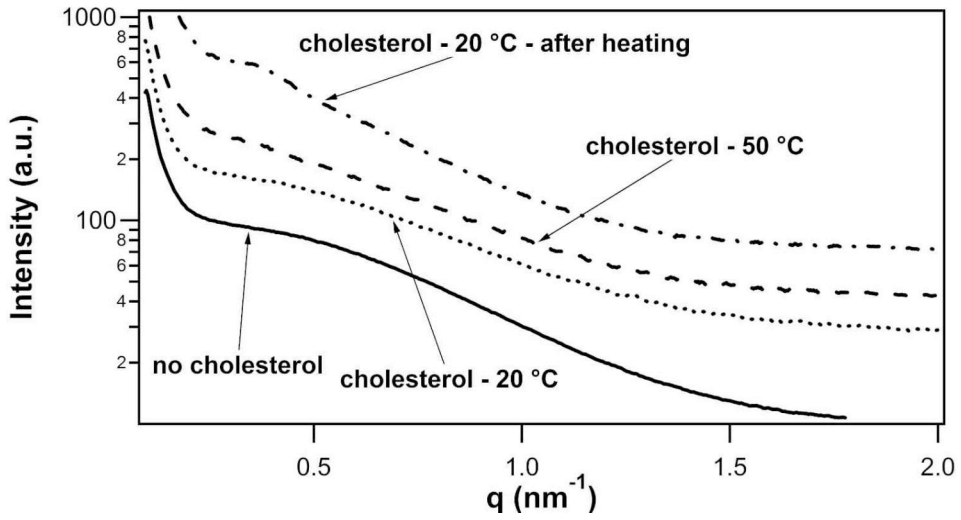

Figure 2. Selected curves during temperature scan, for sample with 5 wt % QS and 50 mol% cholesterol. Curves are vertically shifted.

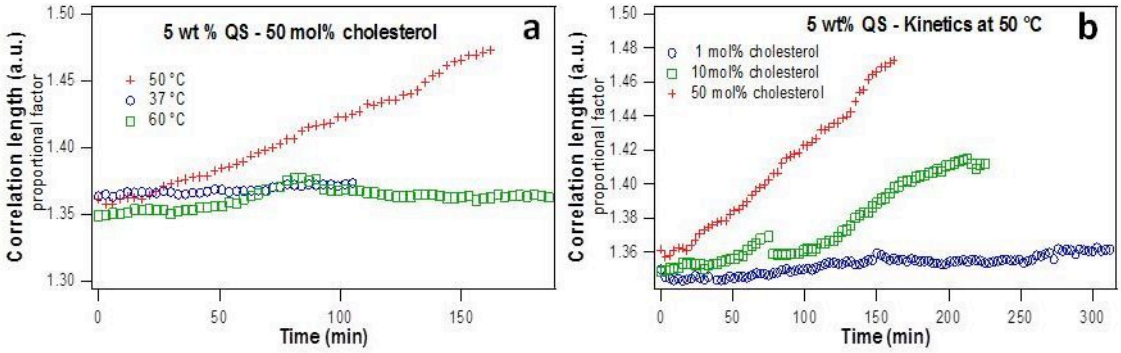

Figure 3. Correlation length factor against time for sample with 5 wt% QS. a. containing 50 mol% cholesterol, at different temperatures; b. different concentrations of cholesterol, at 50 °C.

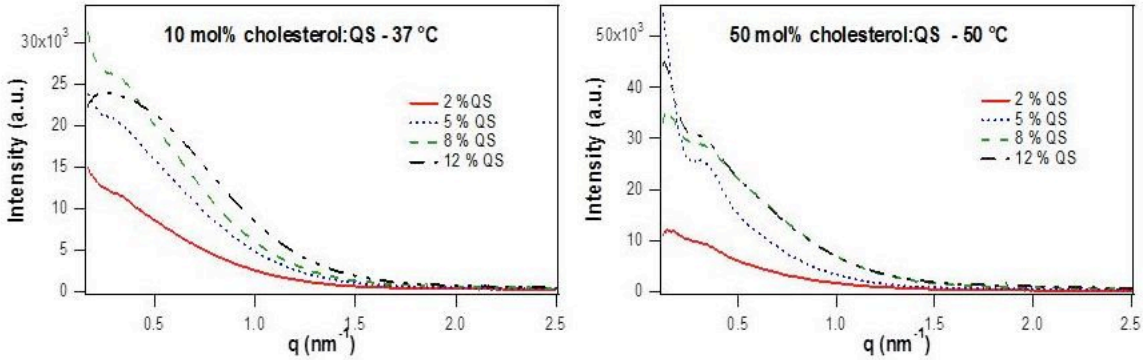

Figure 4. Static curves for different concentrations of QS with: a. 10 mol% cholesterol, at 37 °C; b. 50 mol% cholesterol at 50 °C.

References:

[1] J.F. Scamehorn, J.H. Harwell, Surfactant-based separation processes; Marcel Dekker, New Yourk, 1989

[2] J. Quilez, P. Garcia-Lorda, J. Salsas-Salvado, Potential uses and benefits of phytosterols in diet: present situation and future directions, Clin. Nutr, **22**, 343-351 (2003)

[3] M. Santour, A.C. Mitaine-Offer,M.A,Lacaille-Dubois, The Dioscorea genus: a review of bioactive steroid saponins, J.Nat.Med., 61, 91-101(2007)

[4] R.T. Coughlin, A. Fattorn, C. Chu, A.C. White, S. Winston, Adjuvant activity of QS-21for experimental E.Coli 018 polysaccharide vaccines, Vaccine, 13,17-21(1995)

[5] D. Oakenful,D., G.S. Sidhu, in Toxicants of Plant Origin, Volume II. Glycosides, Cheecke,P.R., Ed.; CRC Press, Inc.:Boca Raton, FL., 1989; pp 97-141

[6] B. Morein, B. Sundquist, S. Höglund, K. Dalsgaard, A. Osterhaus, Nature, 308, 457(1994)

[7] S. Mitra, S. Dungan, Micellar properties of Quillaja Saponin.2. Effect of solubilized cholesterol on solution properties, Colloids ans Surf.B, 17, 117-133(2000)

QUERCETIN NANODISPERSIONS: FROM POLYOXYLGLYCERIDE-BASED NANOPARTICLES TO NANOCRYSTALS

T. Truong Cong, S. Lesieur and V. Faivre

UMR CNRS 8612 – Institut Galien Paris-Sud, 5 rue JB Clement, 92296 Châtenay-Malabry, France

Quercetin, a flavonoid, is one of the most prominent antioxidants in the disease prevention and therapy [1]. However, its use in the pharmaceutical field is limited by its poor bioavailability. Quercetin is insoluble and unstable in aqueous media. To overcome these drawbacks, nanodispersions loading quercetin and nanocrystals were successfully prepared by high pressure homogenization (HPH) process.

Polyoxylglyceride-based formulation containing 1% (w/w) quercetin in lipid had particle size of 207.1 ± 10.7 nm with a narrow distribution (PdI ~ 0.1) and an encapsulation efficiency of 96.4 %. The apparent solubility of the drug was 4500-fold higher compared with that of the original quercetin (0.44 ± 0.25 µg/ml).

Meanwhile, the stability studies demonstrated that quercetin was relatively stable in simulated gastric fluid (SGF) at RT and 37°C; it was unstable in Milli-Q water (pH = 5.6, $t_{1/2}$ = 16.8 h), simulated intestinal fluid (SIF) (pH = 6.5, $t_{1/2}$ = 13.2 h) and HEPES buffer (pH = 7.4, $t_{1/2}$ = 9.8 h) at RT. Testing for chemical stability in the nanodispersions over 3 months, the quercetin content was retained 96.2% at RT and 95.5% at 4°C versus the initial content. Encapsulation significantly improved the chemical stability of quercetin in water in which its half-life was around 17h at RT. As expected, the API has been protected by its incorporation into polyoxylglyceride-based nanodispersions. The global hydrophobicity of nanoparticles was probably sufficient to limit water diffusion process into the drug-containing droplets. Furthermore, a controlled release of the API of interest had been observed during 4 hours, without any burst effect. The polyoxylglyceride-based nanoparticle is one of the promizing nanocarriers for administration of sensitive active ingredients.

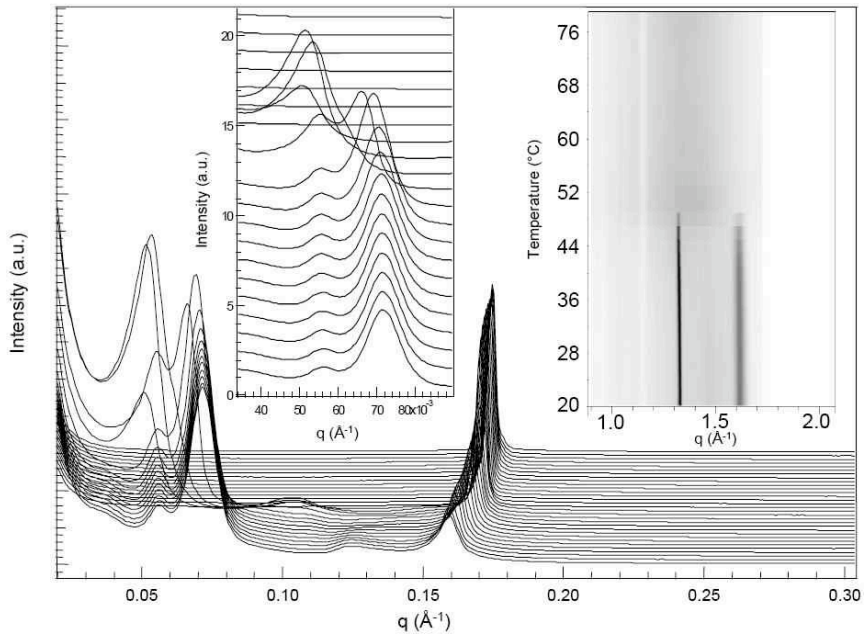

Figure 1. Time-resolved SAXS patterns recorded from 20°C to 80°C of the Gelucire® 50/13 – Phospholipon® 90G anhydrous mixture at 2°C/min with one XRD diagram every minute. *Left inset*: Focus on an isobestic point in the smallest angle region suggesting equilibrium between two structures. *Right inset*: 2D-matrix of the WAXS domain describing the disappearance of the PEG chains helical conformation (q = 1.33 $Å^{-1}$ and 1.62 $Å^{-1}$) with temperature

In this part of the work, and with the help to the Microcalix calorimeter, the Austrian SAXS Beamline allowed to deeply characterize the interactions between the stabilizers used in the formulation (Gelucire® 50/13 and Phospholipon® 90G). First, whereas Gelucire® 50/13 alone tended to crystallize into non-tilted lamellar structure (d = 130 Å) [2], the presence of phospholipids strongly oriented the organization to tilted lamellar phases (d = 87 Å and 107 Å). The temperature-dependent transition between tilted and non-tilted phases, due to Gelucire® 50/13, remained however visible in the mixture. Furthermore, the SAXS imprint of the pure glyceride phase which was present independently of the crystallization process (q = 0.128 $Å^{-1}$) seemed to disappear. The structural organization of Phospholipon® 90G was also changed by the presence of Gelucire® 50/13. There was only one lamellar period which could be detected in the mixture, while two distinct lamellar phases have been described in the pure product (Figure 1).

The aim of the second part was to increase the drug concentration into the nanosuspension with quercetin nanocrystals prepared by HPH. The properties of the quercetin nanocrystals have been investigated regarding size analysis, zeta potential measurement, drug payload, morphology, physico-chemical stability and *in vitro* dissolution. Furthermore, crystallinity and polymorphism were also studied to understand the structure and physical stability of nanocrystals based on X-ray scattering and thermal analysis. Regarding nanocrystal sizes, the average diameter varied from 233.4 to 275.1 nm after redispersion in Milli-Q water. TEM images presented needle-shaped nanocrystals with a length of approximately 100 – 350 nm which was in agreement with the size analysis by *quasi*-elastic light scattering.

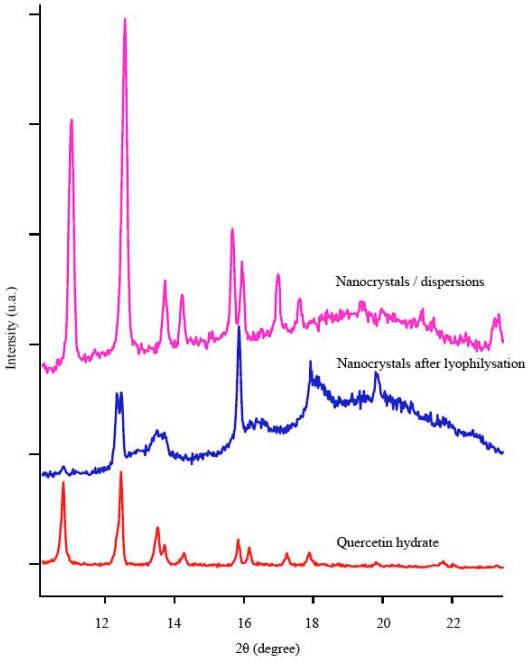

Figure 2. WAXS patterns recorded at 20°C of the nanocrystals both in hydrated state (suspension) or after lyophilization and compared to raw quercetin dihydrate.

The dissolution profiles of raw quercetin suspensions and quercetin nanocrystals in SGF (pH = 1.2) had been done. For the quercetin nanodispersions, the dissolution rate of drug significantly improved versus raw quercetin suspensions. Quercetin-loaded nanoparticles reached 48.7% ± 2.6% dissolution at 6h and about 90% dissolution at 24%. In contrast, raw quercetin released to 32.2 ± 2.6% at 4h and the dissolution slightly decreased until 26.9 ± 2.6% at 24h. According to the Noyes-Whitney equation, particle size reduction could lead to an increase of the surface area and a decrease of the diffusion layer thickness, which could provide an enhanced dissolution rate for drugs. To validate the effect of nanocrystals on the chemical stability of quercetin, a long-term study was performed by HPLC on a suspension containing 3% of nanocrystals. The drug content in nanodispersions reduced about 6% after 3

months at RT and 4°C in the dark. In comparison to chemical stability of quercetin in water ($t_{1/2}$ = 16.8h, the half-life of degradation), quercetin nanocrystals showed no significant alteration in drug content. The chemical stability is explained by two effects. Firstly, the molecules of the surface stabilizer could shield the chemically unstable compound. Secondly, the crystalline structure in nanocrystals results in higher drug stability.
X-ray diffraction had been used here to characterize the quercetin polymorphism [3] depending on its treatment or origin (different suppliers, different recrystallization ways, raw quercetin vs. nanocrystals, lyophilized nanocrystals,…). Thus, nanocrystals corresponded to dihydrate quercetin and were then very sensitive to lyophilization process which had been tried to isolate nanocrystals from the suspension (Figure 2).

References:

[1] S.C. Bischoff; Quercetin: potentials in the prevention and therapy of disease; Current Opinion in Clinical Nutrition and Metabolic Care **11**, 733-740 (2008)

[2] J-B. Brubach, M. Ollivon, V. Jannin, B. Mahler, C. Bourgaux, P. Lesieur, P. Roy; Structural and thermal characterization of mono- and diacyl polyoxyethylene glycol by infrared spectroscopy and X-ray diffraction coupled to differential calorimetry; The Journal of physical chemistry B **108**, 17721-17729 (2004)

[3] G. S. Borghetti, I. M. Costa, P.R. Petrovick, V.P. Pereira, V.L. Bassani; Characterization of different samples of quercetin in solid-state: indication of polymorphism occurrence; Pharmazie **61**, 802-804 (2006)

SELF-ASSEMBLED NANOSTRUCTURES OF FULLY HYDRATED MONOELAIDIN-ELAIDIC ACID AND MONOELAIDIN-OLEIC ACID SYSTEMS

A. Yaghmur[1], B. Sartori[2] and M. Rappolt[2]

1.) Department of Pharmacy, Faculty of Health and Medical Sciences, University of Copenhagen, Universitetsparken 2, DK-2100 Copenhagen, Denmark
2.) Institute of Biophysics and Nanosystems Research (IBN), Austrian Academy of Sciences, Graz, Austria

In recent years, there has been a surge of interest in exploring the effect of *trans* fatty acids (TFAs) on biological membrane properties. The research studies are motivated by an increasing body of evidence suggesting that the consumption of TFAs increases the risk of developing negative health effects such as coronary heart disease and cancer. The ultimate goal of studying the lipid-fatty acid interactions at the molecular level is to predict the biological role of fatty acids in cells. In this regard, it is interesting to elucidate the effect of loading TFAs and their counterparts *cis* fatty acids (CFAs) on the physical properties of lipid model membranes. Here, the present study focuses on discussing the following: (1) the effect of mixing monoelaidin (ME, TFA containing lipid) with its counterpart monoolein (MO, CFA containing lipid) on modulating the fully hydrated self-assembled structure, and (2) the influence of solubilizing oleic acid (OA) and its *trans* counterpart elaidic acid (EA) on the fully hydrated ME system. The ME model membrane was selected due to its sensitivity to variations in lipid composition and temperature. Synchrotron SAXS was applied for studying the temperature-dependent structural behavior of the fully hydrated ME/MO-based system prepared with an equal ME/MO weight ratio, and also for characterizing the fully hydrated OA- and EA-loaded ME systems. WAXS experiments were also performed for characterizing the formed crystalline lamellar phases at ambient temperatures.

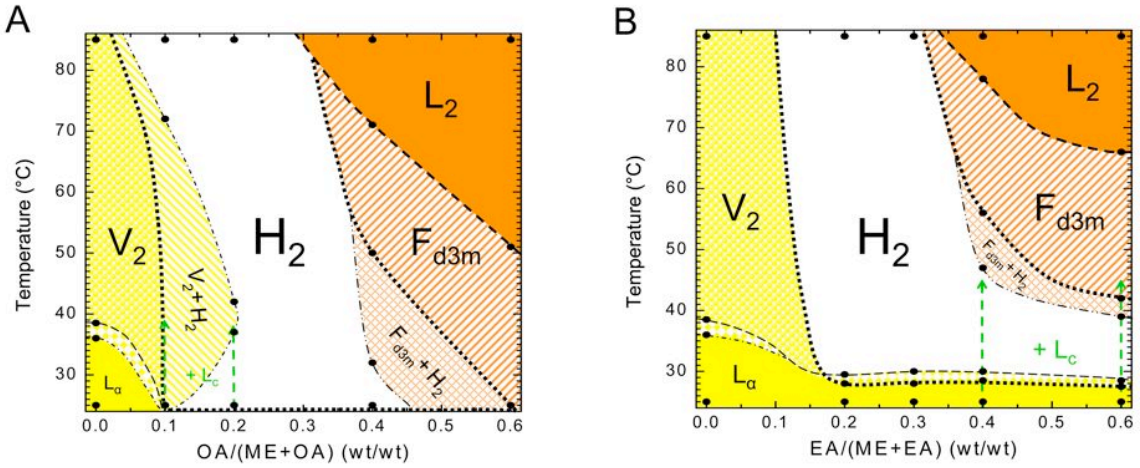

Figure 1. Temperature-dependence behavior of the fully hydrated OA-loaded (A) and EA-loaded (B) ME systems. The experiments for both self-assembled systems were performed with R_{WT} ratio (R_{WT} = mass of OA (or EA)/(mass of OA (or EA) + mass of ME)) in the range of 0-0.6 and were used to construct the partial phase diagrams. The dashed/dotted curves indicate the approximate phase boundaries between the different phases. These phase boundaries are tentative (they are not well characterized).

The fully hydrated ME/EA and ME/OA systems with their rich polymorphism exhibit an interesting temperature-dependent complex behavior [1]. The experimental findings show that the temperature-induced phase transitions are dictated by the solubilized fatty acid concentration and its configuration. Both, EA and OA have a significant impact on the fully hydrated ME system (Figure 1). Similar to previous published studies [4], OA induces a

significantly stronger mean negative membrane curvature as compared to EA. The two phase diagrams are discussed in terms of water-lipid and lipid-fatty acid interactions, membrane bending and lipid packing concepts [1]. A newly observed interesting epitaxial relationship for the lamellar-hexagonal phase transition in the EA-loaded ME system is also illustrated and discussed in details [1]. Epitaxy between the initial and the final phase is given, if a registry between two of their lattice spacings is observed. In the ME/EA sample with R_{WT} value of 0.3 such a case is given for the highly swollen L_α-to-H_2 phase transition: the second order *d*-spacing of the L_α (h = 2) phase and the d_{10}-spacing of the H_2 phase display practically the same lattice spacing in the narrow temperature interval from 27.5 to 28.5 °C. In order to geometrically match the involved lattices and conserving simultaneously the highest symmetry in the interface region, every second layer of rods is aligned in a coplanar fashion with the parent bilayers of the L_α phase, i.e., rod centers and bilayer centers are lying in the same plane (**Figure 2**). Such a peculiar epitaxial relationship between a highly swollen lamellar liquid crystalline and an inverse hexagonal phase is to the best of our knowledge observed for the first time. For further information the interested reader is directed to ref. [1].

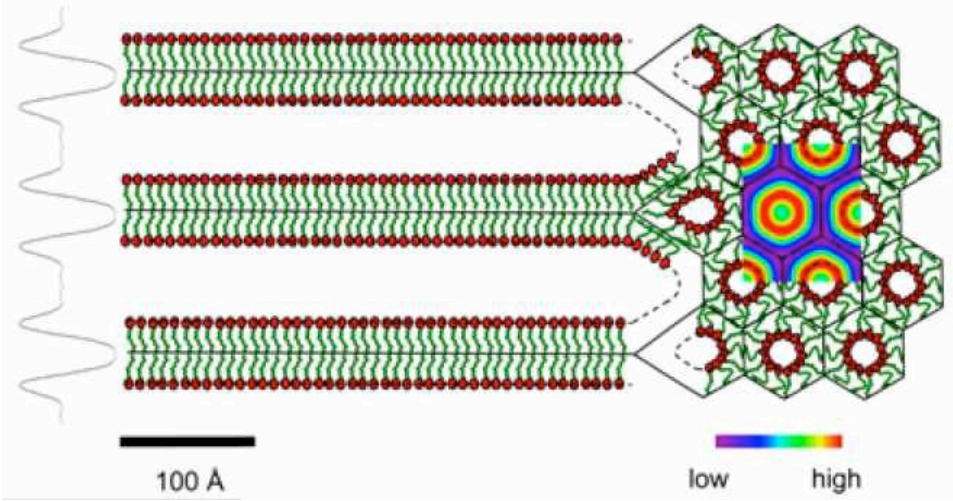

Figure 2. Interface reconstruction involving the L_α and the H_2 phases. For clarity, lipid molecules are superimposed to the outlined locations of the polar interfaces dashed lines and the methyl trough regions (full lines). The epitaxial relationship found for the L_α-H_2 phase transition of the fully hydrated EA/ME-based system at the R_{WT} value of 0.3 at 28.5 °C. The electron density profile of the L_α phase (d = 104.4 Å) is displayed on the left, and the electron density map of the H_2 phase is shown on the right (a value of 60.3 Å).

References:

[1] A. Yaghmur, B. Sartori and M. Rappolt; Self-assembled nanostructures of fully hydrated monoelaidin-elaidic acid and monoelaidin-oleic acid systems; Langmuir **28**, 10105-10119 (2012)

[2] A. Yaghmur, P. Laggner, M. Almgren and M. Rappolt; Self-assembly in monoelaidin aqueous dispersions: direct vesicles to cubosomes transition; PloS ONE **3**, e3747 (2008)

[3] M. Rappolt, G. M. Di Gregorio, M. Almgren, H. Amenitsch, G. Pabst, P. Laggner and P. Mariani; Non-equilibrium formation of the cubic Pn3m phase in a monoolein/water system; Europhys. Lett. **75**, 267-273 (2006)

[4] S. S. Funari, F. Barcelo and P. V. Escriba; Effects of oleic acid and its congeners, elaidic and stearic acids, on the structural properties of phosphatidylethanolamine membranes; J. Lipid Res. **44**, 567-575 (2003)

IN SITU CHARACTERIZATION OF LIPIDIC BUPIVACAINE-LOADED FORMULATIONS

A. Yaghmur[1], S. Weng Larsen[1], M. Schmitt[2,3], J. Østergaard[1], C. Larsen[1], H. Jensen[1], A. Urtti[2] and M. Rappolt[4]

1.) Department of Pharmacy, Faculty of Health and Medical Sciences, University of Copenhagen, Universitetsparken 2, DK-2100 Copenhagen, Denmark
2.) Centre for Drug Research, University of Helsinki, Finland
3.) Division of Biopharmacy and Pharmacokinetics, University of Helsinki, Finland
4.) Institute of Biophysics and Nanosystems Research (IBN), Austrian Academy of Sciences, Graz, Austria

Prolonged controlled release of drugs from safe, biocompatible, and efficient drug delivery systems remains a major challenge in the design of injectable formulations. An interesting approach concerns the application of *low-viscous* stimulus-responsive precursors for the *in-situ* formation of *high-viscous* drug-loaded lyotropic non-lamellar liquid crystalline phases. After injection, the *in situ* formation of non-lamellar phases is attained *via* the self-assembly of the lipids in response to the biological environmental stimuli. The most interesting aspect of these sustained release drug depots is their stability upon exposure to excess water (the dilution effect) or to biological fluids. This study was designed to improve the fundamental understanding of the observed dynamic structural transitions as *low-viscous* water-containing precursors of inverted type micellar solution (L_2) or an isotropic hexagonal (H_2) phase are exposed to excess water under simulated body fluid environmental conditions at 37 °C. To determine such structural events *in situ*, a combination of synchrotron SAXS with remote controlled addition of buffer was used. As model drug compound, the free base form of the local anaesthetic bupivacaine (BUP) was chosen.

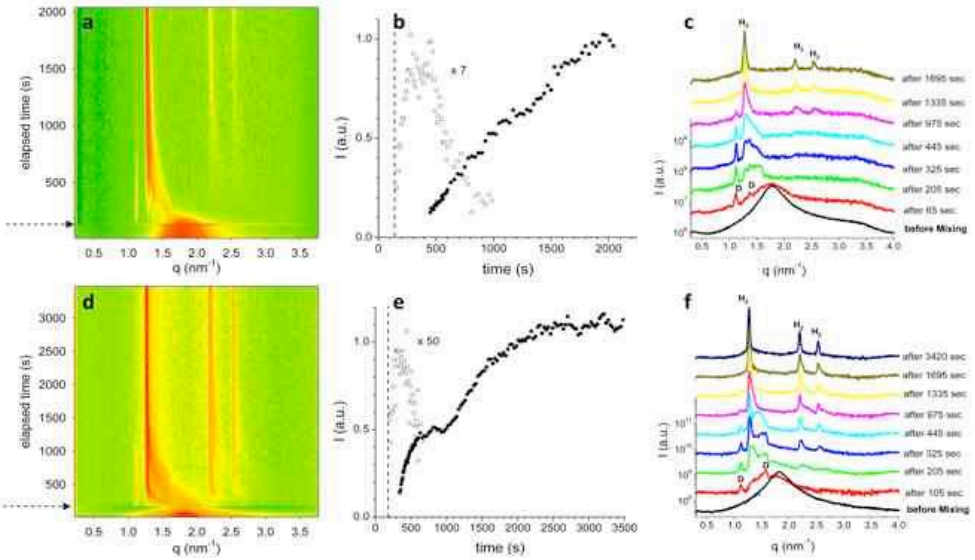

Figure 1. Fast structural transitions observed upon the addition of PBS 7.4 to 2 different precursors (BUP-loaded L_2 phases containing 5 wt% buffer). In panels (a) and (d), the contour plots clearly display the hydration-triggered formation of cubic and inverse hexagonal phases (dashed arrows mark the arrival of the water front). The temporal evolution of the Pn3m cubic (□) and H_2 phases (●) are plotted in (b) and (e) (dashed lines indicate the arrival of the water front). Panels (c) and (f) show selected SAXS patterns of all appearing phases at different elapsed times. The two Bragg reflections of the intermediate cubic phase are marked with "D" and those of the inverted hexagonal phase with "H_2".

The dynamic behaviour of the studied BUP-loaded systems is illustrated in Figure 1. First, we describe the time-resolved SAXS experiments performed on two different L_2 phase precursors (containing 5 wt% buffer). The preformulations were formed with PBS 7.4 (precursor A, see panels a-c) and with PBS 6.0 (precursor B, see panels d-f), respectively. By injecting PBS 7.4 to the L_2 solutions, phase transitions to non-lamellar phases occur, which take place within a few hundred seconds. It is apparent that this hydration stimulus causes significant changes in the structure. The obtained SAXS data reveal though that both precursors A and B respond in a similar manner. As shown in Figures 1a and 1d, initially the L_2 phase is observed - typically characterized by SAXS pattern with a single broad peak at around q = 1.75 nm^{-1} (corresponding characteristic distance of 3.59 nm) – followed by a rapid water-uptake as soon as the phosphate buffer reaches the sample. In both cases, an intermediate bicontinuous cubic phase with Pn3m symmetry (diamond type, D) forms, followed by the appearance of the neat H_2 phase. In Figures 1b and 1e, the formation of these structures is monitored by the most intense Bragg peak of each respective phase. After a lag time of 2-3 minutes, which is typically the time required for the water front to diffuse to the observed sample patch (see the dashed vertical lines), first the cubic phase appears for a period of about 800 sec. Once the cubic phase is vanished, the H_2 phase fully develops and reaches its maximum hydration about 100 sec later. From 1000 sec onwards, the H_2 phase becomes more and more ordered (see the corresponding increase in the intensity), while the hydrational state hardly changes. Representative diffraction pattern examples demonstrating these drastic structural alterations at different elapsed times are presented in Figures 1c and 1f. The basic distinguishing features of the SAXS patterns are the following: within the first few seconds, the system is still mainly composed of L_2 phase, but additional peaks are observed at lower q-values indicating the formation of an intermediate phase coexisting with the L_2 phase. The two strongest reflections of the intermediate phase are marked with "D" and appear at q-values of 1.13 and 1.38 nm^{-1}, respectively. An additional very weak peak is detected at about 1.63 nm^{-1}. It is most likely that these observed peaks indicate the formation of a cubic structure as they are compatible with the reflections (110), (111), and (200) of bicontinuous Pn3m phase with a lattice parameter, a, of 7.86 nm. The first traces of the H_2 phase are visible at about 200-300 sec. In both investigations, the observed H_2 phase has almost identical peak positions and therefore the same corresponding lattice parameter, a, of 5.71 nm. When studying the formation of these particular non-lamellar phases *in situ*, it is important to compare the obtained results with the corresponding static investigations carried out on the same systems, but under experimental equilibrium conditions of full hydration. Only then, we may (i) predict the approximated water swelling speed in these low-water containing preformulations, (ii) understand the involved structural mechanism until having the final fully hydrated structural form, (iii) provide important information on their stability, and (iv) possibly also gain insight into their structure-property relationship. Loading the GMO-based system with BUP induces significant impact on the fully hydrated structure. For R equal 0.06 (R is the solubilised drug to lipid weight ratio), the SAXS pattern taken from the sample prepared with PBS 7.4 indicates the formation of H_2 phase with a lattice parameter value of 5.71 nm; whereas the coexistence of the two phases: the cubic Pn3m (lattice parameter of 7.92 nm) and the H_2 phases (lattice parameter of 5.75 nm) occurs when PBS 7.4 is replaced by PBS 6.0. In order to obtain a fully hydrated sample formed from the precursor B, similar conditions to those given in our injection experiments were applied, i.e. PBS 7.4 was added to a small sample portion of precursor B and the obtained final pH value of the excess buffer was 7.1. Under equilibrium conditions, an identical H_2 phase with almost the same lattice parameter was observed (data not shown). It is interesting to note that the obtained results presented in Figure 1 reveal a relatively fast rearrangement of the lipid and solubilized BUP molecules in excess PBS 7.4

since the H_2 structure in both experiments approaches within about 1000 sec that of the corresponding equilibrated full hydrated systems

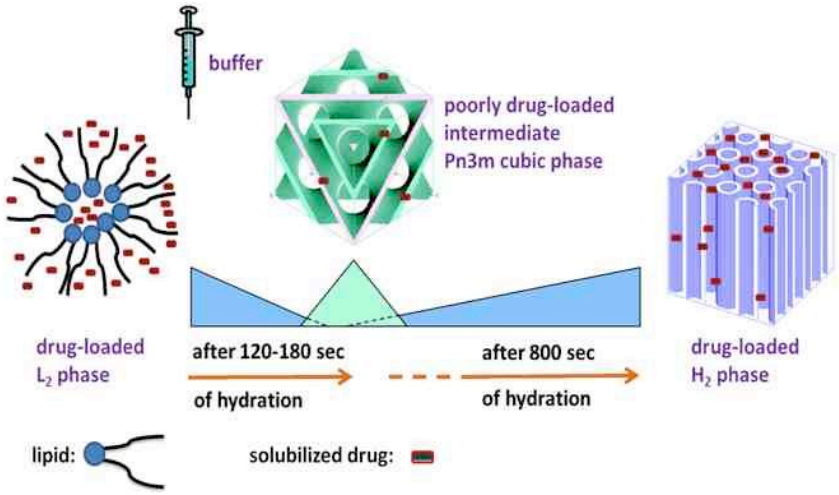

Scheme 1. *In situ* characterization of lipidic bupivacaine-loaded formulations.

The structural mechanism and the possible transition pathways to approach the full hydration and equilibrium conditions are highlighted for the two different precursors [1]. Most strikingly, none of the observed H_2 phase transitions from the self-assembled preformulations are explainable by a simple one-step mechanism, but always an intermediate Pn3m phase forms (Scheme 1). This means that the initial lipid hydration step in these preformulations proceeds at least to some extent the re-distribution of BUP molecules between the polar interface and the hydrophobic regions (the lipid tails and the interstitial areas), i.e. BUP-poor Pn3m phase domains coexist with BUP-rich H_2 phase domains. Interestingly, these Janus-faced – hydrophilic and hydrophobic – rearrangements proceed the fastest utilizing the L_2-phase precursors as they lead to the formation of viscous depots suitable for sustaining drug release. In order to mimic the drug release and transport from these *in situ* formed self-assembled systems after subcutaneous administration, BUP release experiments were also performed by using the rotating dialysis cell model. BUP release rates followed first order kinetics with. The results suggest also that the variations in the lipidic partition coefficient, $K_{l/w}$, between the liquid crystalline nanostructures and the phosphate buffer solution are significantly affecting BUP release rates upon changing pH. This pH sensitivity is consistent with the obtained SAXS data

References:

[1] A. Yaghmur, S. Weng Larsen, M. Schmitt, J. Østergaard, C. Larsen, H. Jensen, A. Urtti and M. Rappolt; *In situ* characterization of lipidic bupivacaine-loaded formulations; Soft Matter **7**, 8291-8295 (2011)

Chemistry

GROWTH OF POUROUS AGGREGATES DURING TEMPLATE DIRECTED SAPO34 ZEOLITE SYNTHESIS

L. Bonaccorsi[1], P. Calandra[2], H. Amenitsch[3], E. Proverbio[1] and D. Lombardo[2]

1.) Dipartimento di Chimica Industriale e Ingegneria dei Materiali, Università di Messina, Salita Sperone, 31. Agata (Messina), Italy
2.) CNR-IPCF, Istituto per i Processi Chimico Fisici - (Sez. Messina) Viale F. Stagno D'Alcontres, 37. Messina, Italy
3.) Institute of Biophysics and Nanosystems Research, Austrian Academy of Sciences, Schmiedlstr. 6, Graz, Austria

The formation of nanoparticles of zeolite Sapo-34 grown on a amine terminated polyamidoamine (PAMAM) dendrimer has been investigated by means of the small angle x-ray scattering (SAXS) technique performed at the SAXS Beamline at the Elettra Synchrotron Radiation Facility. Sapo-34 zeolites, in general, are obtained by a hydrothermal synthesis in presence of a tetraethylammonium hydroxide (TEAOH) template which acts as a structure-directing agent and which is responsible for the final porosity. Among the templates of SAPO-34, in fact, TEAOH has become well-known as it gives rise to good catalytic properties for various reactions. More specifically we observe that the addition of a dendrimer template, in place of the traditional tetraethylammonium hydroxide (TEAOH) template, to the synthesis environment modified the crystallites aggregation with a strong influence on the long-range assembly conditions for the zeolite growth. In order to obtain direct information of the morphological features of the generated aggregates during nanoparticles formation the SAXS measurements have been performed 10 minutes after the mixing of the main reactants in the presence of the water solution of generation G4 PAMAM dendrimers [1] at the concentration of c=4 wt%.

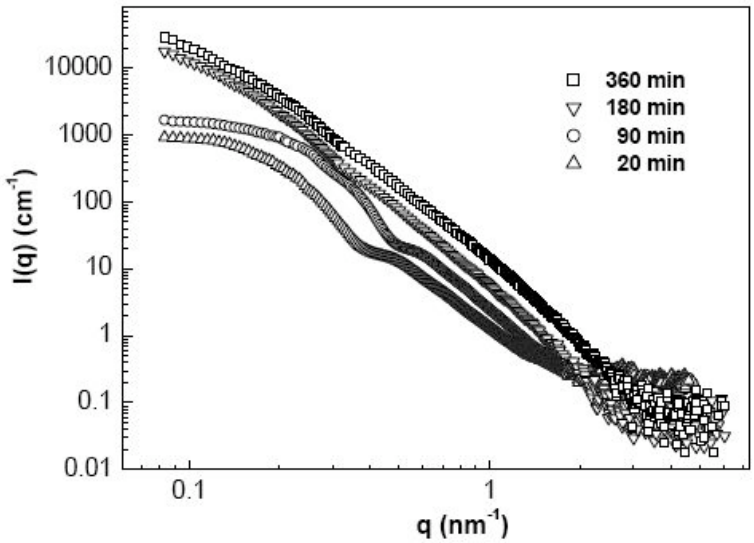

Figure 1A. Evolution of the SAXS intensity profile of G4 poliamidoamine dendrimers (at the water concentration of C=4 wt%) in presence of the mother liquor for the Sapo-34 zeolite synthesis. SAXS profiles at different elapsed time after the mixing (from 20 min up to 360 min) has been recorded at the synthesis temperature of T=40°C

Figure 1A shows the SAXS intensity profile for the G4 Pamam dendrimers in water solution at different elapsed times after the mixing (from 20 min up to 360 min) at the synthesis temperature of T=40°C. Preliminary data analysis evidences a core-shell conformation of the Form Factor (for SAXS spectra up to 90 min.) that is compatible with the growth of the

zeolite phase on the dendrimers surface. As a consequence the long range electrostatic repulsion of the dendrimer amine endgroups, which are responsible of the templating action, is attenuated as the zeolite components begin to condense on them. This cause a rapid dendrimer coalescence with the formation of aggregates. A log-log plot of the last two SAXS spectra of figure 1 (i.e. after the elapsed time of 180 and 360 min. respectively) evidences the presence of a linear region that can be connected with the fractal nature of the generated aggregates.

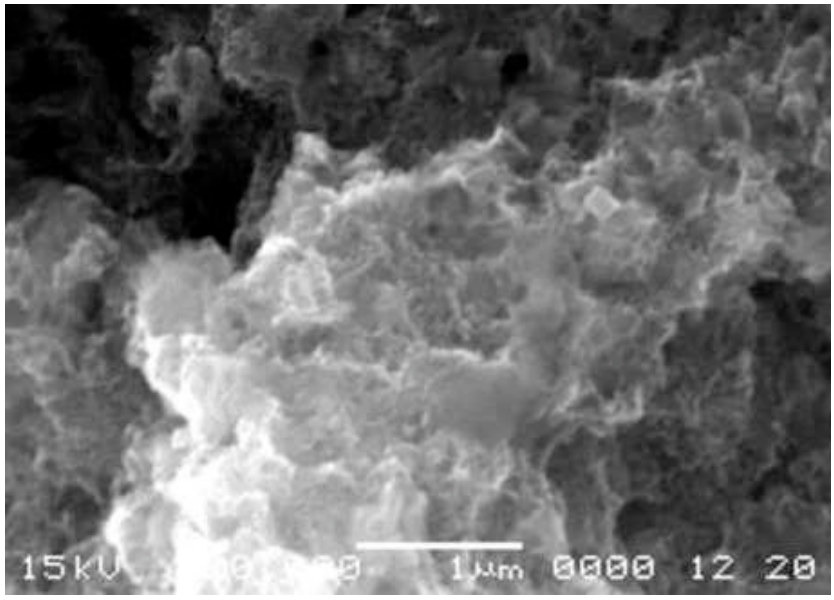

Figure 1B. Scanning electron microscopy images of the generated porous aggregates during the dendrimer template directed sapo-34 zeolite synthesis.

The formationof pourous aggregates during the dendrimer template directed sapo-34 zeolite synthesis is confirmed by scanning electron microscopy experiments (Figure 1B).
The use of the dendrimer template seems to be an interesting possibility in substitution of the traditional tetraethylammonium hydroxide template. The benefits of using a dendrimer nano-template for the nanoparticles formation process in zeolite syntheses rely mainly on the possibility to choice size and composition of the core substrate that means driving size and morphology of the condensed surface structures by changing number and typology as well as spatial distribution of the dendrimer terminal groups. The finding of our results may open new perspectives in the synthesis of organic-inorganic nanostructured materials based on mesoporous frameworks with new characteristics and properties [2-3].

References:

[1] D. Lombardo; Liquid-like Ordering of Negatively Charged Poly(amidoamine) (PAMAM) Dendrimers in Solution. Langmuir **25** 3271-3275 (2009)
[2] L. Bonaccorsi, D. Lombardo, A. Longo, E. Proverbio, A. Triolo; Dendrimer Template Directed Self-Assembly during Zeolite Formation; Macromolecules **42**, 1239-1243 (2009)
[3] D. Lombardo, L. Bonaccorsi, A. Longo, E. Proverbio, P. Calandra; Charge interaction of low generation dendrimers during zeolite formation; Journal of Non-Crystalline Solids **357**, 771–774 (2011)

COBALT FERRITE NANOPOROUS SPHERES THROUGH NORMAL MICELLES ROUTES

G. Campi[1], C. Cannas[2] and L. Suber[3]

1.) CNR- Istituto di Cristallografia, Via Salaria, Km 29.300, Monterotondo (RM), I-00015, Italy
2.) Dipartimento di Scienze Chimiche, Università di Cagliari, Cagliari, 09042, Italy
3.) CNR- Istituto di Struttura della Materia, Via Salaria, Km 29.300, Monterotondo (RM), I-00015, Italy

Magnetic nanoparticles with high magnetization values have found a wide range of biomedical applications, both in vivo and in vitro, (e.g., drug targeting, hyperthermia, and magnetic separation) and are also used for diagnostic purposes, e.g., enhancing the contrast of magnet resonance image. Although magnetic particles with a narrow size distribution have been synthesized through various methods, the products are overwhelmingly dominated by particles smaller than 30 nm. However, for many purposes, it is preferable to fabricate larger nanoparticle assemblies of about 100 nm, because they can be easily moved by an ordinary external magnetic device. It is therefore an interesting challenge to develop approaches to assembling magnetic nanoparticles with suitable sizes (from 30 to 100 nm) and morphology without compromising the surface area, in order to meet the special need of biomedical fields. Up to now, several methods have been developed to fabricate various superstructures from primary nanoparticles, among which, in particular, a number of methods are based on surfactant assisted strategy. In these methodologies, primary nanoparticles self-assemble through noncovalent interactions, creating a secondary architecture whose properties greatly depend on their building blocks. In this context, we have studied the kinetic of the formation and growth of the primary cobalt ferrite nanoparticles as well as their aggregation process, by in situ and time resolved SAXS measurements.

$CoFe_2O_4$ nanoparticles have been synthesized through the formation of normal micelles using sodium dodecyl sulfate (SDS) as surfactant [1-3] with the following steps:

1. aqueous solutions of $CoCl_2$ and $FeCl_2$ in a 1:2 molar ratio have been added in aqueous solutions of SDS in a glass flask and stirred constantly, for 30 min. This solution has been kept in a bath, at 80 °C, in constant mechanical stirring;

2. methylamine solution, heated at the same temperature, has been added. The dark slurry is stirred for 3 h. After the introduction of methylamine, the solution became green, and after a few minutes, the colour changes to dark brown.

The reaction was monitored in a glass flask included in a thermostated batch reactor apparatus; a remote controlled syringe allowed us to add 10 ml of methylamine aqueous solution into the reaction solution and a peristaltic pump continuously flowed the solution mixture in a 1.0 quartz capillary through a closed circuit. We set the camera to a sample detector distance of 1.0 m and operated at photon energy of 8 KeV covering the q range between 0.07 and 3.4 nm^{-1}. Time resolved, in situ measurements, were performed using a Pilatus as detector with a time resolution of 5 sec. Water flowing was also measured in order to asses and subtract the background from the data. The resulting two-dimensional images were integrated to obtain 1d pattern of normalized intensity versus scattering vector q.

SAXS patterns collected during the step 1) are shown in Fig.1; we can observe the formation of SDS and Me(DS)n micelles.

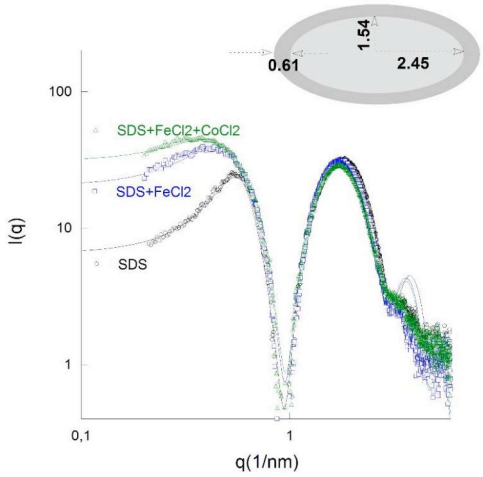

Figure 1. SDS particles in acqueous solution have been modeled with core-shell ellipsoids; the structure factor *S(q)* for charged micelles has been calculated using rescaled mean spherical approximation (RMSA).

After the introduction of methylamine, in the step 2), we observed the SAXS intensity, I, evolving with the formation of $CoFe_2O_4$ primary nanoparticles and their aggregation in larger nanoporous spheres (see Fig. 2), given by

$$I = I_{SDS} + I_{IP} + \sum_{i=1}^{i=2} I_i \tag{1}$$

I_{SDS} is associated with the SDS and Me(DS)n micelles; I_{IP} represents a like-lamellar phase composed by large hexagonal flat particles as indicated by the cryo-TEM images shown in Fig 2A and 2B. This intermediate phase has been modelled as a lorentzian peak and seems to organize and ruling the nucleation and aggregation of primary particles, providing the nucleation sites on the hexagon vertices (inset of Fig. 2B). Primary particles and spherical aggregates have been modelled as 2 sphere populations, I_i

$$I_i(q) = N(i)S(q,R_{HS}(i),f_p(i),?(i))\int_0^{\infty} P(i)_{Schultz-Zimm}(q,R)\left[f_{sphere}(q,R)\right]^2 dR \tag{2}$$

with i=1, 2 and where $N(i)$ is the particles number in the i population with radius R; in order to account for the polydispersivity of the particles, the intensity has been integrated over a *Schutz-Zimm* distribution of R, $P(q,R)$ for each population. Finally, the primary particle interference effects have been modelled in the monodisperse approximation of sticky hard spheres with radius R_{HS} and volume fraction f_p. A typical fit with all the included contributes of eq. 1 are shown in Fig. 3. In Fig. 2C we show the SAXS patterns at the equilibrium, indicating the presence in the solution of nanoporous sphere (size ~ 25nm), shown in the TEM image of the inset, composed through the aggregation of primary particle with size of about 3.5 nm.

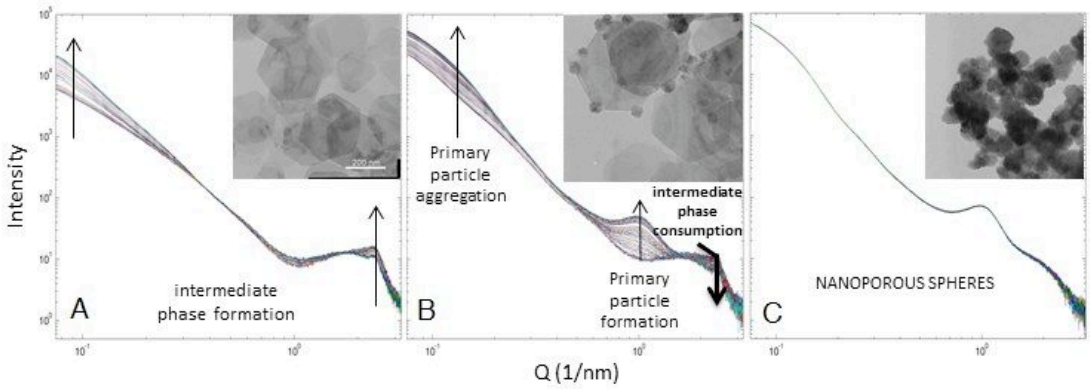

Figure 2. After ammine addition, alongside the [SDS+salt] ellipsoids we observe the following processes: A) formation of an intermediate phase composed by large flat hexagonal particles; B) primary particles nucleate and aggregate on the hexagon vertices; C) consumption of the intermediate phase with the formation of final nanoporous spheres.

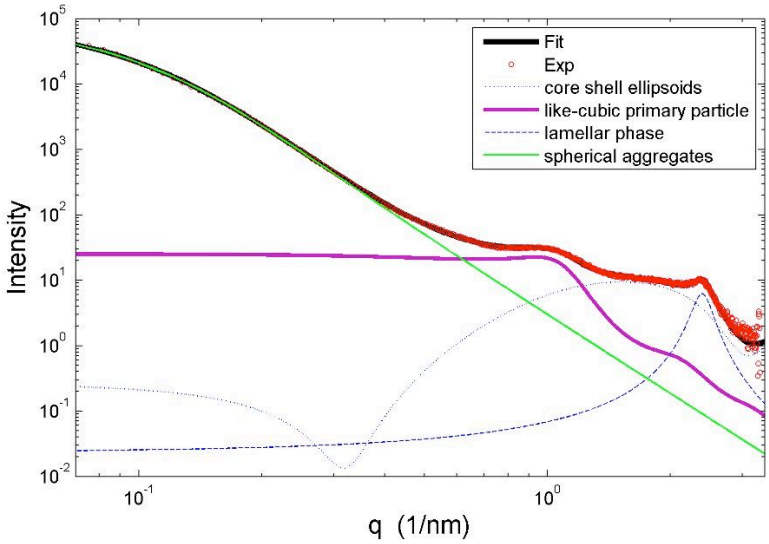

Figure 3. Typical fit of a SAXS pattern collected during the particle formation, obtained by the indicated contributes: core shell SDS + Me(DS)n ellipsoids, primary particles modeled as polydispersed hard sticky spheres, lamellar phase modelled by a lorentzian peak and spherical aggregates.

Further work is required to get deeper insight relative to the nature and evolution of the intermediate phase, as it appears to play a fundamental role in particle formation mechanism. Thus, the results are expected to give a contribution on nanoparticle formation and aggregation mechanisms important for fundamental studies as well as possible applications in nanotechnology.

References:

[1] Feltin, N.; Pileni, M. P. *Langmuir*, **13**, 3927 (1997)
[2] Vestal, C. R.; Zhang, Z. J. *Int. J. Nanotechnol.*, **1**, 240 (2004)
[3] C. Cannas, A. Ardu, D. Peddis, C. Sangregorio, G. Piccaluga, A. Musinu, *Journal of Colloid and Interface Science* **343**, 415–422 (2010)

IN-SITU SAXS/WAXS STUDY OF THE DEVELOPING PROCESS OF GEOPOLYMER STRUCTURES

D. Jozić[1,2] and S. Bernstorff[2]

[1] University of Split, Faculty of Chemistry and Technology, Department of Inorganic Technology, Teslina 10/V, HR-21000 Split, Croatia

[2] Sincrotrone Trieste S.C.p.A., Strada Statale 14, km 163.5 in AREA Science Park, I-34149 Basovizza, Trieste, Italy

Geopolymers, also called polysilates, are amorphous to semi-crystalline three-dimensional alumosilicate polymers. They are also referred to as alkali-activated alumosilicate binders and comprise three classes of inorganic polymers that, depending on the silica to alumina ratio, are based on the following three different monomeric units: (-Si-O-Al-O-) polysilate (PS), $SiO_2/Al_2O_3=2$; (-Si-O-Al-O-Si-O-) polysilatesiloxo (PSS), $SiO_2/Al_2O_3=4$; and (-Si-OAl-O-Si-O-Si-O-) polysilatedisiloxo (PSDS), $SiO_2/Al_2O_3=6$ [1].

Geopolymers have been prepared by mixing powder of metakaoline, alkaline activator solution and water. The sample series D1 was prepared from a suspension composed to satisfy the concentration of sodium hydroxide (c(NaOH)= 9.85 mol/dm^3) and the ratios of SiO_2 / Al_2O_3 = 3.31, Na_2O / Al_2O_3 = 0.90, Na_2O / SiO_2 = 0.27 and H_2O / Na_2O = 5.44. The series D14 was prepared from a suspension composed to satisfy the concentration of sodium hydroxide (c(NaOH)=10.31 mol/dm^3) and the ratio of SiO_2 / Al_2O_3 = 4.13, Na_2O / Al_2O_3 = 1.72, Na_2O / SiO_2 = 0.42 and H_2O / Na_2O = 5.10.

Insitu time resolved SAXS/WAXS measurements [2] have been performed at the Austrian SAXS beamline at the Sincrotrone Trieste. The sample to detector distance has been 2082 mm and the used photon energy 8 keV (λ=1.5 Å). The SAXS and WAXS data have been collected simultaneously by a MAR300 Image Plate and a Pilatus 100k detector, respectively. The exposition time for the SAXS signal was 1-2 seconds and for WAXS 10 seconds.

The obtained WAXS results are shown in Figure 1 for the two series denoted as D1 and D14. In the same figure are presented the WAXS pattern of metakaoline (MK750). The WAXS pattern of the sample denoted as MK750 is characterized by a very diffuse diffraction maximum centred at 2Theta 24.3^o which arises from amorphous alumosilicate. A second diffuse diffraction maximum which belongs to the product of geopolymerization is centred at 29.4^o (in the series D1) and 30.6^o (in the series D14).

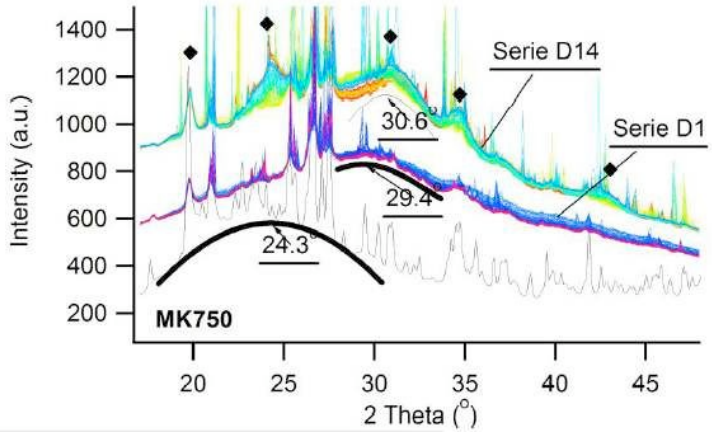

Figure 1. WAXS patterns of the geopolymers series denoted as D1 and D14, prepared at 70^{o}C (with up to 12 hours of geopolymerization). The black line shows the WAXS pattern of metakaoline, and the peaks marked with ♦ are characteristic for Sodalite (PDF 037-0476)

The different positions of the diffuse diffraction maxima indicate different structural arrangements for the series D1 and D14. Another difference in the WAXS pattern is that only the D14 series shows in addition to the dominant diffuse diffraction maximum at 2Theta =30.6^{o} another three correlated diffuse diffraction maximums at the positions 2Theta=24.2^{o}, 34.9^{o}, 42.9^{o}. The positions of these diffraction peaks suggest the presence of structural forms, which are isostructural with the sodalite crystal form (empirical formula $Na_4Al_3Si_3O_{12}Cl$).
These scattering curves were analysed in terms of fractals with the following relation:

$$I(q) \sim \frac{d\Sigma}{d\Omega}(q) = C \cdot q^{-\alpha} \tag{3}$$

where C is the Pareto constant (for the fractal region), and α is the slope of the scattering curve in the log-log plot of the intensity I(q) versus q. The magnitude of the exponent α is directly related to the value of D. The value of the exponent alpha in (3) allows us to distinguish whether there are volume (D_v = α, 2 < α < 3) or surface (D_s = 6-α, 3 <α <4) fractals, respectively [3-5]. The analysis of the SAXS scattering curves indicates two areas that correspond to two different surface fractals dimensions, in both series D1 and D14. For the series D1, the characteristic of q-value ranges for the two fractal dimensions are denoted as A1 ($0.10 \leq q \leq 0.20$ nm^{-1}) and A2 ($0.34 \leq q \leq 0.64$ nm^{-1}) in Figure 2. The change of the fractal dimensions in dependence of the reaction time indicates that a major change of the fractal dimension has happened in the early phase of the geopolymerization process (up to 4 hours), while after this period the fractal dimensions remain almost constant. The final values for the fractal dimensions D_s(A1) = 2.4 and D_s(A2) = 2.2.

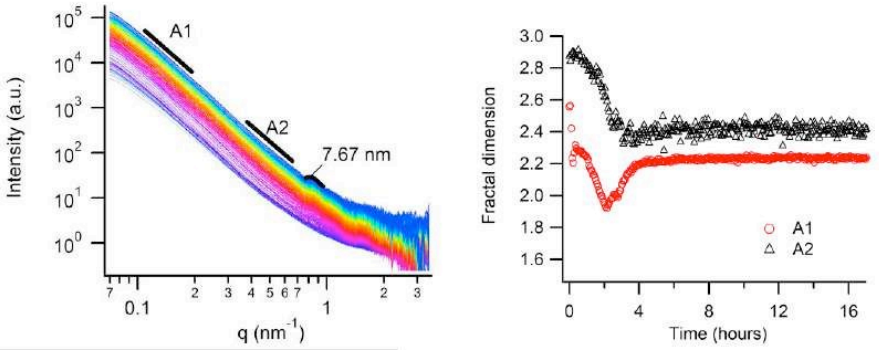

Figure 2. SAXS curves (left), and fractal dimensions in the range of A1 and A2 (right) in dependence of the geopolymerization time for the series D1

In Figure 3 are shown the SAXS curves of the series D14: the first fractal denoted as B1 appears in the region $0.09 \leq q \leq 0.18$ nm^{-1} and the second fractal denoted as B2 in the region $0.36 \leq q \leq 0.80$ nm^{-1}. Compared to series D1, the series D14 shows much more fluctuations of the fractal dimension, and has a longer period of the geopolymerization process (up to 11 hours). The final value of the fractal dimensions are D_s(B1)=2.8 and D_s(B2)=2.3. The SAXS curves show further, that after 8 hours starts to appear a new phase at the position d=7.67nm (series D1), and d=7.32 and 6.42 nm in series D14.

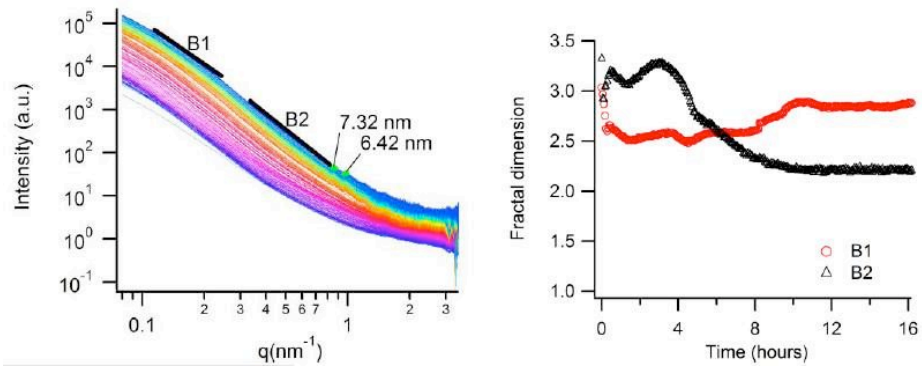

Figure 3. SAXS curves (left), and fractal dimensions in the range of B1 and B2 (right) in dependence of the geopolymerization time for the series D14

References:

[1] Davidovits J. Geopolymers: "Inorganic polymeric new materials", *Journal of Thermal Analysis*, **37**, pp. 1633-1656 (1991)

[2] Dražan Jozić, Siniša Zorica, Darko Tibljaš, Sigrid Bernstorff, "Insitu SAXS/WAXS study of the developing process of geopolymer structures", Proceedings of the 15th European conference on "composite materials" (ECCM15), pp. 2481-1 to 2481-8 (2012)

[3] Malekani K., Rice J. A., Lin J.-S., "Comparison Of Techniques For Determining The Fractal Dimensions Of Clay Minerals", *Clays and Clay Minerals,* **44**, pp. 677-685, (1996)

[4] T. Ficker, A. Len, P. Nêmec, "Notes on hydrates cement fractals investigation by SANS", *Journal of Physics D: Applied Physics*, **40**, pp. 4055-4059 (2007)

[5] Aldo F. Craievich, "SAXS Study of the Porous Fractal Structure of Tricalcium Silicate Dry Gels", *Journal of Applied Crystallography*, **20**, pp. 327-329 (1987)

SAXS STUDY ON POLY(ETHYLENE OXIDE)/LITHIUM AND SODIUM MONTMORILLONITE COMPOSITES

D. Jozić[1], M. Erceg[1], S. Perinović[1] and S. Bernstorff[2]

1.) University of Split, Faculty of Chemistry and Technology, Telina 10/V, 21000 Split, Croatia
2.) Sincrotrone Trieste S.C.p.A., Strada Statale 14 - km 163.5, in AREA Science Park, I-34149 Basovizza, Trieste, Italy

Nowadays, lithium ion batteries are lighter, smaller and cheaper per energy unit than other kinds of batteries. But since they use liquid organic solvents as electrolyte, safety and ecological issues can arise. Therefore, manufacturers are turning to technologies where the liquid electrolyte is replaced with solid polymer electrolyte (SPE), i.e. to lithium polymer batteries. Most lithium polymer batteries on the market today require some fluoropolymers in the matrix which are expensive and difficult to create. Biodegradable poly(ethylene oxide) PEO as SPE has many advantages over its liquid counterparts due to the ease of processing, stable electrochemical characteristics and excellent mechanical properties.[1] However, the high crystallinity of PEO limits the lithium ion transport resulting in a poor ionic conductivity of the PEO electrolytes at room temperature (usually lower than 10^{-6} Scm^{-1}). The incorporation of inorganic nanophases such as nanoclays in the PEO matrix may be used to reduce the crystallinity of PEO. This investigation is focused on the preparation and characterization of PEO nanocomposites with lithium and sodium montmorillonite (LiMMT and NaMMT) as nanoclay in order to establish the influence of LiMMT and NaMMT on the developed composite structure as well as the crystallinity, thermal stability, thermal degradation and kinetics of the thermal degradation of PEO.

PEO/LiMMT and PEO/NaMMT composites with compositions 100/0, 95/5, 90/10, 85/15, 80/20, 75/25, 70/30, 65/35, 60/40, 55/45, 50/50, 45/55, 40/60, 35/65, 30/70, 25/75, 20/80, 15/85, 10/90, 5/95 and 0/100 by weight (where 100/0 represents the mass.% of pure PEO and 0/100 the mass.% of pure LiMMT or NaMMT) were prepared. Melt intercalation was performed at 90°C for 8 hours in a vacuum oven. After 8 hours of intercalation, the samples were removed from the oven, cooled and stored in a desiccator at room temperature.

Small angle X-Ray scattering (SAXS) measurements have been performed at the Austrian SAXS beamline at the Sincrotrone Trieste. The sample to detector distance has been 1132 mm and the used photon energy 8 keV (λ=1.5 Å). The SAXS data have been collected by a MAR300 Image Plate. The exposition time for the SAXS signal was 1-2 seconds.

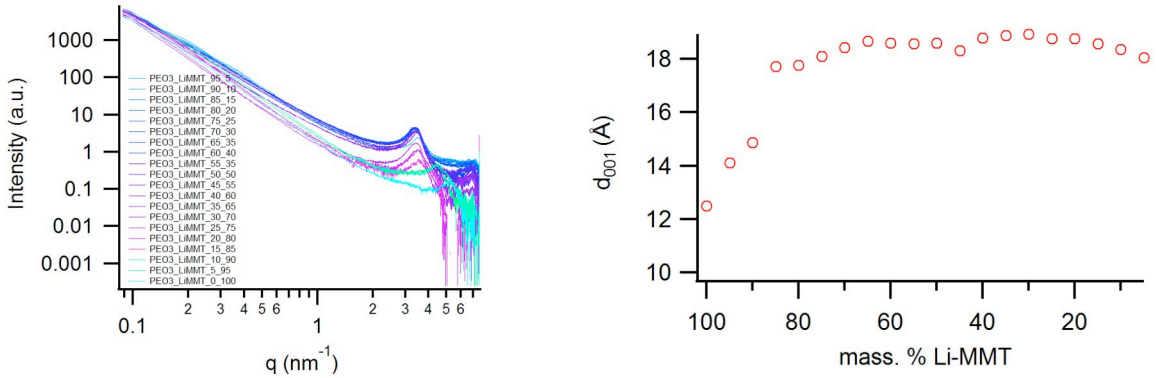

Figure 1. SAXS curves (left) and the corresponding d_{001} values (right) of PEO3-LiMMT composites

Figure 1 shows 1D-SAXS intensity patterns of pure PEO, LiMMT and PEO/LiMMT composite samples named PEO3_LiMMT_x_y (x-mass. % of the PEO and y-mass. % of the

LiMMT). The diffraction maximum which appears at q = 5.02 nm^{-1} in the pure LiMMT sample, is assigned to the interlayer distance for the crystal plane 001 (d_{001}=1.249 nm). In the experimental q range PEO doesn`t show any diffraction maximum. If PEO/LiMMT is formed as intercalation nanoncomposite, the size of the interlayer distance d_{001} of LiMMT increases. But when the process of exfoliation is dominant the structural order gets completely destroyed. A third possible case can be the combination of intercalation and aggregation where as product can appear the intercalated nanocomposite mixed with a sufficient amount of clays. From Figure 1 it becomes obvious that the position of the diffraction maximum (which arises from the plane 001 (d_{001})) shifts from q = 5.02 nm^{-1} (pure LiMMT) to the lower q=4.45 nm^{-1} value by a low addition of LiMMT (5 mass.%) into the PEO.. This shifting means that the interlayer alumosilicate distance increases from 1.249 nm to 1.410 nm. A further addition of LiMMT (above 5 mass.%) shifts the diffraction maximum to even lower q values, indicating that the distance between the layers of alumosilicate in the LiMMT structure in direction [001] increases from 1.249 nm (pure LiMMT) up to 1.893 nm (mixture with 30 mass.% of LiMMT and 70 mass.% of the PEO3).

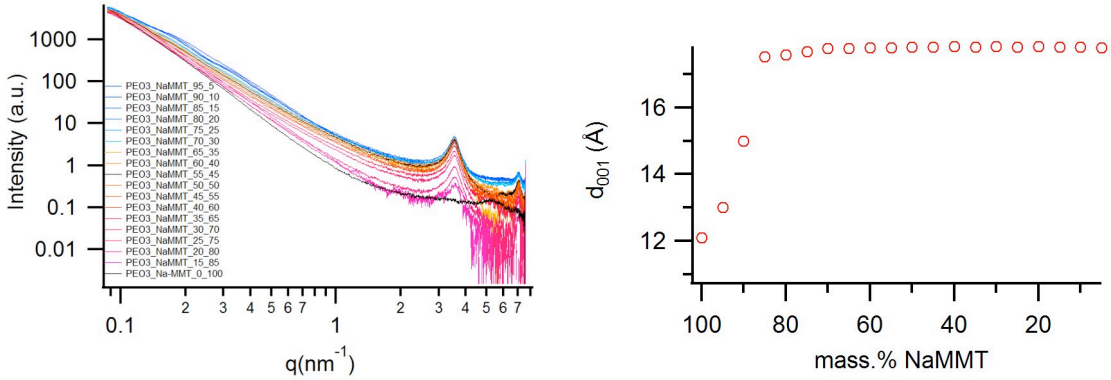

Figure 2. SAXS curves (left) and the corresponding d_{001} values (right) of composites PEO3-NaMMT

Figure 2 shows 1D-SAXS patterns of pure PEO, NaMMT and PEO/NaMMT composite samples named PEO3_NaMMT_x_y (x-mass.% of the PEO and y-mass. % of the NaMMT). The diffraction maximum which appears at q = 5.19 nm^{-1} in the pure NaMMT sample, is assigned to the interlayer distance for the crystal plane 001 (d_{001}=1.209 nm). From Figure 2 it becomes clear that the position of diffraction maximum shifts to lower values when a small amount of NaMMT (5 mass.%) is added into PEO. This shifting corresponds to an increase of the alumosilicate interlayer distance from 1.209 nm (pure NaMMT) to 1.310 nm. A further addition of NaMMT (above 5 mass.%) shifts the diffraction maximum to still lower q values indicating that the distance between the layers of alumosilicate in the NaMMT structure in direction [001] increases from 1.249 nm (pure NaMMT) to 1.827 nm (mixture with 20 mass.% of NaMMT and 80 mass.% of the PEO3).

Reference:

[1] E Quartarone, P. Mustarelli, A. Magistris; PEO-based composite polymer electrolytes; Solid State Ionics **110**, Issues 1–2, 1–141 (1998)

GISAXS INVESTIGATION OF MESOPOROUS SILICA AND TITANIA FILMS CONTAINING Fe_xO_y AND TiO_2 NANOPARTICLES

E. Leontidis[1], I. Andreou[1], H. Amenitsch[2]

1.) Department of Chemistry, University of Cyprus, Kallipoleos 75, 1678 Nicosia, Cyprus
2.) Institute of Biophysics and Nanosystems Research, Austrian Academy of Science, Schmiedlstrasse 6, 8042 Graz, Austria

In the last decade there has been strong scientific interest in the discovery of novel materials for photoelectrochemical applications involving solar radiation [1], with special emphasis on water-splitting for hydrogen production [1,2]. Much attention has been paid to oxide and non-oxide semiconductors as anodes in water-splitting photoelectrochemical cells [3,4]. Oriented films are particularly suitable as anodes, since they may allow more efficient electron transfer from the material-solution interface to the electrode. In the Elettra work we investigated the structure of such oriented films with SiO_2 and TiO_2 as basic materials. The films were prepared using Evaporation-Induced Self-Assembly (EISA) [5,6], which is a sol-gel method, combined with a dipping deposition method. The films were deposited on microscope glass, FTO and silicon substrates.

Two families of SiO_2 films were synthesized, using the pluronic block copolymer P123 and the cationic surfactant cetyl-trimethylammonium bromide CTAB as templates. We attempted to introduce Fe_xO_y and TiO_2 nanoparticles into both these types of films, using two alternative procedures. In one case the Fe^{III} precursor or small TiO_2 nanoparticles were introduced in the sol containing the silica precursor. Calcination of the deposited films was anticipated to yield Fe_xO_y or TiO_2 nanoparticles within the oriented mesoporous SiO_2 films. The second procedure was to use preformed, calcined SiO_2 films, impregnate them either with Fe^{III} or Ti^{IV} precursors and pass the films through a second calcination stage to prepare the oxide semiconductor nanoparticles. The structures of all these films were examined by GISAXS, and some were also measured with WAXS to examine the possible formation of populations of larger (on the surface) and smaller (in the pores of the films) nanoparticles. P123-templated films were found to have a 2D-hexagonal structure under the synthesis conditions used. The b-spacing of the hexagonal lattice (along the out-of-plane direction or the one perpendicular to the substrate) was equal to 196±5 Å before calcination and 132±6 Å after calcination, indicating an expected lattice contraction along the z-direction amounting to 33%. The lattice retained its hexagonal structure in the absence of nanoparticles. Attempts to introduce Fe^{III} precursors or TiO_2 nanoparticles in the synthesis sol led to remarkable changes in the GISAXS patterns (Figure 1 – left-side patterns). It appears that the structures become very disordered (in-plane structure is largely lost) and they exhibit a lamellar layering. Post-impregnation methods provide a satisfactory way for introduction of Fe_xO_y but not of TiO_2 nanoparticles in SiO_2 films.

The second family of SiO_2 films (built with CTAB as a template) were revealed by GISAXS to have a behavior similar to that of P123-based films. The pores of the films tend to be much smaller. The original P63/mmc hexagonal structure of the films before calcination [7] deteriorates dramatically upon calcination, with a z-axis contraction of 50%. This means that particles cannot be easily inserted or grow into the small pores of a damaged structure, hence the effects observed are smaller and the presence of Fe_xO_y or TiO_2 in the final structures much more difficult to detect. Post-impregnation methods in films with such small pores proved to be rather inefficient.

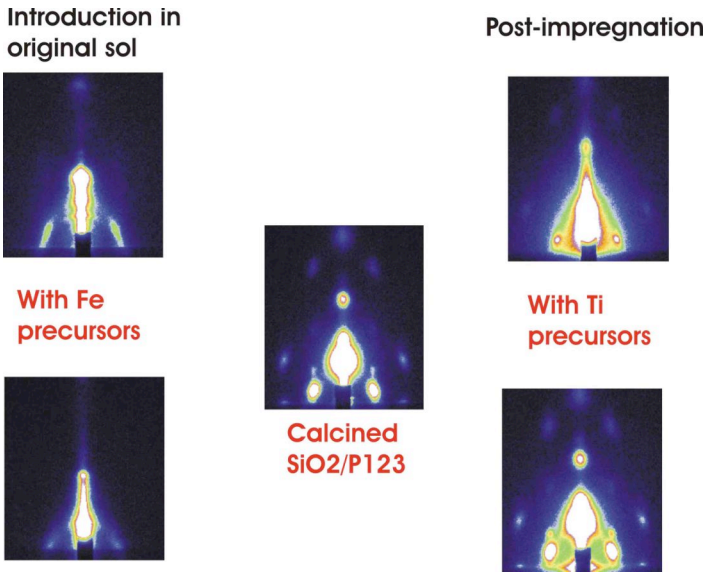

Figure 1. 2D-patterns from calcined films in the absence and presence of nanoparticles of Fe_xO_y or TiO_2. Q_x at the horizontal axis ranges from -1.2 to +1.2 nm^{-1}. Q_z at the vertical axis ranges from 0.6 to 2.9 nm^{-1}.

Two groups of TiO_2-based films were also examined. These were created using the pluronic block copolymers F127 or P123 as templates. The results for both groups are similar: Calcination of the films above 400 °C leads to extensive TiO_2 crystallization in the form of anatase. Little of the original structure remains, and it can be modeled as a strongly distorted cubic structure with a spacing of about 120 Å. Subsequent efforts to introduce Fe inside the films revealed again that the post-impregnation method is inefficient. Scattering at low Q_x can be understood as derived from surface-adsorbed particles and is quite strong in impregnated films (Figure 2). Evidence from various 1D-cuts supports the presence of Fe_xO_y particles when Fe is introduced in the sol stage.

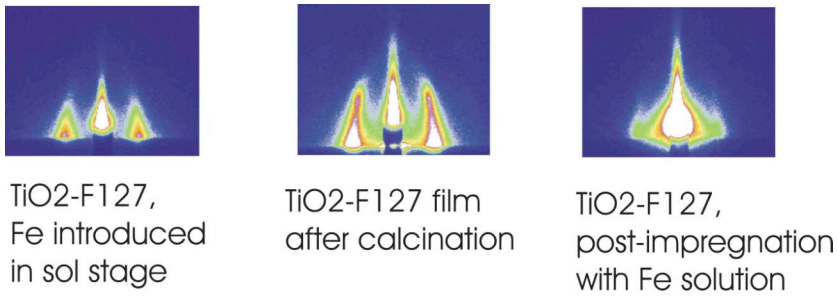

Figure 2. TiO_2-F127 films. 2D-patterns show that most of the in-plane structure is destroyed by calcination, and that post-impregnation likely creates surface deposits instead of allowing insertion of Fe_xO_y nanoparticles in the film pores.

References:

[1] P. V. Kamat, J. Phys. Chem.C, 111, 2834-2860 (2007)
[2] J. Zhu, and M. Zäch, Curr. Op. Colloid Int. Sci. 14, 260-269 (2009)
[3] K. Maeda, and K. Domen, J. Phys. Chem. 111, 7851-7861 (2007)
[4] F. E. Osterloh, Chem. Mater. 20, 35-54 (2008)
[5] C. J. Brinker, Y. Lu, A. Sellinger, H. Fan, Adv. Mater. 11, 579-585 (1999)
[6] D. Grosso, F. Cagnol, G. J. de A. A. Soler-Illia, E. L. Crepaldi, H. Amenitsch, A. Brunet-Bruneau, A. Bourgeois, and C. Sanchez, Adv. Funct. Mater. 14, 309-322 (2004)
[7] D. Grosso, A. R. Balkenende, P. A. Albouy, M. Lavergne, L. Mazerolles, and F. Babonneau, J. Mater. Chem. 10, 2085-2089 (2000)

CHARACTERIZATION OF WATER JET INSTABILITY IN THE PRESENCE OF ADDITIVES USING SAXS

B. Marmiroli, B. Sartori, F. Cacho-Nerin, H. Amenitsch

Institute of Biophysics and Nanosystem Research, Austrian Academy of Sciences, Schmiedlstraße 6, Graz, Austria

The breakup of liquid jets represents a wide area of research in the field of multiphase flows, fully justified by their wide presence both in industrial and in scientific applications [1]. Moreover, the recent development of microfluidic systems has raised great interest in understanding the flows in small spatial dimensions [2]. Such interest has been further increased due to the evolution of free electron lasers and the consequent need to develop new, high throughput techniques to characterize biological macromolecules [3, 4].
Recently, we have used synchrotron SAXS to obtain quantitative information on transient phenomenon dynamics of liquid jets. We have measured the signal of the liquid jet at increasing distance, therefore at increasing time, from the nozzle exit, by scanning SAXS imaging.
In this way, the time dependent morphology of the jet and its subsequent breakup time has been explored for jets of different diameters, nozzle geometry, flow rates. Different solvents (ethanol and isopropanol) have also been investigated.
Since surface tension is the driving force causing the jet instability, surfactants and additives play a critical role in the break-up processes and are routinely added to facilitate processing. In fact, laminar jets have been shown to be stabilized by the presence of surfactants, in either the dispersed or continuous phase [5]. Many studies have been conducted on surfactant but there is still lack of experimental data, especially not based on imaging techniques.

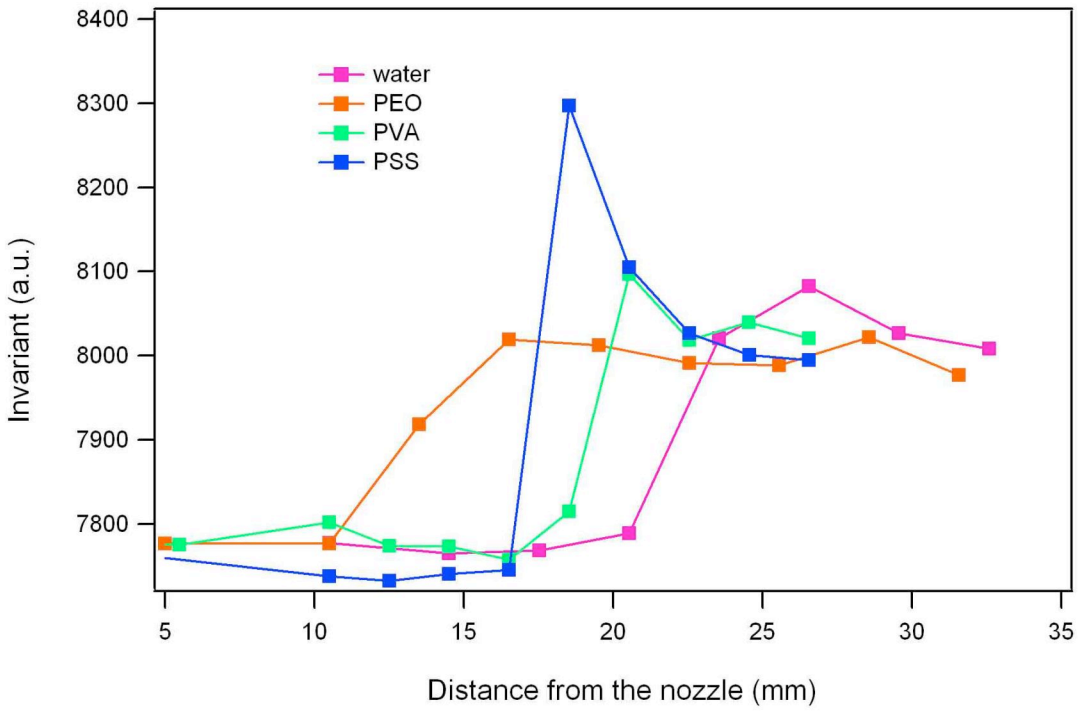

Figure 1. Invariant in function of distance from the nozzle of 100 μm diameter jets composed of pure water and of water with additives. The onset of the jet instability can be seen as a steep increase in the invariant value.

In the present work we have therefore measured the jet behavior of water based mixtures with additives and surfactants by synchrotron SAXS. To produce the jets we have used HPLC tubes of 100μm of diameter and we have measured water solutions of different concentrations of the following additives: Polyvinyl alcohol (PVA), Polystyrene sulfonate (PSS), Polyethylene oxide (PEO).
For each mixture, we have determined the change of jet breakup length and therefore of breakup time with respect to different jet speeds. All additives strongly influence the onset of jet instability.

Acknowledgements:
We would like to thank M. Rappolt for useful discussion, C. Morello and A. Allemandi for technical support.

References:

[1] J. Eggers, E. Villermauc, Physics of liquid jets , Rep. Prog. Phys., **71**, 036601 (2008)
[2] H. Amentitsch, B. Marmiroli,;Time-resolved structure investigation with small angle X-ray scattering using scanning techniques; Rendiconti Lincei, **22** (SUPPL. 1) , S93-S107 (2011)
[3] M. Priebe,S. Kalbfleisch, M. Tolkiehn, S. Köster, B. Abel, J.R. Davies, T. Salditt; Orientation of biomolecular assemblies in a microfluidic jet;, New Journal of Physics, 12, 4 (2010)
[4] H. N. Chapman et al; Femtosecond X-ray protein nanocrystallography ; Nature, 470, 73-78 (2011)
[5] J. Uddin, S.P.Decent, M.J.H.Simmons; The effect of surfactants on the instability of a rotating liquid jet; Fluid Dynamics Research, **40**, 827–851 (2008)

IN-SITU GISAXS INVESTIGATION OF THE STRUCTURAL TRANSITIONS IN BLOCK COPOLYMER THIN FILMS UNDER SOLVENT VAPOR EXPOSURE

C. Sinturel[1], M. Vayer[1], D. Grosso[2], H. Amenitsch[3]

1.) Centre de Recherche sur la Matière Divisée, 1b rue de la Férollerie, 45 071 Orléans Cedex 02, France
2.) Laboratoire Chimie de la Matière Condensée de Paris, UMR UPMC-CNRS 7574, Université Pierre et Marie Curie (Paris 6), Collège de France, 11 place Marcelin Berthelot, 75231, Paris, France
3.) Institute of Biophysics and Nanosystems Research, Austrian Academy of Sciences, Schmiedlstr. 6, 8042 Graz, Austria

The motivation of this project was to understand the reorganization mechanisms of thin films of polylactide (PLA) based block copolymer induced by exposure to vapors of solvents. The goal of the study was to perform accurate *in situ* GISAXS characterizations of the films upon exposure in order to examine the characteristics of the system in the swollen state and thus going further in the comprehension of the phenomenon undergoing in the swollen state that remained uncertain after our first published work [1]. For this purpose, films of PS-PLA were exposed in the sample environment to saturated THF vapors for various durations. Samples were placed in a closed stainless steel chamber with a total volume of 100 mL at 25 °C with a reservoir of solvent of 25 mL in order to reach in the vessel the saturated vapor pressure of solvent (P^0_{THF} = 200 mm Hg at 25°C). *In situ* experiments were performed such that one sample was constantly exposed to the THF saturated atmosphere while scattering patterns were collected every 59 s with an acquisition time of 1s. This sequence was selected to allow an optimal detection of the micro phase separation structure (optimal signal to noise ratio) without deterioration of the molecular structure of the copolymer.

The *in-situ* GISAXS patterns recorded for various durations of solvent exposure are shown in Figure 1. For non-exposed samples (not shown here) and for the shortest exposure times (1 min, 5 min), the GISAXS patterns exhibit a strong off plane radial scattering attributed to randomly oriented PLA domains in the depth profile of the film, characteristic of a poorly ordered system. Upon annealing, the block copolymer progressively evolves from a disorganized state to a well-ordered morphology consisting of an arrangement of hexagonally packed cylinders ordered perpendicularly to the film surface. For longer exposure time (here 35 min.) a 2D hexagonal arrangement of circular PLA domains is observed. The corresponding scattering pattern presents sharp in-plane Bragg peaks, accompanied by diffraction rods in the q_z direction (vertical streaks) generated by the 2D ordered array of PLA cylinders. During the exposure, a contraction of the diffraction ring along the qz direction from qz=0.23 to 0.11 nm^{-1} occurs within the first minutes of exposure, that is related to the swelling of the film. At the same time a much less pronounced increase of the periodicity in the x direction from qx=0.12 to 0.10 nm^{-1} is observed that can be attributed to the adhesion of the block copolymer on the surface of the substrate. One also observes that during the exposure, the scattered intensity becomes progressively less intense which is related to a decrease of the electronic contrast between the scattering domains since the annealing solvent has dilution effect on the polymer concentration in each segregated phases. However, significant scattering is observed during all the duration of the experiment, even for long exposure time, indicating that the swollen state remains micro-separated. This is an important result showing that despite a high degree of swelling, the homogeneous disordered state of the phase diagram is not reached.

Between the two extremes morphologies (worm like and perpendicular cylinders), an intermediate organization can be observed. A careful examination of the scattering pattern after 10 minutes of exposure reveals a new distinct morphology that has been assigned to a bcc phase having the (110) direction of the domains normal to the surface. Indeed one can clearly see the presence of the typical out of plane (101) diffraction spot of the cubic phase. This structural transition which has already been reported in other type of block-copolymer (poly(α-methylstyrene)-block-poly(4-hydroxystyrene) [2] and polystyrene-block-poly(4-vinylpiridine) [3] is herein reported for the first time for PS-PLA. The origin of such phenomenon lay in the selective swelling of one block that modifies the volume ratio of the two blocks which in turn causes a position shift within the phase diagram. In this case, PLA spheres in a PS matrix will be formed from PLA cylinders by a selective swelling of the major phase which decreases the volume ratio PLA/PS. This constitutes the major result of these measurements.

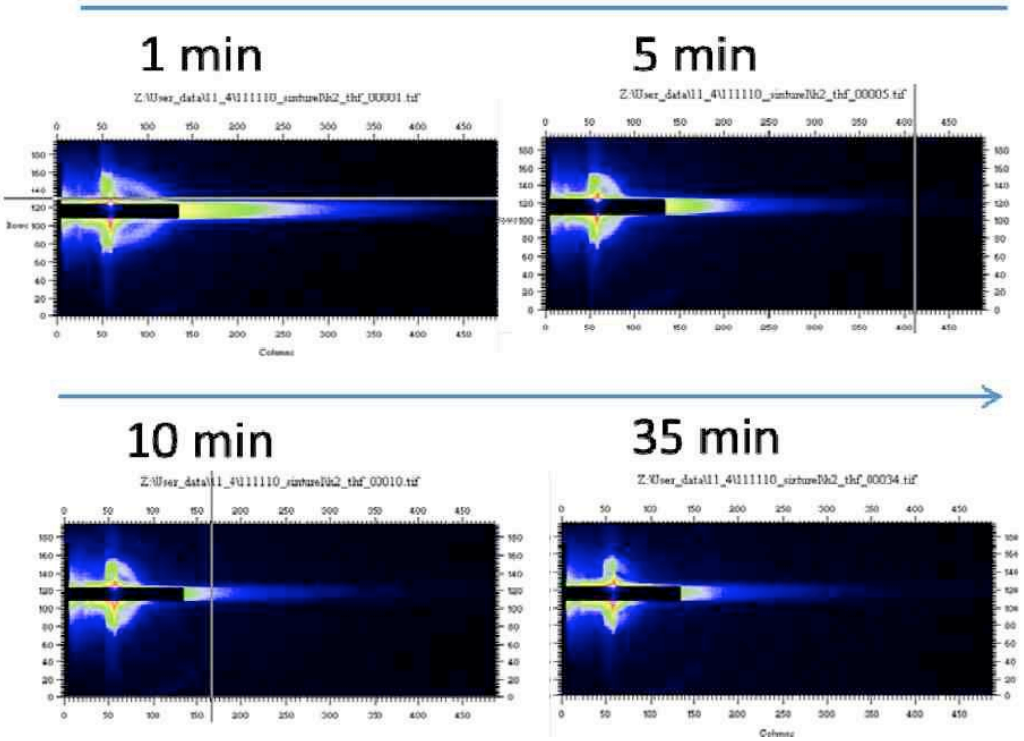

Figure 1. In-situ GISAXS characterizations of a PS-PLA thin film (100 nm) upon solvent annealing

References:

[1] M. Vayer, M.A. Hillmyer, M. Dirany, G. Thevenin, R. Erre, C. Sinturel; Thin Solid Films **518**, 3710-3715 (2010)

[2] J.K. Bosworth, M.Y. Paik, R. Ruiz, E.L. Schwartz, J. Q. Huang, A.W. Ko, D.-M. Smilgies, C.T. Black, C.K. Ober; ACS Nano **2**, 1396-1402 (2008)

[3] E. B. Gowd, M. Bohme, M. Stamm ; Materials Science and Engineering **14**, 012015 (2010)

Publications

Publications in Journals and Reviewed Proceedings 2011

H. Amenitsch, C. Bombelli, S. Borocci, R. Caminiti, F. Ceccacci, S. Concilio, C. La Mesa, G. Mancini, S. Piotto, M. Rappolt
Segregation into domains observed in liquid crystal phases: Comparison of experimental and theoretical data
Soft Matter 7 (7), pp. 3392-3403 (2011)

H. Amenitsch, G. Caracciolo, P. Foglia, V. Fuscoletti, P. Giansanti, C. Marianecci, D. Pozzi, A. Laganà
Existence of hybrid structures in cationic liposome/DNA complexes revealed by their interaction with plasma proteins
Colloids and Surfaces B 82 (1), 141-146 (2011)

H. Amenitsch and B. Marmiroli
Time-resolved structure investigation with small angle X-ray scattering using scanning techniques
Rendiconti Lincei, Vol. 22 - SUPPL. 1, pp. S93-S107 (2011)

E. Jr. Baldassarri, M. G. Ortore, C. Ferrero, S. Finet, F. Spinozzi, P. Mariani
Pressure Effects on G-Quadruplex Structures Stabilized by Two Different Counter-ions
International Review of Biophysical Chemistry, Vol. 2, pp. 142-146 (2011)

B. Boulgaropoulos, Z. Arsov, P. Laggner, and G. Pabst
Stable and unstable lipid domains in ceramide-containing membranes
Biophys. J 100, 2160 (2011)

C.P. Brown, J. MacLeod, H. Amenitsch, F. Cacho-Nerin, H.S. Gill, A.J. Price, E. Traversa, S. Licoccia, F. Rosei
The critical role of water in spider silk and its consequence for protein mechanics
Nanoscale, Vol. 3(9), pp. 3805-3811 (2011)

C.P. Brown, J. MacLeod, H. Amenitsch, F. Cacho-Nerin, H.S. Gill, A.J. Price, E. Traversa, S. Licoccia, F. Rosei
Erratum: The critical role of water in spider silk and its consequence for protein mechanics
Nanoscale, Vol. 3 - 12, pp. 5186 (2011)

M. Buljan, I. Bogdanović-Radović, M. Karlušić, U. V. Desnica, N. Radić, M. Jakšić, K. Salamon, G. Dražić, S. Bernstorff, and V. Holý
Design of quantum dot lattices in amorphous matrices by ion beam irradiation
Physical Review B84, 155312 (2011)
and Virtual Journal of Nanoscale Science & Technology, Chapter "Supramolecular and Biochemical Assembly", Volume 24, Issue 18, 31.10.2011

G. Campi, A. Pifferi, A. Mari, H. Amenitsch, C. Cannas and L. Suber
Dynamic templating role of polynaphtalene sulphonate in the formation of silver nanocrystals in aqueous solution
Journal of Nanoparticle Research 13 (8), 3107-3112 (2011)

G. Campi, A. Mari, A. Pifferi, H. Amenitsch, M. Fratini, L. Suber
Control of silver-polymer aggregation mechanism by primary particle spatial correlations in dynamic fractal-like geometry
Nanoscale, Vol. 3 - 9, pp. 3774-3779 (2011)

I. Capan, J. Bak-Misiuk, B. Pivac, P. Dubček, A. Misiuk, S. Bernstorff, P. Romanowski
Defects in silicon introduced by helium implantation and subsequent annealing
Radiation Physics and Chemistry 80, 1099–1103 (2011)

G. Caracciolo, D. Pozzi, A.L. Capriotti, C. Cavaliere, P. Foglia, H. Amenitsch, A. Laganà
Evolution of the protein corona of lipid gene vectors as a function of plasma concentration
Langmuir, Vol. 27 - 24, pp. 15048-15053 (2011)

G. Caracciolo, D. Pozzi, A.L. Capriotti, C. Marianecci, M. Carafa, C. Marchini, M. Montani, A. Amici, H. Amenitsch, M.A. Digman, E. Gratton, SS. Sanchez, A. Laganà
Factors Determining the Superior Performance of Lipid/DNA/Protammine Nanoparticles over Lipoplexes
Journal of Medicinal Chemistry 54 (12), 4160-4171 (2011)

J. Caron, E. Lepeltier, L.H. Reddy, S. Lepêtre-Mouelhi, S. Wack, C. Bourgaux, P. Couvreur and D. Desmaële
Squalenoyl gemcitabine monophosphate: synthesis, characterisation of nanoassemblies and biological evaluation
Eur.J. Org. Chem., 14, 2615-2628 (2011)

G. Ciasca, M. Chiarpotto, G. Campi, B. Bocca, M. Rodio, A. Pino, A. Ricci, N. Poccia, C. Rossi, A. Alimonti, H. Amenitsch, P. De Sole and A. Bianconi
Reconstitution of aluminium and iron core in horse spleen apoferritin
Journal of Nanoparticle Research 13 (11), 6149-6155 (2011)

S. Costacurta, P. Falcaro, L. Malfatti, D. Marongiu, B. Marmiroli, F. Cacho-Nerin, H. Amenitsch, N. Kirkby and P. Innocenzi
Shaping mesoporous films using dewetting on X-ray pre-patterned hydrophilic/hydrophobic layers and pinning effects at the pattern edge
Langmuir 27 (7), pp. 3898-3905 (2011)

P. Dubček, B. Pivac, S. Milošević, N. Krstulović, Z. Kregar, S. Bernstorff
Pulsed laser ablation of GaAs using nano pulse length
Applied Surface Science 257 (2011) 5358–5361

P. Falcaro, S. Costacurta, L. Malfatti, D. Buso, A. Patelli, P. Schiavuta, M. Piccinini, G. Grenci, B. Marmiroli, H. Amenitsch, P. Innocenzi
Chemical tailoring of hybrid sol-gel thick coatings as hosting matrix for functional patterned microstructures.
ACS applied materials & interfaces 3 (2), 245-251 (2011)

P. Falcaro, F. Normandin, M. Takahashi, P. Scopece, H. Amenitsch, S. Costacurta, C.M. Doherty, J.S. Laird, M.D. H. Lay, F. Lisi, A.J. Hill, D. Buso
Dynamic Control of MOF-5 Crystal Positioning Using a Magnetic Field
Advanced Materials 23 (34), 3901–3906 (2011)

J. Falta, Th. Schmidt, S. Gangopadhyay, T. Clausen, O. Brunke, J. I. Flege, S. Heun
S. Bernstorff, L. Gregoratti and M. Kiskinova
Ultra-thin high-quality silicon nitride films on Si(111)
Europhys. Letters 94 (2011) 16003-(1-5)

M. Faustini, B. Marmiroli, L. Malfatti, B. Louis, N. Krins, P. Falcaro, G. Grenci, C. Laberty-Robert, H. Amenitsch, P. Innocenzi and D. Grosso
Direct nano-in-micropatterning of TiO2 thin layers and TiO 2/Pt nanoelectrode arrays by deep X-ray lithography
Journal of Materials Chemistry 21 (11), pp. 3597-3603 (2011)

F. Federiconi, M. Mattioni, E. Jr. Baldassarri, M.G. Ortore and P. Mariani
How soft are biological helices? A measure of axial and lateral force constants in folate quadruplexes by high-pressure X-ray diffraction
Eur. Biophys. J. 40 (11), 1225-1235 (2011)

V. Holy, M. Buljan, R. Lechner
X-ray characterization of semiconductor nanostructures
Semiconductor Science and Technology 26, 064002 (2011)

P. Innocenzi, L. Malfatti, T. Kidchob, S. Costacurta, P. Falcaro, B. Marmiroli, F. Cacho-Nerin, H. Amenitsch
Densification of sol-gel silica thin films induced by hard X-rays generated by synchrotron radiation
Journal of Synchrotron Radiation 18 (2), pp. 280-286 (2011)

P. Innocenzi, L. Malfatti, G. J. A. A. Soler-Illia
Hierarchical mesoporous films: from self-assembly to porosity with different length scales
Chemistry of Materials, 23, 2501–2509 (2011)

A.-C.J.H. Johnsson, M.C. Camerani, and Z. Abbas
Combined Electrospray-SMPS and SR-SAXS Investigation of Colloidal Silica Aggregation. Part I. Influence of Starting Material on Gel Morphology
J. Phys. Chem. B 115 (5), pp 765-775 (2011)

A.-C.J. H. Johnsson, M.C. Camerani, and Z. Abbas
Combined Electrospray-Scanning Mobility Particle Sizer (ES-SMPS) and Time-Resolved Synchrotron Radiation-Small-Angle X-ray Scattering (SR-SAXS) Investigation of Colloidal Silica Aggregation. Part II. Influence of Aggregation Initiator on Gel Stability
J. Phys. Chem. B 115 (31), pp 9547-9555 (2011)

D. Jozić, I. Knezović and S. Bernstorff
Kinetics of cement hydration with replacement addition of fly ash into aqueous suspension systems
Proceedings of "International Conference on materials, tribology and recycling (matrib 2011)", Vela Luka (Island Korcula), Croatia, 29.6.-1.7.2011, pages 159-166, editors: Z. Schauperl and S. Solic, Croation Society for Materials and Tribology, Zagreb 2011

D. Jozić, J. Mandić, D. Tibljaš and S. Bernstorff
Reuse of fly ash in preparation of geopolymers
Proceedings of "International Conference on materials, tribology and recycling (matrib 2011)", Vela Luka (Island Korcula), Croatia, 29.6.-1.7.2011, pages 167-177, editors: Z. Schauperl and S. Solic, Croation Society for Materials and Tribology, Zagreb 2011

D. Jozić, M. Martinović and S. Bernstorff
Kinetics of cement hydration of type CEM I 42.5R without and with replacement addition of fly ash
Proceedings of "Slovenian-Italian Conference on Materials and Technologies for Sustainable Growth", University of Nova Gorica, Slovnia, 4.-6.5.2011, pp 19-24

K. Jungnikl, M. Rappolt, I. Shyjumon, B. Sartori, P. Laggner, H. Amenitsch
Aerosol Flow Reactor with Controlled Temperature Gradient for In Situ Gas-Phase X-Ray Experiments—Measurements of Evaporation-Induced Self-Assembly (EISA) in Aerosols
Aerosol Science and Technology, Volume 45, Issue 7, Pages 805 – 810 (2011)

M.B. Kerber, M.J. Zehetbauer, E. Schafler, F.C. Spieckermann, S. Bernstorff and T. Ungar
X-ray Line Profile Analysis – An Ideal Tool to Quantify Structural Parameters of Nanomaterials
JOM Vol. 63 No. 7, pp. 61-69 (2011)

G. Khelashvili, M. Rappolt, S. Chiu, G. Pabst, D. Harries
I*mpact of sterol tilt on membrane bending rigidity in cholesterol and 7DHC-containing DMPC membranes*
Soft Matter, Vol. 7 - 21, pp. 10299-10312 (2011)

N. Krins, J.D. Bass, B. Julián-López, P. Evrar, C. Boissière, L. Nicole, C. Sanchez, H. Amenitsch and D. Grosso
Mesoporous SiO2 thin films containing photoluminescent ZnO nanoparticles and simultaneous SAXS/WAXS/ellipsometry experiments
Journal of Materials Chemistry 21 (4), pp. 1139-1146 (2011)

M. Lučić Lavčević, A. Turković, P. Dubček, Z. Crnjak Orel, B. Orel, and S. Bernstorff
GISAXS View of Induced Morphological Changes in Nanostructured CeVO4 Thin Films
Journal of Nanomaterials, vol. 2011, Article ID 303808, 7 pages (2011)

E. Maier, T. Rath, W. Haas, O. Werzer, R. Saf, F. Hofer, D. Meissner, O. Volobujeva, S. Bereznev, E. Mellikov, H. Amenitsch, R. Resel, G. Trimmel
$CuInS_2$-Poly(3-(ethyl-4-butanoate)thiophene) nanocomposite solar cells: Preparation by an in situ formation route, performance and stability issues
Solar Energy Materials and Solar Cells 95 (5), pp. 1354-1361 (2011)

L. Malfatti, D. Marongiu, H. Amenitsch and P. Innocenzi
Simultaneous in situ and Time-Resolved Study of Hierarchical Porous Films Templated by Salt Nanocrystals and Self-Assembled Micelles
The Journal of Physical Chemistry C 2011 115 (26), 12702-12707 (2011)

L. Malfatti, P. Falcaro, B. Marmiroli, H. Amenitsch, M. Piccinini, A. Falqui, P. Innocenzi
Nanocomposite mesoporous ordered films for lab-on-chip intrinsic surface enhanced Raman scattering detection
Nanoscale 3, 3760-3766 (2011)

B. Mandlmeier, J.M. Szeifert, D. Fattakhova-Rohlfing, H. Amenitsch and T. Bein
Formation of Interpenetrating Hierarchical Titania Structures by Confined Synthesis in Inverse Opal
J. Am. Chem. Soc. 133 (43), pp.17274-17282 (2011)

C. Marchini, D. Pozzi, M. Montani, C. Alfonsi, A. Amici, S. Candeloro De Sanctis, M.A. Digman, S. Sanchez, E. Gratton, H. Amenitsch, A. Fabbretti, C.O. Gualerzi and G. Caracciolo
Role of temperature-independent lipoplex-cell membrane interactions in the efficiency boost of multicomponent lipoplexes
Cancer Gene Therapy 18, 543-552 (August 2011)

S. Mura, G. Greppi, A. M. Roggio, L. Malfatti, P. Innocenzi
Polypeptide binding to mesostructured titania films
Microporous and Mesoporous Materials, 142, 1-6 (2011)

D. Ntountaniotis, G. Mali, S.G. Grdadolnik, H. Maria, A. Skaltsounis, C. Potamitis, E. Siapi, P. Chatzigeorgiou, M. Rappolt, T. Mavromoustakos
Thermal, dynamic and structural properties of drug AT1 antagonist olmesartan in lipid bilayers
Biochimica et Biophysica Acta - Biomembranes, Vol. 1808 - 12, pp. 2995-3006 (2011)

A. Pein, M. Baghbanzadeh, T. Rath, W. Haas, E. Maier, H. Amenitsch, F. Hofer, C.O. Kappe, G.Trimmel
Investigation of the formation of CuInS2 nanoparticles by the oleylamine route: Comparison of microwave-assisted and conventional syntheses
Inorganic Chemistry 50 (1), pp. 193-200 (2011)

Š. Perutková, M. Daniel, M. Rappolt, G. Pabst, G. Dolinar, V. Kralj-Iglič, and A. Iglič
Elastic deformations in hexagonal phases studied by small-angle X-ray diffraction and simulations
Physical Chemistry Chemical Physics 13, 3100-3107 (2011)

S.R.C. Pinto, A.G. Rolo, M. Buljan, A. Chahboun, S. Bernstorff, N.P. Barradas, E. Alves, R.J. Kashtiban, U. Bangert and M.J.M. Gomes
Low-temperature fabrication of layered self-organized Ge clusters by RF-sputtering
Nanoscale Res. Lett. **6** (2011) 341

C. Potamitis, P. Chatzigeorgiou, E. Siapi, K.,Viras, T. Mavromoustakos, A. Hodzic, G. Pabst, F. Cacho-Nerin, P. Laggner and M. Rappolt
Interactions of the AT1 antagonist valsartan with dipalmitoyl-phosphatidylcholine bilayers
Biochimica et Biophysica Acta - Biomembranes 1808 (6), 1753-1763 (2011)

N. Radić, K. Salamon, P. Dubček, O. Milat, M. Jerčinović, G. Dražić, S. Bernstorff
Nanoscale multilayers as optical elements for X-ray photolitography
Proceedings of the 34th International Convention Mipro 2011 (Opatija, Croatia, 23-27 May 2011), pages 27 - 30, (2011)

M. Rappolt, and C. Serra
Batteri più forti degli antibiotici, Rappolt prova a "sconfiggerli"
Il Piccolo, Trieste, 26. Oct. 2011, p. 28 (2011)

M. Rappolt, M. Rössle, Y. Kaconis, J. Howe, J. Andrä, T. Gutsmann and K. Brandenburg
X-ray scattering of bacterial cell wall compounds and their neutralization
In: X-Ray Scattering. C.M. Bauwens (ed.), Nova Publishers, Hauppauge NY, ISBN: 978-1-61324-326-8, pp. 133-148 (2011)

D. Ristic, M. Ivanda, M. Marcius, V. Holy, Z. Siketic, I. Bogdanovic-Rakovic, O. Gamulin, K. Furic, M. Ristic, S.. Music, M. Buljan, M. Ferrari, A. Chiasera, A. Chiappini, G.C. Righini
Characterisation of thin LPCVD silicon-rich oxide films
Proceedings of SPIE 8069, 80690P (2011)

D. Ristic, V. Holy, M. Ivanda, M. Marcius, M. Buljan, O. Gamulin, K. Furic, M. Ristic, S. Music, M. Mazzola, A. Chiasera, M. Ferrari, G.C. Righini
Surface characterization of thin silicon-rich oxide films
J. Molecular Struct. 993, 214-218 (2011)

J. Sancho-Parramon, V. Janicki, M. Lončarić, H. Zorc, P. Dubček and S. Bernstorff
Optical and structural properties of Au-Ag islands films for plasmonic applications
Applied Physics A: Materials Science & Processing, Volume 103, Number 3, 745-748 (2011)

E. Schafler
Strength response upon pressure release after high pressure torsion deformation
Scripta Mater. 64 (2), 130-132 (Jan. 2011)

E. Schafler
Effect of hydrostatic pressure on the microstructure and mechanical properties during and after high pressure torsion
Mater. Sci. Forum 667-669, 657-664 (2011)

I. Shyjumon, M. Rappolt, B. Sartori, F. Cacho-Nerin, G. Grenci, P. Laggner, H. Amenitsch
Mesostructured silica aerosol particles: Comparison of gas-phase and powder deposit X-ray diffraction data
Langmuir 27 (9), pp. 5542-5548 (2011)

O. Szekely, Y. Schilt, A. Steiner, U. Raviv
Regulating the Size and Stabilization of Lipid Raft-like Domains and Using Calcium Ions as Their Probe
Langmuir **2011,** 27, (24), 14767-14775

O. Szekely, A. Steiner, P. Szekely, E. Amit, R. Asor, C. Tamburu, U. Raviv
The Structure of Ions and Zwitterionic Lipids Regulates the Charge of Dipolar Membranes
Langmuir **2011,** 27, (12), 7419-7438

P. Szekely, T. Dvir, R. Asor, R. Resh, A. Steiner, O. Szekely, A. Ginsburg, J. Mosenkis, V. Guralnick, Y. Dan, T. Wolf, C. Tamburu, U. Raviv
Effect of Temperature on the Structure of Charged Membranes
Journal of Physical Chemistry B **2011,** 115, (49), 14501-14506

B. A. Taleatu, A. Y. Fasasi, G. Di Santo, S. Bernstorff, A. Goldoni, M. Fanetti, L. Floreano, P. Borghetti, L. Casalis, B. Sanavio, and C. Castellarin-Cudia
Electro-chemical deposition of zinc oxide nanostructures by using two electrodes
AIP ADVANCES 1, 032147 (2011)

C.V.Teixeira, H. Amenitsch, P. Linton, M. Lindén, V. Alfredsson
The role played by salts in the formation of SBA-15, an in situ small-angle X-ray scattering/diffraction study
Langmuir 27 (11), pp. 7121-7131 (2011)

A. Tilley, Y.-D. Dong, H. Amenitsch, M. Rappolt and B.J. Boyd
Transfer of lipid and phase reorganisation in self-assembled liquid crystal nanostructured particles based on phytantriol
Physical Chemistry Chemical Physics 13, pp. 3026-3032 (2011) (with cover page)

A. Turković, P. Dubček, K. Juraić, M. Rakić, S. Bernstorff
Study of γ-irradiated Polymer Electrolyte for Zn Rechargeable Nanostructured Galvanic Cells by SAXS/DSC/WAXD method
Journal of Inorganic and Organometallic Polymers and Materials 21 (3), pp. 706-710 (2011)

E.M.F. Vieira, S.R.C. Pinto, S. Levichev, A.G. Rolo, A. Chahboun, M. Buljan, N.P. Barradas, E. Alves, S. Bernstorff, O. Conde, M.J.M. Gomes
Influence of the deposition parameters on the growth of SiGe nanocrystals embedded in Al_2O_3 matrix
Microelectronic Engineering 88 (2011) 509–513

A. Waheed, M. Mehmood, R. Benfield, J. Ahmad, H. Amenitsch, M. Aslam, A. Rauf, M. Hassan
Small-angle X-ray scattering (SAXS) study of porous anodic alumina - A new approach
Materials Chemistry and Physics, Vol. 131 - 1-2, pp. 362-369 (2011)

A. Yaghmur, B. Sartori, and M. Rappolt
The role of calcium in membrane condensation and spontaneous curvature variations in model lipidic systems
Physical Chemistry Chemical Physics 13, 3115-3125 (2011)

A. Yaghmur, S.W. Larsen, M. Schmitt, J. Oestergaard, C. Larsen, H. Jensen, A. Urtti, M. Rappolt
In situ characterization of lipidic bupivacaine-loaded formulations
Soft Matter, Vol. 7 - 18, pp. 8291-8295 (2011)

A. Yaghmur and M. Rappolt
Recent advances in the characterization of lipid-based nanocarriers
In: Nanotechnologies for Solubilization and Delivery in Foods, Cosmetics and Pharmaceuticals; Nissim Garti and Ididt Yuli-Amar (eds.), DEStech Publication Inc., Lancaster, ISBN: 978-1-60595-016-7, pp. 187-208 (2011)

Publications January to July 2012

M. Bitenc, P. Podbršček, P. Dubček, S. Bernstorff , G. Dražić , B. Orel and Z. Crnjak Orel
The growth mechanism of zinc oxide and hydrozincite: a study using electron microscopy and in-situ SAXS
CrystEngComm 14 (9), 3080-3088 (2012)

B. Boulgaropoulos, M. Rappolt, B. Sartori, H. Amenitsch, G. Pabst
Lipid sorting by ceramide and the consequences for membrane proteins
Biophysical Journal, Vol. 102 (9), pp. 2031-2038 (2012)

M. Buljan, N. Radić, S. Bernstorff, G. Dražić, I. Bogdanović-Radović,V. Holý
Grazing-incidence small-angle X-ray scattering: Application to the study of quantum dot lattices
Acta Crystallographica A 68 (1), pp. 124-138 (2012)

M. Buljan, U.V. Desnica, I. Bogdanović-Radović, N. Radić, M. Ivanda, G. Dražić,
S. Bernstorff and V. Holý
Preparation of regularly ordered Ge quantum dot lattices in amorphous matrices
Vacuum 86 (6), pp. 733-736 (2012)

D. Buso, J. Jasieniak, M.D.H. Lay, P. Schiavuta, P. Scopece, J. Laird, H. Amenitsch, A.J. Hill, P. Falcaro
Highly luminescent metal-organic frameworks through quantum dot doping
Small, Vol. 8 - 1, pp. 80-88 (2012)

C. Cervellati, K. Montin, Squerzanti M, Mischiati C, Ferrari C, Spinozzi F, Mariani P, Amenitsch H, Bergamini CM, Lanzara V
Effects of the regulatory ligands calcium and GTP on the thermal stability of tissue transglutaminase
Amino Acids 42(6), 2233-42 (2012 Jun)

P. Chatterjee, S. Hazra, H. Amenitsch
Substrate and drying effect in shape and ordering of micelles inside CTAB-silica mesostructured films
Soft Matter, Vol. 8 (10), pp. 2956-2964 (2012)

A. Fischereder, T. Rath, W. Haas, H. Amenitsch, D. Schenk, A. Zankel, R. Saf, F. Hofer, G. Trimmel
Investigation of CuInS2 thin film formation by a low-temperature chemical deposition method
ACS Applied Materials and Interfaces, Vol. 4 - 1, pp. 382-390 (2012)

A. Hodzic, P. Zoumpoulakis, G. Pabst, T. Mavromoustakos, M. Rappolt
Losartan's affinity to fluid bilayers modulates lipid-cholesterol interactions
Physical Chemistry Chemical Physics, Vol. 14 - 14, pp. 4780-4788 (2012)

S. Joseph, M. Rappolt & H. Bunjes
Simultaneous synchrotron X-ray diffraction/DSC studies on the polymorphic transitions in solid triglyceride drug carrier nanoparticles
Proceedings of "8th World Meeting on Pharmaceutics, Biopharmaceutics and Pharmaceutial Technology World Meeting", Istanbul (Turkey), 19.-22.03.2012

D. Jozić, S. Zorica, D. Tibljaš, S. Bernstorff
Insitu SAXS/WAXS study of the developing process of geopolymer structures
Proceedings of 15TH European conference on "composite materials" (ECCM15), pp. 2481-1 to 2481-8 (2012)

S. Kler, R. Asor, C.L. Li, A. Ginsburg, D. Harries, A. Oppenheim, A. Zlotnick, U. Raviv
RNA Encapsidation by SV40-Derived Nanoparticles Follows a Rapid Two-State Mechanism
Journal of the American Chemical Society **2012,** 134, (21), 8823-8830

K. Kowlgi, U. Lafont, M. Rappolt, G. Koper
Uniform metal nanoparticles produced at high yield in dense microemulsions
Journal of Colloid and Interface Science 372 (1), pp. 16–23 (2012)

S. Kralj, G. Cordoyiannis, D. Jesenek, A. Zidansek, G. Lahajnar, N. Novak, H. Amenitsch, Z. Kutnjak
Dimensional crossover and scaling behavior of a smectic liquid crystal confined to controlled-pore glass matrices
Soft Matter, Vol. 8 (8), pp. 2460-2470 (2012)

I. Krastanova, V. Sannino, H. Amenitsch, O, Gileadi, F.M. Pisani, S. Onesti
Structural and functional insights into the DNA replication factor Cdc45 reveal an evolutionary relationship to the DHH family of phosphoesterases
Journal of Biological Chemistry, Vol. 287 - 6, pp. 4121-4128 (2012)

S.S. Mandal, S. Bhaduri, H. Amenitsch and A.J. Bhattacharyya
Synchrotron Small Angle X-Ray Scattering Studies of Hemoglobin Non-aggregation Confined Inside Polymer Capsules
J. Phys. Chem. B, 2012, ASAP Article (online published 23.7.2012)

T. H. Nguyen, M. Vayer, D. Grosso, H. Amenitsch, C. Sinturel
Using sol-gel replications to assess the porosity of block-copolymer derived thin films
Journal of Physical Chemistry C, Vol. 116 (9), pp. 5295-5302 (8.3.2012)

S. R. C. Pinto, M. Buljan, A. Chahboun, M.A. Roldan, S. Bernstorff, M. Varela. S.J. Pennycook, N.P. Barradas, E. Alves, S.I. Molina, M. M.D. Ramos and M. J. M. Gomes
Tuning the properties of Ge-quantum dots superlattices in amorphous silica matrix through deposition conditions
Journal of Applied Physics 111, 074316 (2012)

P. Pivette, V. Faivre, L. Mancini, C. Gueutin, G. Daste, M. Ollivon, S. Lesieur
Controlled release of a highly hydrophilic API from lipid microspheres obtained by prilling: Analysis of drug and water diffusion processes with X-ray-based methods Journal of Controlled Release, 158 (3); 393-402, 2012

D Pozzi, C Marchini, F Cardarelli, H Amenitsch, C Garulli, A Bifone, G Caracciolo *Transfection efficiency boost of cholesterol-containing lipoplexes*
Biochimica et Biophysica Acta - Biomembranes, Vol. 1818 (9), pp. 2335-2343 (2012)

A.V. Radhakrishnan, S. K. Ghosh, G. Pabst, V. A. Raghunathan, and A. K. Sood
Tuning DNA-amphiphile condensate architecture with strongly binding counterions
Proc. Natl. Acad. Sci. 109: 6394 - 6398 (2012)

J. Schuster, R. Köhn, M. Döblinger, A. Keilbach, H. Amenitsch, T. Bein
In Situ SAXS Study on a New Mechanism for Mesostructure Formation of Ordered Mesoporous Carbons: Thermally Induced Self-Assembly
J. Am. Chem. Soc. *134 (27),* 11136-11145 (2012)
(*Highlighted in Science (Editors Choice by Phil Szuromi): Science* ***2012,*** *337 (6092), 270)*

F. Spieckermann, G. Polt, H. Wilhelm, M. Kerber, E. Schafler, M.J. Zehetbauer
The role of dislocations for the plastic deformation of semicrystalline polymers as investigated by multireflection X-ray line profile analysis
Journal of Applied Polymer Science, Vol. 125 - 6, pp. 4150-4154 (2012)
doi: 10.1002/app.36570

A. Steiner, P. Szekely, O. Szekely, T. Dvir, R. Asor, N. Yuval-Naeh, N. Keren, E. Kesselman, D. Danino, R. Resh, A. Ginsburg, V. Guralnik, E. Feldblum, C. Tamburu, M. Peres, U. Raviv
Entropic Attraction Condenses Like-Charged Interfaces Composed of Self-Assembled Molecules
Langmuir 2012, 28, (5), 2604-2613

L. Suber and G. Campi
Hierarchic self-assembling of silver nanoparticles in solution
Nanotechnology Reviews 1 (1), 57–78 (2012)

P. Szekely, R. Asor, T. Dvir, O. Szekely, U. Raviv
Effect of Temperature on the Interactions between Dipolar Membranes
Journal of Physical Chemistry B **2012,** 116, (11), 3519-3524

A. Turković, P. Dubček, M. Rakić, M. Lončarić, B. Etlinger, S. Bernstorff *SAXS/DSC/WAXD study of TiO2 nanoparticles and the effect of γ-radiation on nanopolymer electrolyte*
Vacuum, Vol. 86 - 6, pp. 750-753 (2012)

V. Vales, V. Holy, M. Buljan, V. Janicki, S. Bernstorff
Structural and morphological properties of Fe2O3/TiO2 nanocrystals in silica matrix
Thin Solid Films, Vol. 520 - 14, pp. 4800-4802 (2012)

E. M. F. Vieira, J. Martín-Sánchez, A. G. Rolo, A. Parisini, M. Buljan, I. Capan, E. Alves, N. P. Barradas, O. Conde, S. Bernstorff, A. Chahboun, S. Levichev, and M. J. M. Gomes
Structural and electrical studies of ultrathin layers with $Si_{0.7}Ge_{0.3}$ *nanocrystals confined in a* $SiGe/SiO_2$ *superlattice*
Journal of Applied Physics, Vol. 111 (10), art. no. 104323, 9 pages (2012)

A. Yaghmur, M. Rappolt, J. Oøstergaard, C. Larsen, S.W. Larsen
Characterization of bupivacaine-loaded formulations based on liquid crystalline phases and microemulsions: The effect of lipid composition
Langmuir 28 (5), pp. 2881-2889 (2012)

A. Yaghmur, B. Sartori and M. Rappolt
Self-Assembled Nanostructures of Fully Hydrated Monoelaidin-Elaidic Acid and Monoelaidin-Oleic Acid Systems
Langmuir 28, 10105-10119 (2012)

J. Zupanc, D. Drobne, B. Drasler, J. Valant, A. Iglic, V. Kralj-Iglic, D. Makovec, M. Rappolt, B. Sartori, K. Kogej
Experimental evidence for the interaction of C-60 fullerene with lipid vescicle membranes
Carbon 50 (3), pp. 1170-1178 (2012)

International Conferences and Workshops in 2011

H. Amenitsch
Small and Wide Angle Scattering: Its Application to Cosmetics and Pharmaceutics
Studium Conference: "Cosmetics and Pharmaceutics: New Trends in Biophysical Approaches", Orleans, France, 14.02.2011 - 15.02.2011

H. Amenitsch
Grazing Incidence Small Angle Scattering (GISAXS & GISAXD)
7th European Winter School on Neutrons and Synchrotron Radiation (NESY 2011), Planneralm, Austria, 7.-11.3.2011 (invited lecture)

H. Amenitsch
Do We Need Still Synchrotron Radiation for SAXS?
SAXS Laboratory Practice: "New Approaches and Integrated Techniques", Graz, Austria, 02.05.2011 - 03.05.2011 (lecture)

H. Amenitsch
Small angle scattering for the characterization of nanostructured (bio-) materials
XLVI Zakpoane School of Physics: "Breaking Frontiers: submicron structures in physics and biology", Zakopane, Poland, 16.05.2011 - 21.05.2011 (lecture)

H. Amenitsch
Small Angle Scattering: From Nano- to Hierarchical Materials
Ceitec-Elettra Workshops, Sněžné-Milovy, Czech Republic, 3.- 4.06.2011 (lecture)

Baldassarri E. Jr., Spinozzi F., Ortore M. G. and Mariani P.
Self-assembly and stability of G-Quadruplex: counter-ions, pressure and temperature effects
Secondo convegno congiunto SILS-SISN, Trieste 1-3 Settembre 2011

S. Bernstorff
Synchrotron Radiation and Instrumentation
7th European Winter School on Neutrons and Synchrotron Radiation, Planneralm, Austria, 7.-11.3.2011 (invited lecture)

S. Bernstorff
GISWAXS on Advanced Nanostructured Materials
GISAXS 2011 conference, DESY, Hamburg, Germany, 10-12 October 2011 (invited talk)

M. Bitenc, P. Podbrščček, P. Dubček, S. Bernstorff, G. Dražić, Z. Crnjak Orel
Zinc oxide: morphology and growth or how to prepare sphere- and rod-like particles? 1st International Workshop of CoE PoliMat, Ljubljana, Slovenia, 1.-2.12.2011

M. Bitenc, Z. Crnjak Orel, P. Podbrščček, P. Dubček, S. Bernstorff, G. Dražić
ZnO: morphology and growth
European Congress on Advanced Materials and Processes (EUROMAT 2011), Montpellier, France, 12-15 September 2011

Marko Bitenc, Peter Podbrščček, Pavo Dubček, Sigrid Bernstorff, Goran Dražić, Zorica Crnjak Orel
How to prepare sphere- and rod-like ZnO particles?
SLONANO 2011 conference, Ljubljana, Slovenia, 26 - 28 October 2011 (poster)

I. Bogdanović Radović, M. Buljan, M. Karlušić, N. Skukan, I. Božičević, M. Jakšić, N. Radić, K. Salamon and S. Bernstorff
Influence of ion-beam properties on ordering of quantum dots in amorphous matrices
EMRS Spring Meeting 2011, Nice, France, May 9-13, 2011 (poster)

C.P. Brown
Taking inspiration from nature: the biomimetic potential of spider silk
MRS-Africa - Meeting of the Materials Research Society, Victoria Falls, Zimbabwe, December 11-16, 2011 (invited talk)

M. Buljan, S. Bernstorff, U.V. Desnica, I. Bogdanović-Radović, N. Radić, M. Karlušić, G. Dražić, and V. Holý
Preparation of regularly ordered Ge quantum dot lattices in amorphous matrices
EMRS Spring Meeting 2011, Nice, France, May 9-13, 2011 (poster)

M. Buljan, I. Bogdanović-Radović, M. Karlušić, N. Radić, U.V. Desnica, G. Dražić, S. Bernstorff, M. Jakšić and V. Holy
Design of quantum dot lattices by ion beam irradiation
EMRS Spring Meeting 2011, Nice, France, May 9-13, 2011 (talk)

M. Buljan, N. Radić, J. Grenzer, I. Capan, A. Muecklich, S. Bernstorff, V. Holy and B. Pivac
Spatially ordered Ge quantum dots on rippled substrate: structural and electrical properties
EMRS Spring Meeting 2011, Nice, France, May 9-13, 2011 (talk)

M. Buljan, N. Radić, S. Bernstorff and V. Holy
GISAXS analysis of self-ordered quantum dots in amorphous multilayers
EMRS Spring Meeting 2011, Nice, France, May 9-13, 2011 (poster)

M. Buljan, S. R. C. Pinto, A. G. Rolo, J. Martín-Sánchez, J. Grenzer, A. Müecklich, S. Bernstorff, M. J. M. Gomes
Self-assembly of Ge quantum dots and voids in an alumina film
EMRS Spring Meeting 2011, Nice, France, May 9-13, 2011 (poster)

M. Buljan, N. Radić, G. Dražić, S. Bernstorff, V. Holy
Self-assembly of Ge nanoclusters in amorphous matrices
18 znanstveni sastanak Vakuumska znanost i tehnika, Bohinj, Slovenija, Jun 2-3 2011 (invited lecture)

M. Buljan, N. Radić, J. Grenzer, A. Mucklich, S. Bernstorff, V. Holý
Preparation and characterization of self-assembled quantum dots in amorphous matrices
Helmholtz Zentrum Dresden-Rossendorf, Germany, 15.07.2011 (invited seminar)

G. Campi
New experimental approaches for evolution and control of complexity in out of equilibrium systems
VIII International Conference of Complex Systems, Boston, MA, USA, June 26 – July 3, 2011 (oral)

G. Cordoyiannis, D. Jesenek, A. Zidansek, N. Novak, Z. Kutnjak, G. Lahajnar, H. Amenitsch, G. Nounesis, R. Rosso, E.G. Virga, S. Kralj
Universal behaviour of liquid crystals confined in controlled-pore glasses
11th European Conference on Liquid Crystals ECLC 2011, 6-11 February 2011, Maribor, Slovenia

P. Dubček, B. Pivac, I. Capan, M. Buljan, S. Bernstorff, A. Borghesi, A. Sassella, and M. Porrini
SAXS study of nucleation and growth of oxygen precipitates in silicon
EMRS Spring Meeting 2011, Nice, France, May 9-13, 2011 (poster)

A. Fischereder, T. Rath, A. Schenk, W. Haas, H. Amenitsch, D. Meischler, M. Edler, R. Saf, F. Hofer, G. Trimmel
Novel Preparation Methods for Cu_2ZnSnS_4 Layers for Photovoltaic Applications, 26thEuropean Photovoltaic Solar Energy Conference and Exhibition, Hamburg, Germany, September 5, 2011 (poster)

D. Gracin
Nano-structured thin silicon for "third generation solar cells"
Workshop on *"Low-cost solar cells 2011: Opportunities and Challenges for Green Energy"*, Skopje, Macedonia, May 15-18, 2011 (invited talk)

V. Holy
Structural and kinetic study of crystalline semiconductor quantum dots in amorphous matrix
Seminar at Institute of Physics, Slovak Acad. Sci., Bratislava, Slovakia, 25. 3. 2011

V. Holy
Our activities at Elettra,
Seminar at CEITEC institute, Brno, Czech Republic, 3. 6. 2011

V. Holy
X-ray scattering investigation of semiconductor nanocrystals in amorphous matrix
Seminar at the Institute of Crystallography, Bari, Italy, 31. 5. 2011

V. Holy
Synchrotron-related methods for investigation of nanostructures
Slovenian-Croatian Crystallography Meeting CSCM20, Baska, Croatia, 15.-19. 6. 2011

V. Holy
Grazing-incidence x-ray small-angle scattering from self-assembled nanoparticles
8th School on x-ray scattering from surfaces and thin layers, Smolenice, Slovakia 4.10.-7.10.2011

M. Jerčinović, N. Radić, M. Buljan , P. Dubček, M. Ristić, J. Sancho-Parramon, K. Salamon, S. Bernstorff, V. Holý
Nickel nanoparticles formed by magnetron sputtering
18th Slovenian and Croatian vacuum meeting, Bohinj, Slovenia, 02-03 June 2011

D. Jesenek, G. Cordoyiannis, A. Zidansek, G. Lahajnar, Z. Kutnjak, H. Amenitsch, S. Kralj
Layer thickness behaviour of confined smectic liquid crystals
11th European Conference on Liquid Crystals ECLC 2011, 6-11 February 2011, Maribor, Slovenia

D. Jesenek, G. Cordoyiannis, N. Novak, Z. Kutnjak, H. Amenitsch, S. Kralj
Phase behavior character of strongly confined nematic and smectic liquid crystals
11th European Conference on Liquid Crystals ECLC 2011, 6-11 February 2011, Maribor, Slovenia

D. Jozić, S. Bernstorff, P. Dubček, D. Tibljaš, J. Mandić, S. Zorica
Primjena SAXS metode u karakterizaciji geopolimera
Application of the SAXS method in the characterisation of geopolymers
XXII Croatian Meeting of Chemists and Chemical Engineers, Zagreb, Croatia, February 13- 16, 2011

D. Jozić, S. Bernstorff, H. Amenitsch, F. N. Cacho, R. Ciancio
Preparation of unconventional enviromenally friendly inorganic binders
7th European Winter School on Neutrons and Synchrotron Radiation, Planneralm, Austria, March 6-12, 2011 (poster)

D. Jozić, M. Martinović and S. Bernstorff
Kinetics of cement hydration type CEM I 42.5R without and with replacement addition of fly ash
Slovenian-Italian Conference on "Materials and Technologies for Sustainable Growth", University of Nova Gorica, Ajdovscina, Slovenia, 4.-6.5.2011

D. Jozić, I. Knezović and S. Bernstorff
Kinetics of cement hydration with replacement addition of fly ash into aqueous suspension systems
International conference on Materials, Tribology Recycling: MATRIB '11, Vela Luka, Croatia, 29th June - 1st July 2011

D. Jozić, J. Mandić, D. Tibljas and S. Bernstorff
Reuse of fly ash in the preparation of geopolymers
International conference on Materials, Tribology Recycling: MATRIB '11, Vela Luka, Croatia, 29th June - 1st July 2011

K. Juraić, A.Turković, P. Dubček, B. Etlinger, S. Bernstorff
SAXS/DSC/WAXD in situ study of polymer electrolyte for re-chargeable nano-structural galvanic Zn batteries
7th Meeting of Croatian Physical Society, Primošten, Croatia, October 13-16, 2011 (poster)

M. Karlušić, I. Bogdanović Radović, M. Buljan, N. Skukan, I. Božičević, M. Jakšić, N. Radić, U. Desnica, K. Salamon and S. Bernstorff
Ion beam synthesis of Germanium quantum dots embedded in SiO_2: effect of ion beam fluence and annealing temperature
EMRS Spring Meeting 2011, Nice, France, May 9-13, 2011 (poster)

K. Kornmüller, H. Amenitsch, F. Cacho-Nerin, C. Mikl, R. Prassl
Amphiphilic Designer-Peptides as Solubilizing Agents for Apolipoprotein B-100
3rd ÖGMBT Annual Meeting 2011, Puch/Salzburg, Austria, 28./29.9.2011, (poster)

E. Lepeltier, C. Bourgaux, J. Caron, E. Sliwinski, S. Harrisson, D. Desmaele, P. Couvreur
Nanoassemblies of nucleoside analogues coupled to squalene and terpenes : structural analysis
Colloque de l'université Paris Sud 11, Chimie et santé: de la molécule au médicament, Paris, France, 5 May 2011 (poster)

E. Lepeltier, C. Bourgaux, J. Caron, E. Sliwinski, S. Harrisson, D. Desmaele, P. Couvreur
Nanoassemblies of nucleoside analogues coupled to squalene and terpenes : structural analysis
Congrès PharmSciFair, Prague, Tchéquie, 13 - 17 June 2011 (poster)

S. Levichev, E. M. F. Vieira, J. Martín-Sánchez, O. Karzazi, A. Chahboun, M. Buljan, S. Bernstorff, and M. J. M. Gomes
Correlation between structural and electrical properties of MOS structures based on Ge nanocrystals embedded in SiO2 grown by RF- magnetron sputtering
EMRS Spring Meeting 2011, Nice, France, May 9-13, 2011 (poster)

M. Lučić Lavčević, Z. Marijanović, D. Jozić, I. Jerković, S. Bernstorff
Morphology of nanostructures in ZnO thin films
XXII. Croatian Meeting of Chemists and Chemical Engineers, Zagreb, Croatia, February 13-16, 2011

B. Mandlmeier, J.M. Szeifert, D. Fattakhova-Rohlfing, T. Bein
Mesopore formation in 3D macroporous titania films
23. Deutsche Zeolith-Tagung, Erlangen, Germany, 02.-04.03.2011

B. Mandlmeier, J.M. Szeifert, D. Fattakhova-Rohlfing and T. Bein
Hierarchical periodic titania nanostructures as novel anodes for dye-sensitized solar cells
3rd international Conference on Hybrid and Organic Photovoltaics, Valencia, Spain, 15.05.-18.05.2011

B. Marmiroli
Microfluidics and SAXS
SAXS Laboratory Practice New Approaches and Integrated Techniques, Graz, Austria, 2.- 3.05.2011 (lecture)

B. Marmiroli, F. Cacho Nerin, B. Sartori, G. Grenci, J. Perez, P. Laggner, M. Tormen and H. Amenitsch
Quantitative characterization of liquid jet instability at the nanoscale using SAXS
EMRS Spring Meeting 2011, Nice, France, May 9-13, 2011 (talk)

Daniela Marongiu
Hierarchical porous films with controlled pores size and topology: mesopores and nanoboxes
Convegno Nazionale sulla Scienza e Tecnologia dei Materiali, Aci Castello (CT), Italy, 26-29.6.2011

D. Meljanac
GISAXS, GIWAXS and analisys of line bradening x-ray diffraction: Structural properties of thin SnO2 films
Seminar in the frame of a PhD study (mentor D. Gracin) at the University Zagreb, Zagreb, Croatia, December 2011

J. Novak, T. Rath, A. Pein, A. Fischereder, W. Haas, H. Amenitsch, F. Hofer, G. Trimmel
Real Time Study of The Formation of ZnS Nanoparticles
EMRS Spring Meeting, Nice, France, May 10, 2011 (poster)

S. Onesti
Tackling large macromolecular complexes at Elettra: the interplay between protein crystallography, cryoelectron microscopy and small-angle X-ray scattering
9th SESAME Users' Meeting, Amman, Jordan, 12 – 14 November, 2011 (invited talk)

Z. Crnjak Orel
Zinc Oxide /PMMANanocomposites as an Effective UV Absorber
SLONANO 2011 conference, Ljubljana, Slovenia, 26 - 28 October 2011 (invited talk)

M. G. Ortore, F. Piccirilli, F. Spinozzi, P. Mariani, E. Baldassarri, N. Plotegher, I. Tessari, M. Beltramini, A. Perucchi, S. Lupi, H. Amenitsch, and L. Bubacco
Synchrotron SAXS and FTIR experiments monitor the effects of high pressure on a-synuclein amyloid fibrils
Secondo convegno congiunto SILS-SISN, Trieste 1-3 Settembre 2011 (Talk)

G. Pabst, B. Boulgaropoulos, Z. Arsov, and P. Laggner
Label-free determination of compositional fluctuations and macroscopic phase separation in a ternary lipid mixture
Biophysical Society 55th Annual Meeting, Baltimore, USA, 5.- 8.3.2011 (talk)

G. Pabst
Membrane-mediated effects of general anesthetics on ion channels
ORNL Seminar, Oak Ridge, USA, 10.3.2011 (talk))

G. Pabst
Learning about biomembranes by SWAXS
Workshop on Laboratory SAXS Practice (Hecus X-ray Systems), Graz, Austria, 2.-3.5.2011 (talk)

G. Pabst
Stereo-specific effects of anesthetics on lipid membranes
Seminar (University of Erlangen), Erlangen, Germany, 21.7.2011 (talk)

G. Pabst, E. Sevcsik, M. Rappolt, and T. Stockner
Stereo-specific effects of the analgesic drug ketamine on lipid membranes
8th European Biophysics Congress (EBSA), Budapest, Hungary, 23.-27.8.2011 (talk)

G. Pabst, E. Sevcsik, M. Rappolt, and T. Stockner
Membrane mediated effects of general anesthetics on ion channels
8th Liquid Matter Conference, Vienna, Austria, 6.-10.9.2011 (poster)

G. Pabst
Lipid sorting by ceramide and putative consequences for membrane proteins
6th Christmas Biophysics Workshop, Varazdin, Croatia, 12-13.12.2011 (talk)

S. Patlazhan, Y. Rémond, F. Addiego
Effect of molecular weight on the onset of cavitation in polyethylene: experiment and modeling
POLYCHAR 19 – World Forum on Advanced Materials, March 20-24, 2011, Kathmandu, Nepal

B. Pivac, J. Dasovic, R.Slunjski, G. Rasic, P. Dubcek, S. Bernstorff, N. Radic, B. Rakvin, I. Capan,
Si QDs formation in dielectric matrix: a defect study
EMRS Spring Meeting 2011, Nice, France, May 9-13, 2011 (poster)

D. Pozzi, G. Caracciolo, G. Caruso, F. Di Pascasio, P. Foglia, A. Laganà, H. Amenitsch
Nanoparticle-plasma protein interactions: confirmation by nanoLC-MS/MS of existence of hybrid structures in cationic liposome/DNA complexes
XXIV Congresso Nazionale della Societa Chimica Italiana, Lecce, Italy, 11-16 September 2011

N. Radic, K. Salomon, P. Dubcek, G. Drazic, M. Jercinovic, S.Bernstorff
Lateral continuity of ultrathin tungsten layers for X-ray mirrors
EMRS Spring Meeting 2011, Nice, France, May 9-13, 2011 (poster)

N. Radić, P. Dubček, K. Salamon, G. Dražić, M. Jerčinović, S. Bernstorff
Lateral continuity of ultrathin tungsten layers
18th Slovenian and Croatian vacuum meeting, Bohinj, Slovenia, 02-03 June 2011

N. Radić, K. Salamon, P. Dubček, O. Milat, M. Jerčinović, G. Dražić, S. Bernstorff
Nanoscale multilayers as optical elements for X-ray photolitography
34th International Convention Mipro 2011, Opatija, Croatia, 23-27 May 2011

M. Rappolt
How and what can you "see" with X-rays
Intensive SAXS Course for students of the University of Trieste, Sincrotrone Trieste, Italy, 25.11.2011

M. Rappolt
Austrian SAXS Beamline: Activities and Vision
CEI Meeting at the Sincrotrone Trieste, ELETTRA, 19.10.2011

M. Rappolt
X-ray Studies on Drug-Membrane Interactions
29th Cyprus-Noordwijker-Camerino Symposium, Limosol, Cyprus, 2.-9.10.2011 (Invited plenary lecture)

M. Rappolt
Phasing & Analysis of Liquid Crystal SAXS
Workshop on "SAXS Laboratory Practice, Graz, 3.5.2011 (Invited lecture)

M. Rappolt
Synchrotron light for characterizing the formation of curved membranes and membrane fusion processes
German Liquid Crystal Conference 2011, Hamburg, 1.4.2011

M. Rappolt
Synchrotron Light in Biology and Medicine (Part 1)
Membrane Biophysics Course at the University of Ljubljana, 12.1.2011

M. Rappolt
Synchrotron Light in Biology and Medicine (Part 2)
Membrane Biophysics Course at the University of Ljubljana, 19.1.2011

T. Rath, A. Fischereder, A. Schenk, W. Haas, H. Amenitsch, D. Meischler, M. Edler, R. Saf, F. Hofer and G. Trimmel
Preparation of Copper Zinc Tin Sulfide Layers for Photovoltaic Applications via Solution Based Routes
EMRS Spring Meeting, Nice, France, May 9-13, 2011 (talk)

U. Raviv
Using calcium ions to probe the stabilization and size regulation of lipid rafts
Liposomes in Jerusalem - an international conference, May 2011

U. Raviv
Structure and Intermolecular interactions of biomolecular self-assemblies
Japan Biophysical Society meeting, Himeji, September, 2011

U. Raviv
Structure and Intermolecular interactions of biomolecular self-assemblies
Seminar at Nanocenter at Tel-Aviv University, March, 2011

K. Salamon, O. Milat, N. Radić, P. Dubček, M. Jerčinović, S.Bernstorff
Characterization of W/C X-ray multilayer mirrors by small angle X-ray scattering techniques
18th Slovenian and Croatian vacuum meeting, Bohinj, Slovenia, 02-03 June 2011

E. Schafler
Effect of hydrostatic pressure on the microstructure and mechanical properties during and after high pressure torsion
5. Int. Conf. on "Nanomaterials by Severe Plastic Deformation" (nanoSPD5), Nanjing, China, 22. March 2011

E. Schafler
Dislocation density and vacancy concentration in severely deformed metals from line profiles
2. Int. workshop: "X-ray line profile analysis: from basics to practice", Dep. Materials Physics, Eötvös Lorand University Budapest, May 2011

W. Schmidt
Structure refinement of ordered mesoporous carbon materials from X-ray diffraction data
5th International FEZA (Federation of European Zeolite Associations) Conference, Spain, Valencia, 4-7 Jul 2011Spain (talk)

W. Schmidt, H. Amenitsch, A.H. Lu, J.J. Nitz
Adsorption on CMK-5 monitored by in-situ XRD
9th International Symposium on the "Characterization of Porous Solids (COPS 9)", 5.-8. June 2011, Dresden, Germany (talk 20 min)

J. Schuster, B. Mandlmeier, A. Keilbach, R. Köhn, M. Döblinger, H. Amenitsch, T. Dörfler, T. Dennenwaldt, T. Bein
Morphology-Control of Ordered Mesoporous Carbons with Extremely High Porosity
23. Deutsche Zeolith-Tagung, Erlangen, Germany, 02.-04.03.2011

J. Schuster, B. Mandlmeier, A. Keilbach, R. Köhn, M. Döblinger, H. Amenitsch, T. Dörfler, T. Dennenwaldt, T. Bein
Morphology-Control of Ordered Mesoporous Carbons with Extremely High Porosity
5th International FEZA Conference. Valencia, Spain, 03.-07.07.2011

L. Suber, A. Mari, A. Pifferi, H. Amenitsch, M. Fratini and G. Campi
Control of silver-polymer aggregation mechanism by primary particle spatial correlations in dynamic fractal-like geometry
Euromat 2011, Montpelleier, France, 12-15 September 2011 (poster)

C. V. Teixeira, H. Amenitsch, T. Fukushima, J.P. Hill, W. Jin, T. Aida, M. Linden
Helical tape as intermediate in nanotubes formation
X. Brazilian Materials Research Society Meeting, Gramado, RS, Brazil, 25-29 September 2011 (Oral Communication)

F. M. Toma, A. Sartorel, M. Carraro, G. Scoles, M. Bonchio, M. Prato
Functionalization of carbon nanostructures for efficient water oxidation
Hybrid Materials 2011, Strasbourg (France) 6-10 March 2011 (poster)

T. Truong Cong, V. Faivre, C. Gueutin, S. Lesieur
Development of lipid-based nanoparticles for administration of quercetin
XI. Summer School ULLA, Parma, Italy, 2-8 July 2011
A. Turkovic, K. Juraic, M. Rakic, P. Dubcek and S. Bernstorff

SAXS/DSC/WAXD Study of Temperature Evolution in Nanocomposite Polymer Electrolytes with Different Nanofillers
EMRS Spring Meeting 2011, Nice, France, May 9-13, 2011 (poster)

E. M. F. Vieira, J. Martín-Sánchez, S. Levichev, A. G. Rolo, A. Chahboun, M. Buljan, E. Alves, N.P. Barradas, S. Bernstorff, O. Conde, and M. J. M. Gomes
Structural characterization of crystalline SiGe layers grown by RF-Sputtering
EMRS Spring Meeting 2011, Nice, France, May 9-13, 2011 (poster)

A. Yaghmur, S.W. Larsen, M. Schmitt, J. Oestergaard, C. Larsen, C. Jensen, A. Urtti, M. Rappolt
In-situ investigation of lipidic bupivacaine formulations
Conference: "Geometry of Interfaces", Primosten, Croatia, 3.10.2011 - 7.10.2011 (talk)

A. Yaghmur, P. Laggner, M. Almgren, B. Sartori, L. Paasonen, M. Yliperttula, A. Urtti, M. Rappolt
In situ characterization of lipidic aqueous dispersions
Conference: "Geometry of Interfaces", Primosten, Croatia, 3.10.2011 - 7.10.2011 (poster)

ELETTRA Highlights 2010-2011

M. Buljan, N. Radic, J. Grenzer, A. Mucklich, S. Bernstorff, and V. Holy
Growth of spatially ordered Ge nanoclusters in an amorphous matrix on rippled substrates
Elettra Research Highlight, pp. 44-45 (2011)

P. Falcaro, A.J. Hill, K.M. Nairn, J. Jasieniak, J.I. Mardel, T.J. Bastow, S.C. Mayo, M. Gimona, D. Gomez, H.J. Whitfield, R. Riccò, A. Patelli, B. Marmiroli, H. Amenitsch, T. Colson, L. Villanova and D. Buso
Seeding metal organic frameworks using ceramic nano-flaked microparticles
Elettra Research Highlight, pp. 46-47 (2011)

M. Faustini, B. Marmiroli, M. Vayer, C. Sinturel, H. Amenitsch and D. Grosso
Bottom-up approach towards titanosilicate mesoporous pillared planar nanochannels for nanofluidic
Elettra Research Highlight, pp. 54-55 (2011)

G. Pabst, M. Rappolt, H. Jerabek and T. Stockner
Wake me up! Anaesthesia, a membrane mediated loss of sensation?
Elettra Research Highlight, pp. 98-99 (2011)

Contributions to "communicate science in public"

"Lange Nacht der Forschung - an open day at Austrian research facilities", IBN, Graz, Austria, and Outstation (SAXS-beamline at Elettra), Trieste, Italy, April 2011

SAXS training courses

First Tutorial of "Advanced Synchrotron Techniques at ELETTRA (AST 1)", performed at several beamlines of ELETTRA, in Basovizza, on 22+23.3.2011, for students from the Montan University of

Leoben, Austria. Organizers: H. Amenitsch, O. Paris, S. Bernstorff, Elettra / Basovizza (TS), Italy, with tutorials regarding SAXS/WAXS by H. Amenitsch, S. Bernstorff, M. Rappolt; and regarding DXRL by B. Marmiroli.

PhD Thesis / Doktorarbeiten 2011

Michael Edler
Preparation and Characterization of Nanostructured Solar Energy Materials and Nanocomposite Solar Cells
Graz University of Technology, Austria

Achim Fischereder
Synthesis and Characterization of Metal Sulfides for Photovoltaic Applications
Graz University of Technology, Austria

Michael Kerber
X-ray Line Profile Analysis in Theory and Experiment
University of Vienna, Austria

Martin Lončarić
Optical and structural properties of ultrathin films of noble metals,
Faculty of Science, University of Zagreb, Croatia

Andreas Pein
Synthesis and Characterization of Materials for Optoelectronic Devices
Graz University of Technology, Austria

Perrine Pivette
Lipid microspheres obtained by prilling: from the polymorphism of the constituents to the drug release mechanism of a hydrophylic API
Paris-South University, France

Sara R. C. Pinto
Estudo estrutural de Nanocristais de Si1-xGex embebidos em matrizes dieléctricas
University of Braga, Portugal

Jörg Schuster
Morphology Control of Ordered Mesoporous Carbons for High Capacity Lithium Sulfur Batteries
Ludwig-Maximilians-University Munich, Germany

Master Theses (Tesi di Laurea, Diplomarbeit) 2011

Gerald Polt
Mechanisms of Plastic Deformation in γ-Isotactic Polypropylene
University of Vienna, Wien, Austria

Roman Schuster
Characterisation of nanocrystalline metals by X-ray line profile analysis
University of Vienna, Wien, Austria

Tobias Wlochowitz
Zeitaufgelöste Röntgenkleinwinkelstreuung während des Entstehungsprozesses von CdS Nano-Partikeln
University of Erlangen-Nuremberg, Germany

Authors Index

SCIENCE ▪ PASSION ▪ TECHNOLOGY

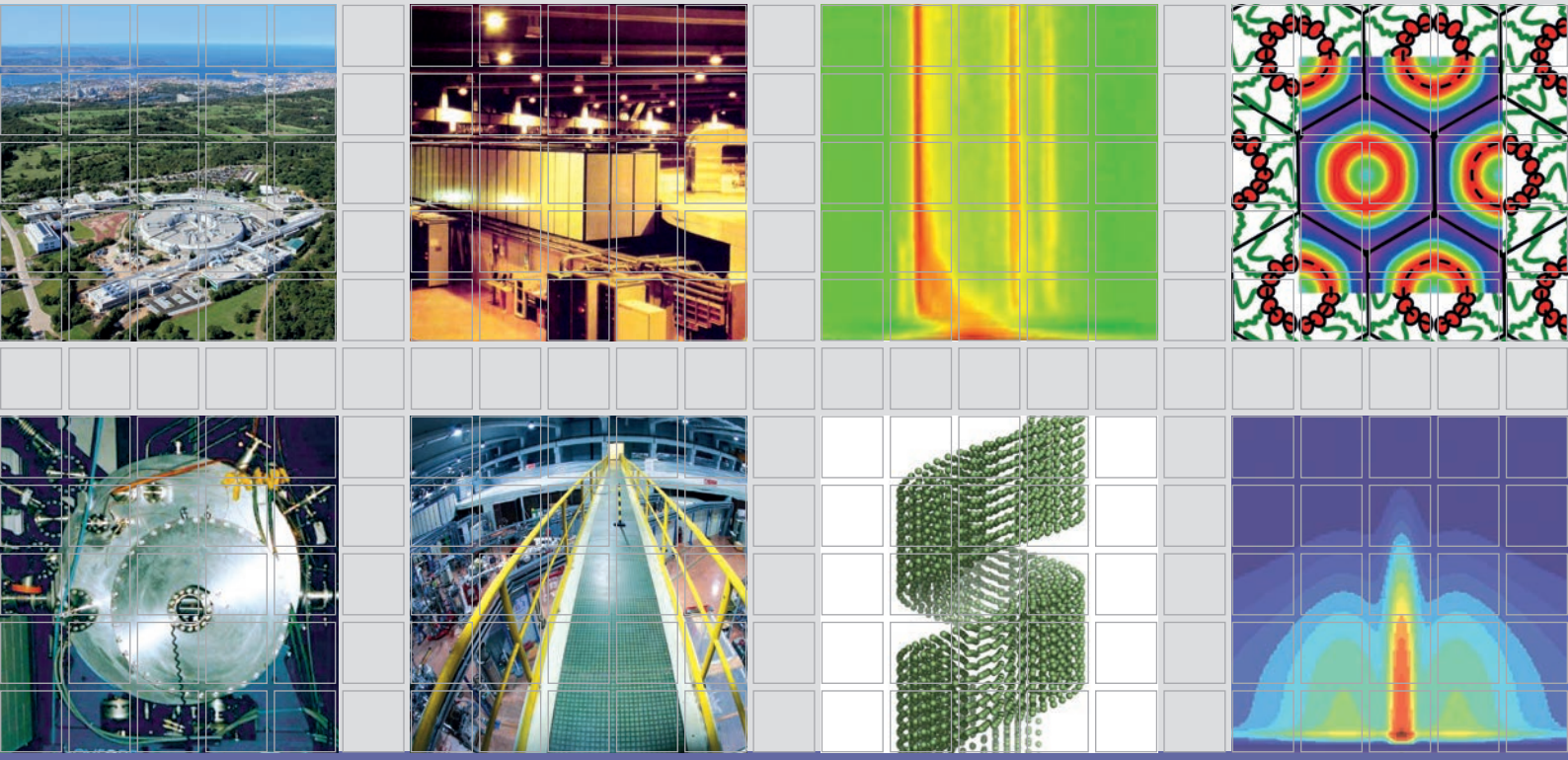

Institute of Inorganic Chemistry
Graz University of Technology
Faculty of Technical Chemistry,
Chemical and Process Engineering,
Biotechnology – TCVB
Stremayrgasse 9/IV8010 Graz, Austria
Tel.: +43 316 873 32145
Fax: +43 316 873 32102
E-mail: amenitsch@tugraz.at
Web: http://ac.tugraz.at

Austrian SAXS Beamline
Outstation of the Institute of
Inorganic Chemistry
Graz University of Technology
c/o Elettra-Sincrotrone Trieste
Strada Statale 14, km 163.5
34149 Basovizza (TS) Italy
E-mail: amenitsch@tugraz.at

Elettra-Sincrotrone Trieste
Strada Statale 14, Km 163,5
34149 Basovizza (TS), Italy
Tel.: +39 040 375 8572
Fax: +39 040 9380 902
E-mail: bernstorff@elettra.eu
Web: www.elettra.eu

Former:
Institute of Biophysics and
Nanosystems Research
Austrian Academy of Sciences
Schmiedlstraße 6, 8042 Graz, Austria